PHYSICAL AND DYNAMICAL CHARACTERISTICS OF EXTREME CLIMATE EVENTS AND THEIR FUTURE PROJECTIONS USING COUPLED MODELS OVER SOUTH ASIAN REGIONS

Thesis Submitted to

UNIVERSITY OF CALICUT

In Partial Fulfillment of the Requirements for the Degree of

Doctor of Philosophy in Physics

Under the Faculty of Science

By

JAMSHADALI V. H.

Postgraduate Department of Physics & Research Centre

Sree Krishna College, Guruvayur

Kerala

January 2024

Dedicated to My Family

DECLARATION

I hereby declare that the thesis entitled **'PHYSICAL AND DYNAMICAL CHARACTERISTICS OF EXTREME CLIMATE EVENTS AND THEIR FUTURE PROJECTIONS USING COUPLED MODELS OVER SOUTH ASIAN REGIONS'** is a genuine record of research work carried out by me at the Post Graduate Department of Physics & Research Centre, Sree Krishna College, Guruvayur for the award of the degree of Doctor of Philosophy in Physics from Calicut University, Kerala, India. The work is done under the supervision and guidance of Dr. Vishnu R., Assistant Professor, Postgraduate Department of Physics & Research Centre, Sree Krishna College, Guruvayur, and under the co-guidance of Dr. Hamza Varikoden, Scientist-F, Centre for Climate Change Research, Indian Institute of Tropical Meteorology, Pune. I also declare that no part of this work has previously been submitted for the award of any degree or diploma at any other university or institution.

Guruvayur

Jamshadali V. H.

CERTIFICATE

This is to certify that the thesis entitled 'Physical and Dynamical Characteristics of Extreme Climate Events and Their Future Projections Using Coupled Models Over South Asian Regions' is an authentic record of the research work carried out by Mr. Jamshadali V. H. under our supervision and guidance in the Department of Physics, Sree Krishna College, Guruvayur, in partial fulfillment of the requirements for the award of the degree of Doctor of Philosophy in Physics. We also certify that this is his original contribution and has not been submitted for the award of any degree or diploma by any other University or Institution.

Dr. Vishnu R.

(Research guide)

Assistant Professor

Department of Physics

Sree Krishna College, Guruvayur

Dr. Hamza Varikoden

(Research co-guide)

Scientist-F

Centre for Climate Change Research

Indian Institute of Tropical Meteorology, Pune

ACKNOWLEDGEMENTS

PREFACE

The South Asian Summer Monsoon (SASM) stands out as a predominant component of the global monsoon system, contributing 80% of the annual rainfall in the area and directly supporting livelihoods and agricultural practices. Due to the indigenous land-sea configuration and the particular atmosphere-ocean-land interaction involved, SASM exhibits unique characteristics in terms of their evolution, variability, and impact. In addition to intraseasonal and interseasonal variations, the South Asian regions frequently experience extreme precipitation events during the monsoon season. These extreme events have the potential to cause property damage, environmental harm, and even fatalities. In the current context of reported climate change and global warming scenarios, understanding the mechanism and variability of the South Asian monsoon and its extremes becomes crucial. This understanding facilitates planning and mitigation purposes and supports the development of proficient forecasts and predictions. It is also essential to comprehend how these events are evolving and may change in the future, particularly for developing countries in the region, such as India. These countries face challenges due to their low adaptive capacity, resulting from both geographical and socio-economic features. It is essential to assess how well global climate models, predominantly used for creating projections, realistically simulate precipitation extremes in these regions. This evaluation becomes crucial for informed decision-making and adaptation strategies in the face of evolving climate patterns. The thesis titled "**Physical and Dynamical Characteristics of Extreme Climate Events and Their Future Projections Using Coupled Models Over South Asian Regions**" aims to explore the characteristics of SASM rainfall and its extremes in prominent regions selected based on spatiotemporal features.

The thesis is structured as follows: **Chapter 1** introduces the study, outlining its scope and objectives. It briefly overviews global monsoon systems and their features, highlighting the variability of the South Asian summer monsoon and extreme rainfall events (EREs) during the season. Additionally, the chapter reviews the previous studies on SASM extremes. It also includes a brief note on the coupled model intercomparison project (CMIP) and projection studies concerning SASM rainfall and its extremes. **Chapter 2** details the data and methodologies employed in the study to address the objectives. The data section gives a concise overview of the observational and model rainfall data used in this study, along with other relevant climatological data. The methodology section covers details such as the study area, methods employed for analyzing the physical and dynamical features of extreme rainfall

events, and the statistical methods adopted in the analysis. **Chapter 3** describes the physical characteristics of the SASM mean and extreme rainfalls over the selected regions and their association with global climate indices. This section illustrates the spatiotemporal variability and associated characteristics of SASM mean and extreme rainfalls and the selection of prominent regions based on the decadal trend of extreme rainfall amounts. Alongside spatial trends, the study illustrates the evolution and dissipation features of EREs in the chosen regions. It also discusses the interannual variability and probability distribution of mean rainfall and EREs and analyzes the association of SASM rainfall and its extremes with various global climate indices. **Chapter 4** illustrates the dynamical characteristics of summer monsoon EREs in the selected regions over South Asia. Exploring the circulation and other meteorological parameters conducive to regional EREs is the primary focus of this chapter. **Chapter 5** presents the selection of CMIP6 GCM models based on their ability to simulate the characteristics of SASM rainfall and EREs. The chapter also analyses the capability of selected CMIP6 GCM models to simulate the regional characteristics of summer monsoon rainfall and extremes. **Chapter 6** explores the projected changes in summer monsoon EREs in the future under different shared socioeconomic pathways (SSP) Scenarios, using the selected CMIP6 models. **Chapter 7** summarizes the overall thesis work, highlighting important findings and concluding remarks. The future prospects of this work and recommendations are presented in **Chapter 8**.

LIST OF PUBLICATIONS

1) **Jamshadali, V.H**., Reji, M.J.K., Varikoden, H. and Vishnu, R., 2021. Spatial variability of South Asian summer monsoon extreme rainfall events and their association with global climate indices. *Journal of Atmospheric and Solar-Terrestrial Physics*, *221*, p.105708. https://doi.org/10.1016/j.jastp.2021.105708

2) Hamza Varikoden, **Jamshadali V. H**., and Vishnu R., 2023. Dynamic aspects of regional extreme rainfall events during the southwest monsoon period over the Indian subcontinent. *Journal of Hydrology.* (Provisionally accepted)

3) Hamza Varikoden, **Jamshadali V. H.**, Catherine George, and Vishnu R., 2023. Historical and Future projections of South Asian summer monsoon extreme rainfall variability using CMIP6 models. *Climate Dynamics* (submitted)

CONFERENCE PRESENTATIONS

1) **Jamshadali V. H**, Hamza Varikoden, Vishnu R (Sep-2020). *Characteristics of extreme rainfall events during the southwest monsoon period and their association with global climate indices.* A three-day International Conference on Aerosol, Air Quality, Climate Change and Impact on Water Resources and Livelihoods in the Greater Himalayas conducted by ARIES (Aryabhatta Research Institute of Observational Sciences).

2) **Jamshadali V. H**, Hamza Varikoden, Vishnu R (Dec-2020). *Spatio-temporal variation of extreme rainfall events during the southwest monsoon period and their association with global forcing mechanisms.* A four-day National Virtual Symposium on Weather and Climate Services over Mountainous Regions – TROPMET-2020 conducted by the Indian Meteorological Society.

CONTENTS

LIST OF FIGURES

LIST OF TABLES

ABBREVIATIONS

99p	99th percentile
AMO	Atlantic Multidecadal Oscillation
APHRODITE	The Asian Precipitation Highly Resolved, Observational Data Integration Towards Evaluation of Water Resources
AUS	Australian monsoon
AZM	Atlantic zonal mode
BoB	Bay of Bengal
CGCM	Coupled ocean-atmosphere general circulation model
CI	Central India
CLIVAR	Climate Variability and Predictability
CMIP5	Coupled Model Intercomparison Project Phase 5
CMIP6	Coupled Model Intercomparison Project Phase 6
CRU	Climate Research Unit
CWD	Maximum length of wet spell, maximum number of continuous days with RR $\geq$ 1mm
DMI	Dipole mode index
EAS	East Asian Summer Monsoon
ECMWF	European Centre for Medium-Range Weather Forecasts
EEIO	Eastern equatorial Indian Ocean
EMI	El Niño Modoki index
ENSO	El Niño-Southern Oscillation
EOF	Empirical orthogonal function
ERE	Extreme rainfall event
ESGF	Earth System Grid Federation
ETCCDI	Expert Team on Climate Change Detection and Indices
GCM	Global climate model
GFI	Global Flood Inventory
GHGs	Greenhouse gases
GMP	Global monsoon precipitation
GPCP	Global Rainfall Climatology Project
HTESSEL	Hydrology Tiled ECMWF Scheme of Surface Exchanges over Land
IFS	Integrated Forecast System

IOD	Indian Ocean Dipole
IOSST	Indian Ocean Sea surface temperature
IPAR	Indo-Pakistan arid region
IPCC	Intergovernmental Panel on Climate Change
ISM	Indian Summer Monsoon
ISMR	Indian summer monsoon rainfall
ISO	Intraseasonal oscillation
ITCZ	Inter-Tropical Convergence Zone
JJAS	June-September
LLJs	Low-level jets
LPS	Low-pressure systems
MCZ	Monsoon core zone
MISO	Monsoon Intraseasonal Oscillation
MJO	Madden Julian Oscillation
MME	Multi-Model Ensemble
MSE	Moist static energy
NAM	North American Monsoon
NCEP/NCAR	National Centers for Environmental Prediction/National Center for Atmospheric Research
NCI	Northcentral India
nd99p	Number of days exceeding 99th percentile
NEMO3.6	Nucleus for European Modelling of the Ocean- revision r9466
NER	Northeastern Region
NH	Northern Hemisphere
NHSM	Northern Hemisphere Summer Monsoon
NOAA	National Oceanic and Atmospheric Administration
NWC	Northern West Coast
OLR	Outgoing longwave radiation
PDF	Probability density function
PDO	Pacific decadal oscillation
PRCPTOT	Annual total precipitation in wet days
R95pTOT	Annual total PRCP of rainfall > 95p
R99pTOT	Annual total precipitation of rainfall > 99p
RCM	Regional climate model

RCPs	Representative concentration pathways
rf99p	Rainfall amount exceeding 99th percentile
Rx1day	Monthly or yearly maximum 1-day precipitation
Rx5day	Monthly or yearly maximum consecutive 5-day precipitation
SAF	South African Monsoon
SAM	South American Monsoon
SAM	South Asian Monsoon
SAS/SASM	Southern Asian Summer Monsoon/ South Asian Summer Monsoon
SCV	Secondary cyclonic vortex
SH	Southern Hemisphere
SHSM	Southern Hemisphere Summer Monsoon
SOM	Self-Organizing Maps
SSPs	Shared socioeconomic pathways
SST	Sea surface temperature
SWC	Southern west coast
TSI	Total solar irradiance
VIMT	Vertically integrated moisture transport
WAF	Western African Monsoon
WCRP	World Climate Research Programme
WGCM	Working Group on Coupled Modelling
WMO	World Meteorological Organization

CHAPTER 1

INTRODUCTION

CHAPTER 1

INTRODUCTION

1.1 An Introduction to Monsoon

'Monsoon' is used to describe a seasonal climate with a noticeable change in the direction of the prevailing winds in the lower troposphere between winter and summer, along with associated precipitation (Ramage, 1971; Rao, 1976). The word 'monsoon' is taken from the Arabic word 'Mausam' (Gadgil, 2006), which means seasons. Arab sailors used this term to represent the seasonal variations of the winds over the Arabian Sea (Ramage, 1971). In common parlance, rainfall during specific rainy seasons is referred to as a monsoon (Gadgil, 2007). The following criteria were put forth by Ramage (1971) to identify the monsoon regions of the world: (1) the predominant wind direction changes by at least 120° between January and July; (ii) the prevailing wind occurs more than 40% of the time on average between January and July. Accordingly, he defined the principal monsoon areas as shown in Figure 1.1. The monsoon is the most energetic climate system in the tropics, and it has a tremendous social and economic impact on billions of people around the world. It is essentially driven by solar forcing and constrained by the planetary-scale overturning circulation (Trenberth et al., 2006; Hsu, 2016). A pair of upper-level twin anticyclones situated in the subtropics of both hemispheres is a common characteristic of tropical monsoon systems (Yim et al., 2014). An empirical orthogonal function (EOF) analysis of multiple variables, including climatological monthly precipitation and low-level wind fields, indicates that the tropical monsoon exhibits two primary modes: a solstitial mode and an equinoctial asymmetry mode (Wang and Ding, 2008).
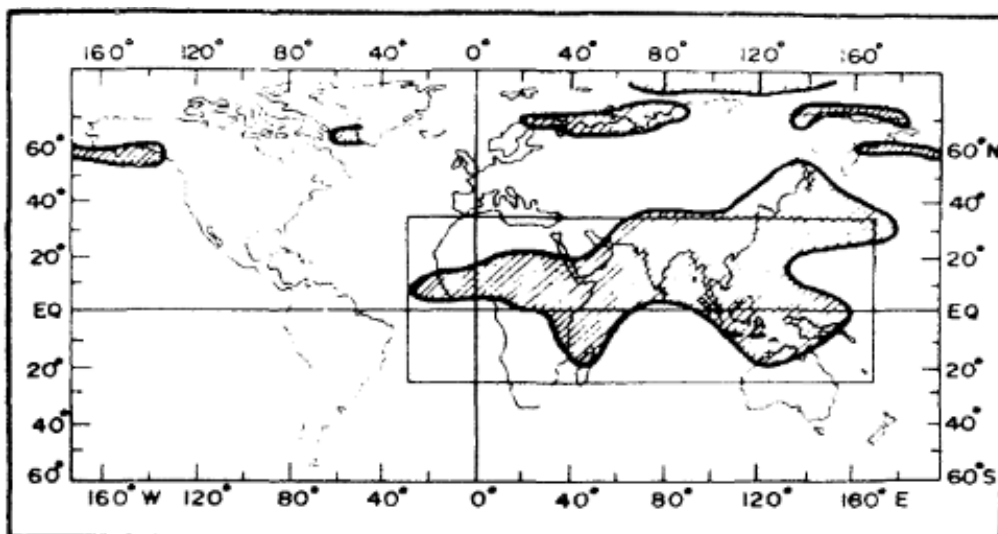
Figure 1.1: Delineation of monsoon region. Monsoonal areas are Hatched. The area inside the box is the classic monsoon climate regime (adapted from Ramage, 1971).

Various studies have thoroughly discussed the complicated nature of the seasonal reversal of winds and the associated precipitation (e.g. Ramage, 1971; Webster et al., 1998; Trenberth et al., 2006; Goswami et al., 2006). The primary cause of all monsoon systems is the springtime solar heating of the land, which contributes to the creation of a land-sea temperature difference (Webster et al., 1998). The fact that the land is warmer than the nearby water causes a contrast, resulting in a low-level flow of moisture from the adjacent oceans, precipitating during convection over monsoonal regions. The latent heat generated by convection high above the ground surface draws in additional rainfall, sustaining the wet season as the monsoon season progresses over the summer. The peak solar heating shifts with the seasons, initially moving towards the equator and subsequently into the Southern Hemisphere (SH), leading to a reversal in temperature and related warming patterns between the land area and adjacent oceans. As a result, the wind direction also reverses, leading to a shift in monsoon rainfall to the opposite hemisphere in response to the seasonal changes. The monsoon system's driving mechanisms are also thought to include the vorticity of the monsoonal winds caused by the Earth's rotation and the moist processes in the atmosphere (Chandrasekar, 2010). The theoretical developments and observational studies suggest an interpretation of the monsoons as localized seasonal migrations of the Inter-Tropical Convergence Zone (ITCZ) (Charney, 1969; Geen et al., 2020). Goswami (2005) explained that the seasonal migration of the ITCZ, or equatorial trough, is in response to the seasonal variation at the latitude of maximum insolation.

1.2 Global Monsoon

Monsoon regions are widely used to describe areas where the winter dry and summer rainy seasons alternate (Webster, 1987; WCRP - World Climate Research Programme). With significant local, regional, and global effects, monsoon systems are the predominant variable in the tropical climate system (WCRP). The monsoon region spans all tropical continents and the tropical waters of the western North Pacific, the eastern North Pacific, and the southern Indian Ocean (WCRP). The evolution of each specific monsoon system is governed by the region's orography, local land-sea arrangements, and feedback from the many components of the climate system (Webster, 1987; Goswami, 2005). The various monsoon domains, based on precipitation characteristics, are defined by regions where annual rainfall exceeds 180 mm, and local summer monsoon precipitation accounts for more than 35% of the annual rainfall (Wang and Ding, 2006). Figure 1.2 represents the global land monsoon regions defined according to rainfall climatology for the period 1901–2020 based on the monthly Climatic Research Unit (CRU) precipitation data.
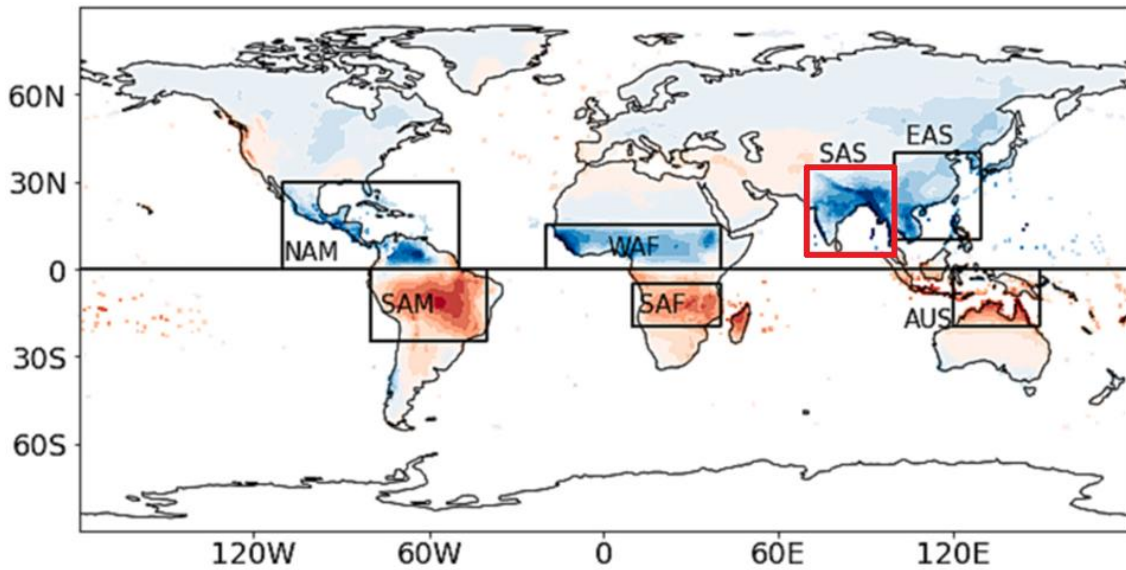
Figure 1.2: The global land monsoon regions defined according to rainfall climatology for the period 1901–2020 by using monthly CRU precipitation data (taken from Fazal et al., 2023).

Global monsoon precipitation (GMP) over land, representing the total amount of summer monsoon precipitation in the land monsoon region, has experienced multi-decadal variations in the last century. It showed a slightly increasing trend in the first half, from 1900 to 1950, followed by a decreasing trend from the 1950s to the end of the 1970s. After 1980, there has been no clear trend (Hsu, 2016). Recent studies, however, have indicated an upward trend in GMP in the Northern Hemisphere (NH) over the past three decades. Conversely, the trend in Southern Hemisphere GMP is weak and insignificant (Deng et al., 2018; Wang et al., 2020). Predicting weather patterns over the ocean has become less certain in the last 30 years. Under global warming scenarios, the Coupled Model Intercomparison Projects (CMIP5, CMIP6) predict a significant increase in GMP in the twenty-first century. Global warming changes the hydrological cycle by increasing the water vapour content in the atmosphere, which contributes positively to surface evaporation and moisture convergence (Hsu, 2016).

The dominant regional monsoon systems over the landmass include the North American monsoon (NAM), the Western African monsoon (WAF), the Southern Asian summer monsoon or Indian Summer monsoon (SAS or ISM), the East Asian summer monsoon (EAS), the South American monsoon (SAM), the South African monsoon (SAF), and the Australian monsoon (AUS) (Figure 1.2) (Webster et al., 1998; Wang and Ding, 2008; Zhou et al., 2016; Wang et al., 2020; Chang et al., 2022). The characteristics and changes of each regional monsoon have been extensively studied over the last few decades (Meehl, 1994; Goswami and Xavier, 2005; Turner and Annamalai, 2012; Chang, 2004; Wang et al., 2008; Manton and McBride, 1992;

Bowmann et al., 2010; Kutzbach and Liu, 1997; Vera et al., 2006). The characteristics of these regional monsoons are briefly described in the following paragraphs.

The NAM is a complex weather pattern that occurs between June and mid-September. The weather is marked by more thunderstorms and rain covering significant parts of the southwest United States and northwest Mexico. More than half of the annual precipitation in the region is obtained during this season. During the NAM, the surface winds in the northern Gulf of California undergo a seasonal reversal, bringing moisture over the region, which results in summer thunderstorms, especially at higher elevations (Tang and Reiter, 1984; Badan-Dangon et al., 1991; Barlow et al., 1998). The NAM shares many similarities, such as onset, seasonal reversal of winds, and the existence of local surface low-pressure centres, with its South Asian counterpart (e.g., Tang and Reiter, 1984; Barlow et al., 1998). However, there are differences in the diurnal cycle, thunderstorms, and nocturnal nature. The NAM is not as strong and impressive as its Indian counterpart, primarily because the Mexican Plateau is not as high (with a mean elevation of 1500m) or as large as the Tibetan Plateau (with a mean elevation of 4500m) in Asia (Higgins et al., 1997). The planetary boundary layer (PBL) over the Mexican Plateau is approximately 850 mb in surface, whereas that of the Tibetan Plateau is 600 mb in surface.

The SAM is one of South America's most notable summertime weather patterns, exhibiting significant seasonal variation in an area between the Amazon and the La Plata Basin (Marengo et al., 2012). The landmass extends across the equator from about 10° N to 55° S. Similar to the NAM, it contributes to more than 50% of the annual precipitation in the region and shares many features with its Asian counterpart (Vera et al., 2006). Moisture transport from the Atlantic Ocean and tropical latitudes, along with midlatitude systems, plays an important role in modulating the seasonal convection and rainfall over the region (Nogués-Paegle et al., 2002).

The Australian summer monsoon widely influences the climate of the Australian tropics during the period from December to March (Suppiah, 1992). The monsoonal area covers over 90% of the Northern Territory, i.e., north of 25°S over Australia (Suppiah, 1992). The AUS exhibits many similar features to its Asian counterpart, including a distinct onset, active-break cycles during the season, and intraseasonal and interannual variability (Davidson et al., 1982; Hendon and Liebmann, 1990a; Drosdowsky, 1996; Wang et al., 2004). The monsoon activity and its variations are characterised by the monsoon equatorial trough in the lower atmosphere, low-latitude westerly winds, the location of the monsoon shear line, and intraseasonal and interannual oscillations in the monsoon circulations. It is also modulated by various triggering

mechanisms such as tropical cyclones, a NH cold surge in the South China Sea, the westward propagation of equatorial westerlies from the Pacific Ocean, and El Niño Southern oscillations (Davidson et al., 1982; Suppiah, 1992).

The Western or Northern African monsoon is a weather phenomenon affecting Africa's western region, particularly the Sahel and the Sahara Desert. The geographical area spans approximately from 5°N to 20°N in latitude and from 10°W to 20°E in longitude. Like other regional monsoons, it is characterised by a seasonal reversal of wind patterns, leading to distinct wet and dry seasons in the affected areas. The WAF is influenced by several factors, including the temperature contrast between the Sahara Desert and the cooler waters of the Atlantic Ocean, as well as the Intertropical Convergence Zone (ITCZ) (Hastenrath, 1991). The onset, duration, and intensity of the Northern African monsoon can vary from year to year. The peak rainfall activity usually occurs in July and August. Factors such as sea surface temperatures (SSTs), atmospheric pressure patterns, and El Niño-Southern Oscillation (ENSO) events in the Pacific Ocean also influence its behaviour (Yim et al., 2014).

The SAF is not as strong and vibrant as other monsoons. The primary drivers of South Africa's climate are its topography and the influence of oceanic currents. During the austral summer (December to February), the ITCZ shifts southward, bringing moist air and rainfall to the region. The SAF is influenced by climate phenomena such as the ENSO and the Indian Ocean Dipole (IOD). El Niño is associated with reduced rainfall over southern Africa, resulting in drought conditions and decreased agricultural productivity. Positive IOD events featuring cooler waters in the eastern Indian Ocean are associated with increased rainfall over southern Africa. In comparison, negative IOD events with warmer waters in the eastern Indian Ocean can result in drier conditions.

Alongside external solar forcing, regional monsoons are modulated by internal feedback processes such as the ENSO, with a more significant influence from the northern hemisphere summer monsoon (NHSM) than the southern hemisphere summer monsoon (SHSM) (Wang et al., 2011). However, apart from the AUS, all regional summer monsoons have shown a non-stationary association with ENSO over the past 55 years. It was discovered that the relationships between regional monsoons and ENSO experienced comparable shifts in the 1970s. The connections strengthened for the summer monsoons in the western North Pacific, Northern Africa, North America, and South America. Still, they weakened during the summer monsoon in India (with a recovery in the late 1990s) (Yim et al., 2014).

More than 50% of the world's population, which primarily relies on agriculture for their subsistence, depends on monsoon rainfall, which is essential to their well-being (WCRP). Due to its effects on more than 65% of the world's population, the variability in the regional monsoon precipitation and atmospheric circulation are of significant scientific and societal importance. Predicting how the monsoon will change in the following decades is extremely important for building infrastructure, managing water resources, and fostering sustainable agricultural and economic growth, especially in less developed countries and regions (Zhou et al., 2016). Numerous studies are being carried out to enhance our knowledge of the predictability of the monsoon, improve the precision of forecasts, and develop scenarios for the effects of human-induced climate change on monsoonal systems globally (WCRP). We can create substantial social and economic benefits by making the most of the advantages of monsoon rain and reducing the impact of extreme events. This is particularly important in countries like those in South Asia and Australia, where we've witnessed these effects over the past few decades. (WCRP).

1.3 Asian Monsoon

The Asian monsoon is one of the predominant components of the global monsoon (Trenberth et al., 2006). Considering the heterogeneity within the monsoon region, it is classified into many subsystems, including the Indian monsoon, the East Asian monsoon, the western North Pacific monsoon, etc. (Kripalani and Kulkarni, 1997; Wang and LinHo, 2002; Yihui and Chan, 2005). It comprises both summer and winter counterparts (Ju and Slingo, 1995; Wang et al., 2006; Wang and Lu, 2017). During the summer monsoon, surface-level south-westerly winds prevail with two branches, i.e. the Arabian Sea and Bay of Bengal (BoB) branches. In the winter monsoon, the prevailing surface winds near the equator blow from the northeast direction, and there is only one branch for it (Wang, 2006). The summer monsoon brings rain to the greater part of India from June to September (JJAS period). The Asian monsoon system contributes 80% of the annual rainfall in the area, directly supporting the livelihoods and agricultural practices of over 20% of the world's population (Turner and Annamalai, 2012). In the context of global climate change, comprehending the mechanism and variability of the Asian monsoon becomes crucial, facilitating the development of proficient forecasts, predictions, and reasonable future projections. While the subsystems of the Asian monsoon have strong mutual linkages, they exhibit variations from synoptic to multidecadal and longer time scales due to their interaction with the Earth's Ocean, land, atmosphere, biosphere, and others via complex land-ocean coupled processes (Huang et al., 2013; Chen et al., 2019). The

influence of ENSO on the Asian summer monsoon (ASM) is crucial (Xie et al., 2016; Li et al., 2017; Zhang et al., 2018. Other global climate variables, such as the IOD (Saji et al., 1999), El Niño Modoki (Ashok et al., 2007; Wang et al., 2018), the Atlantic Multidecadal Oscillation (AMO) (Lu et al., 2006; Wei and Lohmann, 2012), and the North Pacific Victoria Mode on the Madden-Julian Oscillation (Wen et al., 2020), also exert predictable influences on the variability of the Asian monsoon.

1.4 South Asian Summer Monsoon

The South Asian summer monsoon (SASM), commonly referred to as the Indian summer monsoon (ISM), is typically associated with the June-September (JJAS) rainfall over the Indian subcontinent, characterised by a very wet summer and a dry winter (Goswami et al., 2019). ISM and its variability are directly linked to water security, food security, economic growth, and socio-cultural literacy in the region (Gadgil and Gadgil 2006). Similar to other monsoon systems, the SASM is part of an annually reversing wind system and the associated rainfall (Ramage, 1971; Rao, 1976). During this season, monsoonal south-westerlies transport abundant moisture from the tropical Indian Ocean into the subcontinent, resulting in increased precipitation in the region (You and Ting, 2021). It is interpreted that the monsoon is triggered by the northward seasonal migration of the east-west oriented precipitation belt (Inter Tropical Convergence Zone, ITCZ) from the SH in the winter season to the NH in the summer season (Gadgil, 2003).

Due to the indigenous land-sea configuration and the particular atmosphere-ocean-land interaction involved, regional monsoon systems exhibit unique characteristics in terms of their evolution, variability, and impact (Zhou et al., 2016). Unlike other monsoons, the Indian monsoon is a coupled ocean-atmosphere phenomenon in which the elevated Tibetan Plateau heats the warm land and cool ocean, creating a strong north-south gradient that intensifies the monsoon over the Indian subcontinent. Land-surface processes are more sensitive in the Indian monsoon compared to the narrow continental extent of the AUS (Yasunari et al., 2006), and the impact of soil moisture is also significant in relatively dry monsoons such as the Indian monsoon (Misra and DiNapoli, 2014). During the break-off states of the ISM, the EAS is quite active, and vice versa (Qiangen et al., 1986). Zhou et al. (2008) reported that the North African and South Asian monsoons (SAM) have shown significant decreasing tendencies in rainfall intensity and coverage area during the last 54 years. During the summer monsoon season in India, the convective activity has a remote impact on the North African monsoon (Janicot et al., 2009). The Indian monsoon's active and break periods, driven by temperature changes in

the Indian region, can influence the African monsoon about 15–20 days later through atmospheric connections.

The strong low-level winds during the summer season are contributed to by the low-level westerly jets (LLJs) at 850 hPa over the Arabian Sea and the monsoon trough associated with big-scale cyclonic vorticity, which extends from the north BoB to western India. The upper-level winds are characterised by the easterly jet centred around 5°N and the Tibetan anticyclone centred around 30°N (Lau et al., 2012). Compared to other tropical monsoons, the most extensive northward excursion of the rain belt takes place over the Indian monsoon region, where it moves from a mean position of about 5°S in winter to about 20°N in northern summer (Waliser and Gautier, 1993). Figure 1.3 shows the synoptic and smaller-scale circulation features of SASM rainfall.
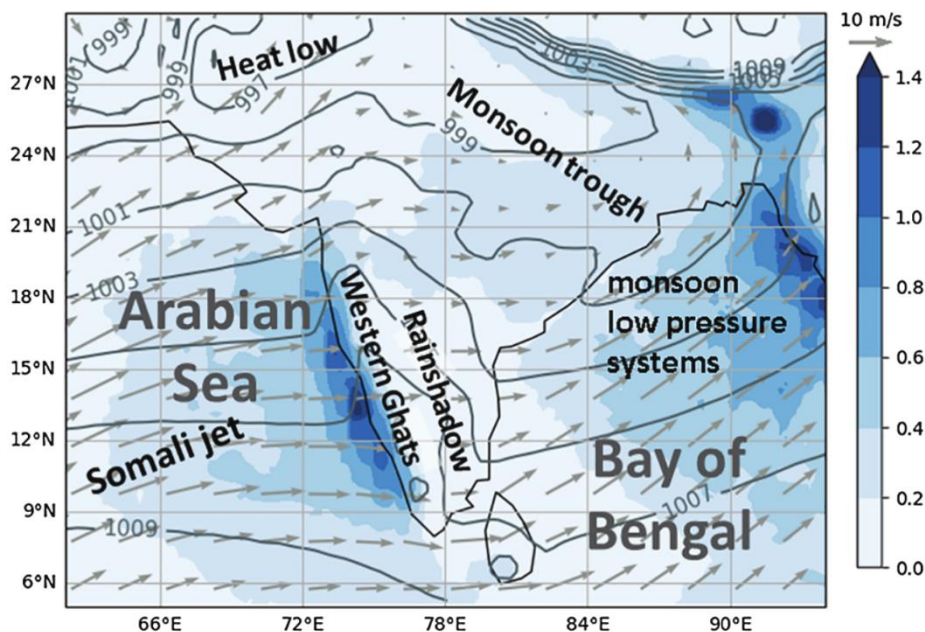
Figure 1.3: Primary synoptic and smaller-scale circulation features of SASM rainfall. Mean rainfall (TRMM 3B42, 1998–2016, blue shading), sea level pressure (ERA-Interim, contours), and 950 hPa horizontal winds (arrows) in June are presented (taken from Fletcher et al, 2020)

Asian summer monsoons, particularly the ISM, exhibit a strong annual cycle, unlike other monsoon systems. The onset stage is characterised by an abrupt transition from the dry season to the rainy season and subsequent seasonal changes (Wang and Ding, 2006). It brings about a significant shift in the hydroclimate of the region, offering relief from the oppressive heat of the pre-monsoon season and replenishing the supply of terrestrial freshwater to meet the demands of the local population (Misra et al., 2017). The onset typically initiates along the

west coast of the Indian subcontinent, specifically in Kerala, usually by the end of May or early June. The monitoring of the onset has evolved from solely relying on precipitation to considering factors such as the wind field, outgoing longwave radiation, rainfall moisture flux convergence, and precipitable water (Fasullo and Webster, 2003; Pai and Rajeevan, 2007; Wang et al., 2009; Lu et al., 2009). The onset process of the ISM is very rapid and takes only a couple of days to complete the dramatic transformation, accompanied by changes in rainfall, outgoing longwave radiation (OLR), and low-level winds from the dry to the rainy season. During the onset, a cross-equatorial low-level jet is established, extending from the Somali jet into the near-equatorial Arabian Sea (Ding, 2007); an onset vortex is often observed (Krishnamurti et al., 1981).

ISM gradually advances northward and eventually merges with the BoB component. By the middle of July, the ISM spread over the whole Indian subcontinent. Although the start of the monsoon season in Kerala is a definitive sign that the system has begun, the development of the ISM in other specific sub-regions of the country is sometimes untimely, notably for rural agrarian households dispersed throughout the nation (Bansod et al., 1991). The onset and demise of the ISM are strongly correlated with large-scale variations in ocean and atmospheric circulation patterns, as well as land-ocean thermal gradients. These variations are, in turn, linked to significant energy transformations and instabilities (Noska and Misra, 2016; Krishnamurti et al., 2017). Misra et al. (2017) demonstrated that substantial interannual variations in the local onset and demise of the ISM are associated with ENSO and the IOD mode. Additionally, it has been ascertained that the onset of monsoon rains in northeast India at an early stage holds the ability to forecast subsequent irregularities in seasonal rainfall patterns and the duration of the monsoon season across the rest of India.

The summer monsoon mean rainfall, averaging about 8 mm day^{-1}, does not constitute a constant downpour but rather exhibits significant variations within the season, spanning from June 1 to September 30. Rainfall during the summer monsoon period displays diverse variabilities, ranging from diurnal to multidecadal periodicities. Alongside daily fluctuations, the monsoon season is characterised by extended active and break spells, often lasting for two to three weeks. Active or robust monsoon spells signify prolonged periods of above-average rainfall, while dry spells indicate intervals when the monsoon recedes from its vigorous activities (Ramamurthy, 1969; Raghavan, 1973). The principal rain-generating systems across the Indian monsoon region are the monsoon low-pressure systems (LPS) and depressions, commonly referred to as synoptic disturbances (Goswami et al., 2003). These systems typically

operate on temporal and spatial scales of 3-5 days and 2000 km. LPS denote regions with comparatively lower atmospheric pressure compared to their surroundings. They can induce cloud formation and precipitation, contributing significantly to monsoonal rainfall. Depressions, on the other hand, represent areas of low atmospheric pressure characterised by closed circulation. They often intensify into tropical cyclones but can also bring heavy rainfall and gusty winds even before they become cyclones (Goswami et al., 1980). Tropical cyclones are powerful storms that originate over warm ocean waters. They can significantly impact the Indian monsoon by bringing heavy rainfall and strong winds, disrupting the normal flow of the monsoon currents. As the lows and depressions are shear instabilities energised by moist convection, large meridional shear of the eastward component of winds, and high values for the cyclonic vorticity at low levels over the monsoon trough region, they favour the growth of these instabilities (Goswami and Ajayamohan, 2001).

1.5 ISM Rainfall Variability
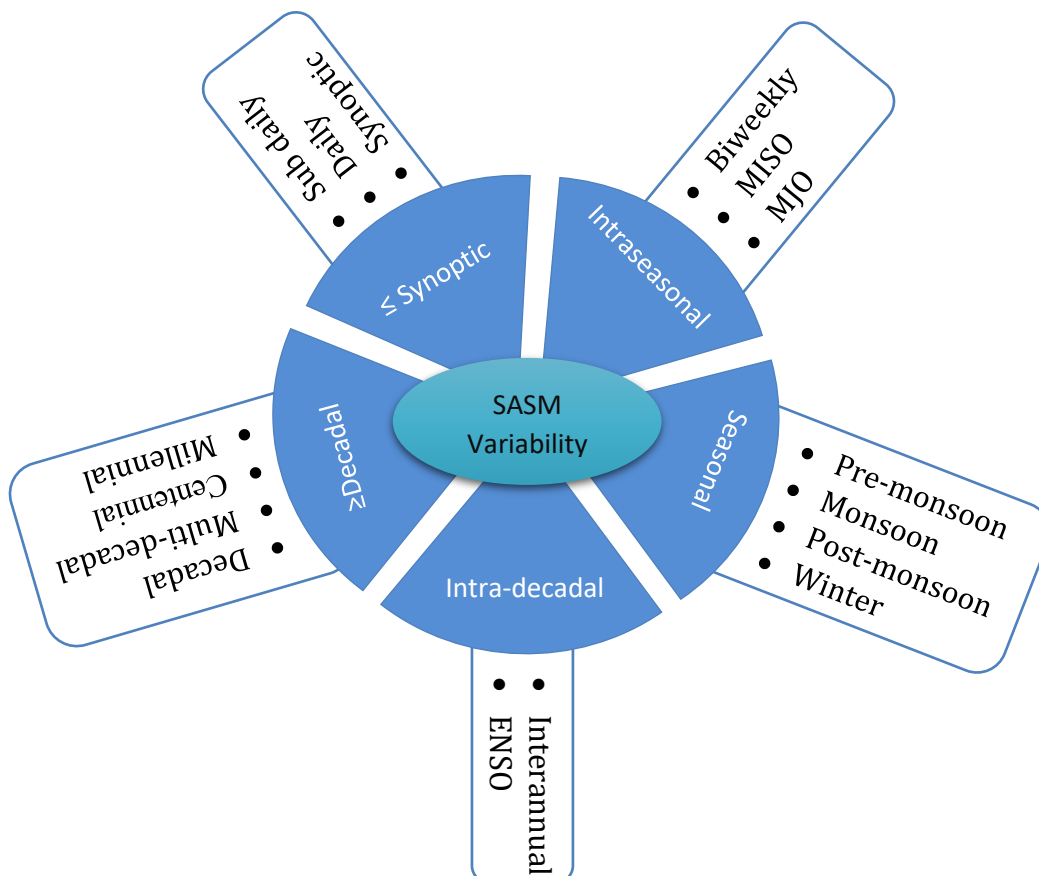
Figure 1.4: Schematic figure representing temporal variability of ISM rainfall

The temporal variability of Indian Summer Monsoon (ISM) rainfall ranges from diurnal to multi-decadal scales and even millennial scales. Figure 1.4 represents a schematic view. Major variabilities are discussed in the following sections.

1.5.1 Diurnal Variability

Diurnal variations refer to the daily cycle of weather patterns and atmospheric conditions associated with the monsoon. The diurnal variation of the monsoon is primarily driven by the differential heating between land and sea (land/sea breezes) and is influenced by several factors, including local wind patterns, topographical features, and the movement of weather systems (Ramege, 1964; Pathan, 1994; Basu, 2007). The nature of the diurnal variation of rainfall varies from place to place and depends on the location, elevation, or topography of the region (Sahany et al., 2010). The diurnal variation in rainfall over an area is dominated by topographical features and synoptic systems such as mesoscale circulations (e.g., land-sea breezes, katabatic-anabatic winds, mountain valley winds, etc.) at the location (Basu, 2007). The diurnal cycle over continental regions is primarily influenced by the solar cycle, and the associated rainfall is closely linked to the region's boundary layer heating and cloud cover (Bhate and Kesarkar, 2019). In the context of India, where a significant portion of the country is situated within the tropical region, the primary driver of diurnal variations in rainfall stems from ground heating induced by solar radiation. This phenomenon plays a pivotal role in shaping the daily patterns of precipitation. The diurnal pattern of rain intensity differs from the mean rainfall and is more prevalent in the Central India region (Varikoden et al., 2012). Various studies have analysed the relationship between intraseasonal oscillation (ISO) and the diurnal variation of summer rainfall in different monsoon regimes (Goswami, 2005; Singh and Nakamura, 2010; Deshpande and Goswami, 2014). The spatial variations in daily rainfall patterns across different parts of the country during active and break phases can be attributed to orographic effects and heterogeneous convective development (Deshpande and Goswami, 2014). Along the west coast, maximum rainfall happens during the morning hours in both the active and break cases, with small diurnal variations. Along the foothills of the eastern Himalayas, during break periods, peak precipitation is observed during the early morning, while the least amount of rainfall is recorded in the afternoon. Over central India, two peaks in the daily weather cycle are observed during the active phases, one in the morning and the other in the evening. Researchers have recently observed a shift in the afternoon peak timing and a rise in rainfall intensity in the central Indian region during the break phase. Additionally, there

has been an observed increase in rainfall intensity throughout all hours of the day during break phases along the west coast of India.

1.5.2 Intraseasonal Variability

The intraseasonal variations in circulations lead to the intraseasonal variations of rainfall (active-break cycles) (Webster et al., 1998; Goswami and Ajayamohan, 2001). According to Dey et al. (2022), the intraseasonal variations of the Indian summer monsoon rainfall (ISMR) are controlled mainly by the Monsoon Intraseasonal Oscillation (MISO) and the Madden Julian Oscillation (MJO). The MISO phenomenon involves the occurrence of active and break spells within the monsoon period. During the active phase, there is enhanced and widespread rainfall across various parts of India, mainly in the central Indian monsoon core region. This phase might bring heavy rainfall, increased cloud cover, and a higher frequency of thunderstorms. On the other hand, during the break phase, there is a reduction in rainfall activity over the monsoon core areas, leading to drier conditions (Singh et al., 1992; Rajeevan et al., 2010; Goswami, 2012). Figure 1.5 illustrates the active and break phases of the ISMR in 1987, as per the criteria established by Rajeevan et al. (2006). MISO is associated with the explicit northward propagation of positive or negative precipitation anomalies (Sikka and Gadgil, 1980). It could be thought of as a manifestation of the fluctuations of the ITCZ within the continental region of the Indian subcontinent (between 10° and 25° N) and the eastern equatorial Indian Ocean (EEIO) (Chattopadhyay et al., 2019). The key characteristics of the active/break cycles associated with MISOs are illustrated by Self-Organizing Maps [SOM (Kohenen, 1990)]. The SOM shows a systematic increase in rainfall over central India during an active phase and a decrease in rainfall over the tip of peninsular India near the Tamil Nadu coast. The SOM also depicts an increase in rainfall over the Himalayan foothills and a reduction in rainfall over central India during the break phase (Chattopadhyay et al., 2019). The length and frequency of active and break spells can modulate the interannual variability of the ISM. Flooding (drought) conditions can develop when active (break) episodes last for a week or longer (Joseph et al., 2009). Long breaks are the underlying process through which monsoon droughts develop. The MISO typically operates on a time scale of approximately 30 to 60 days; its spatial structure is similar to the seasonal mean.

The MJO is a significant climate phenomenon that affects the tropical regions of the Indian Ocean and the western Pacific. The MJO is characterised by a large-scale pattern of enhanced and suppressed rainfall that propagates eastward across the tropics (from the western Indian

Ocean towards the central and eastern Pacific) for approximately 30 to 60 days (Madden and Julian, 1994; Zhang, 2005). The MJO involves the interaction between atmospheric circulation, moisture, and convection, leading to the formation of organised cloud clusters and rainfall anomalies. The MJO has global teleconnections, meaning its effects are felt far from their origin. For example, it can modulate the intensity and frequency of tropical cyclones, influence the onset and withdrawal of the Indian monsoon, and impact weather patterns in America and other regions (Hendon and Liebmann, 1990; Lawrence and Webster, 2002; Bond and Vecchi, 2003; Liebmann et al., 2004; Chattopadhyay et al., 2019).

Based on the findings of Dey et al. (2022), MISO phases are more frequently associated with active/break spells than MJO phases. The phase composite also indicates a lead-lag relationship between the MISO and MJO phases (Dey et al., 2022). Compared to the MJO phase composite, the MISO phase composite demonstrates stronger northward propagation. It has been reported that long active spells (lasting over one week) are mainly observed when either MISO, MJO, or both are active. Conversely, a prolonged break occurs when the MISO and MJO are weak, or at least one (MJO/MISO) is weak (Dey et al., 2022).
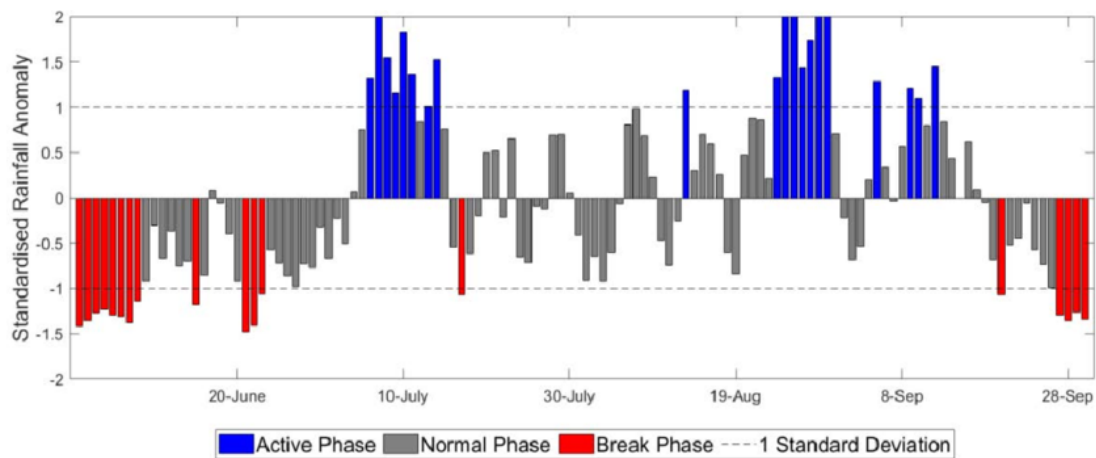
Figure 1.5: Normalized rainfall anomaly in the Indian region for the summer monsoon period of 1987. (taken from Mohanty et al, 2023)

According to Goswami et al. (2003), the active-break cycles arise from the spatiotemporal clustering of lows and depressions and are modulated by monsoon ISOs. Predicting intraseasonal variability is crucial in many sectors, such as agriculture, health, hydrology, and power (Pattanaik et al., 2020).

1.5.3 Interannual Variability

The interannual variability of ISMR is the variation in mean ISMR from year to year and can be classified as a flood year, a drought year, or a normal year. When the percentage deviation of the ISMR for a certain year is 10% above the mean, that year is regarded as a flood year. When it is 10% below the mean ISMR, the year will be drought. Year-to-year variation of ISMR is strongly correlated with food production in the region (Parthasarathy et al., 1988; Webster et al., 1998). Figure 1.6 represents the interannual variability of ISMR from 1871 to 2021. The IOD and ENSO are thought to be the leading causes of the interannual variability of ISMR, especially extreme rainfall events (EREs) (Varikoden and Reji, 2022). The ENSO bridges the ISMR through the equatorial Walker and local Hadley circulations (Goswami, 1998; Varikoden and Preethi, 2013). The calculation of the probability density function (PDF) of ISO activity from combined vorticity and outgoing longwave radiation shows that strong monsoon years are associated with a higher probability of the occurrence of active conditions, and weak monsoon years are associated with a higher probability of the occurrence of break conditions (Goswami and Ajayamohan, 2001). As suggested by Joseph et al. (2011), the prediction skill of the interannual variability of the ISM has two components: "external" as well as "internal". The external forcings primarily contribute through ENSO and internally
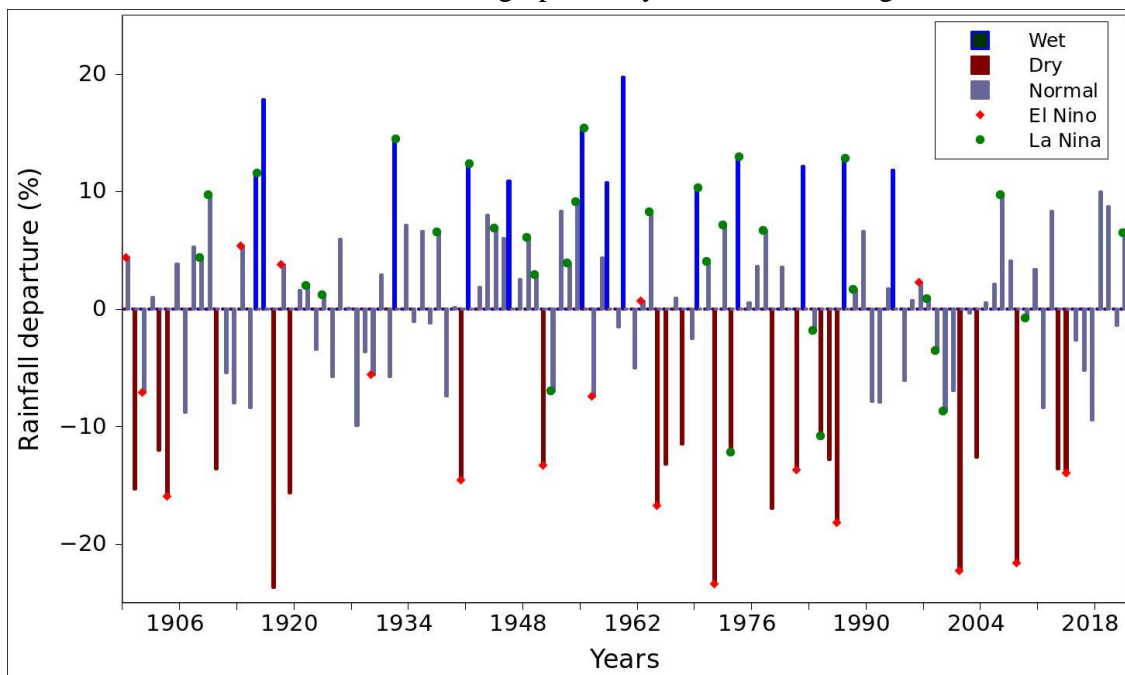
Figure 1.6: The percentage departure of ISMR over the past 122 Years (taken from monsoon online, IITM Pune, https://mol.tropmet.res.in/).

through the nonlinear interaction between ISOs and the seasonal cycle. Some contributions could also come from interactions between the monsoon flow and topography (Krishnamurthy

and Shukla, 2000). The interannual variability of the monsoon becomes very challenging to predict as the internal monsoon ISOs are constrained by external forcings like ENSO (Joseph et al., 2011).

1.5.4 Decadal and Multidecadal Variability

Decadal variability refers to fluctuations and changes in the behaviour of the monsoon over a roughly ten-year timescale. The decadal variability of the ISM can be characterised by positive and negative phases. During a positive phase, the monsoon tends to be more vigorous, resulting in above-normal rainfall. In contrast, a negative phase is associated with weaker monsoon activity and below-normal rainfall. The multidecadal fluctuations cover longer time scales, usually several decades, combining the variabilities above as well as potential slow-changing mechanisms in the climate system. The decadal to multi-decadal scale variability of the ISMR is mainly caused by Pacific decadal oscillation (PDO), Atlantic multi-decadal oscillation (AMO), and external climate forcings, such as greenhouse gases (GHGs), volcanic eruptions, and total solar irradiance (TSI) (Malik et al., 2017). The inter-decadal variability in the ISMR has been linked with the inter-decadal fluctuations of the Pacific (Krishnan and Sugi, 2003; Goswami et al., 2006), North Atlantic (Lu et al., 2006; Zhang and Delworth, 2007; Goswami et al., 2016), and Tropical Indian Ocean SSTs (Vibhute et al., 2020). Along with inter-annual changes, ENSO, PDO, and AMO also have a 50–80-year multi-decadal variability, and their coherence with Asian monsoon shows that they are all likely to be integral parts of a global multi-decadal mode (Goswami et al., 2016). They suggested that long-term variability might result from ocean, atmosphere, and land interactions. Based on the data period 1871–2000, Krishnamurthy and Goswami (2000) found that the inter-decadal variability of the ENSO phenomenon was strongly negatively correlated with the inter-decadal variability of the ISMR, and it is thought to be a manifestation of a global-scale oscillation on a quasi-60-year time scale. The decadal-scale variability of the ISMR is also correlated with the circulation features of the NH (Kripalani et al., 1998). According to numerous studies, dry periods in the ISMR are commonly associated with a negative phase of the AMO followed by a positive phase of the PDO. The observational and simulated datasets confirm the negative correlation of ISMR with PDO on decadal to multi-decadal timescales. In contrast, its correlation with AMO and TSI is not stationary over time (Malik et al., 2017). Due to the intricate interactions between numerous climatic and oceanic variables, it has become difficult to pinpoint the precise causes of these longer-term multidecadal changes (Goswami et al., 2016). Studying how different modes and

climate influences interact with the ISMR can enhance our ability to predict it over a decade to multiple decades.

1.6 Extreme Weather and Climate Events

Extreme weather and climate events refer to significant and often unpredictable deviations from normal weather patterns, taking the form of floods, droughts, heat waves, cold snaps, cyclones, tornadoes, thunderstorms, wildfires, hailstorms, landslides, tsunamis, and more. The unusual occurrence could be either higher than a specific limit in the upper range of observed values for the variable or lower than the limit in the lower range. (WMO- World Meteorological Organization, 2010). "Climate extremes" refers to extreme weather and extreme climatic events, including drought, extremely high temperatures, and excessive precipitation. (IPCC-Intergovernmental Panel on Climate Change, 2012). These events have garnered increased attention recently (Fan and Chen, 2016) due to their profound and far-reaching impacts on society across multiple dimensions, including the environment, infrastructure, economies, and human well-being (IPCC, 2007). Rainfall extremes, or hydroclimatic extremes, hold significant importance in Earth's hydrological cycle (Trenberth, 2011; Krishnan et al., 2016; Giorgi et al., 2019; Veiga and Yuan, 2021), as human activities can influence this cycle through deforestation, urbanisation, and climate change. Unusually heavy rainfall amounts that surpass typical statistical values are considered rainfall extremes. Like other weather extremes, rainfall variability has also exhibited a robust shift in response to warming (Pendergrass et al., 2017). The increased surface evaporation and airborne water content have facilitated the intensity of regional and global water cycles and the likelihood of extreme precipitation (Liu et al., 2015). The highly erratic pattern of a region's rainfall over time and space may indicate a changing climate (Beck et al., 2015).

EREs and their changes have been assessed based on the frequency of occurrences above a threshold, often using a percentile such as 95th, 99th or 99.9[th] (Zhang et al., 2011; Varikoden et al., 2012; Jamshadali et al., 2021). The percentile value is calculated based on the amount of rainfall over a climatological period, and a rainfall event is considered extreme if the rainfall exceeds the selected percentile for the region. The selection of the percentile value depends on the time slice considered, the chosen regions, and the study's objective (Varikoden and Reji, 2022). Many studies frequently appended a threshold value to the percentile value to prevent errors caused by places with climatologically low rainfall (Goswami et al., 2006). The various criteria defined by ETCCDI (Expert Team on Climate Change Detection and Indices) and used to substantiate extreme precipitation events include PRCPTOT (annual total precipitation in

wet days), R99pTOT (annual total precipitation of rainfall > 99p), R95pTOT (annual total PRCP of rainfall > 95p), CWD (maximum length of wet spell, maximum number of continuous days with RR ≥ 1mm), Rx1day (monthly or yearly maximum 1-day precipitation), and Rx5day (monthly or annual maximum consecutive 5-day precipitation)

1.7 Global Precipitation Extremes

Globally, rainfall extremes have increased over the past few decades as one of the impacts of a warming climate. (Fisher and Knutti, 2016; Giorgi et al., 2019; Fowler et al., 2021). This increase in extreme rainfall intensities due to warming is mostly governed by the Clausius-Clapeyron relation, as the rainfall intensity is related to the amount of water vapour in the atmosphere, which in turn is associated with the temperature thermodynamically (O'Gorman and Schneider, 2009; Wasko et al., 2016). A hotter atmosphere has the capacity to contain increased moisture and precipitable water, potentially resulting in more intense precipitation events. Various global climate models (GCMs) and regional climate models (RCMs) are used to explore changes in the characteristics of precipitation, such as intensity, frequency, duration, spatial extension, and correlation with other climate indices (Klutse et al., 2021). Even though the number of EREs has increased globally, a mixed anomaly is shown by various countries towards these EREs. In many countries, rainfall extremes have been recorded at 70% below the normal (Naveendrakumar et al., 2019). To accurately assess the severity of disasters caused by extreme precipitation, it is crucial to understand the variations in both space and time of these intense rainfall events. Most monsoonal and non-monsoonal regions show statistically significant increases in the spatial extension of precipitation extremes in most seasons (Tan et al., 2021). Although there are uncertainties in understanding the changes in rainfall extremes, the observational, theoretical, and modelling studies for the intensification of rainfall extremes show that both short-duration and long-duration rainfall extremes are intensifying with warming at a rate consistent with the increase in atmospheric moisture. (Fowler et al., 2021). The study also pointed out that the increase in short-duration extreme rainfall intensities in some regions is greater than expected from moisture increases alone.

It is necessary to give precise information on precipitation events' variability, occurrence, and distribution to improve preparedness and mitigation strategies against drought and flood disasters. Comprehensive precipitation monitoring based on various precipitation indices will be utilised to guarantee that decision-makers and policymakers can receive quantitative data on precipitation characteristics (Klutse et al., 2021).

1.8 Global Monsoon Extremes

About 62% of the world's population lives in monsoon areas and relies on it for their freshwater requirements and agriculture-related livelihoods. So, the monsoon-related precipitation extremes extensively impact the region's agricultural production, water resources, hydroelectric power generation, and the environment (Mohtadi et al., 2016; Klutse et al., 2021). It is challenging to predict and mitigate its effects on society. Investigating the changes in mean and extreme precipitations over the monsoon regions has received a lot of attention during the past decades (Wang et al., 2020; Chang et al., 2022). The intensified precipitation extremes in the global monsoon region have comparable contributions from thermodynamical and dynamical parameters. The regional disparities in the enhanced precipitation extremes are mostly contributed by changes in dynamical parameters, while changes in thermodynamic parameters contribute a spatially uniform pattern of increase (Chang et al., 2022). Over the past decades, GMP has shown an upward trend in the NH, but the trend in the SH is weak and insignificant. The Rx5day over the monsoon regions is far greater than that over the rest of the land. (Zhang et al., 2018). Rx1day and Rx5day precipitation for the period 1901–2010 are estimated at 7.5% and 4.8% K^{-1}, respectively (Zhang and Zhou 2019).

1.9 South Asian Monsoon Rainfall Extremes

Over one-fifth of the world's population resides in South Asia, which includes nations like Afghanistan, Bangladesh, Bhutan, India, the Republic of Maldives, Nepal, Pakistan, and Sri Lanka. India is the largest nation in South Asia, accounting for approximately 63% of the total land area and having the highest population. Extreme weather occurrences have become more prevalent in South Asian nations during the past few decades. With the influence of powerful seasonal monsoons, weather patterns in the South Asian region are often vulnerable to devastating weather extremes like droughts, floods, and cyclones (Naveendrakumar et al., 2019). The impact of intricate weather processes like clouds and the fluctuations in precipitation over time makes it challenging to forecast and mitigate the consequences on society. Particularly, the frequency and intensity of extreme precipitation events have detrimental effects on the socioeconomic sector (Almazroui, 2020a,b; Liu et al., 2020). Besides extensive floods and droughts, anomalous variations like localised floods and flash floods significantly affect humanity, resulting in homelessness, infrastructural damage, fatalities, and subsequent disease epidemics (Mishra and Shah, 2018). Flooding causes an estimated USD 30 million in economic losses globally each year; however, for India, the annual loss has been estimated to be USD 3 million during the past few decades. (Roxy et al., 2017).

The Northeast or Southwest monsoons are mainly responsible for bringing precipitation to South Asian countries. Except for a few locations/regions at high elevations, most South Asian regions have liquid rainfall. The abundant summer monsoon (June–September) precipitation is crucial for the regional hydrological cycle and serves as the main source of water for maintaining agriculture, power generation, ecosystems, and human livelihoods for the densely populated region of the world, over 1.6 billion people (Webster et al., 1998; Gadgil and Gadgil, 2006; Bookhagen and Burbank 2010). So many analyses exist on monsoon rainfall's spatial and temporal variability, especially monsoon extremes. According to numerous studies, the SASM rainfall has been significantly decreasing over the past few decades (Goswami et al., 2006; Chung and Ramanathan,2006; Bollasina et al., 2011; Krishnan et al., 2013; Singh et al., 2014) with an accompanying rise in aridity (Kumar et al., 2013). Several trend analyses also showed that rainfall extremes during the SAM are becoming relatively frequent (Baidya et al., 2008; Yao et al., 2008; Shrestha et al., 2017). Despite the contradicting patterns of decreased rainfall during the period of 1976–2005 (Salma et al., 2012), parts of South Asia have experienced an increase in the frequency of strong rainfalls and an increase in the possibility of EREs in recent decades (Christensen et al., 2007; Ikram et al., 2016). The frequency and intensity of EREs are influenced by the interannual and intraseasonal variability of ISMR, with the intensity of active (wet) spells manifesting a statistically significant increasing trend and the intensity of break spells (dry) spells manifesting a statistically significant decreasing trend (Varikoden and Reji, 2022). On comparing the IOD and ENSO, the main factors that influence the interannual variability of ISMR, Krishnaswamy et al. (2015) pointed out that in recent decades, IODs have had a greater impact on EREs than the ENSO, particularly in terms of the frequency of EREs. Positive IOD episodes have been occurring more frequently and intensely than expected in recent years. Thus, the current trend of increased IOD occurrences supports the possibility of an impending rise in EREs (Varikoden and Reji, 2022).

The 2018 IPCC report explained how heavy and extreme rainfall is becoming more frequent, intense, and abundant worldwide, especially over the Himalayan Mountain ranges, the Tibetan plateau, and the Indo-Gangetic Plain. Over half of India's natural hazards in 2020 were droughts and floods, according to Amarasinghe et al. (2020). Out of 99 billion US dollars lost in the preceding 50 years from extreme weather events (such as floods, tropical cyclones, heat waves, cold waves, lightning, etc.), roughly 60 billion of the cost in India was directly attributable to regional floods. Moreover, floods in India account for 46.1% of all deaths among all other extreme weather-related incidents. According to the Global Flood Inventory (GFI), created by

Adhikari et al. (2010), short-duration heavy rains account for 64% of flooding and also accounts for almost 11% of total rainfall (Varikoden and Reji, 2022). Figure 1.7 illustrates the mortality distribution resulting from different extreme weather events in India.
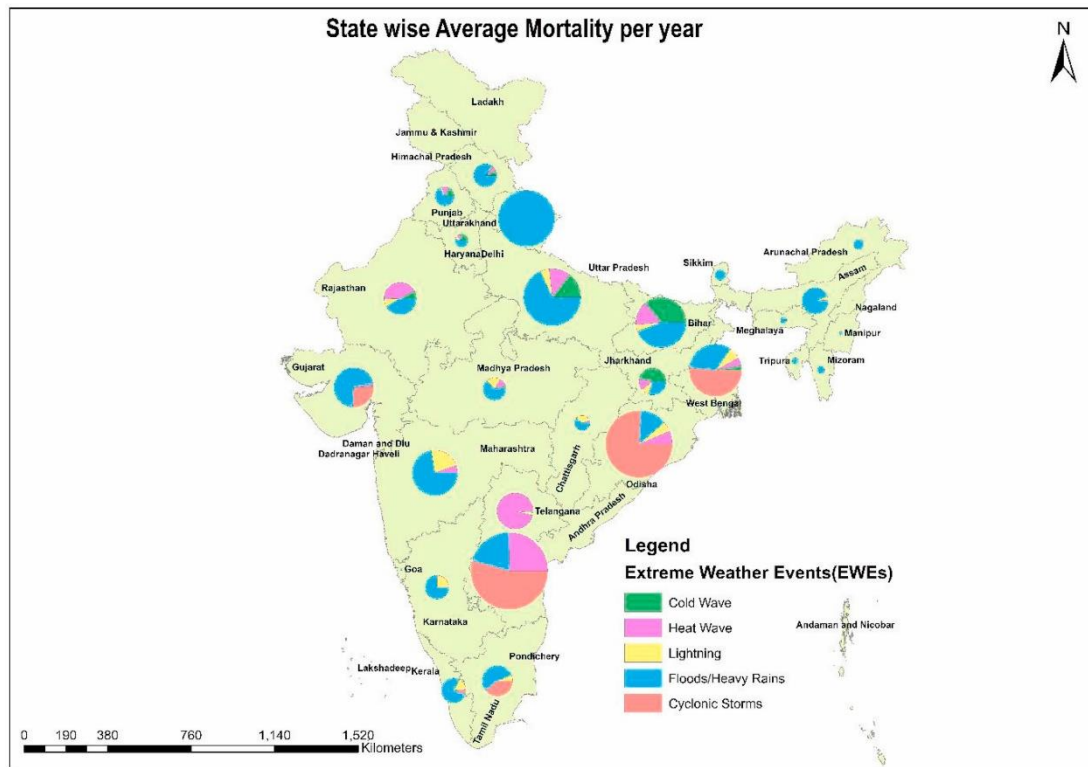
Figure 1.7: The distribution of mortality in India from various extreme weather events during 1970–2019. The circle's size indicates the average mortality in each state, while its sectors represent mortality caused by various extreme events. (taken from Ray et al., 2021).

Several attempts have been made to understand and quantify changes in the properties of extreme precipitation events during the ISM season in the context of global warming (Goswami et al., 2006; Rajeevan et al., 2008; Krishnamurthy et al., 2009; Ghosh et al., 2009, 2012, 2016; Singh et al., 2014; Mishra and Liu, 2014). Goswami et al. (2006) concluded an increase in heavy rainfall events and a decrease in moderate rainfall events over central India, assuming this region is homogeneous for rainfall. However, Ghosh et al. (2009, 2012, 2016) argued that a homogeneous area does not apply uniformly to all places in central India when analysed with a fine-resolution dataset. They pointed out that the spatial aggregate of the intensity and frequency of EREs over central India is significantly increasing; however, on the regional scale, the significant increase is non-uniform. This finding aligns with the suggestion by Meehl et al. in 2005, indicating that an increase in the intensity and frequency of EREs does not follow a uniform spatial distribution in a warmer future climate with increased greenhouse gases. Rajeevan et al. (2008) suggested an increased risk of major floods over central India in a global

warming scenario. The study also demonstrated that ERE's inter-annual, inter-decadal, and long-term trends are modulated by SST variations over the Indian Ocean in the tropics.

Pal and Tabbaa (2010) showed that the probability of extreme monsoon deficiency is generally increasing in India, reaching its highest in northern India. The study by Singh et al. (2014) demonstrated that extreme dry and wet spells during the SASM had statistically significant changes in their intensity and frequency between 1951 and 2011. The ISM displays two clear phases, starting with a more humid early summer followed by a subsequent drier period. Aerosol concentrations may impact precipitation patterns during this drier phase (Gautam et al., 2009; Kharol et al., 2013; Malik et al., 2016). Krishnaswamy et al. (2015) Illustrated the IOD's dominant influence on EREs compared to the ENSO in recent decades, particularly in the frequency of EREs. Krishnan et al. (2016) suggested the collaborative influence of regional land-use change, anthropogenic aerosol forcing, and the accelerated Indian Ocean Sea surface temperature (IOSST) warming signal to weaken the SAM in recent decades. They also showed that a weakened SAM circulation leads to a notable shift in rainfall patterns across central India, favouring more frequent intense localised precipitation events while reducing the occurrence of moderate events. Roxy et al. (2017) found a threefold increase in widespread EREs over central India from 1950 to 2015. The increase in such incidents is caused by greater fluctuations in the low-level monsoon westerlies over the Arabian Sea. This variability results in surges of moisture, causing intense rainfall throughout the central Indian subcontinent. Meenu et al. (2020) demonstrated that the formation of deep convective cloud bands with a deep supersaturated layer throughout the middle and upper atmosphere may lead to heavy and sustained precipitation.

Nikumbh et al. (2020) demonstrated that the interaction of synoptic-scale systems can lead to large-scale EREs, even if individual systems are not sufficiently strong. They also highlighted that a strong LPS alone is not a sufficient condition to create large-scale EREs. However, the simultaneous presence of an LPS and a secondary cyclonic vortex (SCV) can create a giant mid-tropospheric vortex, leading to heavy rainfall. The ISM precipitation study, using CORDEX data, indicates a southward shift of precipitation extremes over South Asia (Suman and Maity, 2020). The study revealed a greater increase in extreme precipitation over the south Indian region compared to north and central India in the period 1971–2017, with the base period being 1930–1970. Sooraj et al. (2020) analysed the role of the Indo-Pakistan arid region (IPAR)

in modulating boreal summer heavy EREs over the monsoon core zone (MCZ) across the Indian subcontinent at sub-seasonal to daily time scales.

Varikoden et al. (2019) analysed the decreasing trend of southwest monsoon rainfall on the southern west coast and the increasing trend of extreme rainfall centred around 15°N in the northern west coast regions. They linked these trends with the northward shift of the Low-Level Jetstream (LLJ) from 10°N to 15°N, which is related to the abnormal warming of the northern Arabian Sea and adjoining continents (Varikoden and Reji, 2022). Analysing the recent Chennai floods, Boyaj et al. (2018) concluded that the intensity of synoptic events in the BoB was modulated by the simultaneous warming of the southern BoB and strong El Niño conditions in the Pacific. This modulation resulted in heavy rainfall events over the peninsular Indian region, particularly centred around Chennai. In conjunction with numerous other factors such as El Niño events, LPS, Indian Ocean warming, and an increasing frequency of the IOD, the magnitude and frequency of EREs in central India are exhibiting an upward trend (Sagar et al., 2017; Krishnan et al., 2016; Varikoden and Reji, 2022). Unlike the effects of climate change, the weakening of monsoon circulation is accountable for the rising trend of isolated EREs (Roxy et al., 2017). The Himalayan regions experience EREs more frequently due to the interaction between the monsoon LPS (moist air with lower-level convergence) and the southward-penetrating westerly trough (dry-cold air with high potential vorticity), facilitated by increased pressure on the Tibetan plateau (Hong et al., 2011; Joseph et al., 2015). EREs are predominantly controlled by Rossby waves through an extensive network of teleconnections in northern India, particularly in areas adjacent to the Himalayan region (Boers et al., 2019). The way in which large-scale atmospheric patterns interact with the local topography plays a vital role in shaping the weather and climate in northeastern areas. A significant increase in EREs has been noticed in the northeast regions in recent years, attributed to the intensification of low-level southerly winds from the BoB and convergence over the region (Varikoden and Revadekar, 2020).

Some earlier studies also have addressed the large-scale physical and dynamical processes of mean monsoon rainfall (Rao, 1976; Webster et al., 1998; Gadgil, 2003; Xavier and Goswami, 2007). However, these studies did not systematically address rainfall extremes on the regional scale. Many scientists have expressed concerns regarding understanding ISM rainfall variability, especially in its extremes. They emphasise the need to validate the mechanisms behind such variability and improve predictions for disaster preparedness due to the significant

impacts on human society (Pai et al., 2014; Ghosh et al., 2016; Xavier et al., 2018; Varikoden and Reji, 2022). Mishra et al. (2020) observed that warming over the Arabian Sea enhanced moisture, but the circulation features failed to transport this moisture to the landmass. Consequently, the warming led to a reduced ISMR. Goswami et al. (2022) attributed the BoB warming in the pre-monsoon season to the weakening of low-level circulation and moisture transport during the southwest monsoon season. This weakening reduces the land-sea thermal contrast, ultimately leading to a deficit in ISMR. However, attributing specific dynamic factors or their causative factors to the rainfall extremes during the ISM season remains challenging. Roxy et al. (2017) attributed the widespread changes in extreme rain events to the dynamic response of the atmosphere rather than thermodynamic factors alone. The enhancement of deep localised convections leading to heavy rainfall events is associated with weak vertical wind shear and increased atmospheric moisture (Krishnan et al., 2016). Shifts in the onset date of the ISM impact the seasonal length and mean rainfall amount in many meteorological subdivisions of India (Bhardwaj and Misra, 2019). Increased variability of low-level monsoon westerlies and warming of the northern Arabian Sea led to increased moisture supply and extreme events in the MCZ (Roxy et al., 2017). Additionally, Nikumbh et al. (2020) found that large-scale factors such as moist ascent, static instability, dynamic lifting, and moisture supply contribute to large-scale EREs during monsoon LPS.

1.10 Historical and Future Projections of ISMR and its Extremes

Due to its devastating effects, climate change is a major concern for human societies and crucial for natural ecosystems. The warming induced by greenhouse gases and the related feedback processes affect the surface energy budget, which in turn creates a significant impact on the Hydrologic cycle of the Earth (Giorgi et al., 2019). Most regions of the world are expected to experience an increase in the severity of EREs due to climate change. Under the warming climate, a decreasing trend in mean rainfall (Kumar et al., 2010; Roxy et al., 2014; Ghosh et al., 2016; Preethi et al., 2017; Radhakrishnan et al., 2017) and an increasing trend in extreme rainfall (Goswami et al., 2006; Fischer and Knutti, 2015; Ghosh et al., 2016; Roxy et al., 2017; Obha, 2021; Jamshadali et al., 2021; Almazroui et al., 2021) were observed in ISMR in the second half of the twentieth century. Studies concluded that thickly populated Asian countries will be susceptible to extreme rainfalls in the future, both in intensity and frequency, under global warming (Veiga and Yuan, 2021). The socioeconomic impacts of these future changes have recently been investigated for different regions (Liu et al., 2020; Zhang and Zhou, 2020; Shi et al., 2021). Using climate model simulations could help evaluate potential climate change

adaptation strategies even though there are still a lot of uncertainties and resolution problems with regional scale projections (Ohba, 2021). Numerical models are frequently used in meteorological applications, notably in weather prediction systems. GCMs and RCMs have been employed in studies to investigate changes in various precipitation characteristics, encompassing frequency, intensity, spatial extent, duration, and timing of these meteorological and climate events. (Klutse et al., 2021). A model merely uses concepts and equations from mathematics to explain a system. In the past few years, several modelling studies have been conducted to comprehend the ISMR variability in both historical and future decades (Sperber et al., 2013; Levine et al., 2013; Wang et al. 2015; Sudeepkumar et al., 2018; Varikoden et al. 2018; Hrudya et al., 2022; Choudhury et al., 2021). Future changes in rainfall will likely have a large socioeconomic influence on disaster mitigation and the environment on both a global and regional scale.

The complex dynamics of ISMR are considered one of the most challenging atmospheric circulation systems to be understood by the scientific community owing to its variability from diurnal (Ramege, 1964; Basu, 2007; Varikoden et al., 2012; Deshpande and Goswami, 2014; Bhate and Kesarkar, 2019) to multi-decadal scale (Goswami et al., 2016; Sankar et al., 2016; Malik et al., 2017; Dwivedi et al., 2022) and its teleconnections with various SST variations (Gadgil et al. 2004; Krishnamurthy and Krishnamurthy, 2014; Chattopadhyay et al., 2016; Singh et al., 2017; Mishra et al., 2017; Li et al., 2017; Nair et al., 2018; Hrudya et al., 2020; Hrudya et al., 2021; Hu et al., 2022; Sandeep et al., 2022; Xavier et al., 2023). The South Asian regions frequently encounter EREs during the summer monsoon season that have the potential to cause property damage, environmental harm, and even fatalities. Identifying and assigning responsibility to critical factors driving potential changes in the ISMR pattern is essential for developing future adaptation strategies across various sectors in response to climate change. Therefore, it is necessary to comprehend how these events are evolving and may change in the future, particularly for developing countries in the region due to their low adaptive capacity arising from geographical as well as socio-economic features. The new-generation coupled ocean-atmosphere models are very good at predicting the SST variabilities related to the above-mentioned sources and brighten the prospect of SAM prediction. It is essential to confirm how well the GCMs, mostly used to create projections, realistically simulate the rainfall extremes in these regions.

The CMIP is a collaborative effort in the field of climate science, initiated by the WCRP's Working Group on Coupled Modelling (WGCM) under the auspicious Climate Variability and

Predictability (CLIVAR) project in 1995 (Meehl et al. 2000). It aims to improve our understanding of how the Earth's climate system works and how it might change in the future. CMIP aims to enhance our understanding of climate change over time, whether caused by natural variations or influenced by changes in radiative forcings, through the use of multiple models. This provides a standardised framework for comparing and evaluating different climate models under common scenarios and conditions. This allows scientists to assess the performance of various climate models in simulating historical climate variations and to make projections about future climate change under different greenhouse gas emission scenarios (Li et al., 2019). The CMIP provides an essential foundation for the IPCC assessments (IPCC 2013), contributing to our understanding of the current state of the climate and potential future changes (Eyring et al., 2016). Earth System Grid Federation (ESGF) data replication centers share multi-model climate data in a standardised format, making it accessible to the broader climate community and users. They manage model output collection, archiving, and retrieval in a specified format.

Along with scientific development and the gradually improved understanding of climate change mechanisms, CMIP has undergone several phases over the years, with CMIP6 being the latest major iteration (Li et al., 2021). CMIP6 was initiated in 2014 to fill the scientific gaps remaining in CMIP5 and address new challenges emerging in climate modeling (Eyring et al., 2016). The CMIP6 has endorsed 23 model intercomparison projects involving 33 modeling groups in 16 countries and formed the basis of the sixth IPCC assessment report published in 2021 (Zhang and Ayyub, 2021). Figure 1.8 represents the schematic of the CMIP6 experiment design. The CMIP DECK experiments and the CMIP6 historical simulations are in the inner part, and they provide the entry card for GCM models that would like to participate in CMIP6 and its endorsed MIPs. The middle and outer rings connect science topics with the corresponding CMIP6 MIPs. CMIP6 made efforts to link RCPs (representative concentration pathways) in CMIP5 with newly proposed SSPs (shared socioeconomic pathways) so that it enhances the robustness of climate projections and provides better support for climate policies (Moss et al., 2010; Vuuren et al., 2014). The CMIP6 introduced four new scenarios (SSP1-1.9, SSP4-3.4, SSP5-3.4-OS, and SSP3-7.0) by keeping four scenarios used in CMIP5 (SSP1-2.6 (RCP2.6), SSP2-4.5 (RCP4.5), SSP4-6.0 (RCP6.0), and SSP5-8.5 (RCP8.5)) to give a more comprehensive selection of futures for scientists to simulate (Zhang and Ayyub, 2021). In these, the tier-1 top priority scenarios are SSP1-2.6, SSP2-4.5, SSP3-7.0 and SSP5-8.5 (O'Neill et al., 2016).
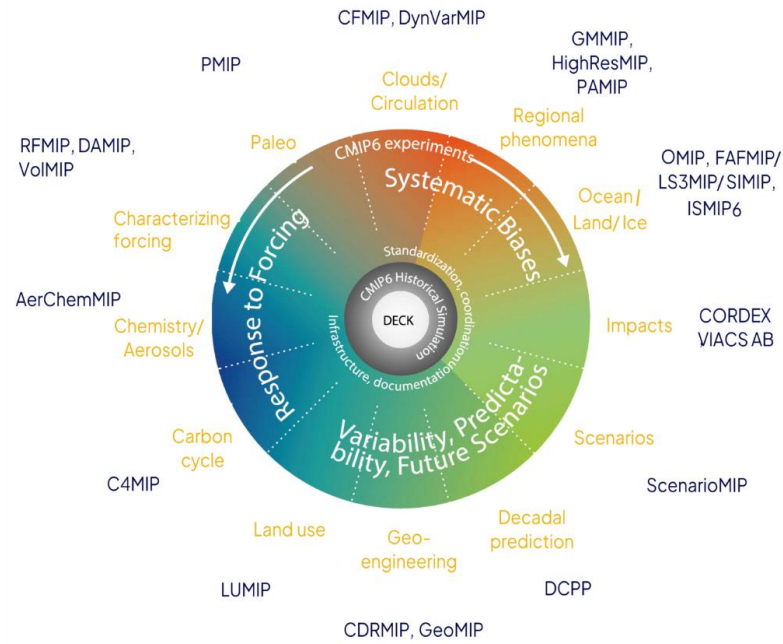
Figure 1.8: Schematic representation of the CMIP6 experimental design (taken from Eyring et al., 2016).

1.11 CMIP Projections and SASM

Predicting the SASM has been a persistent challenge in both scientific research and practical climate forecasting for many years. In the backdrop of climate change, it is essential to identify and attribute the main driving factors behind any prospective changes in the SASM pattern to design future adaptation plans in various sectors. Since the ISM climate is the outcome of linked ocean-atmosphere interactions, a coupled ocean-atmosphere general circulation model (CGCM) is necessary for the seasonal forecast of ISMR (Webster et al. 1998; Wang et al. 2005). The future evolution of ISMR and its teleconnections have been the subject of substantial investigation since the CMIP3 phase (Kripalani et al., 2007; Naveendrakumar et al., 2019; Choudhary et al., 2021). Even though the improved successor CMIP5 included several new elements such as dynamic vegetation, aerosol effects, etc., their coarse spatial resolution is unable to capture the impact of local-scale features such as topography, land-surface feedback, land use changes, etc. in reproducing current climatic conditions (Ghosh et al., 2016; Gusain et al., 2020). In addition, several studies have shown that the CMIP5 models inconsistently overestimate or underestimate the monsoon characteristics over the South Asian and Indian subcontinent for various rainfall indices (Saha et al., 2014; Sharmila et al., 2015). The state-of-the-art CMIP6 models have a significant improvement in capturing the spatiotemporal pattern of monsoon over Indian landmass, especially in the Western Ghats and Northeast foothills of the Himalayas, as compared to CMIP5 models (Gusain et al., 2020;
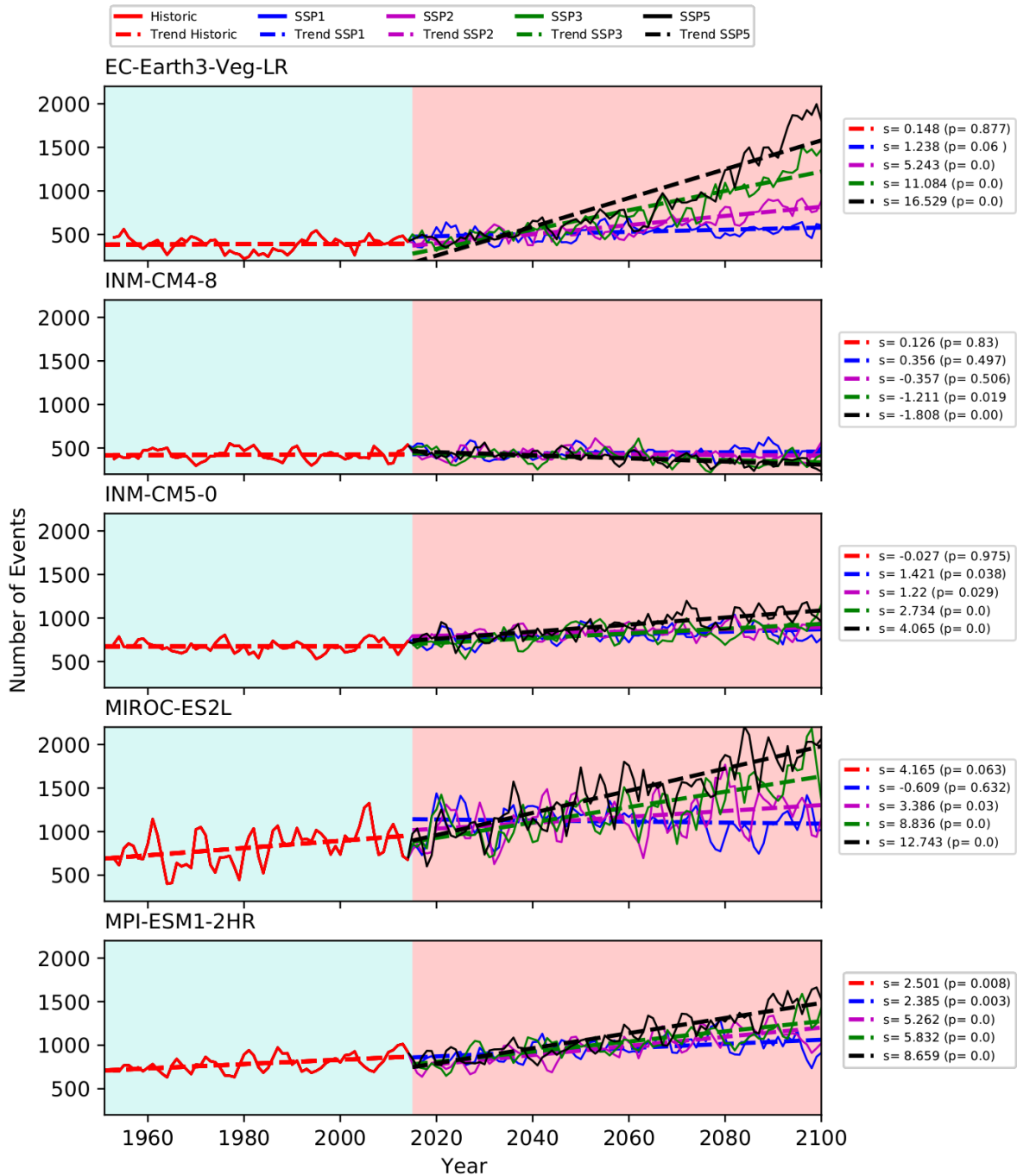
Figure 1.9: The projection of the number of extreme rainfall events over India in various SSP scenarios using CMIP6 models (taken from Suthinkumar et al., 2023)

Khadka et al., 2021). The study demonstrated that CMIP6 outperformed CMIP5, as the model deviation in CMIP6 was notably decreased. The models also show notable progress in simulating the inter-annual, multi-decadal variability and marginal improvement in simulating the ENSO-ISMR correlations (Choudhary et al., 2021). The CMIP6 models exhibit a general improvement in the simulation of climate extremes and their trend patterns compared to observations (Chen et al., 2020; Suthinkumar et al., 2023). The projection of extreme rainfall

events over India in various SSP scenarios using CMIP6 models is represented in Figure 1.9. Advanced climate models in CMIP6 can comprehend intricate climate systems, particularly the dynamics of monsoon patterns in response to a changing climate. Recent ISMR studies based on CMIP6 also include Kumar and Sarthi, 2021; Katzenberger et al., 2021; Qin et al., 2022; Rajendran et al., 2022; Dutta et al., 2022; Darshana et al., 2022; Chowdary et al., 2023; and He et al., 2023.

1.12 Scope and Objectives

From the background presented above, it is understood that the Indian monsoon has no spatially coherent trend and require reassessment of the vulnerability and mitigation projections for the region. The review also demonstrates that the SASM system is responding in a complex fashion to global climatic forcing mechanisms and that no one can anticipate seeing homogeneous changes throughout the monsoon domain. Previous studies have not thoroughly investigated the physical processes, evolution, and dissipation of dynamical parameters, especially on a regional scale. The spatiotemporal variabilities of these regional extreme events are not well established. Some works have focused on the temporal variability of ISMR and its influencing mechanism; however, the regional variability is less explored. Some zones are characterised by an increase in ISMR, while other adjacent zones show a significant decrease. Although the regional variability of extremes is examined in some studies, they have considered the study area more or less homogeneous or extreme analysis is done based on a particular threshold value of rainfall for the entire study region (Goswami et al., 2006; Roxy et al., 2017; Varikoden and Ravadekar, 2020).

The SASM is a complex coupled human-natural system linked with the socio-economic culture of the domain that poses unique challenges to comprehend in the context of escalating anthropogenic activities. The swift and significant alterations in land use, land management, and industrial practices across the subcontinent, coupled with rising temperatures in the Indian Ocean, have impacted the SASM. Regional drivers of extreme events need careful consideration in designing mitigation and adaptation efforts. Anticipating changes in extreme precipitation and understanding its impact on the social economy under climate change is critical. This would help provide a scientific basis for disaster prevention and reduction. Selecting suitable GCM models under CMIP6 and projecting variations in the ISM and extreme rainfall is of utmost importance.

Considering the factors mentioned above, the following objectives were formulated for the thesis. They are:

1) To explore the spatial variability and related characteristics of SASM mean and extreme rainfalls.

2) To identify the regional flood-prone areas over the South Asian region based on the variabilities of extreme rainfall events over these zones.

3) To Explore the physical characteristics of the extreme rainfall events in different time scales over the identified regions.

4) To analyse the association of southwest monsoon rainfall and its extremes with various global climate indices.

5) To find out the favourable conditions for regional extreme rainfall events over the Indian subcontinent, considering circulation and other meteorological parameters

6) To investigate the large-scale dynamical factors leading to various disastrous EREs occurring over the identified regions before, during, and after the events.

7) To validate Global Climate Models in the CMIP6 project and assess the intensity of extreme rainfall events, along with their contributions to seasonal rainfall during the historical period (1950–2014) in the study region.

8) To assess significant spatiotemporal variations in extreme precipitation across the study region under different future warming scenarios using the selected coupled dynamical models.

The study proceeded based on the prescribed objectives and initially explored the spatiotemporal variability and related characteristics of SASM rainfall. Five prominent areas over the South Asian region were identified based on the decadal trend of extreme rainfall in these zones. The study then delved into the physical characteristics of extreme rainfall events on different time scales within the identified regions. Furthermore, it analysed the association of southwest monsoon rainfall and its extremes with various global climate indices. Considering circulation and other meteorological parameters, the study identified favourable conditions for regional extreme rainfall events over the Indian subcontinent. Additionally, the study investigated the large-scale dynamical factors leading to various disastrous EREs occurring over the identified regions before, during, and after the events.

For the projection of SASM rainfall and its extremes in the future, the study first validated Global Climate Models in the CMIP6 project and selected the most suitable models. The intensity of extreme rainfall events, along with their contributions to seasonal rainfall during the historical period (1950–2014) in the study region, was assessed. Significant spatiotemporal variations in extreme precipitation across the study region under different future warming scenarios were analysed in the final stage using the selected coupled dynamical models.

In this thesis, chapter 2 details the data and methodologies employed in the study to address its objectives. Chapter 3 describes the physical characteristics of SASM EREs and their association with global climate indices. Chapter 4 analyses the dynamical characteristics of South Asian summer monsoon EREs. Exploring the circulation and other meteorological parameters conducive to regional EREs is the primary focus of this chapter. Chapter 5 presents the selection of the best CMIP6 GCM models to simulate SASM rainfall and their characteristics in simulating SASM mean and extreme rainfalls. Chapter 6 explores changes and variabilities in summer monsoon EREs during future projections using selected CMIP6 models. Chapter 7 summarises the present work, highlighting the important findings and concluding remarks. The future scope of this work and recommendations are presented in Chapter 8.

CHAPTER 2

DATA AND METHODOLOGY

CHAPTER 2

DATA AND METHODOLOGY

The various data sets used in this study include observational data, model data, reanalysis data products, and climate indices. A description of the data sets is given in Section 2.1, and the methodologies adopted in the study are described in Section 2.2.

2.1 Data

The primary datasets utilised in the study comprise observational gridded rainfall data provided by The Asian Precipitation Highly Resolved, Observational Data Integration Towards Evaluation of Water Resources (APHRODITE) and Climatic Research Unit (CRU) and model rainfall data from various Coupled Model Intercomparison Project phase 6 (CMIP6) global climate models. Reanalysis data products such as wind, pressure, humidity, geopotential height, etc., obtained from National Centers for Environmental Prediction/National Center for Atmospheric Research (NCEP/NCAR) reanalysis products, and various climate indices such as Niño3.4 index, El Niño Modoki Index (EMI), Dipole Mode Index (DMI), Pacific Decadal Oscillation (PDO) index, Atlantic Multidecadal Oscillation (AMO) index, and Atlantic Zonal Mode (AZM) index were also used in the study. Below is a brief description of the various data used.

2.1.1 Observational Rainfall Data

APHRODITE: The Asian Precipitation Highly Resolved, Observational Data Integration Towards Evaluation of Water Resources (APHRODITE) is the only long-term, continental-scale, high-resolution daily product for precipitation and temperature across Asia. It encompasses a dense network of daily rain gauge data for the Asian monsoon domain, covering the Himalayas, South and Southeast Asia, and mountainous regions in the Middle East. The project comprises four subdomains: Monsoon Asia, the Middle East, Russia, and Japan. Additionally, a combined domain product is also made available. The number of valid stations ranges between 5000 and 12000. Data is accessible in netCDF, ASCII, and binary formats. APHRODITE Precipitation Data Version V1101EX_R1, available for a period of 65 years (1951–2015), is one of the most precise gridded daily rainfall datasets at high spatial resolution (0.25° latitude × 0.25° longitude) over the Monsoon Asia domain (http://aphrodite.st.hirosaki-u.ac.jp). This rainfall data is supported by a highly dense network of rain gauge stations, especially in the rainy regions of South Asia, including India. Therefore, APHRODITE data is widely used for studies such as determining a region's precipitation change, evaluating water

resources, verifying high-resolution model simulations, estimating satellite precipitation, and improving precipitation forecasts (Yatagai et al., 2012; Kapnick et al., 2014; Yatagai et al., 2020). The study has utilised APHRODITE Precipitation Data Version V1101EX_R1 to analyse the rainfall features during the summer monsoon period (June to September), as various studies have proven its reliability in analysing long-term trends and their variability over the South Asian monsoon (SAM) domain (Prakash et al., 2015; Varikoden et al., 2015; Kim et al., 2019).

CRU: The monthly rainfall data from the Climatic Research Unit (CRU) are used for the historical analysis of extreme rainfall events (EREs) for the period from 1950 to 2014 during the projection study. The Climatic Research Unit Time-Series Data Version 4.04 (CRU TS v.4.04) is a gridded time-series dataset released on April 24, 2020, covering the period from 1901 to 2019. It has a spatial resolution of 0.5° latitude × 0.5° longitude (Harris et al., 2020). The CRU data covers all land domains of the world except Antarctica and is based on the analysis of more than 4000 weather station records. Although many input records have been homogenised, the dataset itself is not strictly homogeneous (Harris et al., 2020). The CRU data is downloaded from the Centre for Environmental Data Analysis (https://catalogue.ceda.ac.uk/uuid/89e1e34ec3554dc98594a5732622bce9) (Harris et al., 2020).

2.1.2 Rainfall Data from CMIP6 Global Climate Models

In this study, monthly rainfall data from 53 global climate models from the CMIP6 project were utilised to simulate the spatiotemporal changes in extreme rainfall during the summer monsoon season over the Indian subcontinent of the South Asian region. The CMIP6 data were accessed from the Lawrence Livermore National Laboratory (https://esgf-node.llnl.gov/search/cmip6/) (Zhang and Ayyub, 2021). Table 2.1 gives an overview of the 53 CMIP6 models used in the study, their resolution, modelling centres, short names, and spatial resolution.

SL. NO	Model Name	Modelling Centre	Resolution	Key Reference
1.	AWI-CM-1-1-MR	AWI	1×1	Semmler et al, 2018
2.	AWI-ESM-1-1-LR	AWI	1×1	Shi et al., 2020
3.	BCC-CSM2-MR	BCC	1.125×1.125	Xin et al., 2018
4.	BCC-ESM1	BCC	2.8125×2.8125	Zhang et al., 2019
5.	CAMS-CSM1-0	CAMS	1.125×1.125	Rong et al. 2019
6.	FGOALS-f3-L	LASG-CAS	1×1.25	Bao et al., 2019

7.	FGOALS-g3	LASG-CA	2.8125×2	Li et al., 2019
8.	CanESM5	CCCMA	2.8125×2.8125	Swart et al., 2019
9.	ACCESS-ESM1-5	CSIRO	1.25×1.875	Ziehn et al., 2019
10.	ACCESS-CM2	CSIRO-ARCCSS	1.25×1.875	Dix et al., 2019
11.	EC-Earth3	EC-Earth-Consortium	1×1	Döscher et al., 2022
12.	EC-Earth3-AerChem	EC-Earth-Consortium	1×1	Döscher et al., 2022
13.	EC-Earth3-CC	EC-Earth-Consortium	1×1	Döscher et al., 2022
14.	EC-Earth3-Veg	EC-Earth-Consortium	1×1	Döscher et al., 2022
15.	EC-Earth3-Veg-LR	EC-Earth-Consortium	1.125×1.125	Döscher et al., 2022
16.	FIO-ESM-2-0	FIO-QLNM	0.9×1.25	Song et al., 2019
17.	INM-CM4-8	INM	2.5×2	Volodin et al., 2019
18.	INM-CM5-0	INM	2.5×2	Volodin et al., 2019
19.	IPSL-CM6A-LR	IPSL	1.25×2.5	Boucher et al., 2018
20.	IPSL-CM5A2-INCA	IPSL	1.9×3.75	Boucher et al., 2020
21.	IPSL-CM6A-LR-INCA	IPSL	1.25×2.5	Boucher et al., 2021
22.	MIROC6	MIROC	1.4×1.4	Shiogama et al., 2019
23.	MPI-ESM1-2-LR	MPI-M	1.85×1.875	Wieners et al., 2019
24.	NorESM2-MM	NCC	1×1.25	Bentsen et al., 2019
25.	MRI-ESM2-0	MRI	1.125×1.125	Yukimoto et al., 2019
26.	GISS-E2-1-G	NASA-GISS	2×2.5	
27.	GISS-E2-1-H	NASA-GISS	2×2.5	
28.	GISS-E2-2-G	NASA-GISS	2×2.5	
29.	GISS-E2-2-H	NASA-GISS	2×2.5	Rind et al., 2020
30.	GISS -E3-G	NASA-GISS	1×1.25	
31.	NESM3	NUIST	1.85×1.875	Cao et al., 2019
32.	KACE-1-0-G	NIMS-KMA	1×1	Byun et al., 2019
33.	NorESM2-LM	NCC	1×2.5	Seland et al., 2019
34.	NorCPM1	NCC	1.9×2.5	Bethke et al., 2021
35.	GFDL-ESM4	NOAA-GFDL	1×2.5	Horowitz et al., 2018
36.	CESM2	NCAR	0.9×1.25	Danabasoglu and Ghokan, 2019
37.	CESM2-WACCM	NCAR	0.9×1.25	Danabasoglu and Ghokan, 2019
38.	CESM2-FV2	NCAR	1.9×2.5	Danabasoglu and Ghokan, 2019
39.	CESM2-WACCM-FV2	NCAR	1.9×2.5	Danabasoglu and Ghokan, 2019
40.	IITM-ESM	IITM-CCCR	1.875×1.875	Narayanasetti et al., 2019
41.	MPI-ESM-1-2	HAMMOZ-Consortium	1.85×1.875	Storch et al., 2017
42.	KIOST-ESM	KIOST	1.875×1.875	Kim et al., 2019
43.	CIESM	THU	0.95×1.25	

44.	SAM0-UNICON	SNU	1.05×1.25	Park et al., 2019
45.	MCM-UA-1-0	UA	2.2×3.75	Stouffer and Ronald, 2019
46.	E3SM-1-1	DOE- E3SM	1×1	Bader et al., 2019
47.	E3SM-1-0	DOE- E3SM	1×1	Bader et al., 2019)
48.	E3SM-1-1-ECA	DOE- E3SM	1×1	Bader et al., 2020)
49.	TaiESM1	RCEC, Taipei	1×1.25	Lee et al., 2020
50.	CMCC-CM2-SR5	CMCC	0.9×1.25	Lovato et al., 2020
51.	CMCC-CM2-HR4	CMCC	0.95×1.25	Scoccimarro et al., 2017
52.	CMCC-ESM2	CMCC	0.9×1.25	Lovato et al., 2021
53.	CAS-ESM2	LASG-CAS	1.125×1.125	Chai and Zhaoyang, 2020)

Table 2.1: Overview of the 53 CMIP6 models used in the study, their resolution, modelling centres, short names, and spatial resolution

2.1.3 NCEP/NCAR Reanalysis Data Products

The study utilised zonal and meridional components of wind, vertical velocity, specific humidity, air temperature, and geopotential height at different vertical pressure levels from the National Centers for Environmental Prediction/National Center for Atmospheric Research (NCEP/NCAR) reanalysis products. These daily datasets have a spatial resolution of 2.5° × 2.5° latitude-longitude global grids (Kalnay et al., 1996; Kistler et al., 2001). The NCEP/NCAR Reanalysis incorporates millions of observations into a stable data assimilation system using previous data from 1948 to the present. In this project, all the gridded variables are classified into three different categories depending on the degree to which the observations or models influence them. These categories are the most reliable products (type A, including upper-air temperatures, rotational wind, and geopotential height), the less reliable products (type B, including moisture variables, divergent wind, and surface parameters), and the products that can be used with caution (type C, including surface fluxes, heating rates, and precipitation) (Kalnay et al., 1996). A large subset of this data can be obtained from the Physical Sciences Division (PSD) at NOAA in its original four-times-daily format, as daily averages, and in many other formats. This study also used daily-averaged data at different pressure levels for the period 1951–2015. The data is accessed from the National Oceanic and Atmospheric Administration (NOAA) website, available at https://psl.noaa.gov/data/gridded/data.ncep.reanalysis.html.

2.1.4. Climate Indices

Different climate indices are used in this study to understand their relationships with summer monsoon rainfall over the Indian subcontinent. The indices used for this purpose are Niño3.4, Modoki Index, DMI, PDO, AMO and AZM.

Niño3.4 Index: El Niño-Southern Oscillation (ENSO) is a robust, recurring pattern of SSTs and a coupled ocean-atmosphere phenomenon in the central and eastern tropical Pacific Ocean that serves as a major driver of global climate variability (Trenberth et al., 1998). The warm phase and cold phase of ENSO are referred to as El Niño and La Niña, respectively. Each ENSO event exhibits a somewhat different and distinct character. While various indices are used to study ENSO characteristics over the tropical Pacific Ocean, the most commonly employed index is the Niño 3.4 index. As illustrated in Figure 2.1, the Niño 3.4 region spans from 5°N to 5°S, 170°W to 120°W. Typically, a 5-month running mean is used to determine the Niño 3.4 index, and when the Niño 3.4 SSTs surpass +/- 0.4^{0}C for six months or longer, it is classified as an El Niño or La Niña event. The correlation of Niño3.4 with the SAM has been established in several previous studies (e.g., Sikka, 1980; Krishnamurthy and Goswami, 2000; Varikoden and Babu, 2015; Hrudya et al., 2020a, b). The index values are downloaded from the website of NOAA (https://climatedataguide.ucar.edu/climate-data/Niño-sst-indices-Niño-12-3-34-4-oni-and-tni).
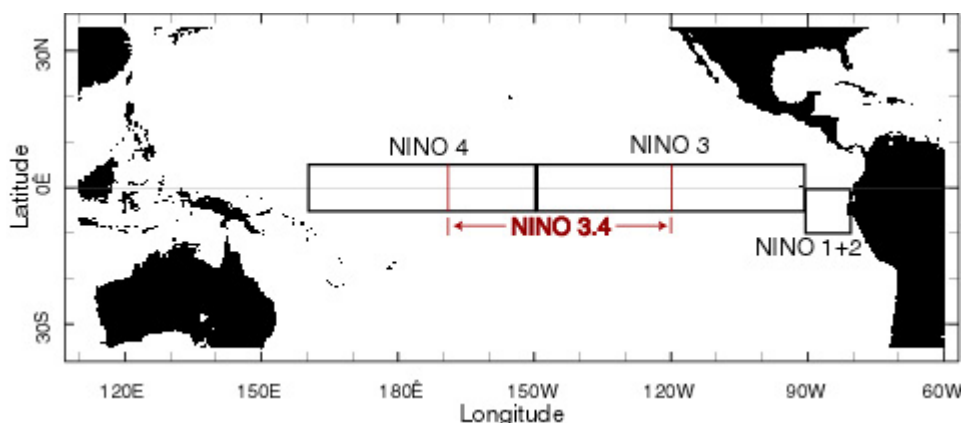
 Figure 2.1: Map of NINO regions (taken from National Oceanic and Atmospheric Administration)(https://www.ncei.noaa.gov/access/monitoring/enso/technical-discussion)

EMI: El Niño Modoki is an ocean-atmospheric flux exchange process in the tropical Pacific Ocean, showing differences from the normal ENSO in terms of its spatiotemporal characteristics and teleconnection patterns (e.g., Ashok et al., 2007; Weng et al., 2007; Kug et al., 2009; Wang and Wang, 2014; Arora and Dash, 2019). El Niño Modoki, similar to the typical El Niño, doesn't notably impact sea surface temperature anomalies in the eastern

Pacific. Instead, it causes a warm anomaly in the central Pacific, surrounded by cold anomalies on both the eastern and western sides of the basin. El Niño events are conducive to the formation of tropical cyclones over the Bay of Bengal (BoB), and El Niño Modoki events are conducive to the formation of tropical cyclones over the Arabian Sea (Sumesh and Kumar, 2013). Considering the tripolar nature of El Niño Modoki, Ashok et al. (2007) formulated the El Niño Modoki Index (EMI), which is represented by the equation $EMI = [SSTA]_A - 0.5 \times [SSTA]_B - 0.5 \times [SSTA]_C$ where, SSTA represents the area averaged Sea Surface temperature (SST) Anomaly over region A (165°E−140°W, 10°S−10°N – Central region), B (110°W−70°W,15°S−5N – Eastern region), and C (125°E–145° E, 10°S−20°N – Western region), respectively. Figure 2.2 represents the EMI regions. Studies have shown that teleconnections associated with El Niño Modoki influence rainfall on the islands of the central Pacific and other remote regions, particularly over India and South Africa (Behera and Yamagata, 2010; Ratnam et al., 2012). During the El Niño Modoki season, relatively higher rainfall is observed over the Indian subcontinent compared to the dry El Niño periods (Ashok et al., 2007). As Camargo et al. (2007) suggested, El Niño Modoki plays a crucial role in predicting various extreme events, including hurricane activity in multiple ocean basins. It may exhibit a stronger tropical-extratropical interaction than El Niño over the decadal time scale.
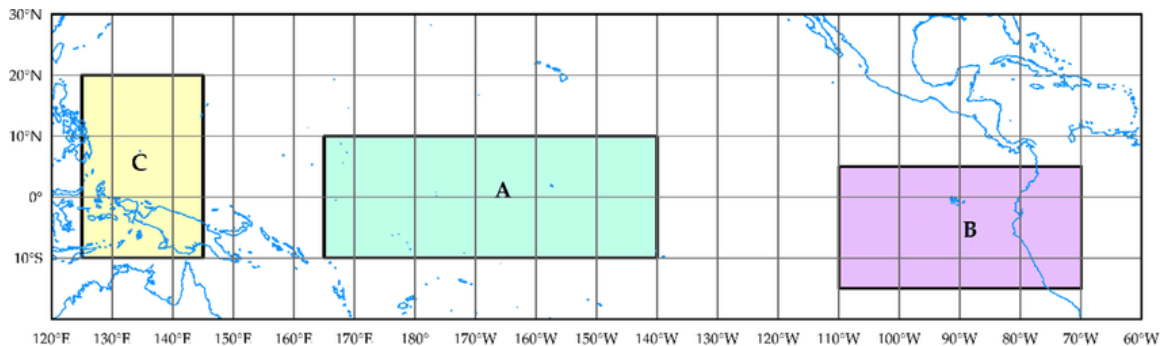
Figure 2.2 Ocean areas associated with El Niño Modoki (taken from Zhang et al., 2022).

DMI: The dipole mode index (DMI) is associated with the Indian Ocean Dipole (IOD). It is defined as the difference in SST between the western equatorial Indian Ocean (50°E to 70°E and 10°S to 10°N) and the southeastern Indian Ocean (90°E to 110°E and 10°S to 0°S) (refer to Figure 2.3). The positive phase of the IOD indicates a warmer western basin compared to the eastern basin, whereas the negative phase implies the reverse situation (Saji et al., 1999). IOD is a major contributing factor to rainfall variability in the region and affects the climate of countries surrounding the Indian Ocean Basin. A negative IOD typically has an adverse effect on Indian Southwest Monsoon rainfall, leading to below-average rain over India. The IOD is

connected to El Niño and La Niña events. Positive IOD events often coincide with El Niño and negative IOD events with La Niña. When IOD and El Niño/La Niña are in phase, their impacts are more pronounced in the region. Conversely, when they are out of phase, the effects of El Niño and La Niña can be less significant. For monitoring the IOD, DMI values above +0.4°C are considered positive, and values below −0.4°C are considered negative. The index data is obtained from https://psl.noaa.gov/gcos_wgsp/Timeseries/DMI/.
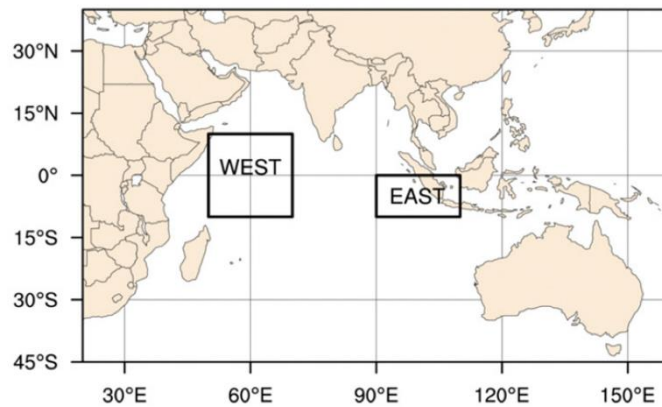
Figure 2.3: DMI regions in the Indian Ocean (taken from Kim et al., 2021)

PDO Index: The PDO (Pacific Decadal Oscillation) is a robust, recurring pattern of SSTs in the north Pacific Ocean, typically found poleward of 20°N (roughly for the region encompassing 20°N to 70°N latitude and 110°E to 100°W longitude). It exhibits periodicities of 15–25 years and 50–70 years (Mantua and Hare, 2002). The PDO is a complex phenomenon involving various factors, including tropical ENSO dynamics, atmospheric teleconnections from the tropics to the North Pacific, and the combined impact of intrinsic and tropically-driven atmospheric forcing on North Pacific SST through surface energy fluxes, Ekman currents, and oceanic Rossby waves. Essentially, it represents a combination of atmospheric and oceanic processes that cover the tropics and extratropics. The ocean's thermal and dynamical inertia contribute to the PDO's low-frequency temporal character, whereas atmospheric processes are responsible for its large-scale spatial coherence (Newman et al., 2016). The positive phase of the PDO pattern consists of negative SSTs in the central and western North Pacific and positive SSTs in the eastern North Pacific. Although the spatial patterns of the PDO and ENSO are very similar, except for their relative magnitudes, the time series of ENSO and the PDO are distinct because ENSO is predominantly an interannual phenomenon. At the same time, the PDO is primarily decadal in scale (Zhang et al., 1997). In the positive PDO phase, El Niño occurs more frequently, while La Niña appears less frequently, and vice versa (Verdon and Franks, 2006).

The stratospheric response to ENSO is more significant when ENSO and PDO are in phase (Hu et al., 2018; Yuan et al., 2018; Rao et al., 2019). Zhou et al. (2014) analysed the dependence of the East Asian winter monsoon on PDO in 2014. The data is downloaded from https://www.ncei.noaa.gov/pub/data/cmb/ersst/v5/index/ersst.v5.pdo.dat.

AMO Index: The AMO (Atlantic Multidecadal Oscillation) is a pattern of SST variability in the North Atlantic Ocean on a multidecadal scale with a period of 60–80 years (Schlesinger and Ramankutty, 1994; Wei and Lohmann, 2012). Its identification dates back to the 1980s, initially documented by Folland et al. in 1984. AMO indices are based on the average SST anomaly for the North Atlantic north of the equator. The AMO is coherently linked to climate variations over many parts of the globe (Sutton and Hodson, 2005; Zhang and Delworth, 2006; Knight et al., 2006; Wang et al., 2009; Wang et al., 2013; Krishnamurthy and Krishnamurthy, 2016; Kayano et al., 2016). Historic, observational, and simulated datasets show a positive correlation of AMO on Indian Summer Monsoon Rainfall (ISMR), indicating increased (or decreased) ISMR during the positive (or negative) phase of the AMO (Wang et al., 2009; Joshi and Pandey, 2011; Krishnamurthy and Krishnamurthy, 2016). AMO Index Data provided by the Climate Analysis Section, NCAR, Boulder, USA, Trenberth and Shea (2006), is obtained from https://climatedataguide.ucar.edu/sites/default/files/2022-03/amo_monthly.txt. It represents a detrended 10-year low-pass filtered annual mean area-averaged SST anomaly over the North Atlantic basin (0N-65N, 80W-0E).

AZM Index: The AZM (Atlantic Zonal Mode) is a dominant mode of interannual variability in the equatorial Atlantic Ocean (Ding et al., 2010). It significantly influences the interannual variability of ISMR (Kucharski et al., 2008; Pottapinjara et al., 2016). The AZM index is calculated as the seasonal mean of SST anomalies in June, July and August months, averaged over the eastern equatorial Atlantic Ocean (5°S to 3°N, 20°W to 10°E). Furthermore, the AZM exhibits an inverse relationship with ISMR, whereby the cold or warm phases of the AZM produce strong or weak ISMR, respectively. Notably, this relationship has significantly strengthened in recent decades (Nair et al., 2018; Sabeerali et al., 2019).

2.2 Methodology

Most data analysis and visualisation are done with Open Grid Analysis and Display System (OpenGrADS v2.0). Formula Translating System (FORTRAN), Climate Data Operator (CDO) command line tool, etc., are also used to support further analyses.

2.2.1 Study Area: The study considered the South Asian region, focusing on the Indian subcontinent. The study area is located between 5°N and 40°N and 65°E and 100°E (Huang et al., 2022), bounded by the Himalayas in the north, the Indian Ocean in the south, the Arabian Sea and the Indus River valley in the west, and the BoB and Ganges River delta in the east (Zhai et al., 2020). The region's topography is highly heterogeneous, and the weather and climate range from wet highlands to arid and semi-arid regions. The elevation of South Asia ranges from mean sea level at the coasts and delta regions to up to 8848 metres in the Himalayas (Zhai et al., 2020). This subcontinent experiences four broad climatic zones as defined by John E Oliver (2008): (i) dry subtropical climate (North-Western India); (ii) equatorial climate (South India); (iii) hot subtropical climate (North-East India); (iv) tropical semi-arid climate (Central India); and (v) Alpine climate (Himalayas). According to the Köppen-Geiger climate classification, the region includes tropical, arid, temperate, and polar climate zones (Yaduvanshi et al., 2021). South Asia is a region with complex atmospheric dynamics and localised climatic changes. High temperatures, periods of high humidity, and significant seasonal fluctuations, such as the monsoon season with substantial rainfall, characterise the climate in South Asia. Most river delta regions in South Asia are heavily populated. The people are also highly reliant on agriculture for their subsistence. Water stress and the possibility of water scarcity will increase in South Asia due to climate change and global warming (Mishra et al., 2020). Several factors, such as the movement of the Inter-Tropical Convergence Zone (ITCZ), local mountain ranges and related orographic circulation, proximity to water bodies (the Arabian Sea, Indian Ocean, and BoB), and large-scale atmospheric circulations, impact the climate of the area.

2.2.2 Detection and Exploration of Extreme Rainfall

The detection and exploration of EREs in the South Asian Regions is the primary objective of the study. Here, the EREs are selected based on the percentile value of the daily rainfall. A similar criterion has been adopted in many previous studies. For example, Varikoden and Revadekar (2020) used this condition to detect EREs in the northeast regions of India. The present study considered daily rainfall during the summer monsoon season as an extreme rainfall event if it exceeds the 99th percentile ($\geq$99p) value. The rainfall amount (rf99p) and the number of days (nd99p) of rainfall exceeding the 99th percentile are calculated to explore the features of EREs. The standard deviations of mean and EREs and the percentage contributions of extreme events to seasonal rainfall are also calculated.

2.2.3 Identification of Regions with Significant Long Term Trends and Characterisation of EREs

The study identified five regions with noticeable rainfall changes in the long-term trends by considering the cases of both mean and extreme rainfalls. It also explored the evolution and dissipation characteristics of the EREs in the identified regions by calculating their composites and lead-lag behaviour. In addition to the linear trends, it also employed Mann-Kandall non-parametric trend analysis (Mann, 1945; Kendall, 1975) to identify the significance of the trends and also estimated Sen's slope to quantify the trend values.

The Mann-Kendall statistic for 'n' number of data values (the variance of the trend statistic S -Var (S)) is computed by the following equation.

$$Var(S) = \frac{1}{18} n(n-1)(2n+5)$$

The standardised statistic 'Z' is given after variance correction as

$$Z = \begin{cases} \dfrac{S-1}{\sqrt{Var(S)}} & , \text{if } S > 0 \\ 0, & \text{if } S = 0 \\ \dfrac{S+1}{\sqrt{Var(S)}} & , \text{if } S < 0 \end{cases}$$

Sen's nonparametric method is used to estimate the actual slope of an existing trend (as change per year)

For 'n' data values, the slopes of all data value pairs are found as

$$Q_i = \frac{x_j - x_k}{j-k} \text{ , where } j > k$$

Sen's slope estimator is the median of the N values of Q_i. The N values of Q_i are ranked from the smallest to the largest, and Sen's estimator is

$$Q = Q_{[(N+1)/2]}, \text{ if N is odd}$$

$$Q = \frac{1}{2}(Q_{[N/2]} + Q_{[(N+1)/2]}), \text{ if N is even}$$

The probability density function (PDF) is used in this study to observe the relative density of precipitation extremes in various periods. In this section, the PDFs of mean and extreme rainfall for the entire period, as well as for the pre-1980 and post-1980 periods, were found. It is a non-parametric method using kernel density estimation on a random sample. The general formula is

$$\hat{f}_h(x) = \frac{1}{n} \sum_{i=1}^{n} K_h(x - x_i) = \frac{1}{nh} \sum_{i=1}^{n} K\left(\frac{x - x_i}{h}\right),$$

where x (x_1, x_2, ..., x_i) is an independent parameter; $\hat{f}$ is the unknown density at any given point of x; K is the kernel density estimation (a non-negative function); and h is the bandwidth with a smoothing parameter (h>0).

2.2.4 Correlation of Mean and Extreme Rainfall with Global Climate Indices

The spatial correlation of rainfall over the Indian subcontinent with different climate indices is analysed to determine their relationship with various global climate forcing mechanisms. A correlation study is conducted with Niño3.4, El Niño Modoki, DMI, PDO, AMO and AZM.

The Pearson correlation coefficient is used to estimate the correlation between climate indices and ISMR. It is a statistical test that estimates the strength of the relationship between different variables. It can range from +1, indicating a perfect positive relationship between the variables, to –1, indicating a perfect negative relationship, with 0 signifying no relationship between the variables.

Pearson correlation coefficient, $r = \dfrac{n(\sum xy) - (\sum x)(\sum y)}{\sqrt{[n \sum x^2 - (\sum x)^2][n \sum y^2 - (\sum y)^2]}}$

Where, n = number of pairs of data, $\sum xy$ = sum of products of the paired data, $\sum x$ = sum of the x scores, $\sum y$ = sum of the y scores, $\sum x^2$ = sum of the squared x scores, $\sum y^2$ = sum of the squared y scores.

A Student's t-test is used to evaluate the strength of the correlation of mean and extreme rainfall with global climate indices at 0.05 significance level.

The Student's t-test formula to calculate the test statistic:

$$t = (r \times sqrt(n - 2))/sqrt(1 - r^2)$$

Where r is the observed correlation coefficient between rainfall and the climatological index, and n is the number of data points.

2.2.5 Dynamical Characteristics of EREs

To explore the cessation and dissipation characteristics of EREs, composites of all the events have been made from 6 days before to 6 days after the events. The evolutionary and dissipation characteristics of the EREs were studied based on the lead-lag composites of horizontal circulations, Relative vorticity, specific humidity anomalies and vertical vorticity. Vertically integrated moisture transport, moisture convergence and vertically integrated moist static energy are also assessed during the EREs over the four different regions.

Relative vorticity (RV) represents the counterclockwise or clockwise rotation of air parcels related to the characteristics of the flow around them, and it can be calculated based on the equation.
$$RV = \frac{\partial v}{\partial x} - \frac{\partial u}{\partial y}$$

Moisture transport represents the movement of moisture through the atmosphere, specifically from the oceans to the continents, and it describes the link between evaporation from the sea and precipitation over the continents (Gimeno et al., 2016). Mass-weighted vertically integrated moisture transport (VIMT) between the 1000 hPa and 300 hPa in the Eulerian framework is given as,

$$VIMT = \sqrt{\left(\frac{1}{g}\int_{1000\ hPa}^{300\ hPa} q\, u\, dp\right)^2 + \left(\frac{1}{g}\int_{1000\ hPa}^{300\ hPa} q\, v\, dp\right)^2}$$

Where q is the specific humidity (g kg^{-1}); u and v are the zonal and meridional winds (m s^{-1}), respectively; g is the acceleration due to gravity (m s^{-2}), and dp is the pressure difference between two pressure levels in hPa (Thapa et al.,2018, Lakshmi et al., 2019).

Moist static energy (MSE) is the sum of internal energy, potential energy and latent energy, and it is widely used to describe the state of an air parcel in the atmosphere. Here, the internal energy is the energy present inside the air parcel or energy required to create the system in a given state; potential energy is due to its height above the earth's surface, and latent energy arises due to the water vapour present in it.

$$MSE = C_P T + gz + L_V r$$

Where C_P is the specific heat capacity for dry air at constant pressure (1005 J Kg^{-1} K^{-1}), T is the air temperature in kelvin, z is the geopotential height in metre, L_V is the latent heat of vapourisation (2.257×10^6 J/kg) and r is the water vapour mixing ratio, and it can be considered as specific humidity q (Kiranmayi and Maloney, 2011; Yano et al., 2017; Yasunaga et al., 2019).

2.2.6 CMIP6 Models

In the projection study, mean and extreme rainfalls were simulated in the historical period and also projected in future periods over the study region for various SSP scenarios. For the historical analysis of extreme rainfall for the period of 1950 to 2014, the data of the CMIP6 models are compared with the monthly rainfall data downloaded from the CRU. The monthly rainfall dataset of models is chosen according to the data available for the historical period

(1950–2014). Since the resolution of each GCM is different, at first, all GCM model data and CRU data were re-gridded to a common 1.5° latitude × 1.5° longitude spatial resolution.

2.2.6.1 Seasonality Check and Taylor Diagram Analysis

The screening of simulating models is done based on their responses to the annual cycle of rainfall and then by Taylor diagram analysis. Firstly, the annual cycle of rainfall for all models was drawn along with CRU data. After finding the ±2 standard deviations of the observational data, all models that did not fall within this range were screened out. In this way, better-performing models that can simulate the summer monsoon rainfall variations on par with observational data and qualify for further analysis have been selected. For the further scrutiny of models to simulate the EREs, which have the nearest spatial pattern to that of the observational dataset, a Taylor diagram (Taylor, 2001) was drawn by taking the 95th percentile of the monthly rainfall data for the summer monsoon season over the historical period. In this part of the study, the 95th percentile is taken as the threshold value for identifying the extreme rainfall event. The CMIP6 rainfall data sets are masked over the ocean to compare with the land only CRU rainfall datasets. Bilinear regridding of all GCM models and CRU data sets was done since all data sets must be on the same grid size for performing spatial correlation and variance analysis for estimating the Taylor diagram. Taylor diagram is a graphical tool used in meteorology and other fields to assess the performance of numerical models or observational data by comparing their correlation, standard deviation, and amplitude with a reference dataset. They are particularly useful for evaluating how well a model reproduces the characteristics of a reference dataset, such as its variability and bias. The central India region with latitude 19°N – 26°N and longitude 75°E – 85°E is selected for computing the annual cycle of rainfall, as the region shows almost spatially homogeneous monsoon characteristics as compared to the large variabilities shown by other regions of the study area (Goswami et al., 2006). To evaluate the CMIP6 models' quantitative capacities of capturing the ISMR, their projected seasonal mean rainfall and extreme rainfall amounts were compared with CRU observational data over land for the historical period 1950-2014. The percentage contribution of extreme rainfall to the seasonal mean is also compared to get a clear idea.

2.2.6.2 CMIP6 Scenarios

In the context of widely reported climate change over the South Asian region, the present study also addressed the notable spatio-temporal changes in extreme precipitation (≥95p) over the study area under four different future warming scenarios (shared socioeconomic pathways, or

SSPs) from 2015 to 2100. The four SSPs selected for projecting the future of extreme precipitation are SSP1-2.6 (RCP2.6), SSP2-4.5 (RCP4.5), SSP3-7.0, and SSP5-8.5 (RCP8.5), where the radiative forces stabilise at approximately 2.6 Wm^{-2}, 4.5 Wm^{-2}, 7.0 Wm^{-2}, and 8.5 Wm^{-2}. The different pathways have integrated future changes in climate forcings (e.g., greenhouse gas emissions, tropospheric aerosols, land use, etc.) with societal impacts (e.g., human development, economy and lifestyle, policies and institutions, technology, and environment and natural resources, etc.) to investigate climate impacts up to 2100 and are considered as key aspects in climate risk assessments with different climate policies as well as provide options for mitigation and adaptation (O'Neill et al., 2017; Zhang and Ayyub, 2021; Andrijevic et al., 2020). The details of SSP scenarios are listed in the IPCC-AR6 (IPCC, 2021). Utilising the selected models, the study focused on the alterations in the spatiotemporal pattern of extreme precipitation during the summer monsoon season under future (2015–2100) warming scenarios, comparing them to the historical period (1950–2014).

CHAPTER 3

PHYSICAL CHARACTERISTICS OF SOUTH ASIAN SUMMER MONSOON EXTREME RAINFALL EVENTS AND THEIR ASSOCIATION WITH GLOBAL CLIMATE INDICES

CHAPTER 3

Physical Characteristics of South Asian Summer Monsoon Extreme Rainfall Events and Their Association with Global Climate Indices

3.1 Introduction

Most South Asian regions are vulnerable to extreme rainfall events (EREs), which lead to major hydrological disasters, adversely affecting flora and fauna and causing large-scale damage to livelihoods and the economy. In the current warming climate scenario, extreme events during the summer monsoon season have been reported more frequently, especially over the Indian subcontinent (Goswami et al., 2006; Shastri et al., 2015; Varikoden and Revadekar, 2020). This chapter explores the spatial variability and the related characteristics of South Asian summer monsoon rainfall and EREs over 65 years, from 1951 to 2015. A statistical method based on the percentile of daily rainfall (≥99th percentile) is used to identify extreme rainfall zones. This section of the study aims to investigate the spatiotemporal features and heterogeneity of EREs at a finer spatial resolution. Moreover, the chapter analyses the association of various climate indices (Niño3.4, Modoki, DMI, PDO, AMO, and AZM) in modulating the mean and extreme rainfalls over the region.

3.2 Climatology of Mean and Extreme Rainfall

The spatial patterns of mean and extreme rainfalls during the summer monsoon season over the South Asian monsoon (SAM) domain are depicted in Figure 3.1. The climatology of the mean rainfall pattern constructed for the study period shows high precipitation over the west coast of India and northeast regions and the coastal areas of Bangladesh and Myanmar. Moderate rainfall is observed across the Himalayan foothills and central Indian regions, with low rainfall in southeast India and the northwest regions (Figure 3.1a). The topographic features of the west coast, Himalayas, and northeastern regions play an essential role in contributing to abnormally high rainfall over these regions during the summer monsoon period compared to other regions (Roe, 2005; Bookhagen and Burbank 2006, 2010; Varikoden et al., 2018; Kuttippurath et al., 2021).

Most climate studies utilise precipitation percentile (or quantile) indices to assess trends and projections of extreme precipitation events (Schär et al., 2016). Identifying extremes through multiyear averaging of precipitation data can lead to misleading interpretations (Parkinson, 1989). The present study identified EREs during the summer monsoon season by determining

the 99th percentile of daily rainfall for the study period. The spatial pattern of rainfall corresponding to the 99th percentile reveals large values in most west coast regions (> 80 mm day^{-1}), some pockets in the northeast, and the foothills of the Himalayas. Central India exhibits moderate values, with some areas exceeding 60 mm day^{-1}. Very low values for 99th percentile rainfall (< 20 mm day^{-1}) are observed in the southeast, northwest, and northern regions such as Jammu, Kashmir, and Ladakh (Figure 3.1b). The spatial distribution of extreme rainfall (> rf99p) during the summer monsoon season shows a high amount (> 175 mm season^{-1}) on the west coast and more than 125 mm season^{-1} in isolated regions of central India, the foothills of the Himalayas, and the northeastern regions (Figure 3.1c). The high values of extreme rainfall in the regions of the West Coast, Uttarakhand, Himachal Pradesh, Meghalaya, and Arunachal Pradesh may be attributed to the influence of topographic features. Extreme rains also impact the Indo-Gangetic plains during the summer monsoon season. The northwest and southeast regions experience very low amounts of rainfall (< 50 mm season^{-1}) even during these extreme episodes.
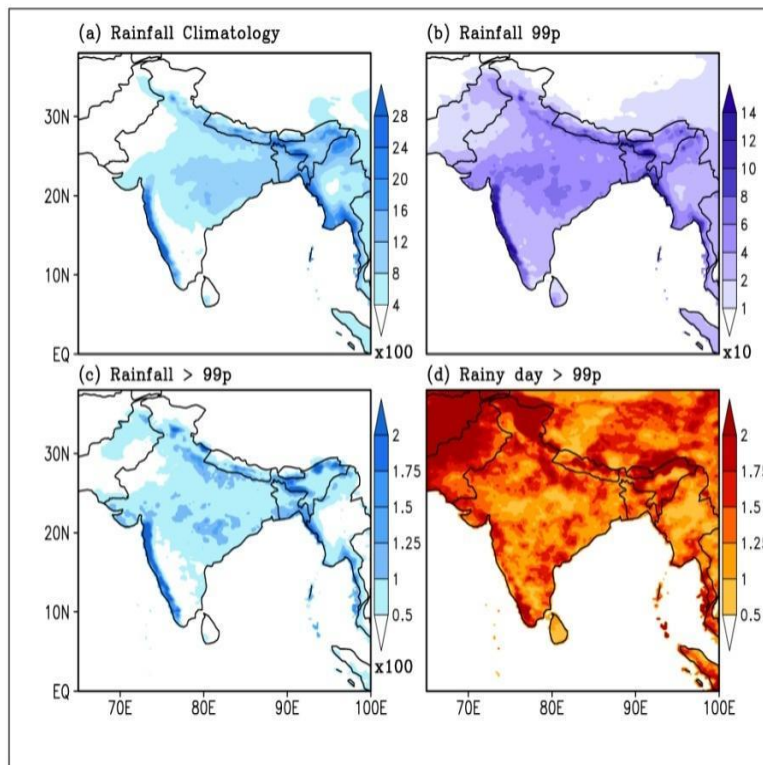
Figure 3.1: Mean and extreme rainfall climatology: (a) summer monsoon rainfall climatology (mm season^{-1}) over the South Asian monsoon domain for the duration 1951-2015(65 years); (b)99th percentile (99p) of daily rainfall during the summer monsoon season from the above 65year period (mm day^{-1}); (c) amount of rainfall exceeding 99p (mm season^{-1}) during summer monsoon period for the duration 1951-2015; (d) number of days exceeding 99p (season^{-1}) during summer monsoon period for the duration 1951-2015.

The climatology of the number of days of extreme rainfall (> nd99p) is depicted in Figure 3.1d. The spatial distribution of the number of extreme rainfall days differs from the distribution of the amount of rainfall from extreme events. The number of extreme events shows high values in the northwestern and northern regions, including Ladakh and Kashmir; however, the rainfall recorded over those regions is negligibly small (< 50 mm season^{-1}) from extreme events. Therefore, these regions are not considered for further analysis due to the minor contribution of rainfall from extreme events. Similarly, the impact of extreme events may become more vulnerable and devastating if more downpour occurs within a short span. Regions like the west coast, some places in central and northeast India, the foothills of the Himalayas, and coastal areas of Myanmar and east Bangladesh contribute a high amount of rainfall from less extreme events.

3.3 Standard Deviation of Mean Rainfall and Extremes

Figure 3.2 provides the spatial distribution of mean and extreme rainfall variability, illustrating deviations from the mean value across the spatial domain. In Figure 3.2a, it is evident that climatological rainfall exhibits high variability over the west coast, extending to Gujarat, central India, the foothills of the Himalayas, and northeastern regions (> 230 mm season^{-1}). The entire Bangladesh and Myanmar coasts also experience high rainfall variability during the summer monsoon season. The spatial variability of extreme rainfall during the season follows a similar pattern to climatological variability but with lower magnitudes (Figure 3.2a, b). This lower variability is attributed to the lower amount of rainfall from extreme events. In other words, the variability of extreme rainfall is directly proportional to the variability of seasonal rainfall. The standard deviation of days with extreme events reveals a distinct pattern crucial for describing the actual impacts of such occurrences (Figure 3.2c). The southern end of peninsular India, the Gujarat region, and the foothills of the central Himalayas exhibit considerable variability in the number of extreme days, with moderate variability in the amounts of extreme rainfall. Uttarakhand, Himachal Pradesh, Arunachal Pradesh, and the Indo-Gangetic plain regions experience high variability in both rainfall and the frequency of extreme events. These regions are prone to more calamities, such as floods and flash floods resulting from substantial amounts of rainfall occurring over consecutive extreme days; furthermore, the variability in these regions is also exceptionally high. Minor deviations in the number of days and significant variations in extreme rainfall amounts over the northern part of the west coast and certain regions in central India render these areas more vulnerable to hazards stemming

from extreme events.
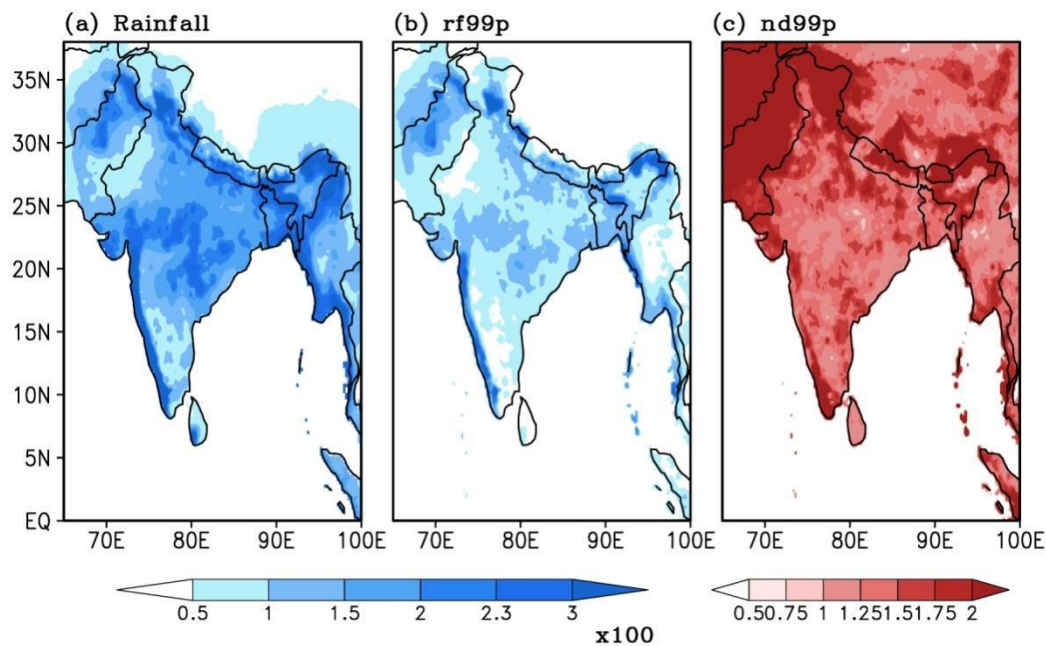
Figure 3.2: Standard deviation of (a) summer monsoon rainfall climatology (mm season^{-1}); (b) Amount of rainfall exceeding 99p (mm season^{-1}) during JJAS season for the duration 1951-2015 (65 years); (c) number of days exceeding 99p (season^{-1}) during JJAS season for the duration 1951-2015.

3.4 Contribution of Extreme Rainfall to the Annual Rainfall

Figures 3.3a&b represent the percentage contribution of extreme rainfall and its number of days to seasonal rainfall. The contribution of extreme rainfall is more significant (>20%) in the southeast and northwest regions, where the rainfall corresponding to the 99th percentile has low values. The contribution of extreme days has high values in the foothills of the Himalayas and the southern parts of the west coast. The Arunachal Pradesh region has an increased contribution of extremes in terms of the amount of rainfall (>30%) and the number of days (>4%). Although extreme rainfall contributes less in the west coast regions and other rainy areas, its impact lies in the combinational effect of the amount of rainfall and its duration. In the southern part of the west coast, around 10°N, the percentage of occurrence of extreme events is high. These events are in high-altitude areas, which amplify the magnitude of devastation and may lead to landslides and other natural disasters. Most of the central India regions have a high amount of rainfall contribution towards the seasonal total from fewer numbers of extreme days, which increases the damage to the population and economy from extreme events.

51
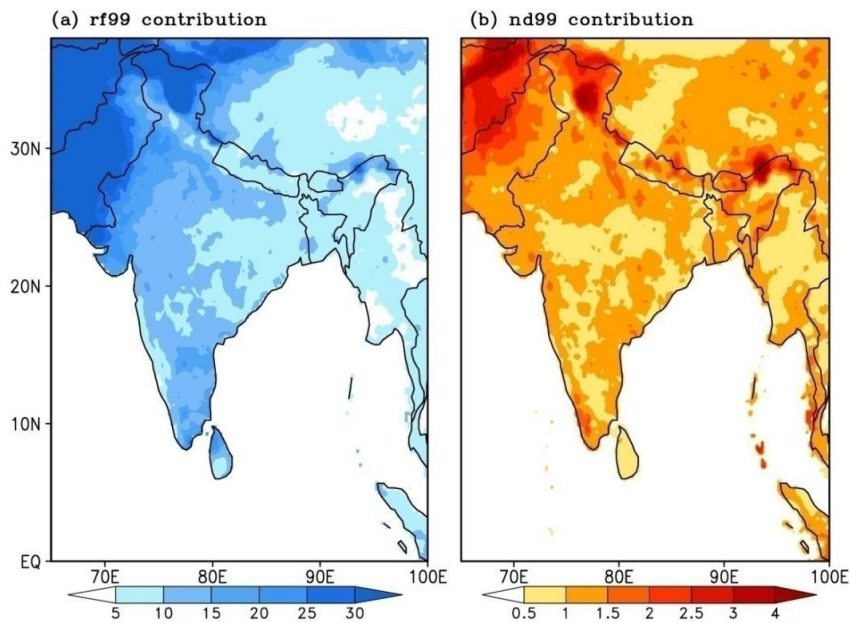
Figure 3.3: Percentage contribution of (a) amount of rainfall exceeding 99p (mm season^{-1}); (b) number of days exceeding 99p (season^{-1}) to the seasonal average.

3.5 Spatial Trends of Mean and Extreme Rainfall

The summer monsoon rainfall exhibits substantial temporal and spatial variabilities, ranging from weak to intense events (Goswami et al., 2006; Varikoden et al., 2012, 2013; Singh et al., 2019). Due to discontinuities within small spatial and temporal scales, the outcomes derived from conventional trend analyses of Indian summer monsoon rainfall (ISMR) conducted over larger regions (e.g., central India by Goswami et al., 2006) are contradicted by analyses performed at finer resolutions (Gosh et al., 2009). The current study unveils that spatial trends are not homogeneous across the spatial domain for both mean and extreme rainfalls (Figure 3.4). The spatial distribution of linear trends in seasonal rainfall is notably negative in most rainy areas of the Indian subcontinent, particularly in the Kongan belts, central Indian region, and northeast regions. In these regions, rainfall is exhibiting a decreasing trend with values less than –0.2 mm season^{-1} decade^{-1}. Conversely, linear trend values are increasing in regions with lower rainfall, suggesting a trend toward wetter conditions in these areas. This indicates that wetter regions are becoming drier, while drier regions are becoming wetter. The spatial trends of extreme rainfall and its events also exhibit a similar pattern, although variations exist in magnitudes and, to a slight extent, in specific regions.

In the case of extreme rainfall, major changes in spatial trends are observed in the west coast, central India, and north Indian regions. In the west coast regions, a negative trend (< –20 mm

season^{-1} decade^{-1}) is evident in the southern part of the Western Ghats (WG); however, rainfall from extreme events shows a positive trend north of 15°N (Figure 3.4b). A similar pattern of contrasting trends in the WG is found for the number of extreme rainy days (Figure 3.4c). Varikoden et al. (2019) identified an increasing trend in summer monsoon rainfall in the northern WG and a decreasing trend in southern parts. They attributed this contrasting trend to the northward migration of the low-level jet stream (LLJ). This northward migration of the LLJ is driven by the abnormal heating of the northern Indian Ocean and adjoining continents (Roxy and Tanimoto, 2007; Vialard et al., 2012; Varikoden et al., 2019), which, in turn, regulates interannual variability. Moreover, Sandeep and Ajaymohan (2015) argued that the weakening of meridional heat transport during the southwest monsoon period also led to the weakening of rainfall in the south of the WG and the strengthening of rainfall in the north. In the case of central Indian regions, the trends' values are highly inhomogeneous, and the regions of positive and negative trends (~15 mm season^{-1} decade^{-1}) are highly localised. This kind of inhomogeneity makes central Indian regions unpredictable in terms of regional extremes and their impacts. As Patnaik and Rajeevan (2010) suggested, synoptic-scale systems mainly contribute to one possible cause for the long-term increasing trend of EREs over central India. The number of days with a greater degree of moist convective instability shows an increasing trend during the summer monsoon period. Roxy et al. in 2017 suggested that despite the decrease in locally available water vapour and the frequency of moisture-laden depressions from the Bay of Bengal, a contemporaneous rise in the magnitude and frequency of heavy and EREs over central India is due to the increased variability of the low-level monsoon westerlies over the Arabian Sea, driving surges of moisture supply to the subcontinent. In north-central India, negative trends are found for both mean and extreme rainfalls. It is interesting to observe that the spatial distribution of extreme rainfall and its events shows a positive trend in the western Himalayas, a negative trend in the central Himalayas, and a positive trend in the eastern Himalayas. The northern part of northeast India (Arunachal Pradesh regions) shows a positive trend in both the mean (> 0.2 mm season^{-1} decade^{-1}) and extremes (> 20 mm season^{-1} decade^{-1}). In the case of regions in Nepal, the mean and extreme rainfall trends show contrasting patterns, with positive trends in mean rainfall and negative trends in extreme rainfall. Similarly, Bangladesh's regions also show contrasting trends for mean and extreme rainfalls.

In addition to the spatial trends, five pronounced regions were selected based on the linear trend of extremes in terms of amount and frequency to gain better insight into the characteristics of extreme events. The selected areas are marked in Figure 3.5 and are represented in the plot

showing the rainfall amounts exceeding the threshold value (Figure 3.4b). The area specifications of the selected regions, along with the seasonal rainfall and standard deviations, are given in Table 3.1. Spatial and lag-lead composites of extreme events and a time series of interannual variability and trends over the selected regions are constructed and analysed in the immediate section.
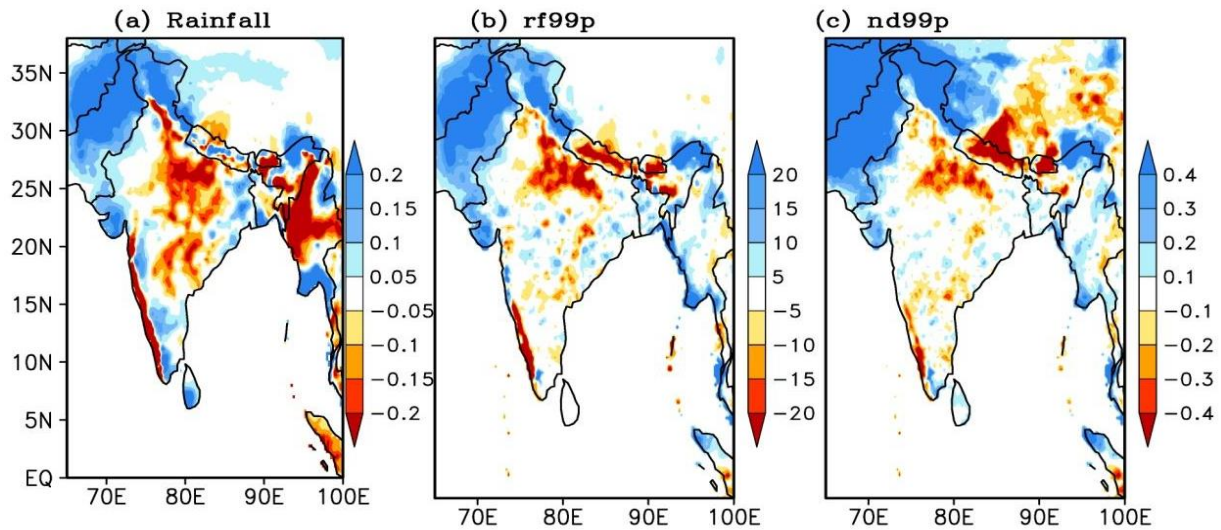
Figure 3.4: The spatial trend of (a) mean rainfall, (b) amount of rainfall exceeding 99p, (c) number of days exceeding 99p. The unit of the trend is mm season^{-1} decade^{-1}.

SL. No.	Name	Symbol	Area Specification	Average rainfall (mm season^{-1})	Standard deviation
1	Southern West Coast	SWC	10°–16° N, 73.5° –77.2° E	1215	222
2	Northern West Coast	NWC	16° –20° N, 72.6° –74.4° E	1802	320
3	Central India	CI	19° – 24.5° N, 75°–85° E	889	131
4	Northcentral India	NCI	24.5° –27.5° N, 73.5° – 85° E	653	111
5	Northeastern Region	NER	21° – 25° N, 88° – 96° E	1164	139

Table 3.1: Name and regions selected for the study along with its mean and standard deviation of rainfall
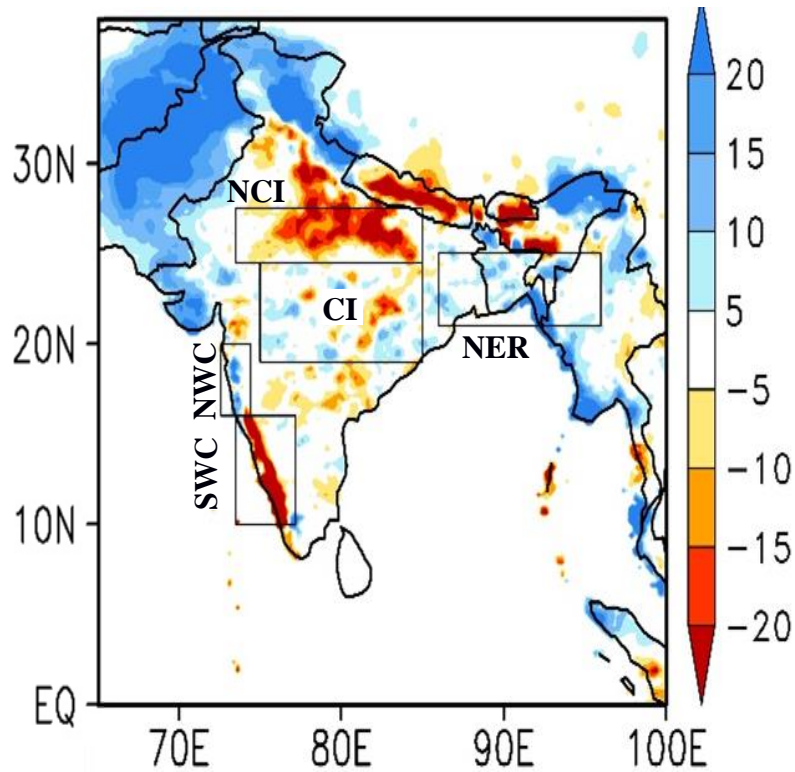
Figure 3.5: The selected areas are marked in the plot showing the rainfall amounts exceeding the 99p threshold value.

3.6 Spatial Composite of Extreme Rainfall Events

After identifying the prominent zones, all rainy days surpassing the 99p threshold value are extracted from the zones. Subsequently, the rainfall composite in the identified regions is found. Figure 3.6 illustrates the spatial distribution of the evolution and dissipation of extreme rainfall activities in the identified regions from 6 days before to 6 days after the extreme event, at intervals of 3 days. The analysis indicates that extreme events are predominantly heterogeneous in space and independent from one region to another. This variability may stem from differences in the driving forces of these extremes, such as synoptic and large-scale influences. Notably, the evolution phase of extreme systems is comparatively slower than the dissipation phase. On the extreme day, rainfall exceeds 100 mm day^{-1} in most grids within the SWC and NWC regions, situated in the western coastal belts of the WG. These two regions were selected separately due to differing trends despite the similarity in the spatial distribution of rainfall. As noted in earlier studies (Sandeep and Ajayamohan, 2015; Varikoden et al., 2019), the northern regions exhibit increasing rainfall trends, while the southern regions show decreasing rainfall trends, i.e., in the NWC and SWC regions, respectively. The lead-lag composite of rainfall extremes over these regions (derived from the area average of rainfall

amounts in the SWC and NWC regions) is presented in Figures 3.7a &b. Rainfall is above normal from 12 days before the extreme event, gradually increasing until three days before the event. However, from that day onward, the rainfall showed a sharp increase until the day of
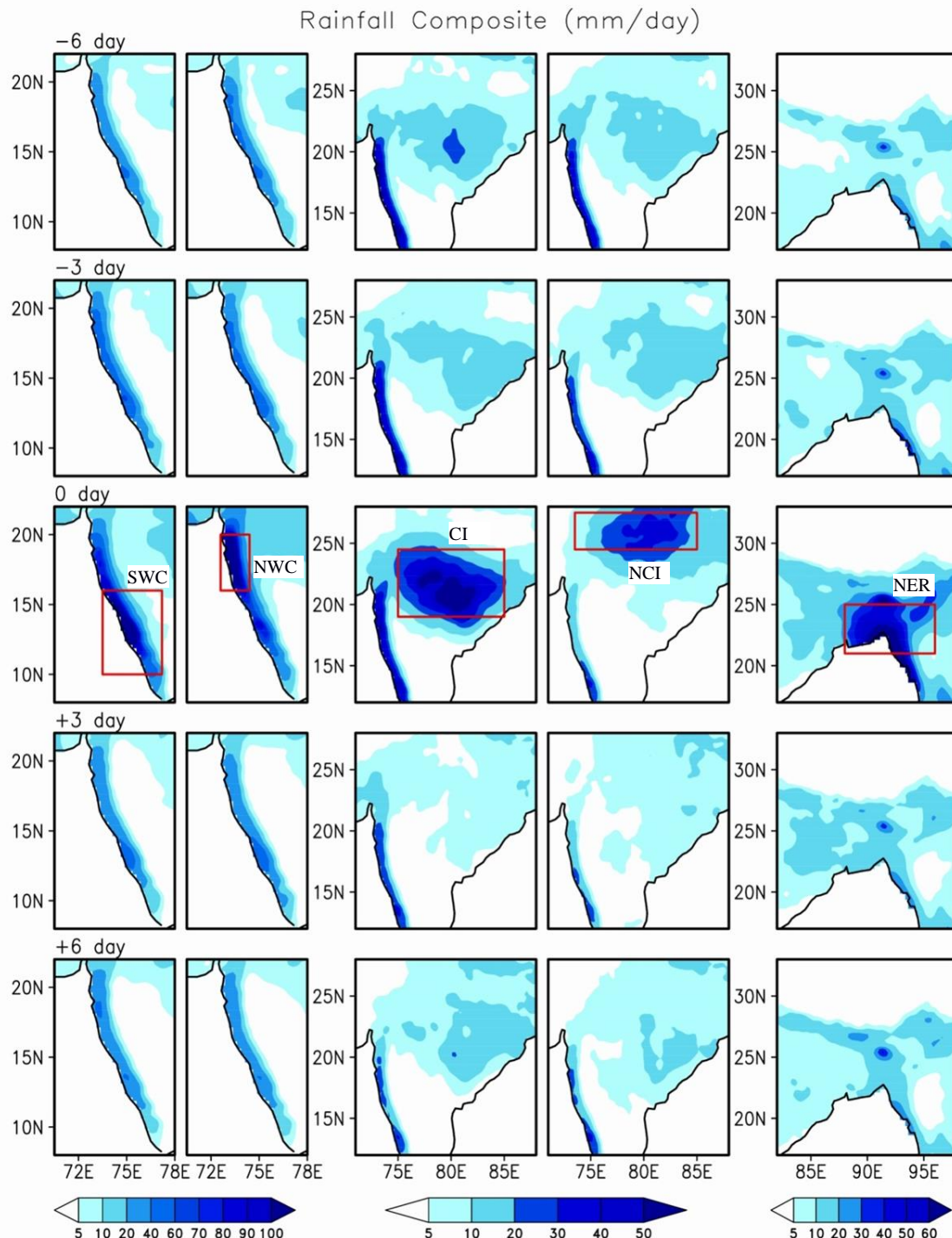
Figure 3.6: Spatial composite of extreme rainfall events over SWC, NWC, CI, NCI, and NER as separate panels.

extreme activity. The cessation of active rainfall is faster than its onset, with the southern region experiencing a sharper decrease than the northern region. The southern region recorded above-normal rainfall about two weeks after the extreme event. However, this prolonged effect is limited to only ten days in the northern region.
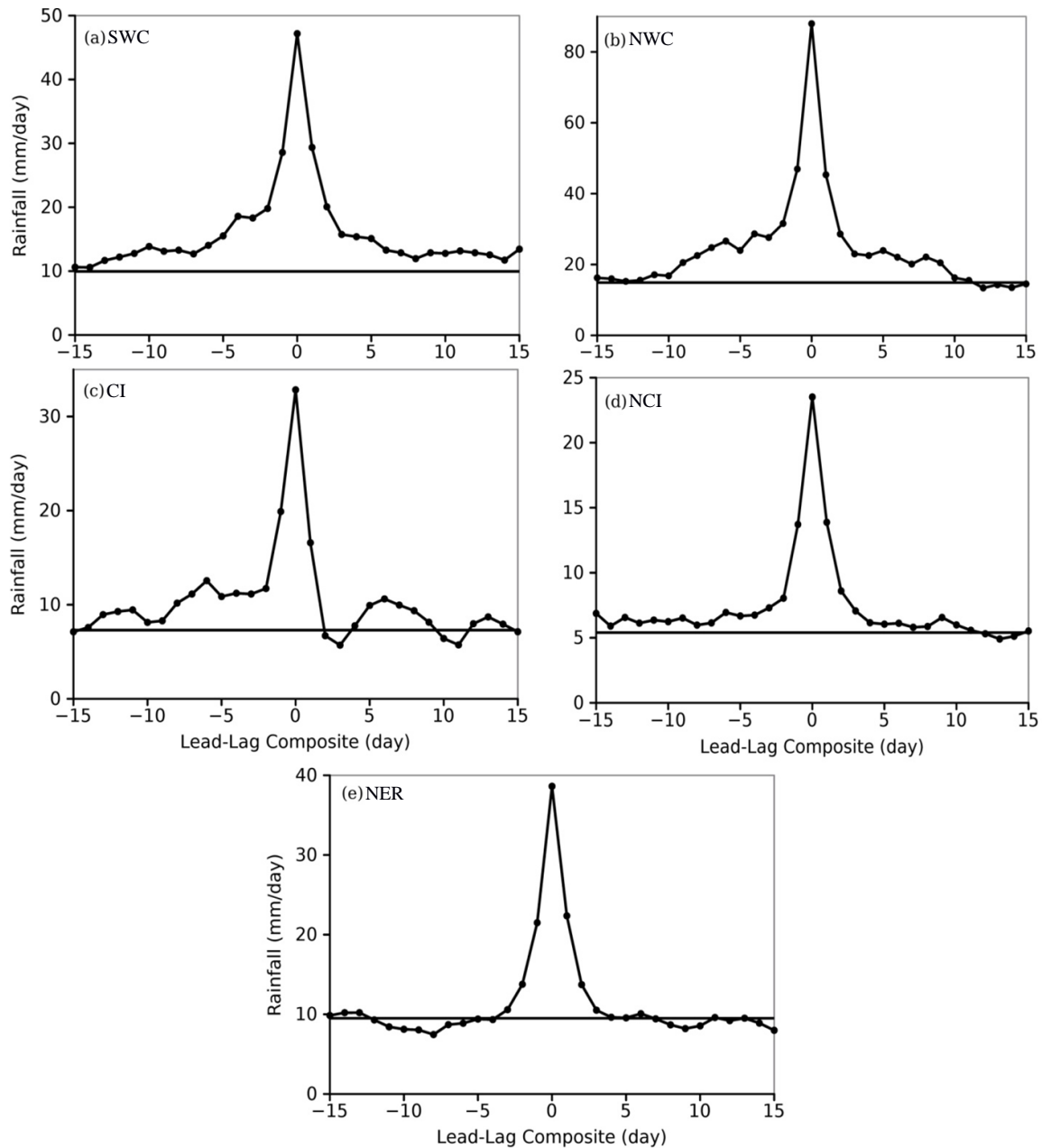
Figure 3.7: Lead lag composite of EREs during the southwest monsoon season for the period from 1951 to 2015. The horizontal line is the mean rainfall for the summer monsoon study period.

In the case of central India (Figure 3.6, third column), rainfall from extreme events is recorded at more than 50 mm day^{-1} in most of the grids. The temporal distribution of the events over

these regions differs significantly from the west coastal belts. A peak in rainfall is observed up to 6 days before the extreme event (represented as -6 days in the third column of Figure 3.6) in small regions experiencing extreme rainfall (> 30 mm day^{-1}). However, a dip in rainfall is noted between this peak and the extreme peak. After the extreme day, the rainfall gradually dissipates and again shows a minor peak. This feature is observed in Figure 3.7c. Following the extreme event, the rainfall exhibits a wavy pattern of approximately six days. As observed in the spatial pattern, the lead-lag composite also demonstrates gradual enhancement and sudden dissipation in rainfall. Soon after the extreme event, the rainfall returns to below-normal conditions.

Extreme events in north-central India and northeast regions are almost independent in both regions (Figure 3.6, fourth and fifth columns). In the north-central regions of India, extreme events are registered only during the day of extreme activity, with rainfall exceeding 50 mm day^{-1}. In the previous days of the EREs over NCI, central India and the west coastal regions had a high amount of rainfall. However, during the extreme day, the west coast regions experience suppressed rainfall compared to the previous days. The sharp evolutional and dissipational nature of NCI extremes can be confirmed by the lead-lag composite of the rainfall activity over this region (Figure 3.7d). The rainfall shows an abnormal increase from the day before the event and decreases within one or two days. In the remaining period, the rainfall is about normal. In the case of the northeast region, a small area of high rainfall activity is seen, and it may be the wettest region in the world, called Cherrapunji (Kuttppurath et al., 2021). However, the extreme rainfall is focused on a small region south of Cherrapunji, and the rainfall amount during the extreme episode is more than 60 mm day^{-1}. The lead-lag composite analysis shows below-normal rainfall in the activity region for about one week before and after the event. Here, the extreme event also develops and dissipates within a short period, which is about three days. Similar findings were also concluded by Varikoden and Revadekar (2020) in the northeast region.

3.7 Inter-annual Variability and Trend Analysis

Figure 3.8 describes the inter-annual variability of seasonal mean and EREs from 1951 to 2015. A three-point smooth is employed in the time series to remove sudden fluctuations in rainfall activity. In all five regions, seasonal rainfall shows less variability compared to the amount of rainfall from extreme events. The three-point smoothed mean of the seasonal total rainfall in regions SWC, NWC, CI, NCI, and NER are 1215, 1816, 890, 653, and 1164 mm season^{-1}, with
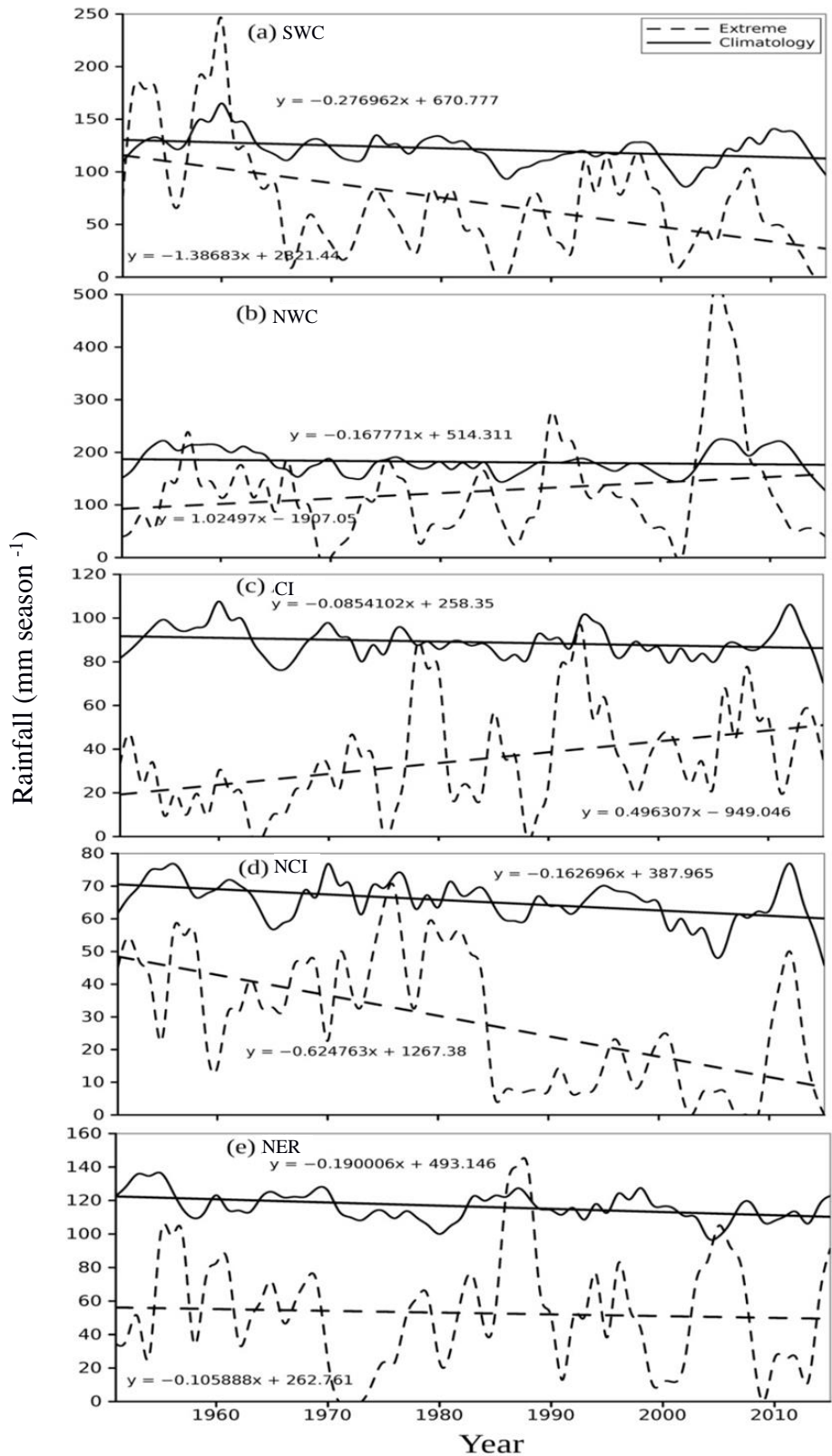
Figure 3.8: Year-to-year variability of mean and extreme rainfall from 1951 to 2015 during the southwest monsoon period for all the study regions. The solid line is for the climatology and the dashed line is for the extreme rainfall. The value of seasonal mean rainfall is divided by 10 to incorporate both mean and extremes in a single plot.

variabilities of 147.6, 232.6, 72.0, 65.0, and 84.2 mm season^{-1}, respectively. However, the

extreme rainfall amounts are 71, 125, 35, 28, and 53 mm season^{-1} with standard deviations of 52.2, 99.2, 22.6, 19.7, and 33.3 mm season^{-1} in regions from SWC to NER, respectively. Concerning long-term trends, most regions show decreasing trends in both seasonal mean and extreme rainfall amounts. The significance of the trends for mean and extreme rainfall values is estimated based on Mann-Kendall trend analysis (Kendall, 1975), and the results are given in Table 3.2. The nature of the slope, p-value, z-value, and Sen's slope are provided in the table. In all regions except NWC, mean rainfall during the period shows a decreasing trend with a 95% confidence level (the Z-values for regions SWC, NWC, CI, NCI, and NER are -2.49, -1.30, -1.96, -3.64, and -3.10, respectively). However, in the case of extreme rainfall, regions SWC, NCI, and NER show significant negative trends with 11.3, 5.9, and 1.3 mm season^{-1} decade^{-1}, respectively. Based on the MK-test, the trends in SWC and NCI are highly confident at the 99.9% level. However, compared with Sen's slope, the trend values are slightly higher in the case of linear trends without any change in direction. The other two regions, NWC and CI, show positive trends with 0.7 and 4.5 mm season^{-1} decade^{-1}, respectively. The trend value in region CI is highly confident at a 99.9% level. Linear trends are more significant for extreme rainfall changes than total seasonal rainfall.

Regions	P-value	Z-value	Sen's slope (mm yr^{-1})	Trends
SWC-mean	0.0129	-2.49*	-2.3	decrease
SWC-extreme	0.0010	-3.30*	-1.13	decrease
NWC-mean	0.1948	-1.30	-2.3	decrease
NWC-extreme	0.7727	0.29	0.07	increase
CI-mean	0.0495	-1.96*	-1.0	decrease
CI-extreme	0.0002	3.72*	0.45	increase
NCI-mean	0.0003	-3.64*	-1.7	decrease
NCI-extreme	0.0000	-4.38*	-0.59	decrease
NER-mean	0.0020	-3.10*	-1.7	decrease
NER-extreme	0.6343	-0.48	-0.13	decrease

* indicate the trends are confident at more than 95 % level

Table 3.2: Results of Mann-Kendall trend analysis for the period 1951-2015

In general, it can be concluded that the west coast regions exhibit contrasting trends for extreme events, with positive trends in the north and negative trends in the south, as briefed by Varikoden et al. (2019). Central Indian regions also show a contrasting trend, with a negative

trend in the north (NCI region) and a positive trend in the south (CI region). On the eastern side, rainfall shows a negative trend for both mean and EREs. Notably, region NWC has non-significant trends for mean and extreme rainfall.

3.8 Probability Distribution of Mean and Extreme Rainfall

The probability density function (PDF) of the rainfall time series from 1951 to 2015 was estimated to characterise the probabilistic distribution structure of the mean and extreme rainfall. The PDF analysis identifies the plausibility of the occurrence of any random variable within an interval, which is calculated by integrating the variable density over that interval. The PDF is non-negative, and the integration over the entire region under the curve is equal to one (Ogungbenro and Morakinyo, 2014). Calculated PDFs for mean and extreme rainfall over five different regions of South Asia for the total period (1951-2015), in addition to the pre-1980s and post-1980s, as depicted in Figure 3.9. From the figure, distinct differences in the pattern of the PDF of mean rainfall (left panels) and extreme rainfall (right panels) can be observed. The PDF of mean rainfall for the entire period is more influenced by the PDF of mean rainfall in the post-1980s period compared to the pre-1980s period. The PDF of mean rainfall peaked on the lower rainfall side, as evidenced by shifting leftward in the post-1980 period when compared to the total and pre-1980 periods. This shift signifies a reduction over time in the amount of mean rainfall associated with the frequency of occurrence. In the case of the PDF of extreme rainfall (right panels), the distribution differs slightly from that of mean rainfall. In the SWC region, the PDF is almost similar for the total and pre-1980 periods, with large fluctuations and lower frequency. However, in the case of post-1980 periods, the PDF curve is narrower, and the peak shifts towards the left, indicating reduced rainfall activity in those regions. The PDF distribution of the NWC region is almost in contrast to the SWC region, except for the total distribution. Here, the PDF for the pre-1980 period is narrower, and the post-1980 period is wider, with high extreme rainfall values (> 500 mm). Varikoden et al. (2019) also discussed these contrasting characteristics of rainfall. Similarly, the regions CI and NCI also show opposite features in the PDF distribution for the pre-and post-1980 periods. The peak of the PDF in the CI region has the same frequency, with a slight shift towards the left and right in their peak concerning the PDF of the total period during the pre-and post-1980 periods, respectively. Most extreme rainfall was concentrated in a 40- 50 mm range in the NCI region during the post-1980 period. In contrast, rainfall was concentrated around the 20 to 35 mm range during the pre-1980 period. Extreme rainfall in all regions except SWC manifests increasing variability in the post-1980 period by demonstrating its wider curve.
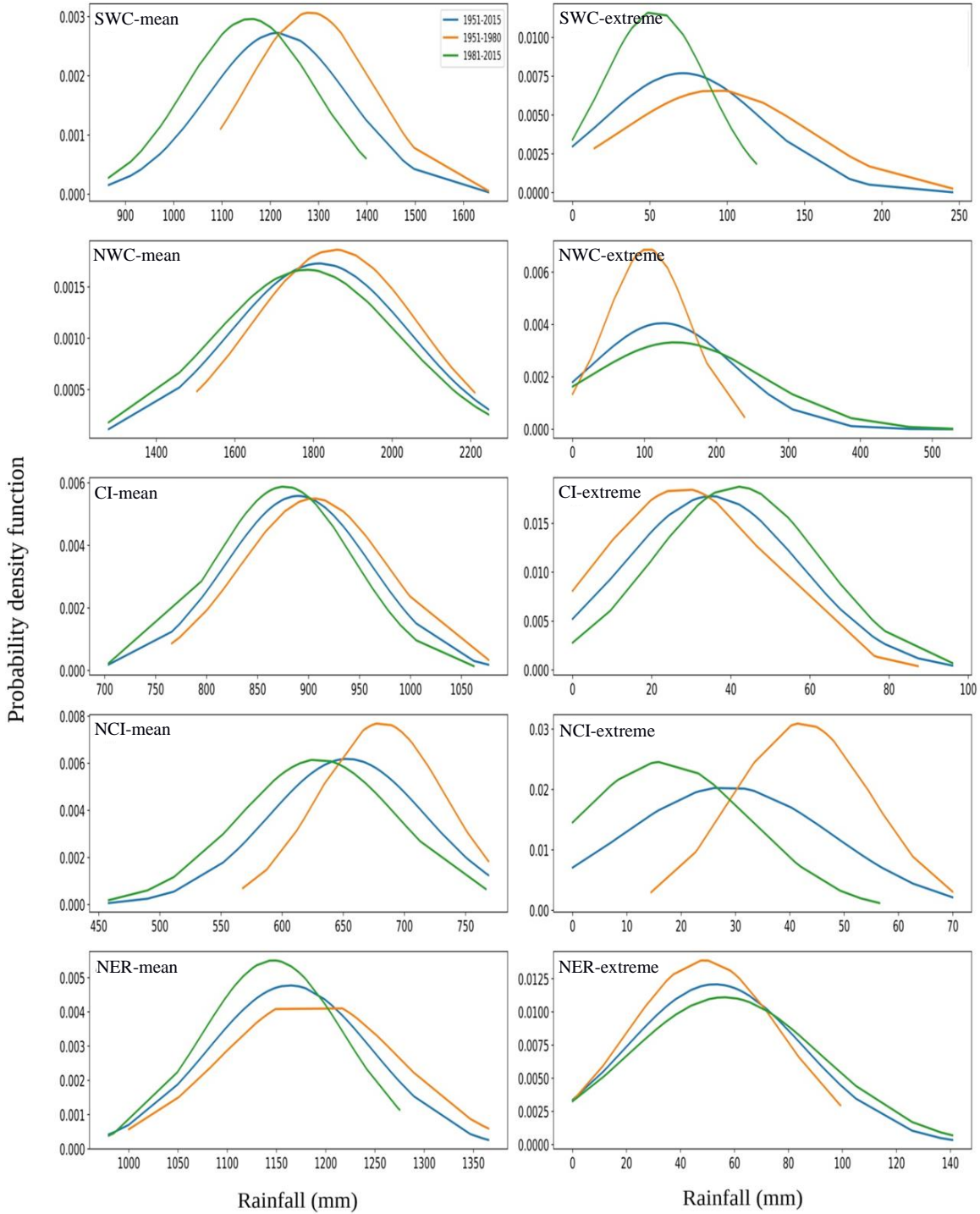
Figure 3.9: Probability density function of mean (left panels) and extreme (right panels) rainfall over five regions of India. The blue line represents the PDF of rainfall for the total period (1951 – 2015), and the red and green curves are PDFs of the pre- and post-1980 periods, respectively.

3.9 Correlation of Mean and Extreme Rainfalls with Global Climate Indices

The present study also investigates the correlation between global climate indices and rainfall over the Indian subcontinent. Spatial correlation is utilised to identify this relationship, and the

strength of the correlation is estimated through the Student's t-test. In Figure 3.10, the spatial correlation of mean and extreme rainfall with global climate indices (Niño 3.4, Modoki, DMI, PDO, AMO, and AZM) is depicted, with hatched lines indicating the 5% significance level. The relationship of ISMR with different climate indices varies across the spatial domain. The Niño index exhibits a broad inverse relationship between mean and extreme rainfall (Figure 3.10 a, b). The regions with a significant inverse relationship with mean rainfall are extensive, covering the entire Indian subcontinent. Previous studies also support these findings (e.g., Sikka, 1980; Pant and Parthasarathy, 1981; Webster and Yang, 1992; Kumar et al., 1999; Krishnamurthy and Goswami, 2000; Varikoden and Babu, 2015; Hrudya et al., 2020 a, b). However, this significant inverse relationship diminishes in the case of extreme events. In the central Indian regions, rainfall does not exhibit any significant relationship, and the relationships fluctuate widely within the regional scale, as Ghosh et al. (2016) indicated. This lack of a significant relationship can be attributed to the fluctuating nature of the relationship between these parameters on a multi-decadal time scale (Seetha et al., 2019; Hrudya et al., 2020b).

The El Niño Modoki index differs from the canonical ENSO index despite both being coupled ocean-atmosphere phenomena in the tropical Pacific Ocean. It distinguishes itself through distinct spatiotemporal features and teleconnection patterns. Characterised by a warm anomaly in the central Pacific flanked by cold anomalies on both sides (Ashok et al., 2007; Ashok and Yamagata, 2009), the Modoki index exhibits a negative correlation with rainfall in most regions, except in east central India, where the relationship is in phase (Figure 3.10 c, d). Unlike the classical ENSO index, the Modoki index shows fewer significant areas. When describing El Niño Modoki extremes, the correlation coefficient is more positively significant throughout central India, with some areas reaching a 95% confidence level, along with enhanced positive values in the northeast regions compared to mean rainfall. Additionally, during extremes, the areas of inverse relationship exhibit a considerable reduction, and slight positive correlation values are observed in the Ganges plains. Dandi et al. (2020) also found that rainfall anomalies are below normal in southern peninsular India and positive over central India during El Niño Modoki years.

The IOD index serves as a gauge of the difference in the Sea Surface Temperature (SST) anomalies between the west and east Equatorial Indian Oceans (Saji et al., 1999). Generally, this index exhibits a positive correlation with the ISMR, although the correlation is not

statistically significant (Ashok et al., 2001, 2003; Ashok and Saji, 2007; Hrudya et al., 2021). However, the current analysis reveals an inverse relationship with both mean and extreme rainfall, except in the central Indian regions. Notably, during extreme events, the strength of the positive relationship intensifies compared to mean rainfall (Figure 3.10 e, f). Significant inverse relationships are observed in the northeast and north-central regions, in addition to
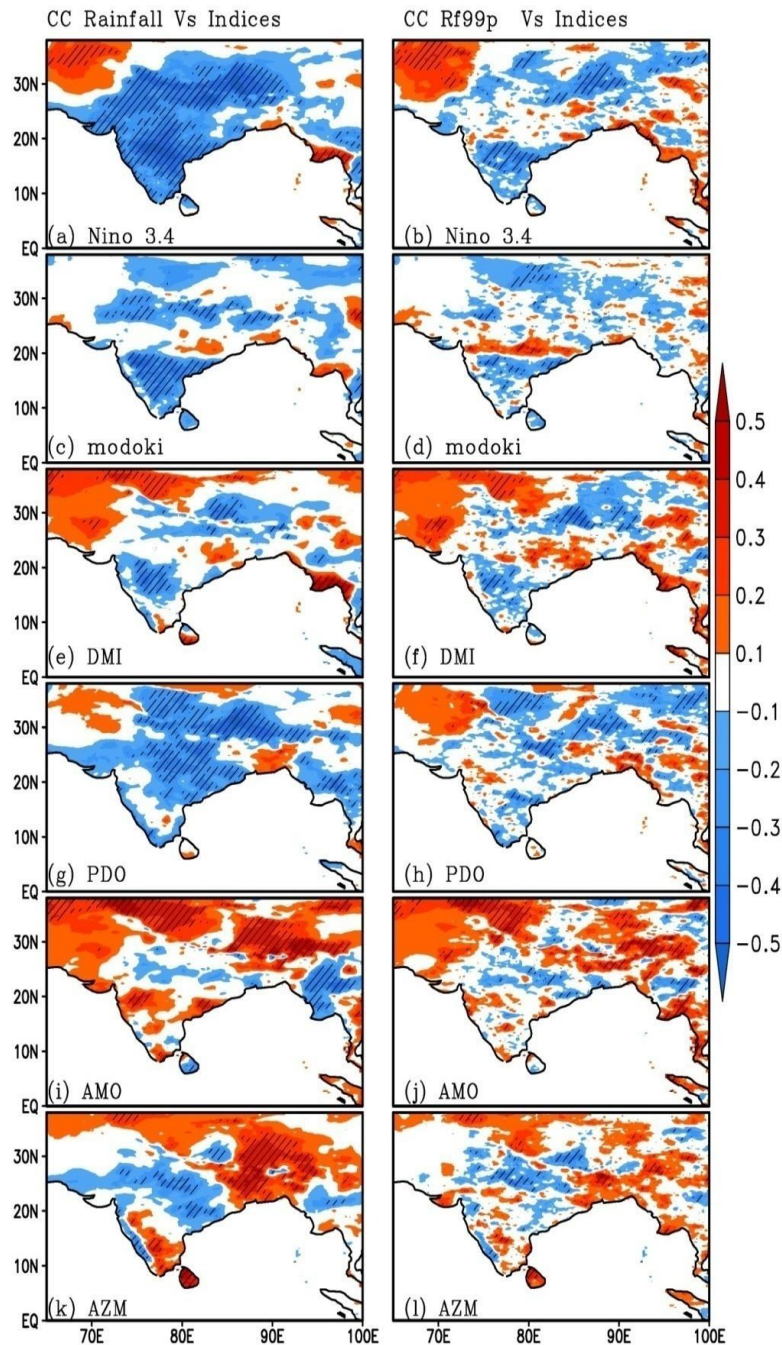
Figure 3.10: Correlation coefficient of the mean (left panel) and extreme rainfalls (right panel) with (a) and (b) Niño 3.4; (c) and (d) El Niño Modoki; (e) and (f) DMI; (g) and (h) PDO; (i) and (j) AMO; (k) and (l) AZM. The hatched lines represent areas with 5% significance level.

peninsular India. Conversely, the relationship is non-significant in the rain shadow regions, and it may be in phase over the peninsular regions. The ongoing warming trend of the equatorial Indian Ocean, coupled with the IOD, is suggested to contribute to more frequent EREs and related hazards in central India (Ajayamohan and Rao, 2008).

The PDO index in the subtropics of the North Pacific Ocean is linked to the ISMR, exhibiting a spatial pattern nearly consistent with the Niño3.4 index in terms of mean rainfall. This relationship holds across most regions, except in the rain shadow areas of southeast peninsular India, where the correlation is slightly positive, though statistically insignificant (Figure 3.10 g). However, when examining extreme events (Figure 3.10 h), this robust negative correlation is not observed in the Indian subcontinent. The correlation coefficients' negative and positive regions exhibit significant variability at the regional scale, making it challenging to establish a conclusive associative relationship between the PDO index and EREs.

The spatial correlation of the AMO index with the ISMR is significantly positive in the peninsular regions and negative in the monsoon core zone, although the correlations are less significant. All the northern regions exhibit high significance with an in-phase relationship between the AMO index and ISMR. In contrast, a significant out-of-phase relationship is observed in the Myanmar region (Figure 3.10 i). This spatial distribution is almost opposite to that of the DMI, particularly over the Indian regions. The relationship with extreme events follows a similar pattern to mean seasonal rainfall with less significance. During extreme events, the regions of significant in-phase relationships are reduced, and out-of-phase regions are enhanced, particularly in central India.

Considering the AZM, unlike the AMO, the mean summer monsoon rainfall is negatively correlated, with statistical significance below the 5% level in the entire central India and the west coastal regions. Significant positive correlations are observed in the northern and northeast regions, as well as the southeastern regions (Figure 3.10 k). In the case of extreme events, the relationship is significant in the regions of the west coastal belts and north-central India. The positive relationships for extremes are almost insignificant in the regions where a significant relationship is observed for mean rainfall (Figure 3.10 l).

In general, a negative relationship between extreme rainfall and PDO, AMO, and AZM can be established in the central Indian regions. However, it is positive for the indices Niño3.4, Modoki, and DMI. In the peninsular regions, an inverse relationship can be attributed to the

indices Niño3.4, Modoki, DMI, and PDO; however, AMO and AZM do not show any consistent relationship. The mechanisms leading to the teleconnection of global climate indices with mean and extreme rainfall, as well as the internal changes occurring over South Asian regions, need further exploration. The present manuscript does not delve into the physical and dynamical mechanisms behind this teleconnection relationship and their multi-decadal changes. This aspect should be studied further.

3.10 Chapter Summary

The analysis of the spatial characteristics of mean and EREs during the summer monsoon season over a 65-year period (1951-2015) reveals that the entire west coast, certain parts of central India, foothills of the Himalayas, and northeastern regions are highly prone to EREs during the season. The number of days exceeding the 99th percentile value also corresponds to the amount of rainfall from these extremes. The contribution of rainfall from extremes to the mean rainfall is more than 20% in most non-monsoonal regions of India but less than 15% in the monsoonal regions like coastal regions of the WG, central and northeast India, as well as the foothills of the Himalayas. The mean rainfall trend is decreasing in most of the Indian subcontinent, except on the leeward sides of the WG and some northeast regions extending to the coastal areas of Bangladesh and Myanmar. The spatial trends in extreme events follow a pattern similar to mean rainfall. However, the northern portions of the west coast show a non-significant increasing trend. The central Indian regions exhibit a mix of highly varying positive and negative trends. These pockets of contrasting trends are isolated, and the significance values are comparatively low.

In conclusion, based on the regional analysis of rainfall composites for extreme events and lead-lag analysis, most extreme events develop within a short span of three days, even though their signature with above-normal rainfall appears almost one week prior to the event. While the southern parts of the west coast, northern parts of central India, and northeast regions show similar trends with more or less comparable values for mean and extremes, contrasting trends are also observed in the other areas, such as the northern part of the west coast and central India. The probability distributions of rainfall in the pre-1980 and post-1980 periods exhibit greater differences in the case of extremes than for mean rainfall. The individual analysis of the correlation of climatological forcing mechanisms with mean and extremes reveals spatial variations. It could not identify any indices as reliable predictors of extreme events in South Asian regions. Due to the interdependence of various forcing mechanisms influencing the

ISMR, their coupled action makes the impacts and vulnerability of extreme events unpredictable.

The next chapter analyses the dynamic characteristics of South Asian summer monsoon EREs. Exploring the circulation and other meteorological parameters conducive to regional ERE is the primary focus of the chapter.

CHAPTER 4

DYNAMICAL CHARACTERISTICS OF SOUTH ASIAN SUMMER MONSOON EXTREME RAINFALL EVENTS

CHAPTER 4

DYNAMICAL CHARACTERISTICS OF SOUTH ASIAN SUMMER MONSOON EXTREME RAINFALL EVENTS

4.1 Introduction

This part of the study investigates the favourable conditions for regional extreme rainfall events (EREs) over the Indian subcontinent from 1951 to 2015 in terms of circulation and other meteorological parameters. The selected regions for the study were determined through the analysis of mean and extreme rainfalls, as discussed in Chapter 3. The large-scale dynamic factors leading to the various EREs over different regions are investigated before, during and after the EREs. Owing to the heterogeneous nature of the study area in terms of topography, presence of waterbodies, and other geographical features, the contribution of the different dynamical factors is different in different regions. To explore the cessation and dissipation characteristics of various EREs in different regions, the lead-lag composites of horizontal circulations, relative vorticity, specific humidity anomalies and vertical velocity are analysed. Moisture convergence, vertically integrated moisture transport and vertically integrated moist static energy are also assessed during the EREs.

4.2 Features of Mean and Extreme Rainfall in the Pronounced Regions

Before exploring the dynamic features of EREs, the analysis of the characteristics of mean rainfall and EREs over the selected study regions during the southwest monsoon period from 1951 to 2015 is conducted. The mean and its standard deviations are given in Figure 4.1a, and the linear trends in the form of Sen's slope values in the regions are expressed in Figure 4.1b. In the case of seasonal mean rainfall, the maximum amount of rainfall is received in the western coastal regions, while northern regions receive more than that in the southern coastal belts. Rainfall extremes also show a similar pattern with a high contribution in the northern west coast (NWC). The extreme rainfall contributes about 6.9% to the seasonal mean in the NWC regions, but it is 5.9% in the southern west coast (SWC) regions. However, the variability of mean and extreme events is high in the northern regions, increasing the uncertainty in the predictability of the rainfall events. The maximum contribution of EREs is observed in northcentral India, followed by central India, 12.4% and 10.1%, respectively. Although the amount of rainfall is high (124 mm season^{-1}) in northwest coastal regions, it contributes only 6.9% to the seasonal rainfall (1815.5 mm season^{-1}). This region also shows high variability

with a standard deviation of 233.73 mm season^{-1} and 62.87 mm season^{-1}, respectively, for mean and extremes.

In addition to the mean and extreme rainfall distributions, results obtained from the Mann-Kendall test for the significance of trends in the identified regions and Sen's slope estimate to obtain the magnitude of trends in the respective regions (Figure 4.1b) are also analysed. All regions show decreasing trends for mean seasonal rainfall, and the trend values for southern west coast (SWC), northern west coast (NWC), central India (CI), northern central India (NCI)

Figure 4.1: (a) Standard deviation of mean and extreme rainfalls over the selected regions (mm season^{-1}) (b) Trend of mean and extreme rainfalls over the selected regions (mm year^{-1}).

and northeastern regions (NER) are –2.32, –2.35, –1.03, –1.69, and –1.75 mm year^{-1}, respectively. They are significant at more than 95% confidence level except in the NWC region.

In the case of EREs, the trends are significant based on the Mann-Kendall test in the SWC and northcentral Indian regions, with more than 99.9% confidence level, but they are not significant in NWC and NER regions. It is also important to point out the nature of mean and extreme trends over the northwest coastal region, where the trend values for mean and extremes are – 2.35 and +0.07, respectively. Furthermore, this region shows large inter-annual variability as manifested with high values of standard deviations for the mean (± 233.73 mm year^{-1}) and extreme rainfall (± 62.87 mm year^{-1}) events (Figure 4.1a) compared to other regions. Moreover, this region is comparatively smaller in geographical extent compared to other regions. Due to the non-predictable variations and other rainfall characteristics, the study has not included this region for further analysis to explore the dynamics of EREs.

4.3 Circulation Features of Extreme Rainfall Events

Previous studies confirm the role of monsoon intraseasonal oscillations (MISOs) through active and break cycles in generating EREs over the Indian subcontinent by modulating synoptic weather disturbances (Singh et al., 1992; Krishnan et al., 2000; Annamalai and Slingo, 2001; Lawrence and Webster, 2001; Goswami et al., 2003; Wang et al., 2005; Varikoden and Revadekar, 2020). The self-induction mechanism of MISOs over the Indian Ocean as the seasonal northward migration of the tropical rain bands can provide some background for the predictability of EREs (Goswami et al., 2019). This analysis focuses on the short-term lead-lag analysis from 6 days before and 6 days after the occurrence of EREs. This is to gain insight into the change in the regional circulation features related to the EREs over the selected regions from their evolution to the dissipation stages. Wind composites have been made at 850 hPa from 6 days back to 6 days ahead of the extreme event to explore the circulation features. Vertical cross-sections of the specific humidity and vertical velocity were also explored to represent the moisture content and magnitude of convection, respectively.

The streaming of low-level circulation, which is associated with a large meridional thermal gradient between the Asian landmass and surrounding oceans, modulates ISM rainfall (Hoskins and Rodwell, 1995; Sagalgile et al., 2017; Patil et al., 2019). Figure 4.2 illustrates the lead-lag composite of wind at 850 hPa during EREs from -6 days to +6 days. In the case of extreme events over the SWCal regions, the low level circulation was weak almost six days prior to the event, especially over the SWCal regions where the wind strength is less than 5 m s^{-1} concerning the day of extreme rainfall. Then, the wind strengthens and reaches its maximum during the extreme day. During the extreme day, the wind strength is more than 18 m s^{-1} over

the SWC regions and the entire Arabian Sea. In addition to the wind strength, the wind direction is modulated from southwesterly to westerly, which helps supply the moisture directly from the ocean source, favouring the orographic rainfall. After the extreme event, the recession of the strong wind from the land mass and southwest monsoon domain begins and gradually reaches its climatological values. However, the rate of weakening of wind is not as fast as that of the evolution period.
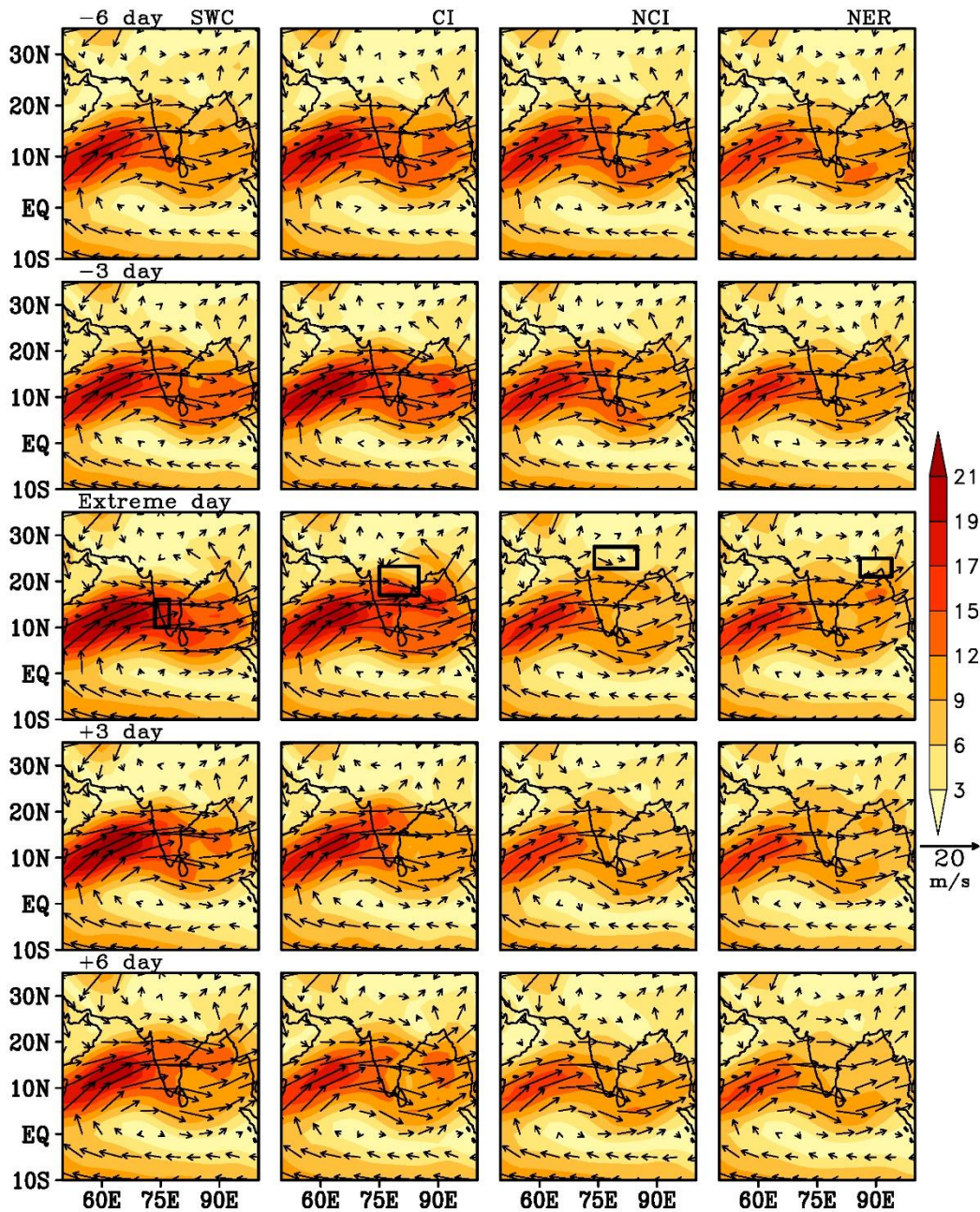
Figure 4.2: Lead-lag composite of wind (ms^{-1}) at 850 hPa during extreme rainfall events over the selected regions.

Similarly, in the case of Central Indian extremes, the wind gradually strengthened from about six days back and directed to the central Indian region, where EREs occurred. During the days of extreme rainfall, the wind strength exceeded 16 m s^{-1} in the CI and more than 18 m s^{-1} over the central Arabian Sea, which helps to bring ample moisture from the oceanic source. The structure of low-level circulation during the central Indian EREs is analogous to the active monsoon situation, and that can also lead to the generation of EREs, and those may be associated with large-scale synoptic events like low pressure systems over central India (Hirschboeck, 1991; Kale et al., 1994). However, the wind strength is slightly lower compared to the extreme events in the SWC regions. Soon after the extreme event, the wind strength decreased considerably by the next three days and further decreased thereafter.

In the case of NCI, the low level Jetstream (LLJ) is weak over the entire South Asian monsoon domain, and it has become a break-like or active to break transition condition. The wind core bypasses through Sri Lanka, and strength also reduces over the central Indian region from about 12 m s^{-1} to 9 m s^{-1}. However, during extreme events, the wind core over the Arabian Sea splits into two components: one passes over the NCI (north of 20° N), and the other passes through the southern tip of peninsular India. This type of circulation structure during the break monsoon season was also reported earlier by Findlater (1971) and Joseph and Sijikumar (2004). This northern core of LLJ can be attributed to the occurrences of extreme events there. After that, the northcentral component gradually dissipates, and the southern component strengthens. This spatial structure indicates the transition from active to break monsoon conditions. Therefore, it can be inferred that the extreme events in NCI regions are mainly produced when the MISO oscillation moves from active to break spells.

The extreme events in the NER are characterised by the southerly winds from the Bay of Bengal (BoB), and the wind strength reaches about 12 m s^{-1} during the extreme day. In general, the strength of low level circulation over the Arabian Sea did not show any remarkable changes during, before and after the extreme event. It is also noted that the circulation has a significant westerly component during the extreme event, and this westerly regime is conducive for moisture transport to the region from the BoB and ultimately leads to abnormal showers there. The contribution of westerly regimes in the northeast regions was also reported by Fujinami et al. (2017), Suthinkumar et al. (2019) and Varikoden and Revadekar (2020).

4.4 Relative Vorticity

Figure 4.3 represents the lag-lead composite of relative vorticity (RV) at 700 hPa during the EREs, its evolution and dissipation periods before and after six days from the extreme day for all four selected regions. The positive RV indicates the convergence of the low level circulation. In the west coast region, the positive RVs are visible in the northern part of the western coastal regions from -6 days onwards, and they gradually increase and spread towards the SWC regions, where the extreme rainfall occurred (Figure 4.3 first column). After the extreme event, the regions of positive RV are confined to the northern regions with an axis over the central Indian
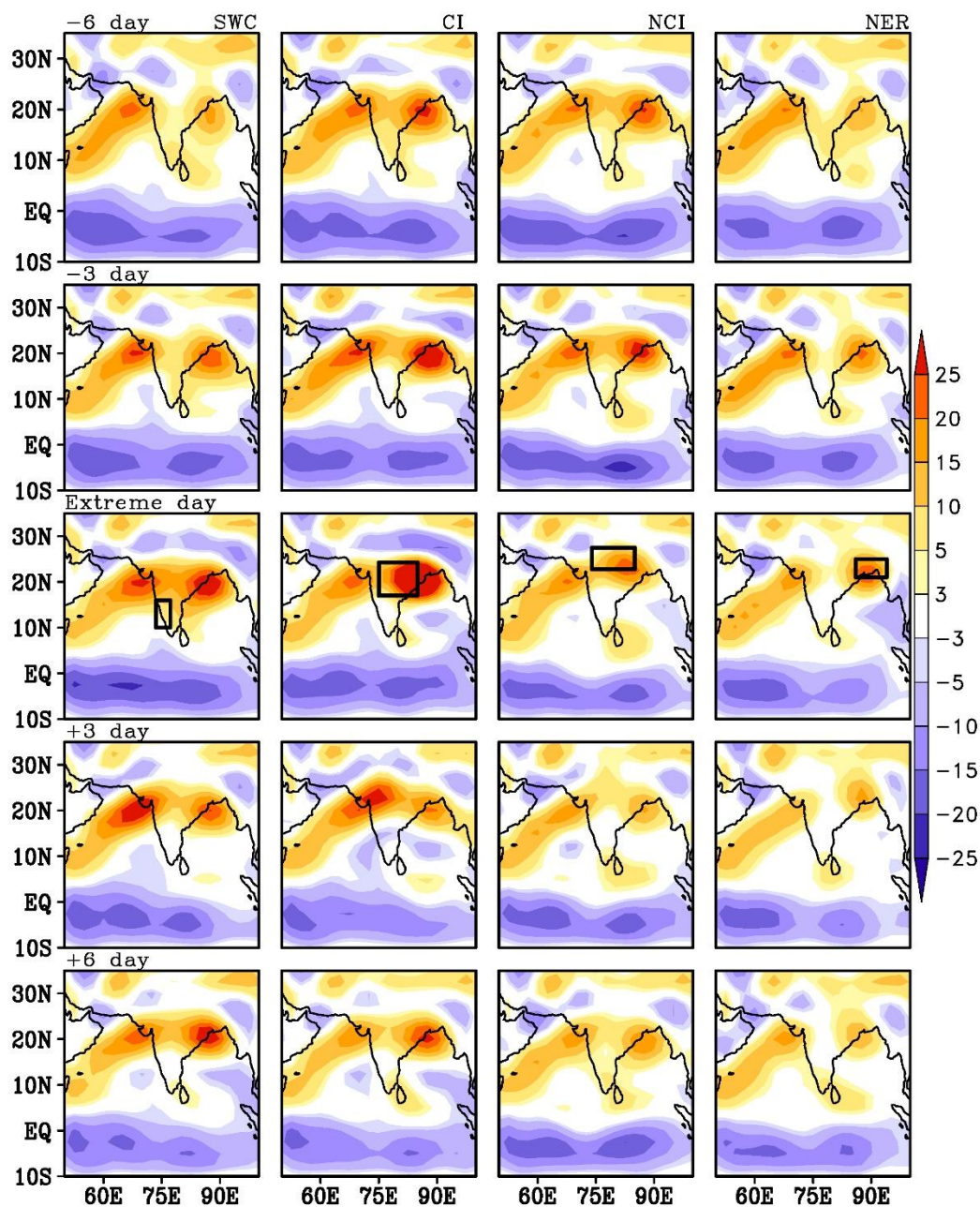
Figure 4.3: Composite structure of relative vorticity (s⁻¹) at 700 hPa before, during, and after the extreme rainfall events over different regions of the Indian subcontinent.

regions. The axis of positive RV is situated in the northern regions of the west coast (WC), and this is due to the meridional gradient of the low level jet stream, as seen in Figure 4.3. The core of LLJ is observed through Peninsular India, primarily through the regions of the EREs, and therefore, there are relatively lower values of positive RV there.

The CI regions are also characterised by positive RV in the case of CI extreme events. The intensity of convergence progressively increases till the day of the extreme events. It recedes almost suddenly, and a divergence zone appeared in the peninsular region, indicating a sudden dissipation of the organised rainfall systems. A similar mode of evolution and dissipation is seen in the case of northern central Indian extremes. However, positive RV intensity is comparatively lower compared to central Indian extremes. In addition to the low level convergence over the northern regions, a similar convergence zone was noticed in the southern tip of Peninsular India. This mode of spatial structure is characterised by the active break transition, as briefed above (Figure 4.3). In this case, the positive RV is almost stagnant in both regions with slight temporal variability. In the case of northeast extremes (Figure 4.3, fourth column), the positive RV is distinct in the regions of EREs. The large-scale axis of positive RV through central India is not so distinct in this case, and it indicates the apparent difference from other extreme cases in other regions of the Indian subcontinent. From the figure, it is evident that the low level convergence zone is persistent over the foothills of the Himalayas, and it indicates a break-like monsoon condition. In all the cases, a positive RV is apparent over the Arabian Sea and is consistent with the northern part of the LLJ; there, the meridional gradient of wind is strong, leading to low level convergence.

4.5. Moisture Transport During Extremes

Rainfall activity during the southwest monsoon season has a direct link to the amount of moisture transported to the land area of Indian subcontinent from the surrounding oceans, especially from the Arabian Sea and southern Indian Ocean (Ghosh et al., 1978; Mohanty et al., 1984; Sadhuram and Rao, 1998; Swapna and Kumar, 2002; Izumo et al. 2008; Levine and Turner, 2011; Seetha et al., 2020). Figure 4.4 presents the composite of vertically integrated moisture transport (VIMT, kg m^{-1} s^{-1}) over WC, CI, NCI and NER during EREs in the southwest monsoon period. In the case of EREs over the WC, the VIMT shows its maximum value (> 375 kg m^{-1} s^{-1}) over the central and eastern Arabian Sea, including the southwest coast of the Indian peninsula. The moisture transport during these extreme periods is westerly; therefore, it is conducive for surplus rainfall over the SWC regions of the Indian subcontinent.

Lakhmi et al. (2019) also reported that the persistent presence of high VIMT leads to EREs. Rathna et al. (2016) also reported that the reduced moisture led to deficit rainfall over the Western Ghats (WG) from 2003 to 2012 due to the reduction in the LLJ at 850 hPa. Therefore, the moisture supply towards the continents during the extreme events over the SWC regions is distinct in Figure 4.4. Similarly, the spatial pattern of the flow of moisture transport during extreme events over CI is almost similar to that of the WC. However, the magnitude of the moisture transport is less during the CI extreme events. Two peaks of VIMT are observed on the spatial domain; one is over the central Arabian Sea, and the other is over the north BoB, including the central Indian land mass. This high amount of moisture leads to extreme events over there. The moisture is directed from the Arabian Sea to peninsular India, especially over CI, which is almost like the pattern seen during the active monsoon period, as discussed in the low level circulation section.

However, in the case of NCI and NER, the spatial structure of moisture transport is almost like the break or active to break transition periods of the intraseasonal oscillation of the southwest
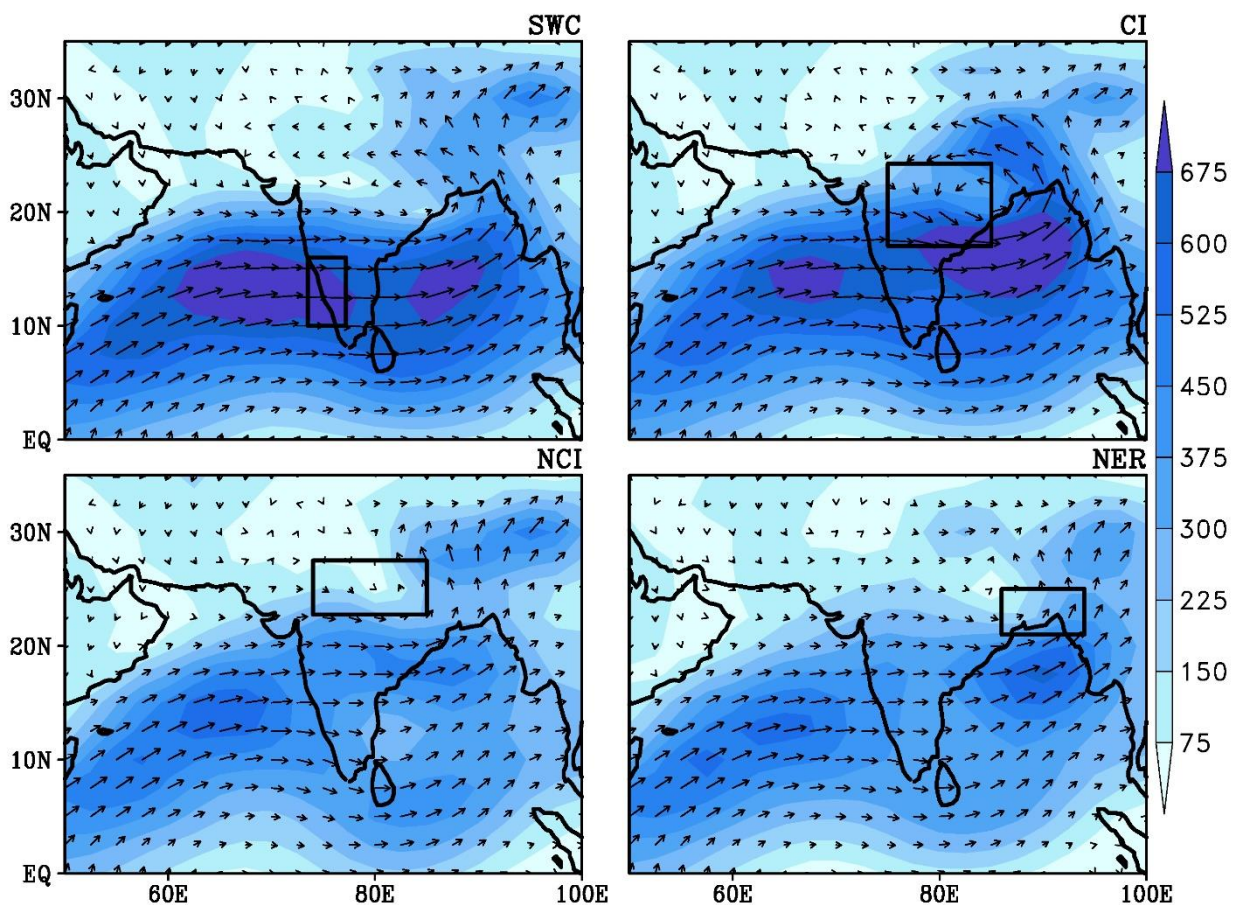
Figure 4.4: Composite of vertically integrated moisture transport from the surface to 300 hPa (kg m^{-1} s^{-1}) during extreme rainfall events over the four selected regions.

monsoon. In the case of NCI, the moisture transport shows two pathways after splitting it from the Arabian Sea; one goes to the southern tip of peninsular India, and the other goes through north India. This north Indian component favours the excess rainfall over the NCI, even though the magnitude of the moisture is lower compared to the west coastal and central Indian regions, which is consistent with the rainfall during the extreme events, as shown in Figure 4.1. The amount of rainfall in the NCI is lower when compared with the rainfall in the WC and central Indian regions. The primary source of moisture in the NCI is also from the Arabian Sea, as depicted in Figure 4.4 (left bottom). Similarly, the moisture transport during extreme events in the NER is high over the central Arabian Sea and north BoB, including the NER of the land mass. The value of VIMT exceeds $600\,\text{kg}\,\text{m}^{-1}\,\text{s}^{-1}$ during extreme events over the NER; therefore, it supplies abundant moisture from the BoB. Moreover, the flow pattern is also dominant with westerly regimes, as explained in low level circulation patterns. In general, the VIMT is
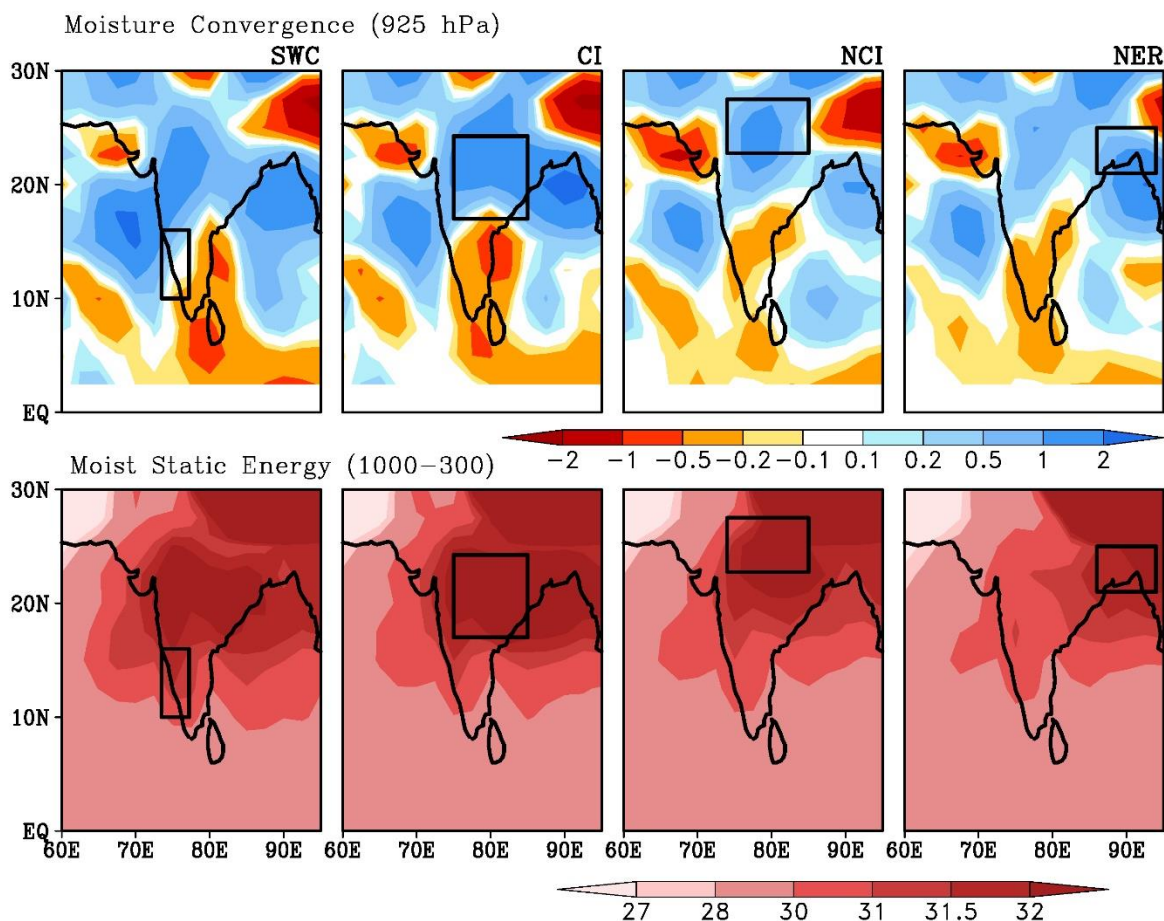
Figure 4.5: Spatial structure of low level moisture convergence at 925 hPa (upper panels, $\times\,10^{-7}\,\text{kg}\,\text{m}^{-2}\,\text{s}^{-1}$) along with vertically integrated moist static energy (bottom panels, $\times\,10^{2}$ $\text{K J}\,\text{kg}^{-1}$) during the extreme rainfall events in the southwest monsoon period.

abnormally high in places of extreme rainfall, and the primary source of moisture to the WC, CI, and NCI regions is the Arabian Sea; however, it is the BoB in the case of NER.

The low level moisture convergence at 925 hPa is also consistent with the regions of the EREs over the Indian subcontinent (Figure 4.5 upper panels) because during periods of EREs, the LLJ creates convergence in the atmospheric boundary layer. In the SWC, the core zone of the low-level moisture convergence is observed north of the LLJ core. As explained earlier, the LLJ hit the WG directly on the windward side of the WG, which is enough to supply abundant moisture to the region. The maximum convergence is observed over the CI, NCI and NER, with a slight spatial shift in the core location of the convergence zone. However, strong convergence is apparent in the ERE regions. Generally, an axis of convergence is distinct over the monsoon core zone (MCZ) with slight variations in intensity concerning the regions of extreme rainfall. The bottom panel of Figure 4.5 is the vertically integrated moist static energy (VIMSE, K J kg^{-1}) during the EREs to indicate the measure of moist convection and latent heat, and the MSE anomalies are also approximately in phase with precipitation (Maloney, 2009; Kiranmayi and Maloney, 2011). Here, the VIMSE is used to explore the dynamics of extreme events in the different regions of the Indian subcontinent during the summer monsoon season. The VIMSE shows high values during EREs in all the regions, as shown in the figure. The spatial pattern of the VIMSE is almost similar to the spatial pattern of the moisture convergence at the surface level, which indicates the convective activity as evidenced by the high values of moist static energy. The extreme events over the SWC regions are less convective than other regions because the moisture pumping to the WC is mainly through the core of LLJ and the orographic uplift of moisture after impinging the WG. However, in the NER, the values of VIMSE are higher; therefore, the degree of convection is higher than that of the WG. Kumar et al. (2014) stated that the clouds are shallower over the WG and deeper over the northeastern regions (especially over the Myanmar coast), hence the changes in the intensity of rainfall as manifested by the values of VISME. The maximum values of VISME coincide with the regions of EREs, except over the southwest coast, attributed to the flow of moisture-laden LLJ to the region.

4.6 Lead Lag Composites of Humidity and Vertical Velocity

To explore the role of humidity and vertical wind at different vertical levels during, before and after the EREs, the study analyzed these parameters during ± 10 days of the event (Figure 4.6). It is found that the two zones of anomalous specific humidity can be seen at lower levels,

around 850 hPa and at 500 hPa, over the SWC regions, indicating the surplus moisture in lower and middle levels (Figure 4.6 top panels). The specific humidity is about 2 g kg^{-1} higher than the climatological values in these two vertical levels; however, these high values persist only during EREs. Moreover, abnormal values of specific humidity are not sufficiently intense to produce an extreme event compared to other homogeneous regions. In general, the moisture over these regions is high, as seen in Figure 4.4; therefore, a slight increase in the moisture leads to abnormal rainfall over these regions, and it will amplify the characteristics of the WG. The WG regions are characterised by complex topography ranging from zonally oriented coastal planes to high mountain peaks in the WG (Venkatesh and Jose, 2007; Revadekar al., 2018). The moisture-laden low level westerlies ascent after impinging the mountain ranges,
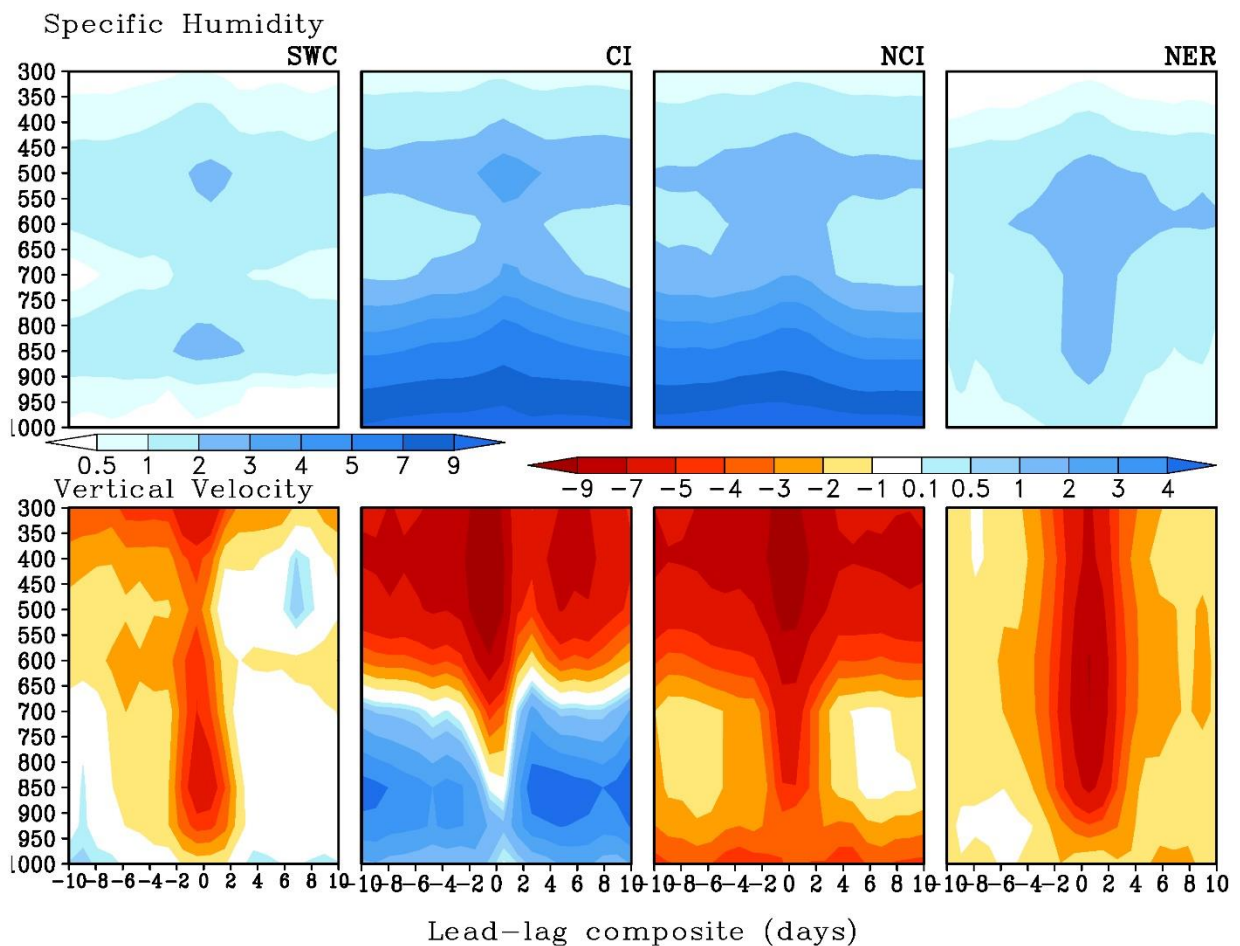
Figure 4.6: Lead-lag composite of the vertical cross-section of anomalies of specific humidity (g kg^{-1}) and vertical velocity ($\times$ 10^{-2} Pa s^{-1}) over the west coast, central India, north central India and northeast regions. The zero value in the x-axis indicates the day of extreme events, and negative (positive) values indicate the parameters' evolution (dissipation) features.

which lie perpendicular to the flow pattern of the monsoon LLJs (Joseph and Sijikumar, 2004), and it causes rigorous vertical motion, as seen in Figure 4.6 (bottom panels). In the SWC, the upward vertical velocity (negative values) is high during the extreme rainfall day, extending from the surface to 300 hPa level, indicating a strong updraft of the clouds that leads to heavy precipitation in the WG regions. Similarly, the NER is enriched with moisture from the nearby waterbodies, the BoB and the Arabian Sea. Therefore, a slight enhancement in the moisture leads to surplus moisture enrichment and heavy rainfall when accompanied by the vertical updraft, as seen in the figure. The mid-level moisture enhancement is observed almost four days ahead of the extreme events and lasts about 10 days even after the extreme. The vertical velocity begins to increase from about 6 days before the event at the mid-levels (about 500 hPa), and it reaches its peak during the extreme event with an intense upward vertical velocity (> 7 Pa s^{-1}) registered from the surface to about 300 hPa.

In the case of CI and NCI, the specific humidity and vertical velocity distributions are entirely different from those of the SWC and NER. The specific humidity anomalies over the CI and NCI regions are found to be high, almost three times more than those of the SWC and NER regions. As seen earlier, the vertically integrated moisture flux is less over these regions; therefore, an abnormally high amount of moisture is needed to produce an extreme rainfall event. In both these regions, the specific humidity is maximum at lower levels (850 hPa), gradually decreasing to higher altitudes; it shows a secondary maximum at about 500 hPa, and this secondary peak is evident in all the regions. However, the low level vertical velocity over CI regions is not so strong except during the extreme rainfall day. It is more interesting to note that a dominant zone of downdraft is recorded at about 850 hPa, but updraft is much higher at higher levels, from about 800 hPa. This kind of downdraft is not visible in the NCI, and a vertical velocity peak is observed at the higher levels (400 hPa). Therefore, it can be concluded that specific humidity and vertical velocity are the prime factors for the EREs in CI and NCI regions. In general, the extreme events in the SWC and NER are when the vertical velocity is supported by specific humidity; however, in the CI and NCI, EREs occur when the vertical velocity is supported by specific humidity.

This study systematically explored the dynamical features of regional EREs in the Indian subcontinent during the summer monsoon period from 1951 to 2015. It has been found that the long term trends of EREs are heterogeneous over the subcontinent. However, there is regional homogeneity in trends, and those regions are identified, and their dynamical characteristics

unravelled before, during, and after the EREs. This kind of study has not been conducted earlier in this region. Therefore, it is essential to understand the atmospheric circulation features, humidity distribution, and vertical velocity features before, during and after the EREs. The study of EREs and their dynamics has several critical applications. Understanding the dynamics of EREs can help in developing effective flood management strategies. Flood-prone areas can be identified by analysing the trends, frequency, and intensity of EREs for taking appropriate measures to alleviate the impact of floods. By studying the dynamics of EREs, farmers and water resource managers can develop better water management and crop planning strategies. Engineers can design suitable infrastructure better equipped to withstand EREs by understanding their spatial characteristics and dynamics. Moreover, scientists can develop better models to predict future extreme weather events and help communities plan disaster preparedness in the changing climate. This information can be used by insurance companies, emergency management agencies, and many other stakeholders to develop risk management strategies and prepare for extreme weather events.

4.7 Chapter Summary

Spatial patterns of EREs (rainfall exceeding the 99th percentile) over the Indian subcontinent and their dynamic features were analysed during the southwest monsoon period from 1951 to 2015. It is found that the spatial trend shows apparent differences in the mean and extreme rainfalls. The EREs show an increasing trend in the north and a decreasing trend in the south of the west coastal regions. Similarly, north central and central Indian regions show contrasting rainfall trends during the extremes. Based on the spatial trends, four regions were selected to explore the underlying dynamics of the EREs during the southwest monsoon period. The SWC, NCI and NER show negative trends among the selected regions, but the trend is positive for the CI regions.

The circulation features at 850 hPa reveal distinct differences over different regions. The SWC regions show that the wind is at its maximum on the day of the extreme event, and the wind speed reaches more than 19 ms^{-1} over the Arabian Sea. The wind strength increases rapidly before the event but dissipates gradually after the event. During the extreme period, the moisture-laden wind directly hits the western coastal regions; therefore, the high moisture transport leads to heavy rainfall. In the case of central India, the wind core is located over the Arabian Sea and extends to central India, and the same can also be observed in the moisture transport and, thus, the rainfall. The NCI and NER show relatively weaker winds and moisture

transport at 850 hPa. During the extremes in the NCI, the LLJ core splits into two, and the northern branch causes the extreme event; however, in the NER, the wind shows westerly regimes over the areas of the extreme rainfall event.

From the moisture transport analysis, it can be inferred that the prime moisture source for the extreme events over SWC, CI, and NCI is the Arabian Sea; however, for the NER, the prime source is the BoB. The RV also shows positive regions over the extreme rainfall event, indicating low level convergence. This low-level convergence is also confirmed based on low-level moisture convergence. The vertically integrated moist static energy shows high values in the regions of extreme rainfall in consensus with moisture convergence at 1000 hPa. The evolution and dissipation of the moisture and vertical velocity from the lead-lag vertical cross-section indicate the uniqueness of the individual regions. The SWC and NER regions are climatologically moisture abundant; any slight increase in the vertical velocity will lead to heavy rainfall associated with high upward motion of moisture. However, the CI and NCI show high moisture over the entire atmospheric column, along with high updrafts during EREs.

The next Chapter presents the selection of the best CMIP6 GCM models to simulate SASM rainfall and their characteristics in simulating SASM mean and extreme rainfalls.

CHAPTER 5

CHARACTERISTICS OF SUMMER MONSOON EXTREME RAINFALL EVENTS BASED ON CMIP6 HISTORICAL SIMULATIONS

CHAPTER 5

CHARACTERISTICS OF SUMMER MONSOON EXTREME RAINFALL EVENTS BASED ON CMIP6 HISTORICAL SIMULATIONS

5.1 Introduction

The South Asian regions frequently encounter extreme rainfall events during the summer monsoon season that can potentially cause property damage, environmental harm, and even fatalities. Therefore, it is essential to comprehend how these events are evolving and may change in the future, particularly for developing countries in the region due to their low adaptive capacity as a result of geographical as well as socio-economic features. Identifying and assigning responsibility to key factors influencing potential shifts in South Asian summer monsoon rainfall is essential for developing effective adaptation policies across various sectors in response to climate change. It is essential to confirm how well the global climate models (GCMs), mainly used to create projections, realistically simulate the rainfall extremes in these regions. This study utilised selected models from the Coupled Model Intercomparison Project Phase 6 (CMIP6) to evaluate the intensity of extreme rainfall events and their percentage contribution to seasonal rainfall during the historical period (1950–2014) across South Asian regions during the summer monsoon season. Rainfall simulations from the CMIP6 models were evaluated against the observational gridded rainfall data from the Climatic Research Unit (CRU).

5.2 Validation and Selection of Models

In the present study, the selection of the most suitable models for the historical simulation of SASM rainfall is effectively conducted by assessing the performance of the 53 CMIP6 models (refer to Chapter 2 section 2.1.2) in replicating the annual cycle of SASM rainfall, followed by Taylor diagram analysis. The monthly rainfall dataset of models is chosen according to the data available for the historical period (1950–2014). Since the resolution of each GCM is different, all GCM model data and CRU observational data were re-gridded to a common 1.5° latitude × 1.5° longitude spatial resolution before performing the validation.

5.2.1 Annual Cycle of Rainfall

In this research, the ability of CMIP6 GCM models was assessed in comparison with CRU rainfall data to check whether they were successful in reproducing the characteristics of summer monsoon rainfall over the Indian subcontinent in the historical period. It is necessary

to compare the simulated rainfall to observational data while taking both temporal and spatial perspectives. A homogenous region in central India between latitude 19–26°N and longitude 75–85°E is considered to validate and subsequently choose the best simulating models from CMIP6 that reproduce the characteristics of SASM mean rainfall and extremes. The annual cycle of rainfall (multi-year averaged monthly variation in rainfall) of all 53 CMIP6 models, the Multi-Model Ensemble (MME) of the models, and the CRU gridded observational rainfall data are compared to see the seasonality of the rainfall for the historical period and is shown in Figure 5.1. The thick black line represents the annual rainfall variation of observational CRU data. The thin coloured lines represent different models, and the thick red line represents their MME. In the figure, it is clear that all the models predict rainfall to be at its lowest from January to May and show a marked increase in June as the southwest monsoon begins, then persists till September and again decreases. This suggests that almost all models exhibit a seasonal pattern of rainfall that peaks between July and August that is consistent with observational data, as was also noted by Zhai et al. (2020) and Banerjee and Singh (2022) in their examinations of the CMIP6 models. It was found that CMIP6 simulations have more robust accuracy than CMIP5 for climate parameters, especially rainfall (Zhai et al., 2020). However, it was seen that while some models overestimated the observed SASM rainfall intensity, many of them underestimated it. Two of the models, i.e., INM-CM4-8 and INM-CM5-0, are highly overestimating the seasonal rainfall by 41% and 24%, respectively. 49 models are underestimating the CRU data, of which GISS-E2-2-G, GISS-E2-1-G, GISS-E2-1-G, GISS-E2-2-H, CanESM5, ACCESS-ESM-15, ACCESS-CM2, and FGOALS-g3 are the most underestimated, disproving them for further analysis. The overestimation of INM models and the underestimation of Canadian models in capturing ISMR seasonal variation are proved by Katzenberger et al. (2021).

Additionally, compared to the CRU data, the yearly variation of MME underestimates the summertime rainfall pattern, demonstrating the inadequacy of all models in capturing seasonality. The CRU data peaks at 11 mm day^{-1}, while MME is at 7.5 mm day^{-1}. Gupta et al. (2020) have noted the sizeable intermodel spread and uncertainty in the CMIP6 models' ability to simulate the ISMR. Li et al. (2021) observed that the simulation effect of CMIP6 for total rainfall in South Asia is slightly worse than that of CMIP5. They claim that the simulation of total rainfall in CMIP6 does not generally outperform CMIP5, and its performance varies regionally. Wang et al. (2020) demonstrated the biases in the MME simulation by comparing the summer monsoon rainfall of the Global Rainfall Climatology Project (GPCP) with several

CMIP6 models. It has been suggested by Kumar and Sarthi (2021) that the large model-to-model spread in rainfall on a sub-seasonal scale over the Indian landmass may be caused by variations in the strength and location of lower and upper-level winds, which in turn affect moisture incursion from the Arabian Sea and the Bay of Bengal (BoB). Therefore, a more accurate depiction of moisture circulation is needed in the models under consideration to limit and resolve the significant variability in the simulated rainfall compared to the actual rainfall.

Therefore, to screen the models better at capturing the ISM rainfall patterns during the southwest monsoon period in the central Indian region, all the models were shortlisted that fell within the range of ±2 standard deviations of the observational data (Figure 5.1). This is done to select the most encouraging models for additional study and to prevent overestimating and underestimating models at the next level. Even though the seasonal changes are captured differently by each model, 22 models fell within the ±2 standard deviations of the observational CRU data. Thus the 22 models Qualified for further analysis are EC-Earth3, EC-Earth3-
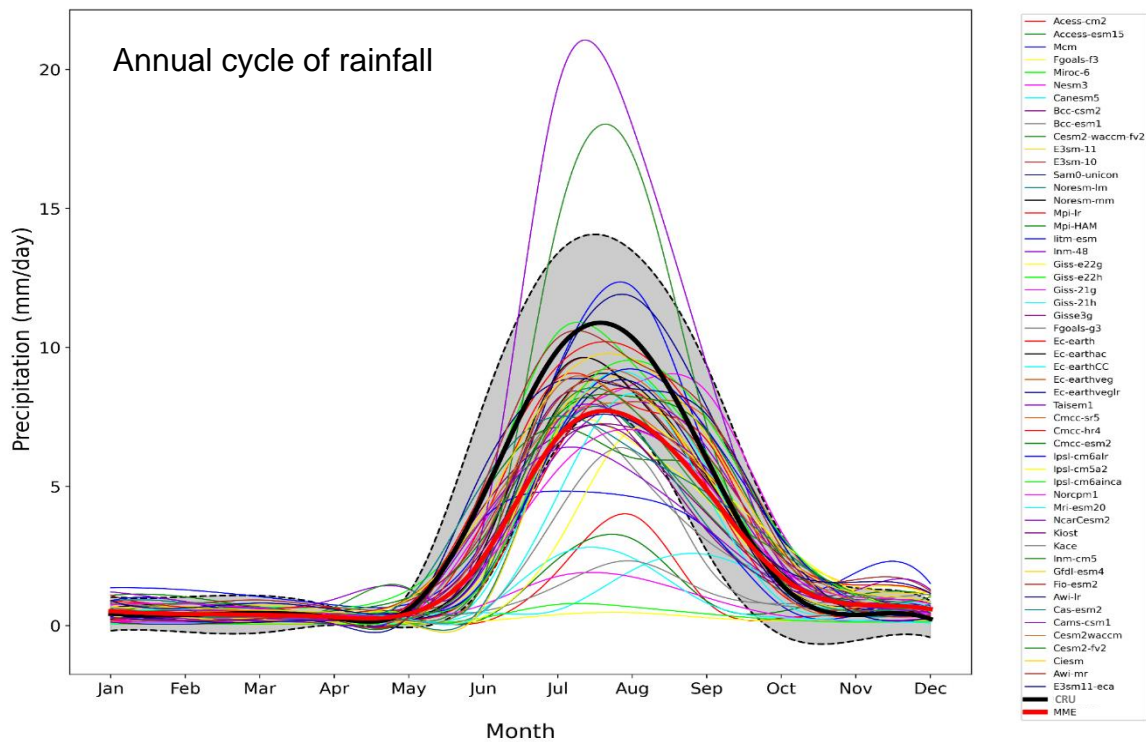
Figure 5.1: The annual cycle of rainfall over central India (19°–2 6°N, 75°–85°E) for the 53 CMIP6 models along with their multimodel ensemble (MME) and observational rainfall data (CRU) for the historical period (1950-2014). The thin lines represent the various models, and the thick black line and red line in the plot represent the MME and CRU data, respectively. The precipitation within ±2 standard deviation of the CRU data is represented as the shaded portion.

AerChem, EC-Earth3-CC, EC-Earth3-Veg, EC-Earth3-Veg-LR, MIROC-6, NorESM2-MM, IPSL-CM6A-LR-INCA, IPSL-CM6A-LR, CIESM, FIO-ESM2, CESM2-FV2, CESM2-WACCM, CESM2-WACCM-FV2, SAM0-UNICON, CESM2, E3SM-1-1, MPI-ESM1-2-LR, CMCC-CM2-SR5, CMCC-ESM2, AWI-CM-1-1-MR and NESM3.

5.2.2 Taylor Diagram Analysis

The Taylor diagram analysis is conducted by taking the 95th percentile of the monthly averaged summer monsoon rainfall (mm day^{-1}) of the chosen 22 models against the observational data over the historical period (Figure 5.2). This is to ensure the consistency of the results presented in the seasonality study and to pick the most accurate models with spatial patterns that are most similar to the observational dataset in simulating the 95th percentile of summer monsoon rainfall. The figure compares the normalised standard deviation and pattern correlation values of the models and observation data.

Most of the models were found within the range of correlation coefficients of 0.8 and 0.9. Relatively poor performances were seen in the FIO-ESM-2-0, CMCC-ESM2, CMCC-CM2-SR5, CIESM, and MPI-ESM1-2-LR CMIP6 models. From the Taylor diagram, the models with correlation coefficients greater than 0.8 and normalised variance between 0.9 and 1.1 were screened (Figure 5.2) for further study. Based on this, five models were selected for the historical simulation of SASM mean and extreme rainfalls: EC-Earth3, EC-Earth3-AerChem, EC-Earth3-CC, EC-Earth3-Veg, and NorESM2-MM.

Previous studies also highlighted the excellent simulation quality of NorESM2-MM and EC-Earth models in projecting ISMR (Prodhomme et al., 2016; Katzenberger et al., 2021; Zhang et al., 2021; Mitra, 2021; Chen et al., 2022). EC-Earth is an atmosphere-ocean coupled general circulation model (GCM) based on the seasonal forecasting system from the European Centre for Medium-Range Weather Forecasts (ECMWF). EC-Earth3 is the model's third generation and is the basic standard-resolution atmosphere-ocean physical model configuration whose version 3.3 is used for CMIP6 experiments. Eight different configurations of EC-Earth3 are used for various scientific purposes. The EC-Earth3 configurations include model elements for numerous physical domains and system elements that describe the atmosphere, ocean, sea ice, land surface, atmospheric composition, dynamic vegetation, ocean biogeochemistry, and the Greenland Ice Sheet. EC-Earth3 standard configuration consists of the atmosphere model IFS (Integrated Forecast System), which includes the land surface module HTESSEL (Hydrology Tiled ECMWF Scheme of Surface Exchanges over Land), and the ocean model NEMO3.6

(Nucleus for European Modelling of the Ocean- revision r9466), which includes the sea ice module LIM3 (Louvain-la-Neuve Ice Model - Improved form of LIM3.6 taking into account the differences in albedo and temperature among the sea ice categories in each grid point). The OASIS3-MCT coupler, a project to create general coupling software, transmits coupling variables between the various component models. The physical interfaces are specified by describing the variables exchanged and the algorithms utilised. There are 27 partners in the EC-Earth consortium, located in 10 different European nations. (Döscher et al., 2022). The Norwegian Earth System Model version 2 medium resolution (NorESM2-MM) is the second generation of the coupled Earth System Model (ESM) developed by the Norwegian Climate Center. NorESM employs the isopycnic coordinate Hamburg Ocean Carbon Cycle (iHAMOCC) model in conjunction with the Bergen Layered Ocean Model (BLOM) to simulate ocean biogeochemistry. A separate atmospheric aerosol module is also used. The physics and dynamics of the atmospheric component have also undergone particular modifications and tunings in NorESM2. The description of aerosols and their connection to clouds and radiation has undergone specific advancements (Seland et al., 2020). Further analysis of the extreme rainfall events during the southwest monsoon season and their contribution to seasonal rainfall was done on these selected five models.
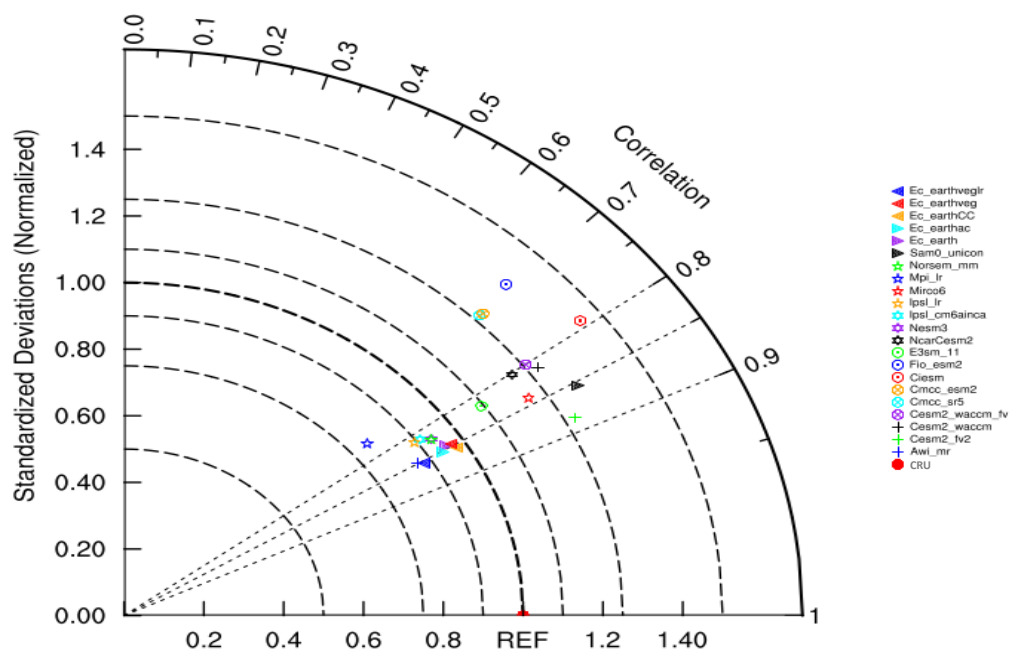
Figure 5.2: Taylor diagram of 95th percentile of summer monsoon rainfall over the central India region (19°-26°N, 75°-85°E) for the historical period (1950-2014) of the 22 CMIP6 models with reference to observational CRU rainfall data.

The selected models EC-Earth3, EC-Earth3-AerChem, EC-Earth3-CC, EC-Earth3-Veg, and NorESM2-MM are denoted in the remaining portions of the thesis and in figures as EC-Earth, EC-EarthAC, EC-EarthCC, EC-EarthVeg, and NorESM, respectively, for convenience.

5.3 Historical Simulations

5.3.1 Climatology of ISMR

The climatology of the summer monsoon seasonal rainfall for the historical period from 1950 to 2014 for the five selected CMIP6 models and CRU observational data is given in Figure 5.3. All the models exhibit almost similar spatial variability to the observational rainfall. The intensity of the rainfall is at its maximum with >10 mm day^{-1} in most regions of the west coast, the Himalayas and their foothills, and the northeast. It also crosses more than 15 mm day^{-1} in the central and eastern Himalayas in the NorESM model. Mean rainfall of 5 to 10 mm day^{-1} is observed in the central Indian region. Just like CRU, the low rainfall of <5 mm day^{-1} in the northwestern and southeast regions is also captured by all models.

Compared to the NorESM model, the EC-Earth models are good at capturing rainfall in the west coast regions, with better performance by EC-EarthAC, followed by EC-EarthVeg and EC-EarthCC. However, all the EC-Earth models underestimate the northern parts of the west coast, the coastal regions of Maharashtra, by about 5 mm day^{-1}. NorESM underestimates the rainfall by 5 mm day^{-1} in the entire coastal areas of the west coast and, at the same time, slightly overestimates the rainfall in the rain shadow regions close to the Western Ghats. NorESM more successfully captures the central Indian region's seasonal rainfall than EC-Earth models, although slight underestimation is seen in the western and northwestern regions of central India, just like what is observed in EC-Earth models. EC-EarthVeg and EC-EarthCC models performed well in the central Indian region when compared with other EC-Earth models. All the models have to be improved to capture the increased summer monsoon rainfall in the transition regions of semi-arid to monsoon core areas in the western regions of central India, especially in northwestern India and also in the rain shadow regions of the northern west coast. All EC-Earth models are performing almost similarly in the Himalayan and northeastern regions, underestimating a 5 mm day^{-1} rainfall in the Meghalaya areas. All models capture the western Himalayan and foothill regions well; however, models do not perfectly simulate the rainfall area extended to the Jammu region. All EC-Earth models slightly overestimate the central Himalayan region's rainfall (<5 mm day^{-1}) and significantly overestimate the eastern Himalayan regions (about 10 mm day^{-1}) almost equally, whereas the NorESM Model's

estimation shows a >10 mm day^{-1} overestimation with CRU in these regions. NorESM almost closely represents the northeastern region's southwest monsoon rainfall close to the observation. The models also underestimate the rainfall intensity in the coastal Myanmar region close to the northern BoB.

In conclusion, models successfully simulate the mean rainfall features like maximum rainfall zones (southwest coast, central and north-central India, northeast, and the foothills of the Himalayas) and minimum rainfall zones (arid and semi-arid regions in the north of India, and monsoon shadow regions of southeast India). In addition to the spatial structure, the selected models also satisfactorily capture rainfall amounts during the southwest monsoon period.
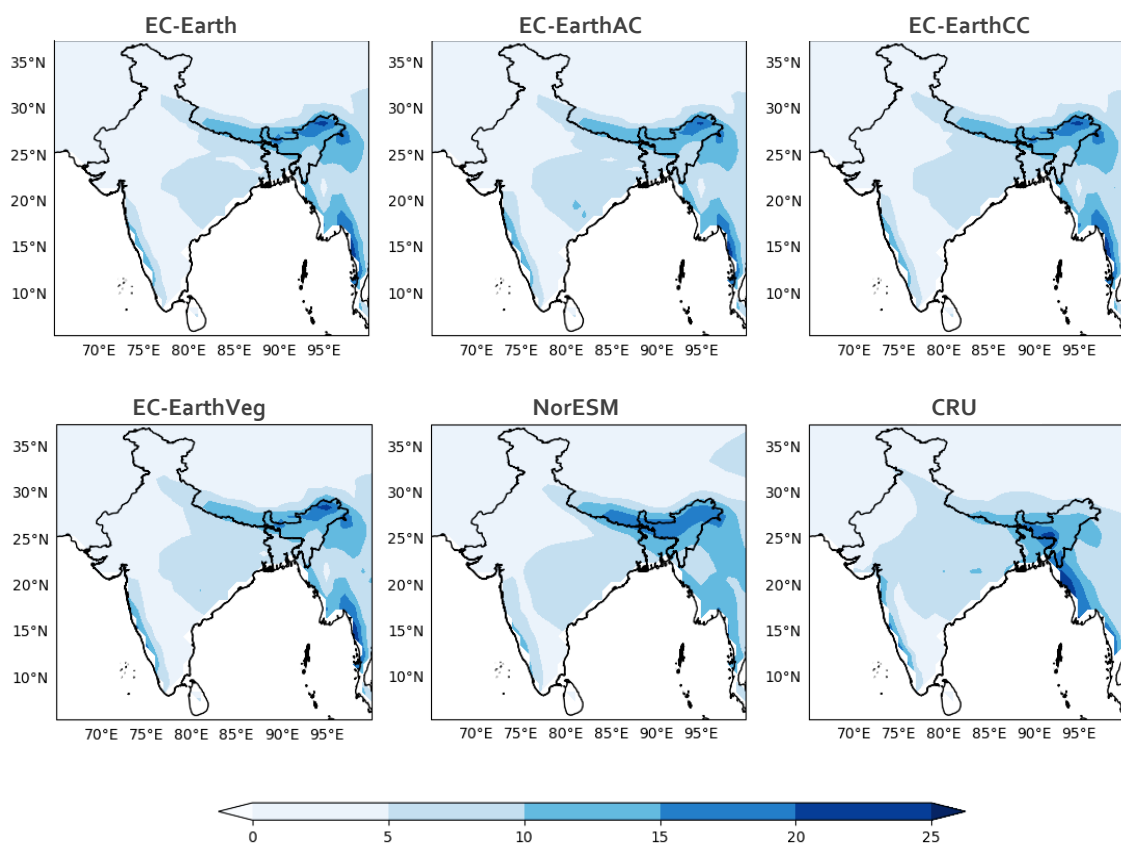
Figure 5.3: Climatology of rainfall (mm day^{-1}) for the five selected CMIP6 models and CRU for the historical period of 1950–2014.

5.3.2 Spatial Distribution of 95th Percentile of Rainfall

An extreme rainfall event over the study area is defined in terms of the 95th percentile of the rainfall over the historical period 1950–2014. In this phase of the study, monthly rainfall data is collected from CMIP6 GCM models and CRU. Setting a higher percentile, such as the 99th percentile, as the threshold already utilized in the physical and dynamical analysis of extreme

rainfall, may result in insufficient data values for analysis. This could potentially lead to erroneous inferences. If the rainfall in a grid reaches or exceeds this threshold ($\geq 95^{th}$ percentile) value, it is considered an extreme rainfall event. Figure 5.4 represents the 95th percentile of summer monsoon rainfall for the selected five CMIP6 models and CRU data. It is noted that the 95th percentile has high values of rainfall (>20 mm day^{-1}), similar to observational data in the West Coast, Northeast, and central and eastern Himalayan regions. Moderate values (15 to 20 mm day^{-1}) are observed in central India. Very low values (<10 mm day^{-1}) are registered in the northern Jammu, Kashmir, and Ladakh regions, and even less than 5 mm day^{-1} in some areas of the southeast monsoon trough and northwest arid regions, where the average rainfall values are negligibly small.
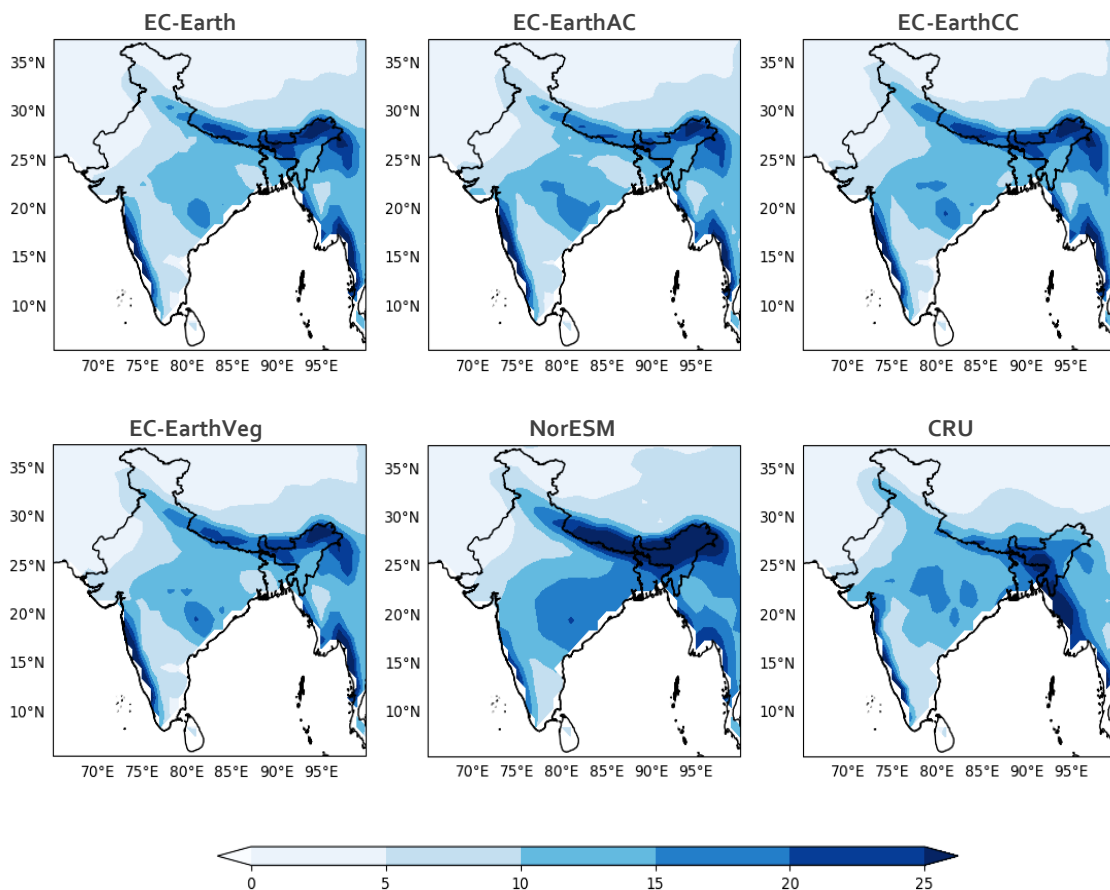
Figure 5.4: 95th percentile of rainfall (mm day^{-1}) for the 5 CMIP6 models and CRU for the historical period of 1950–2014.

The EC-Earth models satisfactorily simulate the 95th percentile over the southern west coast regions, with a slight overestimation, and the NorESM model exhibits an underestimation of approximately 5 mm day^{-1}. On the northern west coast, EC-Earth models indicate an overestimation of >10 mm day^{-1} around 18˚N in the coastal area. While EC-EarthAC and EC-

EarthCC models successfully replicate the increased threshold over the northern west coast in the Gujarat region, the EC-Earth and EC-EarthVeg models are unable to project the same. The EC-Earth models, particularly EC-EarthCC, demonstrate accurate projections of the central Indian threshold of the rainfall, with EC-EarthCC being the most reliable, followed by EC-EarthAC and EC-EarthVeg. In the western part of central India, EC-EarthAC performs well, with EC-EarthCC following closely behind. The NorESM model achieves notable success in projecting the 95th percentile in the southern and western regions of central India despite an overestimation of rainfall by 5 mm day^{-1} on its eastern side. Additionally, the increased area of threshold extends to the northeastern region.

The EC-Earth models exhibit superior performance in capturing the Himalayan regions compared to NorESM. However, most models tend to overestimate the rainfall threshold in the central and eastern Himalayan regions. EC-EarthAC provides a more accurate representation of the western and central Himalayan regions. On the other hand, NorESM demonstrates better simulation of the northeastern regions compared to the EC-Earth models. The threshold values in northwest and southeast India are consistent across all models and are closely aligned with CRU, particularly in the case of NorESM. Notably, the EC-Earth models display a slight decrease in threshold values in the southeast regions, particularly in the Madurai coast regions of Tamil Nadu and the southern coastal regions of Andhra Pradesh.

5.3.3 Spatial Pattern of Extreme Rainfall

Extreme rainfall, defined as rainfall exceeding the 95th percentile threshold value, is depicted in Figure 5.5 for the chosen models along with the CRU data. The spatial distribution pattern of extreme rainfall intensity closely resembles that of the 95th percentile but with higher values. The model's simulations have a similar pattern to the observational data, and they efficiently captured the extreme rainfall amount in the monsoonal regions, including central India (15 to 20 mm season^{-1}), the southern and central west coast (>25 mm season^{-1}), and the northwestern Himalayan regions (15 mm season^{-1}). Models also succeeded in capturing the extreme rainfall over non-monsoonal regions like northwest and southeast India.

On the West Coast, all EC-Earth models exhibited similar performance in estimating extreme rainfall in the southern regions, with satisfactory results. However, a slight overestimation was observed in the northern coastal regions around 18˚N. As discussed in the context of the 95th percentile threshold, EC-Earth models did not adequately capture the intensified extremes in the southern Gujarat regions. In contrast, NorESM slightly underestimated extremes over the

west coast, with a decrease of about 5 mm season^{-1} in the southern regions and a more significant underestimation exceeding 10 mm season^{-1} in the northern regions.

All EC-Earth models project central Indian rainfall extremes almost equally and in line with CRU. EC-EarthAC, in particular, captures the increased area extension of extreme rainfall to the semi-arid regions in northwestern India more accurately. Notably, all EC-Earth models, except the basic EC-Earth model, exhibit a 5 mm season^{-1} increase in extreme rainfall in the Odisha regions of central India. However, EC-Earth underestimates extremes in the southwestern portions of central India, a contrast to other EC-Earth models. In the NorESM model, there is an overestimation of central Indian extremes by more than 5 mm season^{-1} in the eastern parts, extending to northeastern regions, as observed in the 95th percentile simulation.
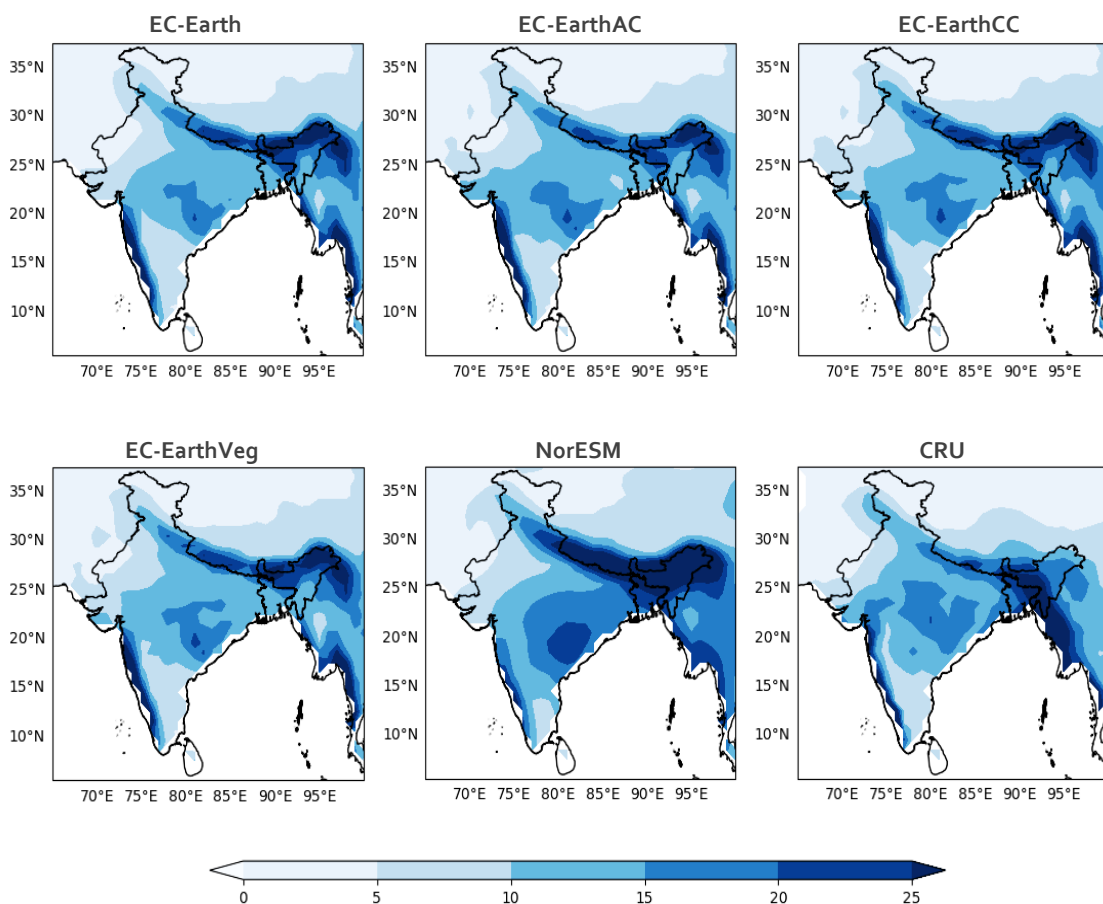
Figure 5.5: Extreme rainfall amount (rainfall ≥95th percentile, mm season^{-1}) for the five CMIP6 models and CRU for the historical period of 1950 –2014.

Similar to the 95th percentile projection, all EC-Earth models simulated extreme rainfall very well in the western Himalayan regions, with a slight overestimation in the central and eastern Himalayan regions, and a slight underestimation in the Meghalayan regions. NorESM

represents extreme rainfall in the northeastern regions more satisfactorily compared to EC-Earth models. In the northwest and southeast Indian regions, extreme rainfall is neatly projected by all EC-Earth models, while NorESM shows an overestimation in the northern parts of southeast India. Additionally, NorESM indicates increased extreme rainfall in the rain shadow regions of the Western Ghats. The extremes of the northwest region are better represented by EC-EarthAC, followed by EC-EarthVeg and EC-EarthCC.

5.3.4 Contribution of Extreme Rainfall to the Seasonal Rainfall

In addition to the extreme rainfall amount, the study also analysed the percentage contribution of extreme rainfall to the seasonal rainfall during the historical period, as presented in Figure 5.6. The contribution of extreme rainfall is greater (>20%) in northwest regions, where the rainfall corresponding to the 95th percentile has low values, and the seasonal rainfall is also negligible in these regions. The southeast rain shadow regions also exhibit a comparatively high percentage contribution of >12%, attributed to the low values of mean rainfall in the summer monsoon season. When compared with observational data, the EC-Earth models precisely project the contribution of extreme rainfall to the seasonal rainfall in the west coast, central India, Himalayan, and northeast regions. NorESM also presents the central Indian, west coast, and northeastern regions in a satisfactory manner.

The most accurate representation of contribution in the southern west coast regions is provided by EC-EarthVeg. However, other EC-Earth models exhibit a >2% overestimation. The NorESM model, on the other hand, indicates a 2% underestimation in the southern west coast regions. For the northern west coast contributions, the NorESM model performs well, displaying a slight overestimation. Conversely, all EC-Earth models demonstrate a 4–6% overestimation in the northern west coast regions. Among the EC-Earth models, EC-EarthAC satisfactorily simulates the contribution of extreme rainfall in the eastern regions of central India, with a slight <2% overestimation. Following closely is EC-EarthVeg with a >2% overestimation. Additionally, EC-Earth models also show a 4–6% increased contribution in the western regions of central India. NorESM also simulates the contribution of extreme rainfall in the central Indian region, with a 2–4% overestimation; however, it overestimates contributions in the northwestern arid and semi-arid regions of the Indian landmass by up to 8%. The EC-Earth models effectively simulate the Himalayan regions, with EC-EarthAC outperforming EC-EarthVeg. In contrast, NorESM tends to overestimate contributions in the western Himalayas, showing a 4–6% increase. The representation of extreme rainfall in the

Jammu, Kashmir, and Ladakh regions is accurate in the EC-Earth models, while NorESM is not adequate to represent the contributions over these regions. NorESM performs well in representing the northeastern regions; however, the EC-Earth models exhibit an almost 2% overestimation in the northeastern regions.
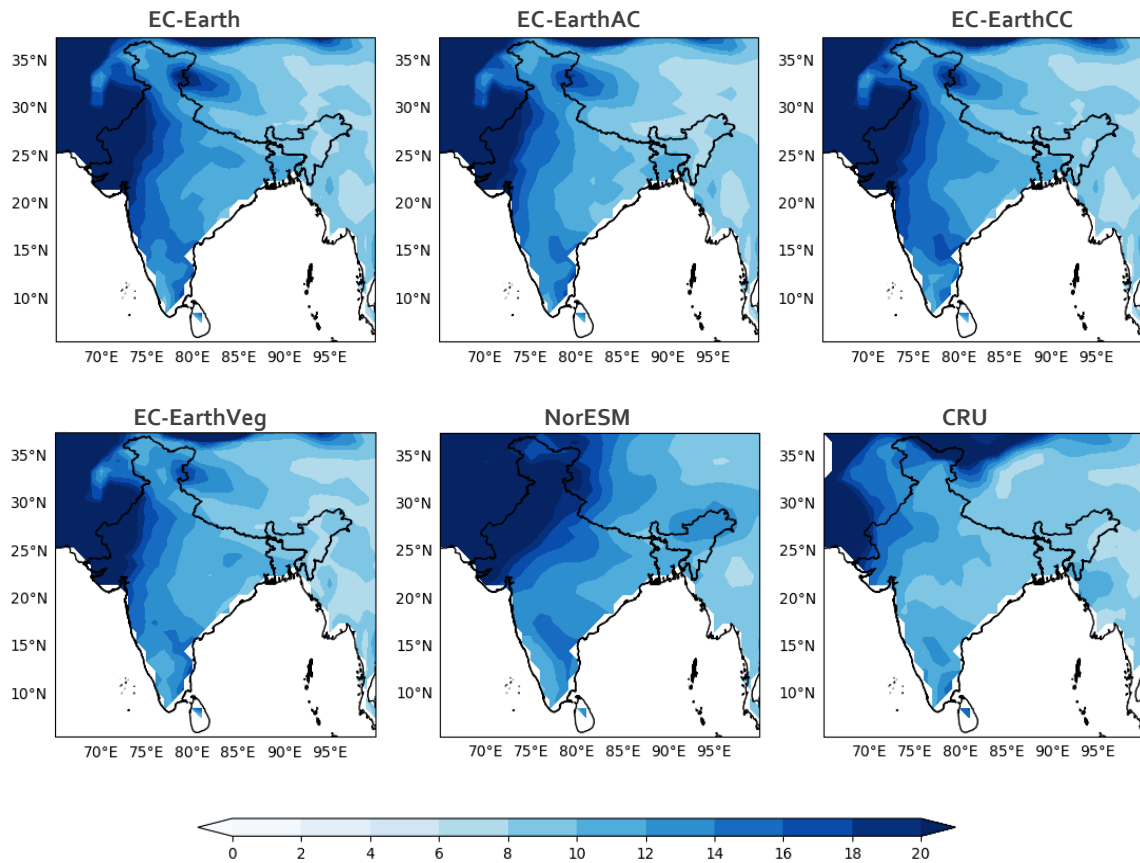
Figure 5.6: Percentage contribution of extreme rainfall to the seasonal rainfall for the five CMIP6 models and CRU from 1950 –2014..

5.4 Chapter Summary

The selected models exhibited similar spatial patterns for mean and extreme rainfalls in the historical period when compared with observational CRU data. However, there are consistent regional biases across CMIP6 models, manifesting as overestimation and underestimation, particularly in monsoonal regions such as the West Coast, central India, the Himalayas and its foothills, and the northeastern regions. The EC-Earth models and NorESM demonstrated the ability to simulate central Indian seasonal rainfall quite well, although the spatial coverage of good estimation is somewhat reduced. The NorESM model outperformed EC-Earth models in simulating central Indian and northeastern regional seasonal rainfall patterns. In contrast, EC-

Earth models excelled in capturing the west coast, particularly the southern region, and also in the western Himalayan regions.

The EC-Earth models performed well in simulating extreme rainfall events in central India, whereas NorESM tended to overestimate the observational data. The EC-Earth models provided reasonable estimates for extreme rainfalls on the west coast regions, whereas the NorESM models exhibited a slight underestimation. The variabilities in extreme rainfall in the central and eastern Himalayan regions were not adequately captured by any models. However, the EC-Earth models effectively represented extreme rainfall in the western Himalayan region, while NorESM showed a slight overestimation. The models slightly underestimated extreme rainfall patterns in the northern west coast and northeast regions of India, as well as in the coastal areas of Myanmar. On the other hand, extreme rainfall in the northwest and southeast Indian regions was accurately projected by all EC-Earth models.

Even though CMIP6 has evolved more than its older missions in capturing land-sea interactions and anthropogenic forcings, the complexity of land-sea interactions hinders the model's ability to simulate the summer monsoon extreme rainfall features, especially over the northern west coast and northeast regions of the subcontinent. The coming chapter explores changes and variabilities in summer monsoon extreme rainfall using selected CMIP6 models during future projections.

CHAPTER 6

CHANGES AND VARIABILITIES OF SUMMER MONSOON EXTREME RAINFALL EVENTS DURING FUTURE PROJECTIONS USING CMIP6 MODELS

CHAPTER 6

CHANGES AND VARIABILITIES OF SUMMER MONSOON EXTREME RAINFALL EVENTS DURING FUTURE PROJECTIONS USING CMIP6 MODELS

6.1 Introduction

India's economic growth, food and water security, social well-being, and prosperity are significantly influenced by the Indian Summer Monsoon Rainfall (ISMR) (Gusain et al., 2019). In the background of increased climate change in South Asia, this study examines significant spatiotemporal variations in extreme precipitation ($\geq$95p) across the study region using Coupled Model Intercomparison Project Phase 6 (CMIP6) models under four different future warming scenarios, also known as Shared Socioeconomic Pathways (SSPs), for the period 2015–2100. The Tier-1 SSP scenarios considered in the study are SSP1-2.6, SSP2-4.5, SSP3-7.0, and SSP5-8.5. Using the selected models (EC-Earth, EC-EarthVeg, and NorESM), the study focuses on how future warming scenarios and socioeconomic changes between 2015 and 2100 may affect the spatiotemporal pattern of extreme precipitation during the summer monsoon season compared to the historical period of 1950–2014. For a better insight into future changes, projection studies are also conducted for three distinct future periods: near-term (2015–2035), mid-term (2047–2067), and far-term (2079–2099).

6.2 Validation and Selection of Models

Coupled Model Intercomparison Project Phase 6 (CMIP6) models are validated and selected for the projection study as briefed in Chapter 5, Section 2. In the initial stage, models are evaluated based on their responses to the annual cycle of rainfall during the historical period spanning from 1950 to 2014. Subsequently, a Taylor diagram analysis is performed based on the 95th percentile of rainfall to ensure the consistency of the results and to identify the most accurate models exhibiting spatial patterns most similar to those of the observational dataset. In the historical projection (refer to Chapter 5, Section 5.3), all the selected models have performed well, with some flaws in capturing the extreme rainfalls in different climatic divisions differently. Due to the heterogeneous nature of the study area, no one has performed exceptionally well in capturing the minute details all over the study area. All EC-Earth models performed almost similarly in their historical projections. However, the EC-Earth3-AerChem and EC-Earth3-CC models could not be included in future analyses due to the unavailability

of data for future projections. Thus, the future analysis is conducted for models EC-Earth3, EC-earth3-Veg, and NorESM2-MM models.

6.3 Future Projections

The projected spatiotemporal changes in the future period for extreme rainfall during the summer monsoon season over the South Asian regions are analysed in this study. Along with the extreme rainfall, the projected changes in the seasonal rainfall, the 95th percentile of the seasonal rainfall, and the contribution of extreme rainfall to the seasonal mean are also validated for the future period of 2015–2100. For a detailed analysis and to get a better understanding, the future period is divided into three terms: the near-term future period (2015–2035), the mid-term future period (2047–2067), and the far-term future period (2079–2099), and the characteristics of extreme rainfalls over these periods are also analyzed. Significant results are noted under the various scenarios, which reflect the possible effects of various SSPs on the summer monsoon rainfall extremes over the South Asian region.

6.3.1 Projections of Extremes for the Period 2015-2100

6.3.1.1 Seasonal Rainfall

The projected seasonal mean of summer monsoon rainfall (mm day^{-1}) for the future period (2015–2100) by the three selected models in (i) SSP1-2.6, (ii) SSP2-4.5, (iii) SSP3-7.0, and (iv) SSP5-8.5 scenarios are represented in Figure 6.1. The EC-Earth models project a significant change of 5 mm day^{-1} in future for seasonal rainfall on the west coast regions, southwestern regions of central India, and western Himalayan regions. These changes are evident in all scenarios, with the most pronounced effects observed in the SSP5-8.5 scenario followed by the SSP3-7.0 scenario. No noticeable changes are projected in the central and eastern Himalayan, northeastern, northwestern India, and southeastern India regions. When transitioning from the SSP1 to SSP5 scenarios in the EC-Earth models, the rainfall area in the southwestern regions of central India gradually increases and merges with the expanded rainfall area on the northern west coast. Additionally, the seasonal mean over the Odisha region shows an increasing trend during the transition from SSP1 to SSP5. In various scenarios, the rate of increase in seasonal rainfall over the central Indian regions is lower in EC-EarthVeg than in EC-Earth.

On the other hand, NorESM anticipates a substantial rise in seasonal rainfall of 5mm day^{-1}, limited to central India across all scenarios. This increase is notably pronounced in the eastern areas near the Odisha Coast, encompassing the states of Odisha, Chhattisgarh, and Jharkhand,

as well as the southwestern regions comprising Maharashtra, Karnataka, and the southern regions of Gujarat. The prominent shift in central Indian precipitation is most evident in the SSP5-8.5 scenario, and the expanded rainfall area extends to the upper Bay of Bengal (BoB)

Figure 6.1: The projected seasonal mean of summer monsoon rainfall (mm day^{-1}) for the future period (2015-2100) by EC-Earth, EC-EarthVeg, and NorESM models in (i) SSP1-2.6, (ii) SSP2-4.5, (iii) SSP3-7.0, and (iv) SSP5-8.5 scenarios

regions through the coastal area. A consistent increase in the projected mean is observed in the southwestern parts of central India across all SSPs. Furthermore, there is a 5mm day^{-1} increase in seasonal rainfall in the rain shadow regions in the southeast, particularly in its northern portions, leading to a reduction in the area of the rain shadow region in the future. Insignificant alterations are observed on the West Coast, and no noticeable changes are seen in other regions across all scenarios.

6.3.1.2 95th Percentile of Rainfall

The projected 95th percentile of summer monsoon rainfall (mm day^{-1}) for the future period (2015–2100) by the three selected models in (i) SSP1-2.6, (ii) SSP2-4.5, (iii) SSP3-7.0, and (iv) SSP5-8.5 scenarios is given in Figure 6.2. The EC-Earth models project a significant increase of 5 mm day^{-1} in the 99th percentile threshold value in the western parts of central India, along with a slight increase in the eastern parts, particularly pronounced under the SSP5-8.5 and SSP3-7.0 scenarios. These models also anticipate notable changes in the western Himalayas and southeastern coastal regions, with a slight increase in the northern west coast regions. The spatial enhancement in the central Indian and northern west coast regions results in a reduced rain shadow region in the southwest, characterized by a small threshold value for extreme rainfall. The EC-Earth models predict an elevated threshold of >5 mm day^{-1} in the central Himalayan regions across all scenarios, with the most pronounced effect observed in SSP5-8.5. Specifically, in the Odisha region, the EC-Earth models indicate a <5 mm day^{-1} increase in the threshold value compared to neighbouring areas. This change is most visible in SSP3-7.0 and SSP5-8.5. However, in the case of EC-EarthVeg, such an increase is only noticed in SSP5-8.5. Neither model projects any remarkable change in the northwest semiarid regions or northeastern regions of the study area.

According to NorESM projections, a significant increase of 5 mm day^{-1} is expected in central India, particularly under scenario SSP5-8.5, with increased intensity extending to the coastal regions of the upper BoB and also to the western regions. Additionally, there will be a slight increase on the west coast, especially in the northern regions, under scenario SSP5-8.5, creating a continuous zone of increased threshold with central India. A noteworthy increase in the western Himalayan region under scenario SSP1-2.6 is also observed. However, as observed in EC-Earth models, the projected increase in the threshold in the coastal regions of southeast India is not extensively present in NorESM, with an exception on the southern Andhra coast. The anticipated increase in the threshold value of 5 mm day^{-1} in the northwest semiarid regions

of India is expected in all scenarios, with the maximum area of coverage in SSP5-8.5. This model projection anticipates no appreciable change in the northeastern regions across various scenarios, except in SSP5-8.5. In this scenario, the northeastern region forms a continuous zone with the central Indian region, exhibiting an increased threshold.
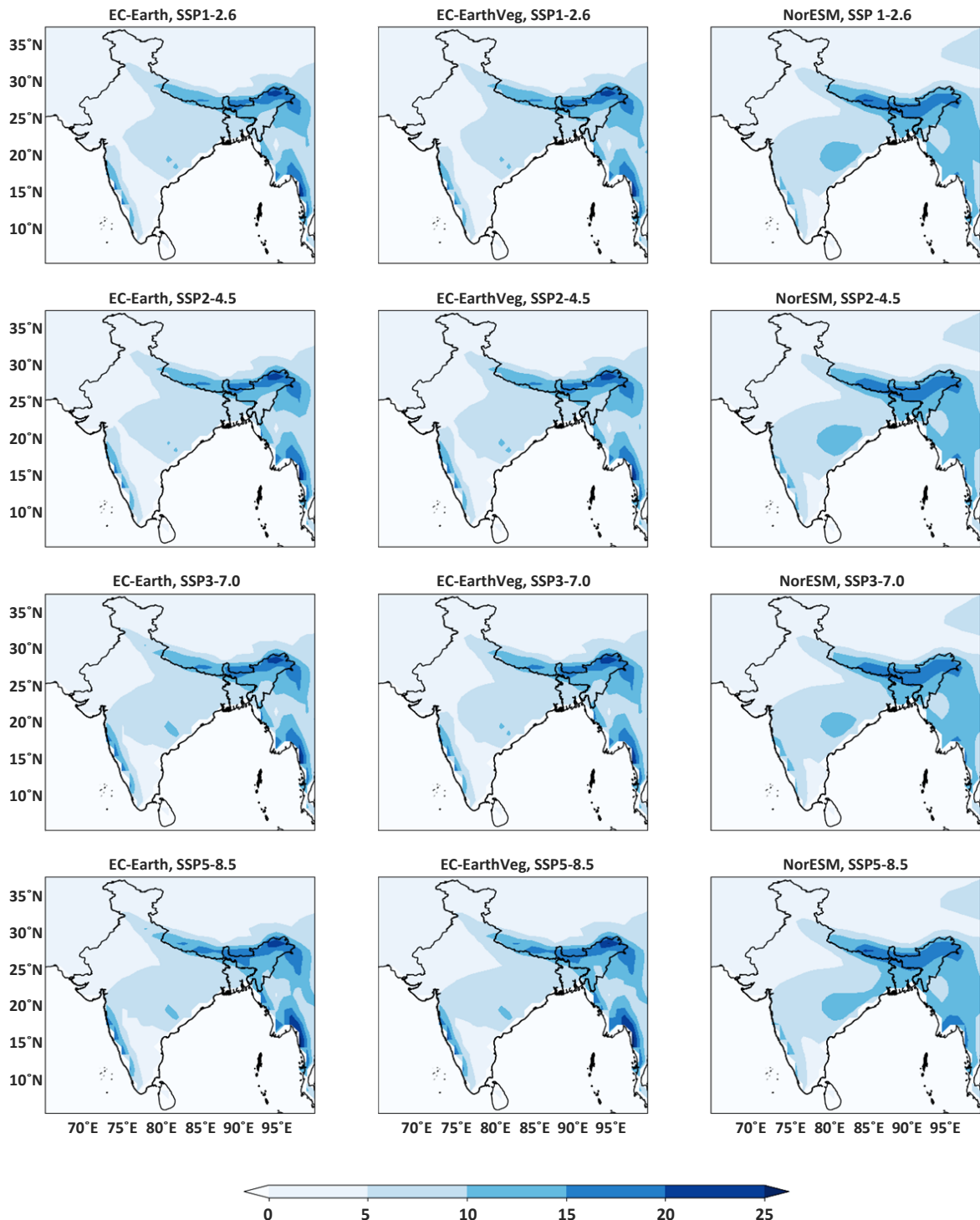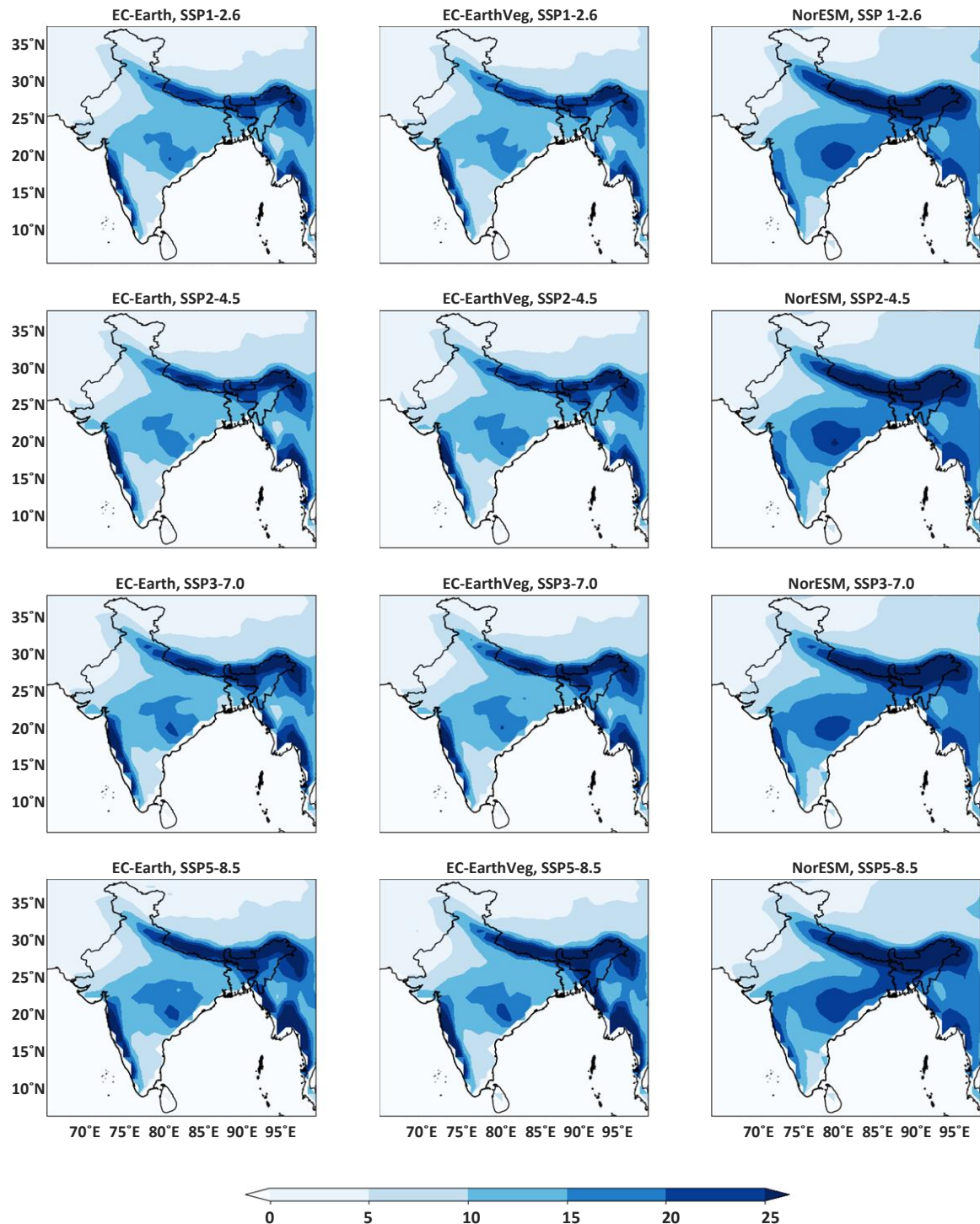

Figure 6.2: The projected 95th percentile of summer monsoon rainfall (mm day^{-1}) for the future period (2015-2100) by EC-Earth, EC-EarthVeg, and NorESM models in (i) SSP1-2.6, (ii) SSP2-4.5, (iii) SSP3-7.0, and (iv) SSP5-8.5 scenarios

6.3.1.3 Extreme Rainfall

The projected extreme rainfall during the summer monsoon (mm season^{-1}) for the future period (2015–2100) by the three selected models in (i) SSP1-2.6, (ii) SSP2-4.5, (iii) SSP3-7.0, and (iv) SSP5-8.5 scenarios are represented in Figure 6.3. The EC-Earth models project a significant increase in extreme rainfall, ranging from 5 to 10 mm season^{-1}, for central India and the west coast regions. This trend is most pronounced in the SSP5-8.5 scenario, followed by the SSP3-7.0 scenario. The expanded area of extreme rainfall is primarily observed in the northern regions of the west coast and the southwestern areas of central India, making these regions more susceptible to the impacts of intense rainfall in the future. Additionally, the zone of extreme rainfall extends to the rain shadow regions behind the Western Ghats. Consequently, there is a notable reduction in the area of rain shadow regions in southeast India, with this effect being particularly prominent in the SSP5-8.5 scenario. The regional increase in extreme rainfall along the west coast shows a gradual progression from SSP1 to SSP5 in both EC-Earth models. However, the substantial spatial expansion of extreme rainfall in the rain shadow regions behind the Western Ghats is not anticipated in EC-EarthVeg. In comparison with EC-Earth, EC-EarthVeg demonstrates a significant increase in central Indian extremes under the SSP5-8.5 scenario, despite a reduced projection of extremes in the SSP3-7.0 scenario. Additionally, the EC-Earth models exhibit a noticeable change of 5 mm in season^{-1} in the western and central Himalayan regions, with nearly equal effects across all scenarios. However, the EC-Earth models do not indicate any substantial changes in projections for the northeastern regions in the future. Furthermore, the northwest semiarid regional extreme rainfall is projected to increase in the future according to both EC-Earth models in all scenarios, showing similar trends.

NorESM indicates a consistent rise in extreme rainfall, measuring less than 10 mm season^{-1}, across both central India and the west coast regions when transitioning from SSP1-2.6 to SSP5-8.5 scenarios. Along the east coast in central India, the expanded area experiencing increased extreme rainfall forms a continuum with the northeast region. The increased extreme rainfall region in central India extends to the northern west coast and makes a continuum with the west coast region also. However, NorESM does not detect significant changes in the northwestern Himalayan and northeastern regions under any of the projected scenarios. In the southwest rain shadow regions, NorESM predicts a 5 mm season^{-1} escalation in extreme rainfall, affecting most areas but leaving a small region unaffected at the southeastern tip. Additionally, the model

anticipates a noteworthy 5 mm season^{-1} gradual increase in extreme rainfall in the northwest semiarid regions when progressing from SSP1 to SSP5.

Figure 6.3: The projected extreme rainfall during the summer monsoon (mm season^{-1}) for the future period (2015-2100) by EC-Earth, EC-EarthVeg, and NorESM models in (i) SSP1-2.6, (ii) SSP2-4.5, (iii) SSP3-7.0, and (iv) SSP5-8.5 scenarios

6.3.1.4 Contribution of Extreme Rainfall to the Seasonal Rainfall

The projected percentage contribution of summer monsoon extreme rainfall to the seasonal rainfall for the future period (2015–2100) by the three selected models in (i) SSP1-2.6, (ii) SSP2-4.5, (iii) SSP3-7.0, and (iv) SSP5-8.5 scenarios is depicted in Figure 6.4. The EC-Earth
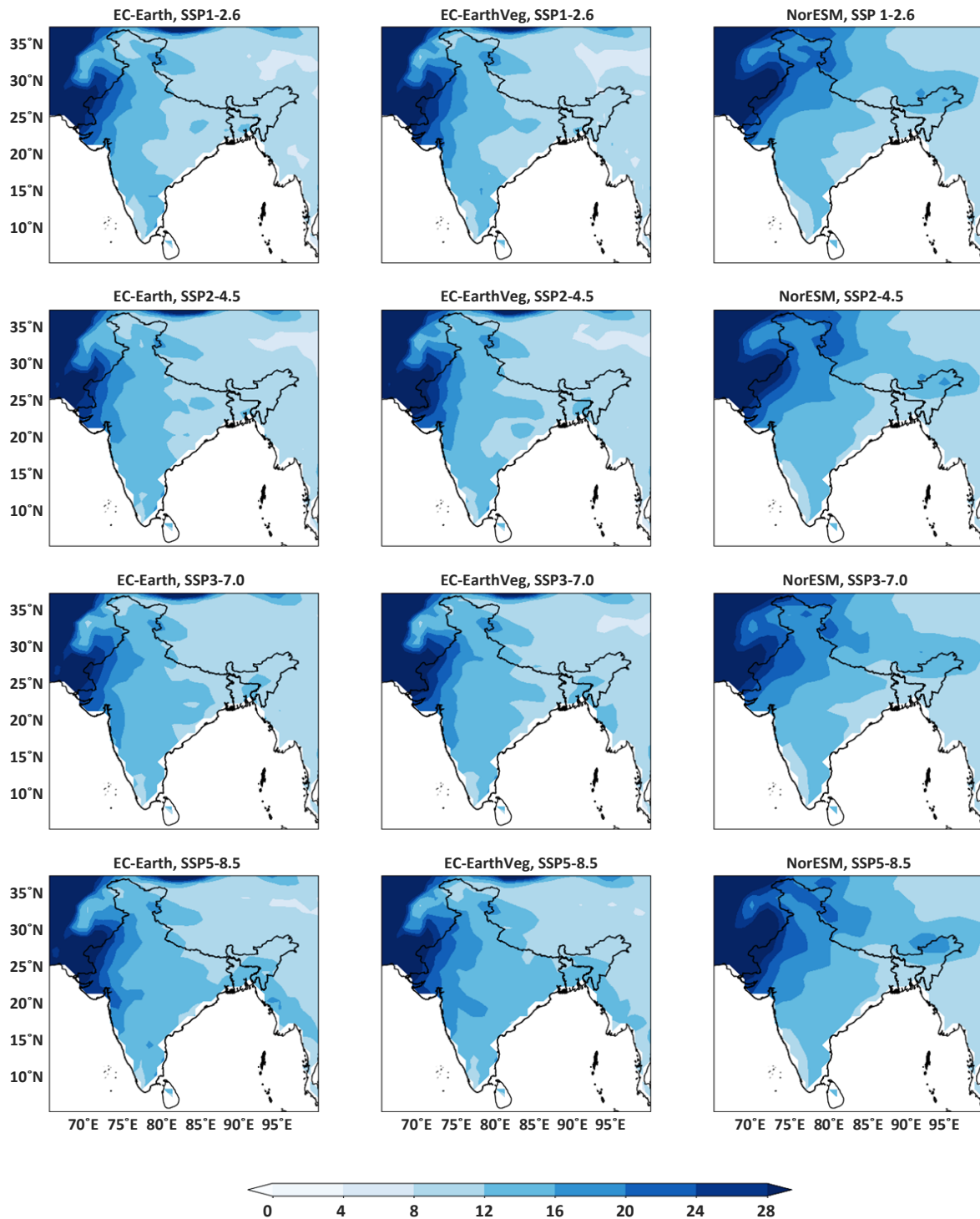
Figure 6.4: The projected percentage contribution of extreme rainfall to the seasonal rainfall for the future period (2015-2100) by EC-Earth, EC-EarthVeg, and NorESM models in (i) SSP1-2.6, (ii) SSP2-4.5, (iii) SSP3-7.0, and (iv) SSP5-8.5 scenarios

models suggest a reduced contribution of approximately 4% in extreme rainfall on the west coast regions, most notably evident in SSP1-2.6 and then in SSP3-7.0 scenarios. Additionally, a 4–8% decrease is projected in central India regions, particularly in the coastal and inland areas of the upper Bay of Bengal (BoB), with the most noticeable effects observed in the SSP1-2.6 and SSP2-4.5 scenarios. The northeast semiarid regions of India and the southeast rain shadow regions exhibit a 4–8% decrease in contribution in the future, with a relatively equal impact across all scenarios. While a more than 8% decrease is projected in the Ladakh area, the extreme rainfall contributions in the Jammu and Kashmir regions predict only a maximum 4% decrease in these models. The Himalayan and northeastern regions also show a 4% decrease, approximately in all scenarios, with the most pronounced effects observed in SSP1-2.6.

The NorESM model also exhibits a decreased contribution of approximately 4% in the west coast regions across all scenarios, with less evident impact in the SSP1-2.6 scenario compared to others. The reduction in the central Indian contribution, exceeding 4%, is particularly notable in the Odisha region, extending to the coastal and inland areas of the upper Bay of Bengal. This spatial enhancement of decreased contribution is most pronounced in the SSP1-2.6 and SSP3-7.5 scenarios. In the northern regions, including Jammu, Kashmir, and Ladakh, NorESM models indicate a decrease of >10% in extreme rainfall contribution compared to EC-Earth models. An anticipated >8% decrease is observed in the northwest semiarid regions of India, with a projected almost 8% decrease in the northeastern and Himalayan regions. The southeast rain shadow regions show a 4–8% decrease in the contribution of extreme rainfall in the future across all scenarios.

6.3.2 Projections of Extremes in the Near-term

6.3.2.1 Extreme Rainfall

Figure 6.5 depicts the projected extreme rainfall during the summer monsoon (mm season^{-1}) for the near-term (2015-2035) for the three models in (i) SSP1-2.6, (ii) SSP2-4.5, (iii) SSP3-7.0, and (iv) SSP5-8.5 scenarios. The EC-Earth models indicate significant increases in extreme rainfall intensity in various regions under different scenarios. Specifically, EC-Earth shows a noteworthy rise in extreme rainfall intensity in the western Himalayan region under the SSP1-2.6 scenario. Additionally, there is a substantial increase of 5 mm season^{-1} in the central Indian Odisha region under the SSP3-7.0 and SSP5-8.5 scenarios. In the west coast regions, a notable increase in extreme rainfall of 5 mm season^{-1} is only observed on the leeward side of the northern portions of the Western Ghats, most evident in SSP3–7.0. Slight changes

are also observed in northeastern regions under SSP2-4.5 and SSP1-2.6 scenarios, northwest arid and semiarid regions in all scenarios, with the maximum change projected in SSP5-8.5, followed by SSP2-4.5, and central Himalayan regions in SSP3-7.0. In comparison with EC-
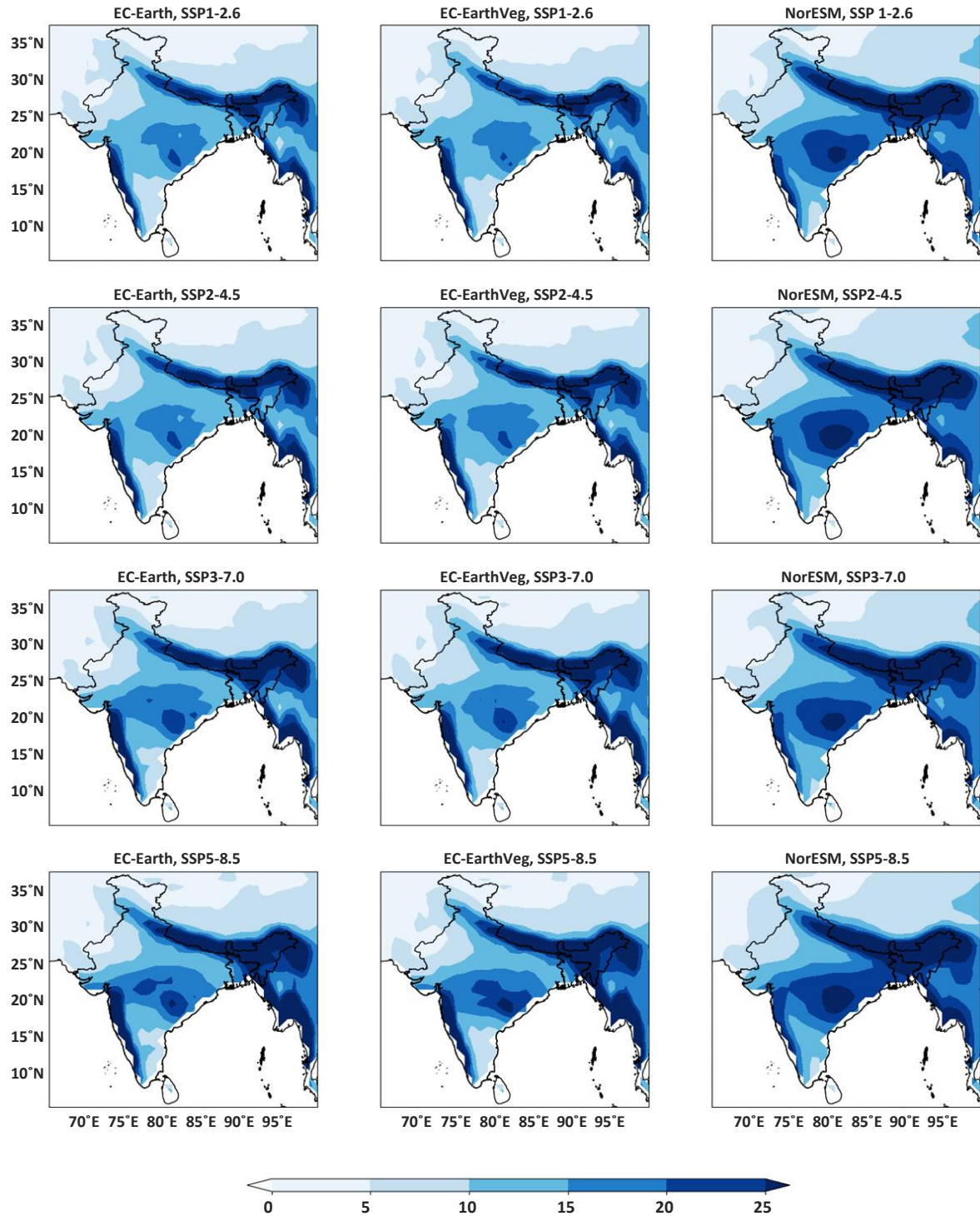

Figure 6.5: The projected extreme rainfall during the summer monsoon (mm season^{-1}) for the near-term (2015-2035) by EC-Earth, EC-EarthVeg, and NorESM models in (i) SSP1-2.6, (ii) SSP2-4.5, (iii) SSP3-7.0, and (iv) SSP5-8.5 scenarios

Earth, EC-EarthVeg shows only slight changes on the leeward side of the northern west coast and western Himalayan regions in scenarios SSP3-7.0 and SSP1-2.6, respectively. Additionally, EC-EarthVeg projections for the central Indian region in the SSP1-2.6 and SSP2-4.5 scenarios remain unchanged, exhibiting no remarkable deviation from historical data. However, there is a slight decrease in extreme rainfall intensity under the SSP3-7.0 and SSP5-8.5 scenarios. Unlike EC-Earth, EC-EarthVeg demonstrates a slight increase in extreme rainfall in the northwestern semiarid regions, but only in the SSP3-7.0 scenario. No noticeable changes are observed in southeastern India or in the northeastern regions by the projections of EC-EarthVeg under any scenario.

Meanwhile, NorESM exhibits a substantial increase in extreme rainfall intensity, approximately 5 mm season^{-1}, in the central Indian Odisha region under the SSP1-2.6, SSP2-4.5, and SSP5-8.5 scenarios, in descending order. The northern west coast regions also experience a similar increase under the SSP1-2.6, SSP3-7.0, and SSP5-8.5 scenarios. Furthermore, NorESM demonstrates a significant increase in the northwest Himalayas under the SSP1-2.6 scenario and a slight decrease in the SSP3-7.0 scenario. Appreciable changes are not projected in the southern west coast, northwest, and southeast regions of India, or in the northeastern regions.

6.3.2.2 Contribution of Extreme Rainfall to the Seasonal Rainfall

Figure 6.6 gives the projected percentage contribution of summer monsoon extreme rainfall to the seasonal mean for the near-term (2015-2035) for the 3 models in (i) SSP1-2.6, (ii) SSP2-4.5, (iii) SSP3-7.0, and (iv) SSP5-8.5 scenarios. The contribution of extreme rainfall to the seasonal mean is projected to significantly decrease (>8%) in the northwest arid and semi-arid regions of India, including Gujarat, Rajasthan, Punjab, and Haryana. This trend is also observed in the northern regions of Himachal Pradesh and Ladakh, according to all models and scenarios in the near-term. This decrease can be attributed to the fact that these regions receive very little rainfall during the summer monsoon season. Similarly, a major decrease in contribution is noted in rain-shadow regions in the south. In the monsoonal regions of central India, the west coast, and the northeast, the models project a substantial decrease (<8%) in the near-term. Moreover, the decreased contribution becomes more pronounced in the inland regions around the upper Bay of Bengal (BoB).

Figure 6.6: The projected percentage contribution of summer monsoon extreme rainfall to the seasonal mean for the near-term (2015-2035) by EC-Earth, EC-EarthVeg, and NorESM models in (i) SSP1-2.6, (ii) SSP2-4.5, (iii) SSP3-7.0, and (iv) SSP5-8.5 scenarios

In the EC-Earth model, a noticeable decline of approximately 8% in contribution is observed in the central Indian and Himalayan regions, particularly prominent in the SSP1-2.6 scenario.

On the west coast, the decrease is around 4%, equally noticeable across all scenarios except SSP3-7.0, where no significant change is projected around 17˚N. The diminished contribution of about 4% in the northern Jammu and Kashmir regions is projected consistently across all scenarios, most notably in SSP3-7.0. The marginal decrease in the northeastern region is also more pronounced in SSP3-7.0. In the northwest arid and semiarid regions, a substantial decrease is more evident in the SSP5-8.5 scenario. Similarly, the projected decrease in the southeast rain shadow region is more observable in the SSP5-8.5 scenario. EC-EarthVeg also projects a reduced contribution similar to EC-Earth in most regions, with some variations across scenarios. The central Indian and Himalayan regions show a more pronounced decrease of about 8%, primarily in the SSP3-7.0 scenario and then in SSP1-2.6. Insignificant changes are expected in the west coast regions. The reduced contribution in the northwestern regions is more notable in SSP1-2.6, followed by SSP3-7.0. In the northeastern regions, an insignificant decrease is most evident in SSP3-7.0, followed by SSP1-2.6. In the northern Jammu and Kashmir regions, changes are projected in all scenarios, most notably in SSP5-8.5. The southwest regional decrease is more pronounced in the SSP3-7.0 scenario.

In NorESM, a noticeable decline in contribution is observed in the central Indian region, particularly prominent in the SSP5-8.5 scenario and subsequently in the SSP3-7.0 scenario. Additionally, the southern west coast region exhibits a 4% reduction in the contribution of extreme rainfall to the seasonal value, predominantly observed in the SSP1-2.6 and SSP3-7.0 scenarios, respectively. The northwest regional decrease is most evident in the SSP1-2.6 scenario. The northeast regional decrease is more pronounced in the SSP5-8.5 scenario and then in the SSP2-4.5 scenario. The projected decrease in the southeast region is equally significant in the SSP1-2.6 and SSP3-7.0 scenarios.

6.3.3 Projections of Extremes in the Mid-term
6.3.3.1 Extreme Rainfall
Figure 6.7 gives the projected extreme rainfall during the summer monsoon (mm season^{-1}) for the mid-term (2047-2067) for the three selected models in (i) SSP1-2.6, (ii) SSP2-4.5, (iii) SSP3-7.0, and (iv) SSP5-8.5 scenarios.

EC-Earth projects an increase in the intensity of extreme rainfall of about 5 mm season^{-1} in central India, particularly expanding spatially towards the southern and western sides. The projected extreme rainfall gradually increases in these regions when transitioning from SSP1-
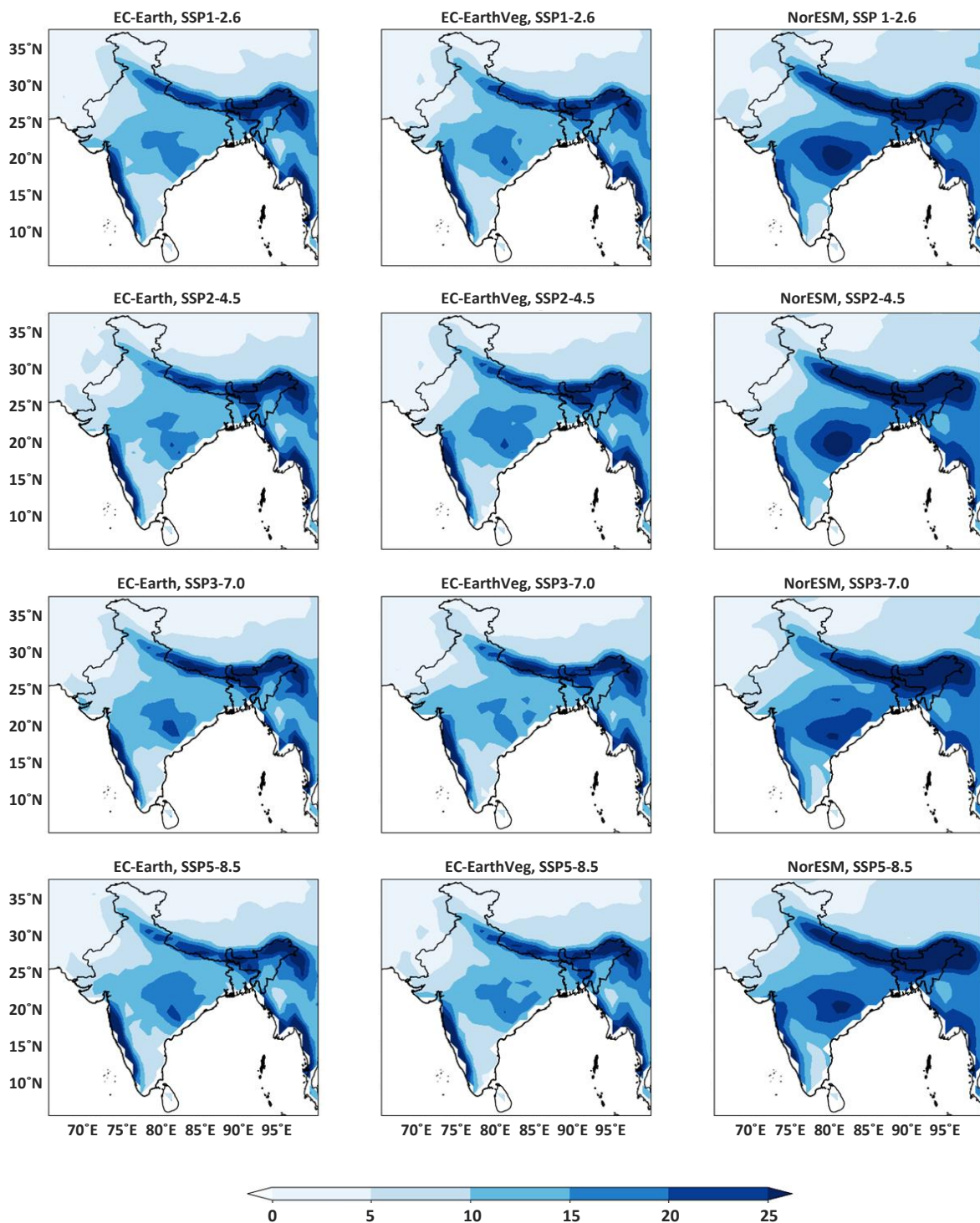
Figure 6.7: The projected extreme rainfall during the summer monsoon (mm season^{-1}) for the mid-term (2047-2067) by EC-Earth, EC-EarthVeg, and NorESM models in (i) SSP1-2.6, (ii) SSP2-4.5, (iii) SSP3-7.0, and (iv) SSP5-8.5 scenarios

2.6 to SSP5-8.5. The projected extremes in the northwestern semiarid regions of India are depicted almost equally in all scenarios. No significant changes are expected in other regions. On the west coast, a slight increase is observed on the leeward side of the Western Ghats in

scenario SSP5-8.5. An insignificant increase is also noticeable in the northeastern region under SSP5-8.5. EC-EarthVeg projects a significant increase of >5 mm season^{-1} in the central India region, particularly in the Odisha area, with the most pronounced effects seen in the SSP3-7.0 scenario. In the SSP5-8.5 scenario, the area with increased extreme rainfall is also expanding to the southwestern region, creating a continuum with the northern west coast. Both EC-Earth models anticipate a slight increase in precipitation in the western and central Himalayas across all scenarios. However, no significant changes are anticipated in other regions by EC-EarthVeg, including the west coast, northwest India, southeast India, western Himalaya, and northeastern regions.

NorESM predicts an increase in extreme rainfall exceeding 10 mm season^{-1} across all central Indian regions, with the increased precipitation area extending from the Odisha coast to the northern Bay of Bengal coastal regions and inland areas to the southwest. This is most prominent in the SSP1-2.6 and SSP5-8.5 scenarios. Additionally, NorESM anticipates a noticeable increase in extreme precipitation in the northern west coast region. A 5 mm season^{-1} increase is also projected in the western Himalayas, particularly in the SSP1-2.6 scenario. The substantial increase in arid and semiarid regions in the northwest is more evident in the SSP5-8.5 scenario. In contradiction to EC-Earth models, NorESM projects a 5 mm season^{-1} extreme rainfall increase in the southeast rain shadow regions in all scenarios, most notably in SSP3-7.0 and SSP5-8.5. No significant changes are anticipated in the northeastern regions.

6.3.3.2 Contribution of Extreme Rainfall to Seasonal Rainfall

Figure 6.8 gives the projected percentage contribution of summer monsoon extreme rainfall to the seasonal mean for the mid-term (2047-2067) by the three selected models in (i) SSP1-2.6, (ii) SSP2-4.5, (iii) SSP3-7.0, and (iv) SSP5-8.5 scenarios. The expected percentage contribution in the mid-term resembles the projection pattern of the near-term, with the decreased contribution of extreme rainfall more pronounced in the northwestern and southeastern regions of India. In EC-Earth models, the decreased contribution of around 8% in the eastern parts of central India is particularly noticeable in SSP2-4.5, followed by SSP1-2.6. The regional coverage of the decreased contribution is higher in the mid-term compared to the near-term. The reduced contribution of extreme rainfall, as projected by EC-Earth models, reaches its maximum in the western part of central India and the northwestern semiarid part of India under SSP2-4.5 and SSP5-8.5 scenarios. A 4–8% decrease is estimated for the west coast regions in all scenarios. In the EC-Earth model, the regional decrease in projected extremes in
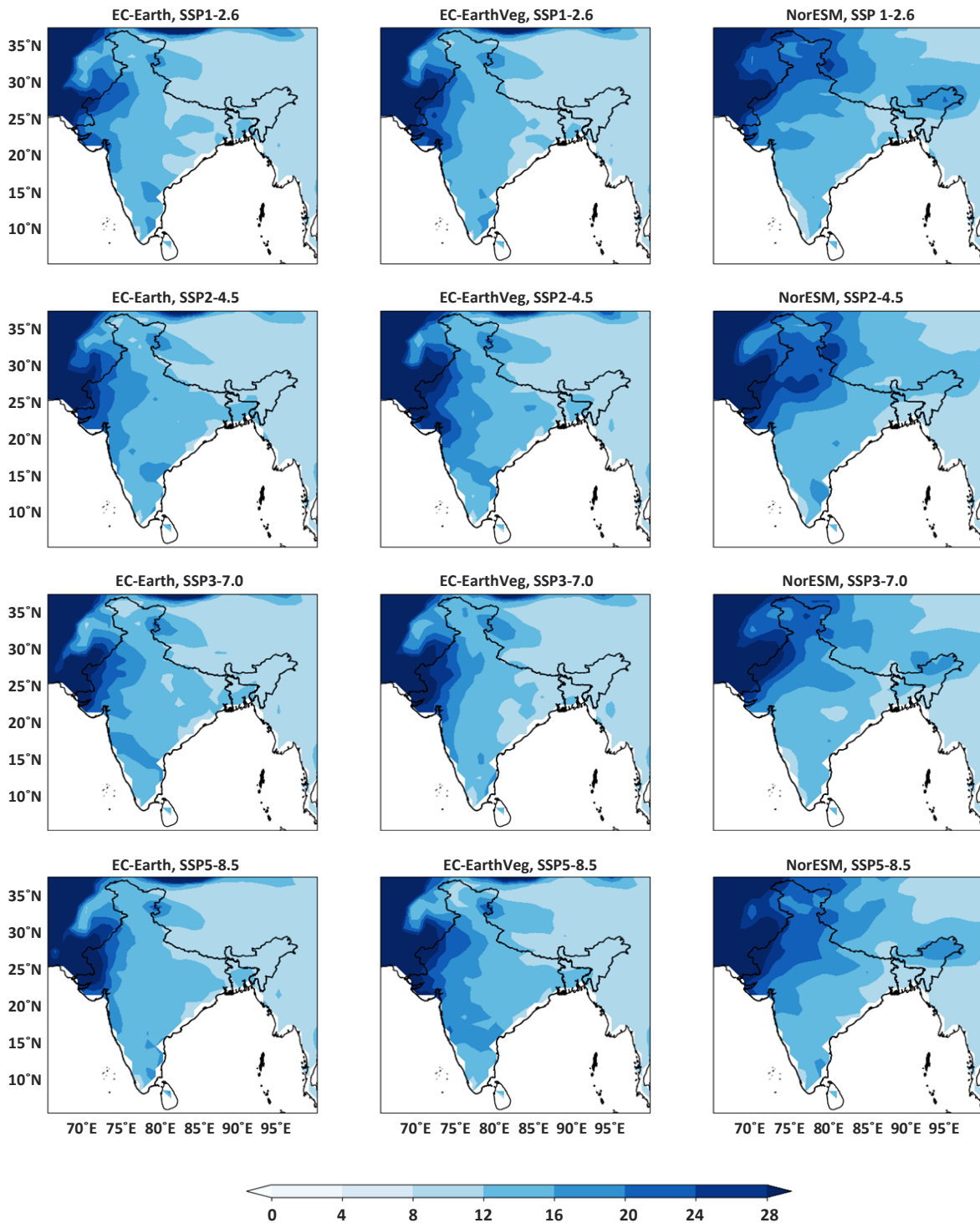
Figure 6.8: The projected percentage contribution of summer monsoon extreme rainfall to the seasonal mean for the mid-term (2047-2067) by EC-Earth, EC-EarthVeg, and NorESM models in (i) SSP1-2.6, (ii) SSP2-4.5, (iii) SSP3-7.0, and (iv) SSP5-8.5 scenarios

southeast India is more pronounced in SSP3-7.0, while in the EC-EarthVeg model, it is more evident in SSP5-8.5. Although the projected change in the northeastern region is not

significant, it is noticeable in the SSP1-2.6 scenario of the EC-EarthVeg model.

In the NorESM model, the diminished contribution of extreme rainfall, approximately 4–8%, is most pronounced in SSP3–7.0. A 4% reduction in contribution is also observed in the NorESM model in the southern west coast regions under all scenarios. Changes in the west coast regions and southeast India are insignificant in all scenarios. The decreased contribution in the Jammu, Kashmir, and Ladakh regions is more noticeable in SSP3-7.0. The reduction in the northeastern region is also more evident in SSP3-7.0.

6.3.4 Projections of Extremes in the Far-term
6.3.4.1 Extreme Rainfall

Figure 6.9 represents the projected extreme rainfall during the summer monsoon (mm season^{-1}) for the far-term (2079-2099) by the three selected models in (i) SSP1-2.6, (ii) SSP2-4.5, (iii) SSP3-7.0, and (iv) SSP5-8.5 scenarios. As projected by EC-Earth models, there is a significant increase of more than 10 mm season^{-1} in extreme rainfall in central India in SSP5-8.5, followed by SSP3-7.0 scenarios. Although the changes exhibit an ascending trend from SSP1-2.6 to SSP5-8.5, a substantial shift is observed in the higher warming scenarios as compared to SSP1-2.6 and SSP2-4.5. EC Earth models also predict a more than 10 mm season^{-1} increase in the northern west coast regions for SSP3-7.0 and SSP5-8.5 scenarios; however, the changes in the windward side of the southern west coast are not noticeable. EC Earth models project a slight increase in the central and western Himalayan regions, particularly evident in SSP3-7.0 and SSP5-8.5. The slight change in the semiarid regions of northwestern India is also more pronounced in the SSP3-7.0 and SSP5-8.5 scenarios. It is noteworthy that the projections anticipate a 5mm season^{-1} in the southeastern rain shadow regions, and the area will become more prone to extreme rainfalls in the far future under higher warming scenarios such as SSP3-7.0 and SSP5-8.5. EC-Earth also forecasts a slight change in the northeastern regions, noticeable only in the SSP5-8.5 scenario.

The EC-EarthVeg model projections are nearly identical to those of EC-Earth, with only minor variations. In the top-warming scenarios, the intensification of extreme rainfall in the central Indian region is more pronounced in EC-EarthVeg, while spatial enhancement in the southeastern regions is more prominent in EC-Earth. NorESM also predicts a significant increase of 10 mm day^{-1} in extreme rainfall in the central Indian region under the SSP5-8.5 scenario, followed by the SSP2-4.5 scenario. Moreover, an increase of only 5 mm season^{-1} is anticipated in the SSP1-2.6 and SSP3-7.0 scenarios. Similar to the EC-Earth models, NorESM
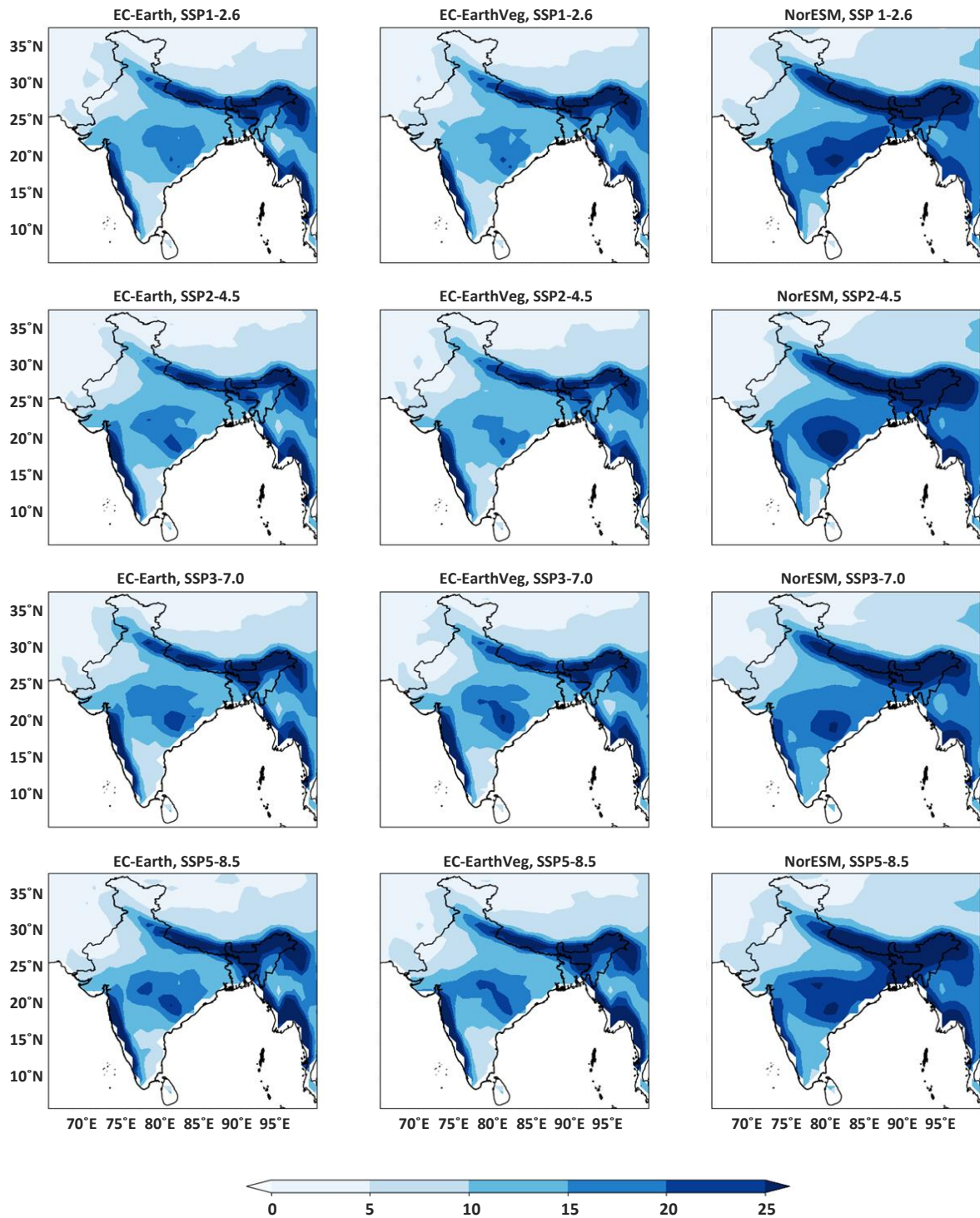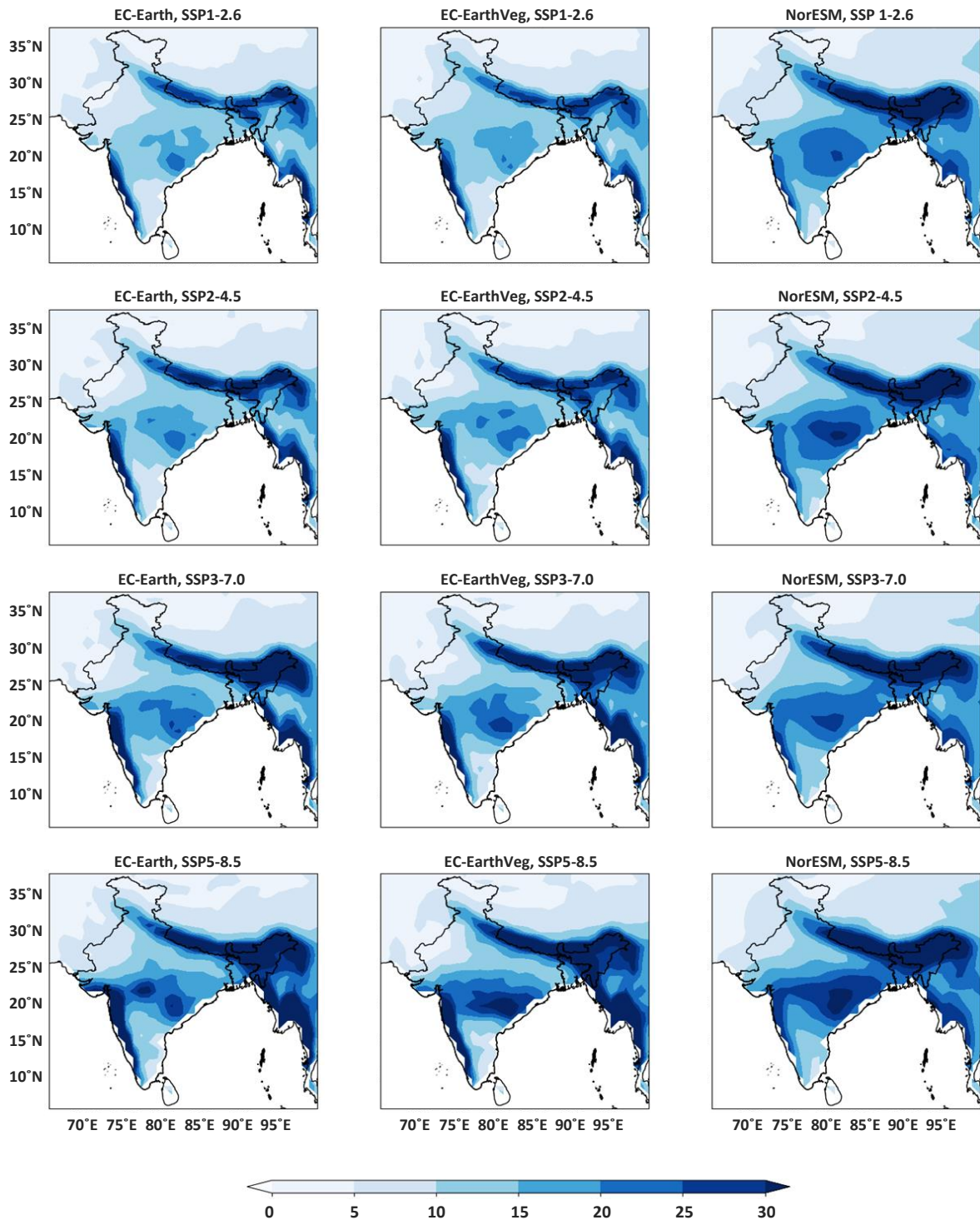
Figure 6.9: The projected extreme rainfall during the summer monsoon (mm season^{-1}) for the far-term (2079-2099) by EC-Earth, EC-EarthVeg, and NorESM models in (i) SSP1-2.6, (ii) SSP2-4.5, (iii) SSP3-7.0, and (iv) SSP5-8.5 scenarios

projects a more than 10 mm season^{-1} increase in the northern west coast regions for the SSP3-7.0 and SSP5-8.5 scenarios. The model also anticipates a 5 mm season^{-1} increase in the northwest semiarid regions and southeast India. The northwest regional increase is present

almost equally in all scenarios; however, the southeast increase is not significant in SSP1-2.6. The NorESM model projects no significant change in extreme rainfall in the Himalayan and northeastern regions.

6.3.4.2 Contribution of Extreme Rainfall to the Seasonal Rainfall

Figure 6.10 presents the projected percentage contribution of summer monsoon extreme rainfall to the seasonal mean for the far-term (2079-2099) by the three selected models in (i)SSP1-2.6, (ii)SSP2-4.5, (iii)SSP3-7.0, and (iv)SSP5-8.5 scenarios. The expected percentage contribution in the far-term closely resembles the near- and mid-term projections. Notably, there is a significant decrease in contribution in the northwestern, northern, and southeastern regions. In EC-Earth models, a noticeable 4% reduction in contribution is observed in the southern west coast under SSP3-7.0 and in the northern west coast in EC-Earth under SSP1-2.6. However, this trend is less visible in the upper Bay of Bengal coastal regions compared to other future terms. In the eastern part of central India, an 8% decrease is evident in EC-EarthVeg under SSP1-2.6. In the western part of central India and the northwest semiarid regions, the decrease is widely observed in lower radiative forcing scenarios in both EC-Earth models. Nevertheless, in the southeast rain shadow regions, the 4% decrease is more prominent in higher forcing scenarios. A significant decrease in the northeastern regions is projected in EC-Earth under SSP2-4.5, followed by EC-EarthVeg in SSP1-2.6.

In NorESM, the west coastal changes, characterized by a 4% decrease, are observed in both the southern and northern regions under SSP1-2.6. Notably, substantial central Indian and northeastern regional changes ranging from 4% to 8% are most evident in SSP3-7.0. Conversely, the northwestern and northern regional changes are consistently depicted across all scenarios.

6.4. Chapter Summary

Climate models project both significant and insignificant increases in seasonal and extreme rainfalls for both monsoonal and non-monsoonal regions over the study area in the future, depending on the scenarios considered. The EC-Earth models forecast a 5 mm day^{-1} increase in seasonal rainfall for the west coast, southwestern regions of central India, and the western Himalayas. The NorESM model predicts significant changes in central India and rain shadow regions of southeast India. In all model projections of extreme rainfall, the increased change in the northern regions of the west coast and southwestern regions of central India could lead to
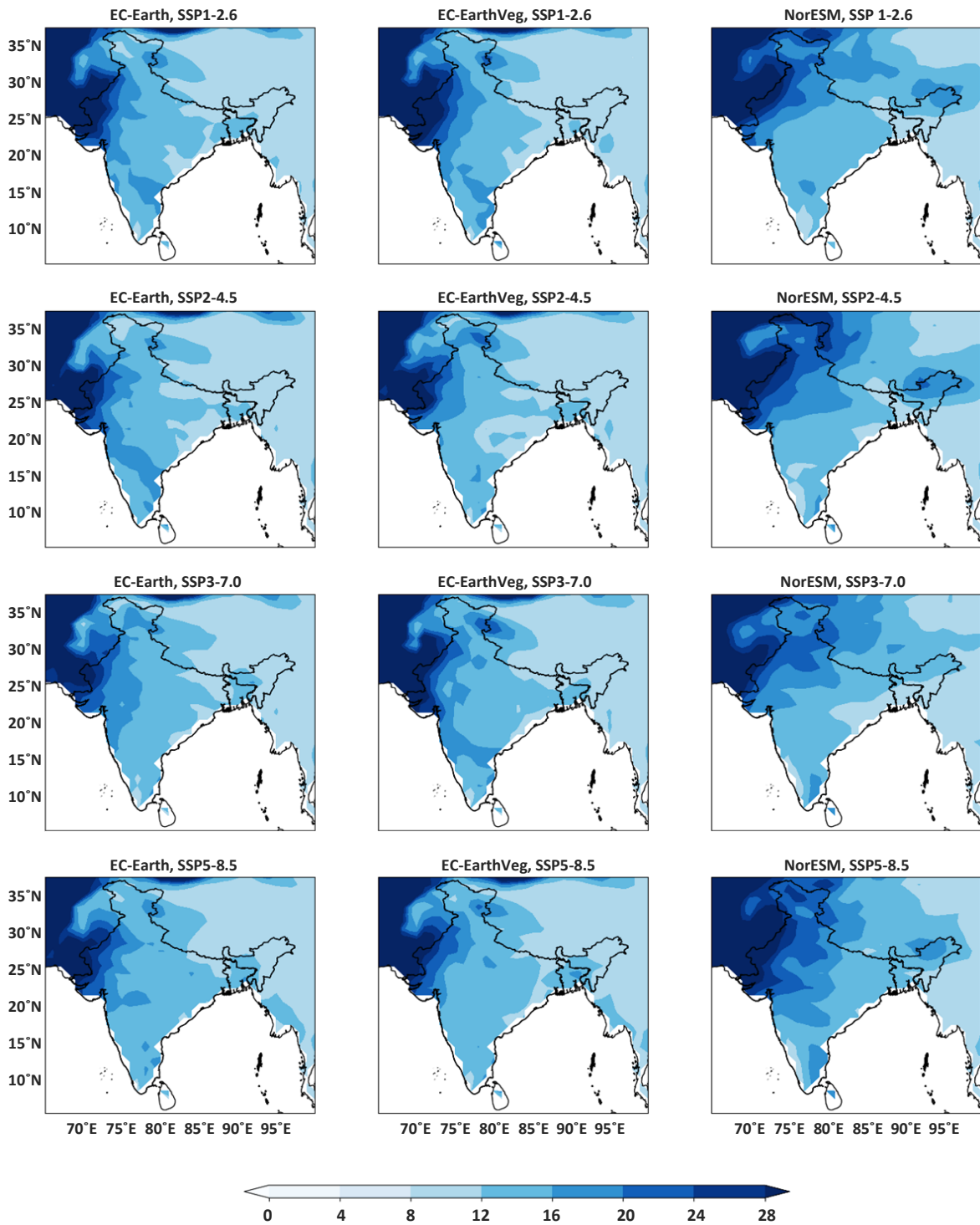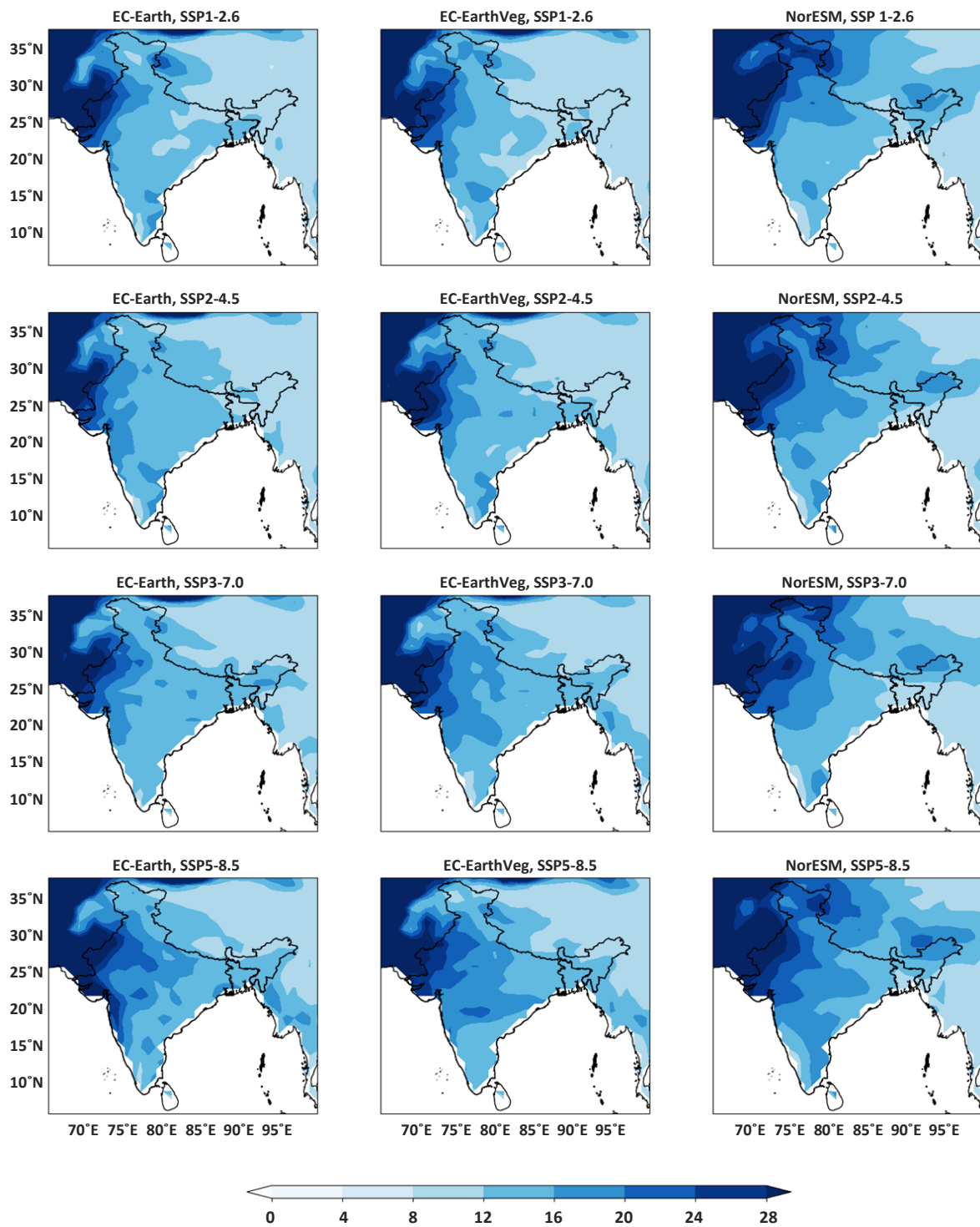
Figure 6.10: The projected percentage contribution of summer monsoon extreme rainfall to the seasonal mean for the far-term (2079-2099) by EC-Earth, EC-EarthVeg, and NorESM models in (i) SSP1-2.6, (ii) SSP2-4.5, (iii) SSP3-7.0, and (iv) SSP5-8.5 scenarios

heightened vulnerabilities in the area, especially in higher forcing scenarios. Moreover, the zone of extreme rainfall extends to the rain shadow regions behind the Western Ghats, resulting in a noticeable reduction in the area of rain shadow regions in the future, particularly in the

SSP5-8.5 scenario. Additionally, the northwest semiarid regional extreme rainfall is projected to increase in the future. In the case of NorESM, the pronounced extreme area in central India extends through the coastal region to the northeastern regions in the SSP5-8.5 scenario. The contribution of extreme rainfall to seasonal rainfall is observed to decrease more in northwestern semiarid India, southeast rain shadow regions, and Ladakh and Himachal Pradesh areas.

The projections for the selected future terms yield valuable insights. In the west coast region, no significant changes in extreme rainfall are projected in the near-term. However, a substantial increase in extreme rainfall is anticipated in the mid- and far-terms on the northern west coast, particularly under the SSP5-8.5 scenario. In the central Indian region, EC-Earth models predict intensified extreme rainfall along with an expansion in the extreme rainfall affected area, most notably in the far-term. Additionally, these changes are also notable in the NorESM model. In the western Himalayan region, a significant increase in extreme rainfall is projected by models in the near-term, especially in the SSP1-2.6 scenario. In contrast, no change in extreme rainfall is expected in the mid- and far-terms in the above region. The percentage contribution of extreme rainfall to the seasonal mean decreases slightly in monsoonal areas in all future terms, particularly in the SSP1-2.6 scenario.

The next chapter summarizes the thesis work, highlighting important findings and concluding remarks.

CHAPTER 7

SUMMARY AND CONCLUSIONS

CHAPTER 7

SUMMARY AND CONCLUSIONS

The present thesis seeks to comprehend the physical and dynamical characteristics of South Asian Summer Monsoon (SASM) rainfall and its extremes. In this study, extreme rainfalls within a region were delineated based on the percentile value of daily rainfall (99th percentile) across grid points in the specified area. Prominent regions within the monsoonal zone exhibiting prominent characteristics were identified by examining the linear decadal trends of extreme rainfall amounts during the summer monsoon season. The analysis encompasses the physical attributes of extreme rainfalls in these identified regions, including their evolution and dissipation features, linear trends over the years, and probability density functions. Furthermore, the study delves into the correlation of these extreme rainfalls with various climate forcing mechanisms, aiming to discern their teleconnections with global sea surface temperature (SST) variations in the Pacific, Atlantic, and Indian oceans. The dynamical characteristics of extreme rainfall events (EREs) in the selected regions were explored in terms of circulation features, relative vorticity, specific humidity anomalies, vertical vorticity, vertically integrated moisture transport, moisture convergence, and vertically integrated moist static energy during these events. In the concluding segment of the study, efforts are made to simulate extreme rainfall amounts in the historical period and project their variations in future periods over the study region for various Shared Socioeconomic Pathway (SSP) scenarios, utilising Coupled Model Intercomparison Project phase 6 (CMIP6) Global Climate Models (GCMs).

The primary part of the study involves detecting and exploring EREs in the South Asian regions. This study considers daily rainfall during the summer monsoon season as an extreme case if it surpasses the 99th percentile value in the climatological period. The study calculated both the rainfall amount and the number of days with rainfall exceeding the 99th percentile. Additionally, the standard deviations of mean and extreme rainfalls and the percentage contributions of extreme rainfall to seasonal rainfall were computed to investigate the characteristics of EREs. The analyses reveal that SASM mean and extreme rainfalls display significant variability in spatial and temporal scales across different regions of the Indian subcontinent throughout the study period (1951–2015).

The spatial pattern of rainfall corresponding to the 99th percentile reveals large values in most of the west coast regions, some pockets in the northeast, and the foothills of the Himalayas. Central India exhibits moderate values, and very low values are observed in the southeast, northwest, and northern regions such as Jammu, Kashmir, and Ladakh. The high amounts of extreme rainfall in the regions of the West Coast, Uttarakhand, Himachal Pradesh, Meghalaya, and Arunachal Pradesh may be attributed to the influence of topographic features. The Indo-Gangetic plains are also impacted by extreme rains during the summer monsoon season. The northwest and southeast regions experience very low amounts of extreme rainfall. The spatial distribution of the number of extreme rainfall days is different from the distribution of the amount of rainfall from extreme events. The number of extreme rainfall days shows high values in the northwestern and northern regions, including Ladakh and Kashmir; however, the extreme rainfall recorded over those regions from these extreme events is small.

The standard deviation follows a pattern similar to climatological variability but with lower magnitudes. The standard deviation of the number of days with extreme rainfall reveals a distinct pattern crucial for describing the actual impacts of such occurrences. Considerable variability in the number of extreme days, with moderate variability in the amounts of extreme rainfall, is observed in the southern end of peninsular India, the Gujarat region, and the foothills of the central Himalayas. Uttarakhand, Himachal Pradesh, Arunachal Pradesh, and the Indo-Gangetic Plain regions experience high variability in both rainfall and the frequency of extreme events. In most non-monsoonal regions of India, the contribution of rainfall from extremes to the mean rainfall is more than 20%, while it is less than 15% in monsoonal regions such as the coastal regions of the Western Ghats, central and northeast India, as well as the foothills of the Himalayas.

The spatial distribution of linear trends in seasonal rainfall is notably negative in most rainy areas of the Indian subcontinent, particularly in the Kongan belts, central Indian region, and northeast regions. The spatial trends of extreme rainfall and its events also exhibit a similar pattern, although variations exist in magnitudes and, to a slight extent, in the spatial extension of the regions. In the case of extreme rainfall, major changes in spatial trends are observed on the west coast, central, and north Indian regions. In the central Indian regions, the values of trends are highly inhomogeneous, and the regions of positive and negative trends are highly localised, with comparatively low significance. In northcentral India, negative trends are found for both mean and extreme rainfalls.

Five regions exhibiting significant long-term rainfall variations are identified in the subsequent phase of the study, considering the decadal trends of both mean and extreme rainfalls. The investigation delves into the evolution and dissipation characteristics of EREs within these identified regions by computing their composites and examining lead-lag behaviour. In addition to analysing linear trends, the study employs the Mann-Kendall non-parametric trend analysis to ascertain the significance of trends and estimate Sen's slope values for quantifying these trends. Probability density functions (PDF) for both mean rainfall and extreme events are determined for the identified regions, and the resulting distributions are graphically presented to illustrate potential changes in rainfall patterns.

The analysis of the spatial composite of EREs and the lead-lag analysis over the selected regions indicates that extreme events are predominantly heterogeneous in space and the features of EREs are independent from one region to another. Most extreme events develop such a situation within a short span of three days, even though their signature of above-normal rainfall is apparent almost one week before the event. Unlike other regions, extreme events in north central India (NCI) and northeastern regions (NER) show a sharp evolution without noticeable previous signs. In the case of central India (CI) regions, the rainfall exhibits a wavy pattern with an approximately 6-day period during evolution as well as dissipation. While the southern parts of the west coast, northern parts of central India, and northeastern regions show similar linear trends with more or less comparable values for mean and extremes, contrasting trends are also observed in other regions, such as the northern part of the west coast and central India.

The probability distributions of rainfall in the pre-1980 and post-1980 periods exhibit greater differences in the case of extremes than for mean rainfall. The PDF of mean rainfall for the entire period is more influenced by the PDF of mean rainfall in the post-1980s period compared to the pre-1980s period. This shift signifies a reduction over time in the amount of mean rainfall associated with the frequency of occurrences of extreme events. Such a pattern is not significant in the case of extremes. The wider curve for the extremes in the post-1980 period in regions, except for the southern west coast (SWC), demonstrates the increased variability of extremes in that period over these regions.

The exploring of the spatial correlation of different climate indices with rainfall over the Indian subcontinent is used to ascertain their relationship with both mean rainfall and EREs. A correlation study was conducted with Niño 3.4, El Niño Modoki, DMI, PDO, AMO, and AZM

indices, and the significance of the correlation values was determined through the student's t-test. The individual analysis of the correlation between climatological forcing mechanisms and mean and extreme events revealed spatial variations. Moreover, it was unable to identify any indices as reliable predictors of extreme events in South Asian regions. The interdependence of various forcing mechanisms influencing the Indian summer monsoon rainfall results in their coupled action, contributing to elevated impacts and vulnerability during extreme events.

To explore the underlying dynamics of the EREs during the southwest monsoon period, four regions were selected based on the spatiotemporal variability of extreme rainfall. The northern west coast region exhibited large inter-annual variability, nonsignificant trends, and other rainfall characteristics for both mean and extremes; therefore, the region is excluded from further analysis. To investigate the cessation and dissipation characteristics of EREs, composites of all extreme events are created in the selected regions from 6 days before to 6 days after the events, spanning the period from 1951 to 2015. The evolutionary and dissipation characteristics of the ERE were examined based on lead-lag composites of horizontal circulations, relative vorticity, specific humidity anomalies, and vertical vorticity. Additionally, vertically integrated moisture transport, moisture convergence, and vertically integrated moist static energy were assessed during the EREs across the four different regions.

The 850 hPa circulation features reveal distinct differences across various regions. In the SWC regions, the wind strength increases rapidly before the event but gradually dissipates afterwards. During the extreme period, low-level moisture-laden winds directly hit the western coastal regions and the Western Ghats, leading to heavy rainfall over the region. In the CI region, the wind core extends from the Arabian Sea to central India, and a similar pattern is observed in moisture transport and rainfall. The Bay of Bengal (BoB) wind component also reaches its maximum during the extreme event. In the NCI and NER, winds and moisture transport at 850 hPa are relatively weaker. During NCI extremes, the Low-Level Jet (LLJ) core splits into two, with the northern branch causing the extreme event. In the NER, southerly wind regimes prevail over the areas of EREs. Moisture transport analysis suggests that the primary moisture source for extreme events in SWC, CI, and NCI is the Arabian Sea, while for the NER, the main source is the BoB.

The relative vorticity (RV) also reveals positive values over the regions during EREs, indicating low-level convergence. During the evolution period of extremes in the WC and CI regions, positive relative vorticity gradually increases and spreads toward the concerned

regions. The intensity of positive RV is comparatively lower in the NCI and NER extremes compared to the central Indian and West Coast extremes. In the case of NCI extremes, a convergence zone was also noticed at the southern tip of peninsular India. For EREs over the SWC, the vertically integrated moisture transport (VIMT) shows its maximum value over the central and eastern Arabian Sea, including the southern west coast of the Indian peninsula. Moisture transport during these extreme periods is westerly. The moisture transport over CI is almost similar to that of the WC, but two peaks of VIMT are observed in the spatial domain: one over the central Arabian Sea, and the other over the north BoB and the adjoining central Indian land mass. In the case of NCI, the moisture transport shows two pathways after splitting from the Arabian Sea: one goes through the southern tip of peninsular India, and the other goes through North India. Moisture transport during extreme events in the NER is high over the central Arabian Sea and north BoB, including the northeastern land mass. Its strength is almost similar to extremes in the NCI region.

The low-level convergence is confirmed based on low-level moisture convergence. Vertically integrated moist static energy shows high values in regions experiencing extreme rainfall, consistent with moisture convergence at 1000 hPa. This suggests increased convective activity in these regions during extreme events. The evolution and dissipation of moisture and vertical velocity in the lead-lag vertical cross-section indicate the uniqueness of individual regions. The SWC and NER regions are climatologically moisture-abundant; even a slight increase can result in heavy rainfall associated with a high upward motion of moisture. However, the CI and NCI exhibit high moisture levels throughout the atmospheric column and elevated updrafts during EREs.

The projection study attempted to simulate extreme rainfall during the historical period using CMIP6 GCM models and projected their variations in future periods over the study region for various SSP scenarios. For the historical analysis of extreme rainfall from 1950 to 2014, model simulations were compared with monthly rainfall data from the Climatic Research Unit (CRU). Given the varying resolutions of each GCM, all GCM model data and CRU data were initially re-gridded to a common 1.5° latitude × 1.5° longitude spatial resolution.

The screening of simulation models was conducted based on their responses to the annual cycle of rainfall, followed by Taylor diagram analysis. The annual cycle of rainfall for all models was plotted, and those models that failed to fall within the range of ±2 standard deviations of the CRU data were excluded. Consequently, 22 models performing better in simulating

summer monsoon rainfall variations comparable to observational data were selected. A Taylor diagram analysis was done using the 95th percentile of monthly rainfall data for the summer monsoon season of the selected twenty two models against the CRU data over the historical period. It is to scrutinise further models in simulating the 95th percentile of seasonal rainfall with spatial patterns closest to the observational dataset. Models with correlation coefficients greater than 0.8 and normalised variance between 0.9 and 1.1 were filtered out from the Taylor diagram. Subsequently, five models were chosen for their performance in simulating EREs. The selected models are EC-Earth3, EC-Earth3-AerChem, EC-Earth3-CC, EC-Earth3-Veg, and NorESM2-MM.

To assess the quantitative capabilities of CMIP6 models in reproducing Indian summer monsoon rainfall, their projected seasonal mean and extreme rainfall amounts were compared against CRU observation data over land for the historical period spanning 1950–2014. The study also examined the percentage contribution of extreme rainfall to seasonal rainfall for a more comprehensive understanding. While the selected models exhibited similar spatial patterns for mean and extreme rainfall during the historical period, consistent regional biases emerged across CMIP6 models, manifesting as both overestimation and underestimation, particularly in monsoonal regions. such as the West Coast, central India, the Himalayas and its foothills, and the northeastern regions. The EC-Earth models and NorESM demonstrated the ability to simulate central Indian seasonal rainfall quite well, although the spatial coverage of good estimation is somewhat reduced. The NorESM model outperformed EC-Earth models in simulating central Indian and northeastern regional seasonal rainfall patterns. In contrast, EC-Earth models excelled in capturing the west coast, particularly the southern region, and also in the western Himalayan regions.

The EC-Earth models performed well in simulating extreme rainfall events in central India, whereas NorESM tended to overestimate the observational data. The EC-Earth models provided reasonable estimates for extreme rainfalls on the west coast regions, whereas the NorESM models exhibited a slight underestimation. The variabilities in extreme rainfall in the central and eastern Himalayan regions were not adequately captured by any models. However, the EC-Earth models effectively represented extreme rainfall in the western Himalayan region, while NorESM showed a slight overestimation. The models slightly underestimated extreme rainfall patterns in the northern west coast and northeast regions of India, as well as in the

coastal areas of Myanmar. On the other hand, extreme rainfall in the northwest and southeast Indian regions was accurately projected by all EC-Earth models.

Even though CMIP6 has evolved more than its older missions in capturing land-sea interactions and anthropogenic forcings, the complexity of land-sea interactions hinders the model's ability to simulate the summer monsoon extreme rainfall features, especially over the northern west coast and northeast regions of the subcontinent. Despite the advancements in CMIP6 over its predecessors in capturing land-sea interactions and anthropogenic forcings, the intricate nature of these interactions hindered the models' ability to simulate summer monsoon extreme rainfall features, particularly over the West Coast and northeastern regions of the subcontinent.

The present study also addressed notable spatiotemporal changes in extreme precipitation (≥95th percentile) over the study area under four different future warming scenarios (Shared Socioeconomic Pathways, or SSPs) spanning from 2015 to 2100. The four selected SSPs for projecting the future of extreme precipitation are SSP1-2.6 (RCP2.6), SSP2-4.5 (RCP4.5), SSP3-7.0, and SSP5-8.5 (RCP8.5), corresponding to radiative forces stabilizing at approximately 2.6 Wm^{-2}, 4.5 Wm^{-2}, 7.0 Wm^{-2}, and 8.5 Wm^{-2}. For a detailed analysis of projected extreme rainfall during the summer monsoon season across South Asian regions in the future, the study period is divided into three terms: the near-term (2015–2035), mid-term (2047–2067), and far-term (2079–2099). This study validates the projection of climatology, the 95th percentile, and the percentage contributions of extreme rainfall amounts during the summer monsoon season in future periods.

Climate models project both significant and insignificant increases in seasonal and extreme rainfalls for both monsoonal and non-monsoonal regions over the study area in the future, depending on the scenarios considered. The EC-Earth models forecast a 5 mm day^{-1} increase in seasonal rainfall for the west coast, southwestern regions of central India, and the western Himalayas. The NorESM model predicts significant changes in central India and rain shadow regions of southeast India. In all model projections of extreme rainfall, the increased change in the northern regions of the west coast and southwestern regions of central India could lead to heightened vulnerabilities in the area, especially in higher forcing scenarios. Moreover, the zone of extreme rainfall extends to the rain shadow regions behind the Western Ghats, resulting in a noticeable reduction in the area of rain shadow regions in the future, particularly in the SSP5-8.5 scenario. Additionally, the northwest semiarid regional extreme rainfall is projected to increase in the future. In the case of NorESM, the pronounced extreme area in central India

extends through the coastal region to the northeastern regions in the SSP5-8.5 scenario. The contribution of extreme rainfall to seasonal rainfall is observed to decrease more in northwestern semiarid India, southeast rain shadow regions, and Ladakh and Himachal Pradesh areas.

The projections for the selected future terms yield valuable insights. In the west coast region, no significant changes in extreme rainfall are projected in the near-term. However, a substantial increase in extreme rainfall is anticipated in the mid- and far-terms on the northern west coast, particularly under the SSP5-8.5 scenario. In the central Indian region, EC-Earth models predict intensified extreme rainfall along with an expansion in the extreme rainfall affected area, most notably in the far-term. Additionally, these changes are also notable in the NorESM model. In the western Himalayan region, a significant increase in extreme rainfall is projected by models in the near-term, especially in the SSP1-2.6 scenario. In contrast, no change in extreme rainfall is expected in the mid- and far-terms in the above region. The percentage contribution of extreme rainfall to the seasonal mean decreases slightly in monsoonal areas in all future terms, particularly in the SSP1-2.6 scenario.

CHAPTER 8

FUTURE SCOPE AND RECOMMENDATIONS

CHAPTER 8
FUTURE SCOPE AND RECOMMENDATIONS

The present study analysed the physical and dynamic characteristics of summer monsoon mean rainfall and extreme rainfall events (EREs) in the selected regions over the South Asian domain and verified the regional heterogeneity in the physical aspects and evolutional features of extreme rainfall events. Moreover, the study realised the complexity of the correlation between mean rainfall and regional extreme rainfall events with various climate-forcing mechanisms. Furthermore, the projection study on various shared socioeconomic pathways (SSPs) using coupled model intercomparison project phase 6 (CMIP6) global climate models revealed the probability of increased extreme rainfalls, especially on the Odisha region extending to the upper BoB coastal region, northern west coast area meeting with the southwestern portion of central India, southeastern rain shadow regions in the Indian peninsula and also on the western Himalayan regions in the future for various SSPs. This study can be extended to the following undermentioned areas, which may benefit the regional understanding of the monsoon extremes and can be used for potential mitigation strategies.

➤ The study analysed the spatiotemporal heterogeneous nature of monsoon seasonal rainfall and extremes across different regions of South Asia. This analysis can be extended by incorporating additional rainfall and climate data from various sources and by adjusting the criterion of extreme events. It will enhance the process of regional weather and climate analysis, offering valuable insights for forecasting and future predictions.

➤ The evolution and dissipation of dynamic parameters during extremes have significant impacts on global monsoons, weather prediction systems, mitigation efforts, and the maintenance of hydrological balance worldwide. The dynamical analysis can be further extended to regions beyond South Asia to comprehend other global monsoon domains.

➤ This research analysed the teleconnections between various global climate-forcing mechanisms and the mean rainfall, as well as extreme events over the South Asian region from 1951 to 2015. The study can be extended to analyse the recent changes in the teleconnection patterns of various forcing mechanisms on ISMR mean and extremes.

➢ The study independently analysed the evolution and dissipation features of various dynamical parameters during regional extremes. The clustering effect of synoptic features during extremes on a regional scale can be explored further to establish connections between the dynamical and thermodynamic features of extremes and their evolution over the region during EREs.

➢ This study utilised monthly rainfall data to project extreme events in the South Asian domain. Regional projection analysis, employing daily rainfall data from CMIP6 GCMs, can be done to obtain precise results regarding future climate variability over the region.

Bibliography

Adhikari, P., Hong, Y., Douglas, K.R., Kirschbaum, D.B., Gourley, J., Adler, R. and Robert Brakenridge, G., 2010. A digitized global flood inventory (1998–2008): compilation and preliminary results. *Natural Hazards*, *55*, pp.405-422. https://doi.org/10.1007/s11069-010-9537-2

Ajayamohan, R.S. and Rao, S.A., 2008. Indian Ocean dipole modulates the number of extreme rainfall events over India in a warming environment. Journal of the Meteorological Society of Japan. Ser. II, 86(1), 245-252. https://doi.org/10.2151/jmsj.86.245.

Almazroui, M., 2020. Changes in temperature trends and extremes over Saudi Arabia for the period 1978–2019. *Advances in Meteorology*, *2020*, pp.1-21. https://doi.org/10.1155/2020/8828421

Almazroui, M., 2020a. Rainfall trends and extremes in Saudi Arabia in recent decades. *Atmosphere*, *11*(9), p.964. https://doi.org/10.3390/atmos11090964

Almazroui, M., Saeed, F., Saeed, S., Ismail, M., Ehsan, M.A., Islam, M.N., Abid, M.A., O'Brien, E., Kamil, S., Rashid, I.U. and Nadeem, I., 2021. Projected changes in climate extremes using CMIP6 simulations over SREX regions. *Earth Systems and Environment*, *5*(3), pp.481-497. https://doi.org/10.1007/s41748-021-00250-5

Amarasinghe, U., Amarnath, G., Alahacoon, N. and Ghosh, S., 2020. How do floods and drought impact economic growth and human development at the sub-national level in India?. *Climate*, *8*(11), p.123. https://doi.org/10.3390/cli8110123

Andrijevic, M., Crespo Cuaresma, J., Muttarak, R. and Schleussner, C.F., 2020. Governance in socioeconomic pathways and its role for future adaptive capacity. *Nature Sustainability*, *3*(1), pp.35-41. https://doi.org/10.1038/s41893-019-0405-0

Annamalai, H. and Slingo, J.M., 2001. Active/break cycles: Diagnosis of the intraseasonal variability of the Asian summer monsoon. Climate Dynamics, 18(1), 85-102. https://doi.org/10.1007/s003820100161

Arora, K. and Dash, P., 2019. The Indian ocean dipole: a missing link between El Niño Modokiand tropical cyclone intensity in the North Indian ocean. *Climate*, *7*(3), p.38. https://doi.org/10.3390/cli7030038

Ashok, K. and Saji, N.H., 2007. On the impacts of ENSO and Indian Ocean dipole events onsub-regional Indian summer monsoon rainfall. Natural Hazards, 42(2), 273-285. https://doi.org/10.1007/s11069-006-9091-0.

Ashok, K. and Yamagata, T., 2009. The El Niño with a difference. Nature, 461(7263), 481-484. https://doi.org/10.1038/461481a.

Ashok, K., Behera, S.K., Rao, S.A., Weng, H. and Yamagata, T., 2007. El Niño Modoki and its possible teleconnection. Journal of Geophysical Research: Oceans, 112(C11). https://doi.org/10.1029/2006JC003798.

Ashok, K., Guan, Z. and Yamagata, T., 2001. Impact of the Indian Ocean dipole on the relationship between the Indian monsoon rainfall and ENSO. Geophysical Research Letters, 28(23), 4499-4502. https://doi.org/10.1029/2001GL013294.

Ashok, K., Guan, Z. and Yamagata, T., 2003. Influence of the Indian Ocean Dipole on the Australian winter rainfall. Geophysical Research Letters, 30(15). https://doi.org/10.1029/2003GL017926.

Badan-Dangon, A., Dorman, C.E., Merrifield, M.A. and Winant, C.D., 1991. The lower atmosphere over the Gulf of California. *Journal of Geophysical Research: Oceans*, *96*(C9), pp.16877-16896. https://doi.org/10.1029/91JC01433

Baidya, S.K., Shrestha, M.L. and Sheikh, M.M., 2008. Trends in daily climatic extremes of temperature and precipitation in Nepal. *Journal of Hydrology and Meteorology*, *5*(1), pp.38-51.

Banerjee, D. and Singh, C., 2022. An appraisal of seasonal precipitation dynamics over the North-West Himalayan region under future warming scenarios. *International Journal of Climatology*, *42*(4), pp.2328-2350. https://doi.org/10.1002/joc.7368

Bansod, S.D., Singh, S.V. and Kripalani, R.H., 1991. The relationship of monsoon onset with subsequent rainfall over India. *International journal of climatology*, *11*(7), pp.809-817. https://doi.org/10.1002/joc.3370110707

Barlow, M., Nigam, S. and Berbery, E.H., 1998. Evolution of the North American monsoon system. *Journal of Climate*, *11*(9), pp.2238-2257. https://doi.org/10.1175/1520-0442(1998)011<2238:EOTNAM>2.0.CO;2

Basu, B.K., 2007. Diurnal variation in precipitation over India during the summer monsoon season: Observed and model predicted. *Monthly weather review*, *135*(6), 2155-2167. https://doi.org/10.1175/MWR3355.1.

Beck, F., Bárdossy, A., Seidel, J., Müller, T., Sanchis, E.F. and Hauser, A., 2015. Statistical analysis of sub-daily precipitation extremes in Singapore. *Journal of Hydrology: Regional Studies*, *3*, pp.337-358. https://doi.org/10.1016/j.ejrh.2015.02.001

Behera, S. and Yamagata, T., 2010. Imprint of the El Niño Modoki on decadal sea level changes. *Geophysical Research Letters*, *37*(23). https://doi.org/10.1029/2010GL045936

Bhardwaj, A. and Misra, V., 2019. Monitoring the Indian summer monsoon evolution at the granularity of the Indian meteorological sub-divisions using remotely sensed rainfall products. Remote Sensing, 11(9), p.1080. https://doi.org/10.3390/rs11091080

Bhate, J. and Kesarkar, A., 2019. Sensitivity of diurnal cycle of simulated rainfall to cumulus parameterization during Indian summer monsoon seasons. *Climate Dynamics*, *53*(5-6), pp.3431-3444. https://doi.org/10.1007/s00382-019-04716-1

Bhatt, C.M., Rao, G.S., Farooq, M., Manjusree, P., Shukla, A., Sharma, S.V.S.P., Kulkarni, S.S., Begum, A., Bhanumurthy, V., Diwakar, P.G. and Dadhwal, V.K., 2017. Satellite-based assessment of the catastrophic Jhelum floods of September 2014, Jammu & Kashmir, India. *Geomatics, Natural Hazards and Risk*, *8*(2), pp.309-327. https://doi.org/10.1080/19475705.2016.1218943

Boers, N., Goswami, B., Rheinwalt, A., Bookhagen, B., Hoskins, B. and Kurths, J., 2019. Complex networks reveal global pattern of extreme-rainfall teleconnections. *Nature*, *566*(7744), pp.373-377. https://doi.org/10.1038/s41586-018-0872-x

Bollasina, M.A., Ming, Y. and Ramaswamy, V., 2011. Anthropogenic aerosols and the weakening of the South Asian summer monsoon. *science*, *334*(6055), pp.502-505. https://www.science.org/doi/abs/10.1126/science.1204994

Bond, N.A. and Vecchi, G.A., 2003. The influence of the Madden–Julian oscillation on precipitation in Oregon and Washington. *Weather and Forecasting*, *18*(4), pp.600-613. https://doi.org/10.1175/1520-0434(2003)018<0600:TIOTMO>2.0.CO;2

Bookhagen, B. and Burbank, D.W., 2006. Topography, relief, and TRMM-derived rainfall variations along the Himalaya. Geophysical Research Letters, 33(8). https://doi.org/10.1029/2006GL026037.

Bookhagen, B. and Burbank, D.W., 2010. Toward a complete Himalayan hydrological budget: Spatiotemporal distribution of snowmelt and rainfall and their impact on river discharge. Journal of Geophysical Research: Earth Surface, 115(F3). https://doi.org/10.1029/2009JF001426.

Bowman, D.M., Brown, G.K., Braby, M.F., Brown, J.R., Cook, L.G., Crisp, M.D., Ford, F., Haberle, S., Hughes, J., Isagi, Y. and Joseph, L., 2010. Biogeography of the Australian monsoon tropics. *Journal of Biogeography*, *37*(2), pp.201-216. https://doi.org/10.1111/j.1365-2699.2009.02210.x

Boyaj, A., Ashok, K., Ghosh, S., Devanand, A. and Dandu, G., 2018. The Chennai extreme rainfall event in 2015: The Bay of Bengal connection. *Climate Dynamics*, *50*, pp.2867-2879. https://doi.org/10.1007/s00382-017-3778-7

Camargo, S.J., Emanuel, K.A. and Sobel, A.H., 2007. Use of a genesis potential index to diagnose ENSO effects on tropical cyclone genesis. *Journal of Climate*, *20*(19), pp.4819-4834. https://doi.org/10.1175/JCLI4282.1

Chaluvadi, R., Varikoden, H., Mujumdar, M. and Ingle, S.T., 2021. Variability of West Pacific subtropical high and its potential importance to the Indian summer monsoon rainfall. International Journal of Climatology, 41(7), 4047-4060. https://doi.org/10.1002/joc.7057

Chandrasekar, A., 2010 (new edition 2022). *Basics of atmospheric science*. PHI Learning Pvt. Ltd.

Chang, C.P., 2004. *East asian monsoon* (Vol. 2). World Scientific.

Chang, M., Liu, B., Wang, B., Martinez-Villalobos, C., Ren, G. and Zhou, T., 2022. Understanding future increases in precipitation extremes in global land monsoon regions. *Journal of Climate*, *35*(6), pp.1839-1851. https://doi.org/10.1175/JCLI-D-21-0409.1

Change, I.P.O.C., 2007. Climate change 2007: The physical science basis. *Agenda*, *6*(07), p.333.

Charney, J. G., 1969: The intertropical convergence zone and the Hadley circulation of the Atmosphere. Proc. WMO/IUGG Intern. Symp. On Numer. Weather Predict. Jpn. Meteorol. Agency, III, pp. 73–79.

Chattopadhyay, R., Joseph, S., Abhilash, S., Mandal, R., Dey, A., Phani, R., Ganesh, S., Kaur, M., Pattanaik, D.R. and Sahai, A.K., 2019. Understanding the intraseasonal variability over Indian region and development of an operational extended range prediction system. *Mausam*, *70*(1), pp.31-56.

Chattopadhyay, R., Rao, S.A., Sabeerali, C.T., George, G., Rao, D.N., Dhakate, A. and Salunke, K., 2016. Large-scale teleconnection patterns of Indian summer monsoon as revealed by CFSv2 retrospective seasonal forecast runs. *International Journal of Climatology*, *36*(9), pp.3297-3313. https://doi.org/10.1002/joc.4556

Chen, H., Sun, J., Lin, W. and Xu, H., 2020. Comparison of CMIP6 and CMIP5 models in simulating climate extremes. *Sci. Bull*, *65*(17), pp.1415-1418.

Chen, L., Qu, X., Huang, G. and Gong, Y., 2019. Projections of East Asian summer monsoon under 1.5 C and 2 C warming goals. *Theoretical and Applied Climatology*, *137*, pp.2187-2201. https://doi.org/10.1007/s00704-018-2720-1

Chen, R., Duan, K., Shang, W., Shi, P., Meng, Y. and Zhang, Z., 2022. Increase in seasonal precipitation over the Tibetan Plateau in the 21st century projected using CMIP6 models. *Atmospheric Research*, *277*, p.106306. https://doi.org/10.1016/j.atmosres.2022.106306

Choudhury, B.A., Rajesh, P.V., Zahan, Y. and Goswami, B.N., 2021. Evolution of the Indian summer monsoon rainfall simulations from CMIP3 to CMIP6 models. *Climate Dynamics*, pp.1-26. https://doi.org/10.1007/s00382-021-06023-0

Chowdary, J.S., Saikrishna, T.S., Ramu, D.A., Darshana, P., Parekh, A., Gnanaseelan, C. and Osuri, K.K., 2023. Symmetric and asymmetric response of Indian summer monsoon rainfall to different ENSO decay phases in observations and CMIP6 models. *Global and Planetary Change*, *220*, p.104000. https://doi.org/10.1016/j.gloplacha.2022.104000

Christensen, J.H., Hewitson, B., Busuioc, A., Chen, A., Gao, X., Held, I., Jones, R., Kolli, R.K., Kwon, W.T., Laprise, R. and Magaña Rueda, V., 2007. Regional climate projections. Chapter 11. https://www.osti.gov/etdeweb/biblio/20962141

Chung, C.E. and Ramanathan, V., 2006. Weakening of North Indian SST gradients and the monsoon rainfall in India and the Sahel. *Journal of Climate*, *19*(10), pp.2036-2045. https://doi.org/10.1175/JCLI3820.1

Dandi, R.A., Chowdary, J.S., Pillai, P.A., Sidhan NS, S., K, K. and SSVS, R., 2020. Impact of El Niño Modoki on Indian summer monsoon rainfall: Role of western north Pacific circulation in observations and CMIP5 models. *International Journal of Climatology*, *40*(4), pp.2117-2133. https://doi.org/10.1002/joc.6322.

Darshana, P., Chowdary, J.S., Parekh, A. and Gnanaseelan, C., 2022. Relationship between the Indo-western Pacific Ocean capacitor mode and Indian summer monsoon rainfall in CMIP6 models. *Climate Dynamics*, *59*(1-2), pp.393-415. https://doi.org/10.1007/s00382-021-06133-9

Davidson, N.E., McBride, J.L. and McAvaney, B.J., 1983. The onset of the Australian monsoon during winter MONEX: Synoptic aspects. *Monthly Weather Review*, *111*(3), pp.496-516. https://doi.org/10.1175/1520-0493(1983)111<0496:TOOTAM>2.0.CO;2

Deng, K., Yang, S., Ting, M., Tan, Y. and He, S., 2018. Global monsoon precipitation: Trends, leading modes, and associated drought and heat wave in the Northern Hemisphere. *Journal of Climate*, *31*(17), pp.6947-6966. https://doi.org/10.1175/JCLI-D-17-0569.1

Deshpande, N.R. and Goswami, B.N., 2014. Modulation of the diurnal cycle of rainfall over India by intraseasonal variations of Indian summer monsoon. *International journal of climatology*, *34*(3), pp.793-807. https://doi.org/10.1002/joc.3719

Dey, A., Chattopadhyay, R., Joseph, S., Kaur, M., Mandal, R., Phani, R., Sahai, A.K. and Pattanaik, D.R., 2022. The intraseasonal fluctuation of Indian summer monsoon rainfall

and its relation with monsoon intraseasonal oscillation (MISO) and Madden Julian oscillation (MJO). *Theoretical and Applied Climatology*, *148*(1-2), pp.819-831. https://doi.org/10.1007/s00704-022-03970-4

Ding, Y., 2007. The variability of the Asian summer monsoon. *気象集誌. 第 2 輯*, *85*, pp.21-54. https://doi.org/10.2151/jmsj.85B.21

Döscher, R., Acosta, M., Alessandri, A., Anthoni, P., Arneth, A., Arsouze, T., Bergmann, T., Bernadello, R., Bousetta, S., Caron, L.P. and Carver, G., 2021. The EC-earth3 Earth system model for the climate model intercomparison project 6. *Geoscientific Model Development Discussions*, *2021*, pp.1-90. https://doi.org/10.5194/gmd-15-2973-2022

Drosdowsky, W., 1996. Variability of the Australian summer monsoon at Darwin: 1957–1992. *Journal of Climate*, *9*(1), pp.85-96. https://doi.org/10.1175/1520-0442(1996)009<0085:VOTASM>2.0.CO;2

Dutta, U., Hazra, A., Chaudhari, H.S., Saha, S.K., Pokhrel, S. and Verma, U., 2022. Unraveling the global teleconnections of Indian summer monsoon clouds: expedition from CMIP5 to CMIP6. *Global and Planetary Change*, *215*, p.103873. https://doi.org/10.1016/j.gloplacha.2022.103873

Dwivedi, S., Pandey, P. and Goswami, B.N., 2022. Nonstationarity and potential multi-decadal variability in Indian Summer Monsoon Rainfall and Southern Annular Mode teleconnection. *Climate Dynamics*, *59*(3-4), pp.671-683. https://doi.org/10.1007/s00382-022-06146-y

Enfield, D.B., Mestas-Nuñez, A.M. and Trimble, P.J., 2001. The Atlantic multidecadal oscillation and its relation to rainfall and river flows in the continental US. *Geophysical research letters*, *28*(10), pp.2077-2080. https://doi.org/10.1029/2000GL012745

Eyring, V., Bony, S., Meehl, G.A., Senior, C.A., Stevens, B., Stouffer, R.J. and Taylor, K.E., 2016. Overview of the Coupled Model Intercomparison Project Phase 6 (CMIP6) experimental design and organization. *Geoscientific Model Development*, *9*(5), pp.1937-1958. https://doi.org/10.5194/gmd-9-1937-2016

Fan, L. and Chen, D., 2016. Trends in extreme precipitation indices across China detected using quantile regression. *Atmospheric Science Letters*, *17*(7), pp.400-406. https://doi.org/10.1002/asl.671

Fasullo, J. and Webster, P.J., 2003. A hydrological definition of Indian monsoon onset and withdrawal. *Journal of Climate*, *16*(19), pp.3200-3211. https://doi.org/10.1175/1520-0442(2003)016<3200a:AHDOIM>2.0.CO;2

Fazal, A.M., Varikoden, H. and Reji, M.J.K., 2023. Long term trends and variabilities of rainfall of the global monsoon systems during boreal and austral summer seasons. *Global and Planetary Change*, *229*, p.104251. https://doi.org/10.1016/j.gloplacha.2023.104251

Findlater, J., 1971. Mean monthly airflow at low levels over the western Indian Ocean. HM Stationery Office.

Fischer, E.M. and Knutti, R., 2016. Observed heavy precipitation increase confirms theory and early models. *Nature Climate Change*, *6*(11), pp.986-991. https://doi.org/10.1038/nclimate3110

Fletcher, J.K., Parker, D.J., Turner, A.G., Menon, A., Martin, G.M., Birch, C.E., Mitra, A.K., Mrudula, G., Hunt, K.M., Taylor, C.M. and Houze, R.A., 2020. The dynamic and thermodynamic structure of the monsoon over southern India: New observations from the INCOMPASS IOP. *Quarterly Journal of the Royal Meteorological Society*, *146*(731), pp.2867-2890. https://doi.org/10.1002/qj.3439

Folland, C.K., Parker, D.E. and Kates, F.E., 1984. Worldwide marine temperature fluctuations 1856–1981. *Nature*, *310*(5979), pp.670-673. https://doi.org/10.1038/310670a0

Fowler, H.J., Lenderink, G., Prein, A.F., Westra, S., Allan, R.P., Ban, N., Barbero, R., Berg, P., Blenkinsop, S., Do, H.X. and Guerreiro, S., 2021. Anthropogenic intensification of short-duration rainfall extremes. *Nature Reviews Earth & Environment*, *2*(2), pp.107-122. https://doi.org/10.1038/s43017-020-00128-6

Fujinami, H., Sato, T., Kanamori, H. and Murata, F., 2017. Contrasting features of monsoon precipitation around the Meghalaya Plateau under westerly and easterly regimes. Journal of Geophysical Research: Atmospheres, 122(18), 9591-9610. https://doi.org/10.1002/2016JD026116

Gadgil, S. and Gadgil, S., 2006. The Indian monsoon, GDP and agriculture. Economic and political weekly, 4887-4895. https://www.jstor.org/stable/4418949.

Gadgil, S., 2003. The Indian monsoon and its variability. Annual Review of Earth and Planetary Sciences, 31(1), 429-467. https://doi.org/10.1146/annurev.earth.31.100901.141251

Gadgil, S., 2006. The Indian monsoon: 1. Variations in space and time. *Resonance*, *11*, pp.8-21. https://doi.org/10.1007/BF02855775

Gadgil, S., 2007. The Indian monsoon: 3. Physics of the monsoon. *Resonance*, *12*, pp.4-20. https://doi.org/10.1007/s12045-007-0045-y

Gadgil, S., Vinayachandran, P.N., Francis, P.A. and Gadgil, S., 2004. Extremes of the Indian summer monsoon rainfall, ENSO and equatorial Indian Ocean oscillation. *Geophysical Research Letters*, *31*(12). https://doi.org/10.1029/2004GL019733

Gautam, R., Hsu, N.C., Lau, K.M. and Kafatos, M., 2009, September. Aerosol and rainfall variability over the Indian monsoon region: distributions, trends and coupling. In *Annales Geophysicae* (Vol. 27, No. 9, pp. 3691-3703). Göttingen, Germany: Copernicus Publications. https://doi.org/10.5194/angeo-27-3691-2009

Geen, R., Bordoni, S., Battisti, D.S. and Hui, K., 2020. Monsoons, ITCZs, and the concept of the global monsoon. *Reviews of Geophysics*, *58*(4), p.e2020RG000700. https://doi.org/10.1029/2020RG000700

Ghosh, S., Das, D., Kao, S.C. and Ganguly, A.R., 2012. Lack of uniform trends but increasing spatial variability in observed Indian rainfall extremes. *Nature Climate Change*, *2*(2), pp.86-91. https://doi.org/10.1038/nclimate1327

Ghosh, S., Luniya, V. and Gupta, A., 2009. Trend analysis of Indian summer monsoon rainfall at different spatial scales. Atmospheric science letters, 10(4), 285-290. https://doi.org/10.1002/asl.235.

Ghosh, S., Vittal, H., Sharma, T., Karmakar, S., Kasiviswanathan, K.S., Dhanesh, Y., Sudheer, K.P. and Gunthe, S.S., 2016. Indian summer monsoon rainfall: implications of

contrasting trends in the spatial variability of means and extremes. PLoS One, 11(7), p.e0158670. https://doi.org/10.1371/journal.pone.0158670.

Ghosh, S.K., Pant, M.C. and Dewan, B.N., 1978. Influence of the Arabian Sea on the Indian summer monsoon. Tellus, 30(2), 117-125. https://doi.org/10.3402/tellusa.v30i2.10324

Gimeno, L., Dominguez, F., Nieto, R., Trigo, R., Drumond, A., Reason, C.J., Taschetto, A.S., Ramos, A.M., Kumar, R. and Marengo, J., 2016. Major mechanisms of atmospheric moisture transport and their role in extreme precipitation events. Annual Review of Environment and Resources, 41, 117-141. https://doi.org/10.1146/annurev-environ-110615-085558

Giorgi, F., Raffaele, F. and Coppola, E., 2019. The response of precipitation characteristics to global warming from climate projections. *Earth System Dynamics*, *10*(1), pp.73-89. https://doi.org/10.5194/esd-10-73-2019

Goswami, B. B., Murtugudde, R. and An, S. I. 2022, Role of the Bay of Bengal warming in the Indian summer monsoon rainfall trend. Climate *Dynamics,* 59, 1733–1751. https://doi.org/10.1007/s00382-021-06068-1

Goswami, B.B., Mukhopadhyay, P., Khairoutdinov, M. and Goswami, B.N., 2013. Simulation of Indian summer monsoon intraseasonal oscillations in a superparameterized coupled climate model: Need to improve the embedded cloud resolving model. *Climate dynamics*, *41*, pp.1497-1507. https://doi.org/10.1007/s00382-012-1563-1

Goswami, B.N. and Mohan, R.A., 2001. Intraseasonal oscillations and interannual variability of the Indian summer monsoon. *Journal of Climate*, *14*(6), pp.1180-1198. https://doi.org/10.1175/1520-0442(2001)014<1180:IOAIVO>2.0.CO;2

Goswami, B.N. and Xavier, P.K., 2005. Dynamics of "internal" interannual variability of the Indian summer monsoon in a GCM. *Journal of Geophysical Research: Atmospheres*, *110*(D24). https://doi.org/10.1029/2005JD006042

Goswami, B.N., 1998. Interannual variations of Indian summer monsoon in a GCM: External conditions versus internal feedbacks. *Journal of Climate*, *11*(4), pp.501-522. https://doi.org/10.1175/1520-0442(1998)011<0501:IVOISM>2.0.CO;2

Goswami, B.N., 2005. The Asian monsoon: interdecadal variability. *The Global Monsoon System: Research and Forecast*, *1266*, pp.455-471.

Goswami, B.N., Ajayamohan, R.S., Xavier, P.K. and Sengupta, D., 2003. Clustering of synoptic activity by Indian summer monsoon intraseasonal oscillations. Geophysical Research Letters, 30(8). https://doi.org/10.1029/2002GL016734

Goswami, B.N., Keshavamurty, R.N. and Satyan, V., 1980. Role of barotropic, baroclinic and combined barotropic-baroclinic instability for the growth of monsoon depressions and mid-tropospheric cyclones. *Proceedings of the Indian Academy of Sciences-Earth and Planetary Sciences*, *89*, pp.79-97. https://doi.org/10.1007/BF02841521

Goswami, B.N., Kripalani, R.H., Borgaonkar, H.P. and Preethi, B., 2016. Multi-decadal variability in Indian summer monsoon rainfall using proxy data. In *Climate change: multidecadal and beyond* (pp. 327-345). https://doi.org/10.1142/9789814579933_0021

Goswami, B.N., Venugopal, V. and Chattopadhyay, R., 2019. South Asian monsoon extremes. In *Tropical Extremes* (15-49). Elsevier. https://doi.org/10.1016/B978-0-12-809248-4.00002-9.

Goswami, B.N., Venugopal, V., Sengupta, D., Madhusoodanan, M.S. and Xavier, P.K., 2006. Increasing trend of extreme rain events over India in a warming environment. Science, 314(5804), 1442-1445. https://doi.org/10.1126/science.1132027.

Gupta, V., Singh, V. and Jain, M.K., 2020. Assessment of precipitation extremes in India during the 21st century under SSP1-1.9 mitigation scenarios of CMIP6 GCMs. *Journal of Hydrology*, *590*, p.125422. https://doi.org/10.1016/j.jhydrol.2020.125422

Gusain, A., Ghosh, S. and Karmakar, S., 2020. Added value of CMIP6 over CMIP5 models in simulating Indian summer monsoon rainfall. *Atmospheric Research*, *232*, p.104680. https://doi.org/10.1016/j.atmosres.2019.104680

Hamed, K.H. and Rao, A.R., 1998. A modified Mann-Kendall trend test for autocorrelated data. *Journal of hydrology*, *204*(1-4), pp.182-196. https://doi.org/10.1016/S0022-1694(97)00125-X

Harris, I., Osborn, T.J., Jones, P. and Lister, D., 2020. Version 4 of the CRU TS monthly high-resolution gridded multivariate climate dataset. *Scientific data*, *7*(1), p.109. https://doi.org/10.1038/s41597-020-0453-3

Hastenrath, S., 1991 (new edition 2012). *Climate dynamics of the tropics* (Vol. 8). Springer Science & Business Media.

He, L., Zhou, T. and Chen, X., 2023. South Asian summer rainfall from CMIP3 to CMIP6 models: biases and improvements. *Climate Dynamics*, *61*(3-4), pp.1049-1061. https://doi.org/10.1007/s00382-022-06542-4

Hendon, H.H. and Liebmann, B., 1990. A composite study of onset of the Australian summer monsoon. *Journal of Atmospheric Sciences*, *47*(18), pp.2227-2240. https://doi.org/10.1175/1520-0469(1990)047<2227:ACSOOO>2.0.CO;2

Hendon, H.H. and Liebmann, B., 1990a. The intraseasonal (30–50 day) oscillation of the Australian summer monsoon. *Journal of Atmospheric Sciences*, *47*(24), pp.2909-2924. https://doi.org/10.1175/1520-0469(1990)047<2909:TIDOOT>2.0.CO;2

Higgins RW, Yao Y, Wang XL. Influence of the North American monsoon system on the US summer precipitation regime. Journal of climate. 1997 Oct;10(10):2600-22. https://doi.org/10.1175/1520-0442(1997)010<2600:IOTNAM>2.0.CO;2

Hirschboeck, K.K., 1991. Climate and floods. US Geol. Surv. Water-Supply Pap, 2375, 67-88.

Hong, C.C., Hsu, H.H., Lin, N.H. and Chiu, H., 2011. Roles of European blocking and tropical-extratropical interaction in the 2010 Pakistan flooding. *Geophysical Research Letters*, *38*(13). https://doi.org/10.1029/2011GL047583

Hoskins, B.J. and Rodwell, M.J., 1995. A model of the Asian summer monsoon. Part I: The global scale. Journal of Atmospheric Sciences, 52(9), 1329-1340. https://doi.org/10.1175/1520-0469(1995)052<1329:AMOTAS>2.0.CO;2

Hrudya, P.H., Varikoden, H. and Vishnu, R., 2020. A review on the Indian summer monsoon rainfall, variability and its association with ENSO and IOD. Meteorology and Atmospheric Physics, 1-14. https://doi.org/10.1007/s00703-020-00734-5.

Hrudya, P.H., Varikoden, H. and Vishnu, R., 2021. A review on the Indian summer monsoon rainfall, variability and its association with ENSO and IOD. *Meteorology and Atmospheric Physics*, *133*, pp.1-14. https://doi.org/10.1007/s00703-020-00734-5

Hrudya, P.H., Varikoden, H., Vishnu, R. and Kuttippurath, J., 2020. Changes in ENSO-monsoon relations from early to recent decades during onset, peak and withdrawal phases of Indian summer monsoon. Climate Dynamics, 55(5), 1457-1471. https://doi.org/10.1007/s00382-020-05335-x.

Hsu, P.C., 2016. Global monsoon in a changing climate. *The Monsoons and Climate Change: Observations and Modeling*, pp.7-24. https://doi.org/10.1007/978-3-319-21650-8_2

Hu, C., Zhang, C., Yang, S., Chen, D. and He, S., 2018. Perspective on the northwestward shift of autumn tropical cyclogenesis locations over the western North Pacific from shifting ENSO. *Climate Dynamics*, *51*, pp.2455-2465. https://doi.org/10.1007/s00382-017-4022-1

Hu, P., Chen, W., Wang, L., Chen, S., Liu, Y. and Chen, L., 2022. Revisiting the ENSO–monsoonal rainfall relationship: new insights based on an objective determination of the Asian summer monsoon duration. *Environmental Research Letters*, *17*(10), p.104050. doi 10.1088/1748-9326/ac97ad

Huang, J., Mondal, S.K., Zhai, J., Fischer, T., Wang, Y., Su, B., Wang, G., Gao, M., Jiang, S., Tao, H. and Lin, Q., 2022. Intensity-area-duration-based drought analysis under 1.5 C–4.0 C warming using CMIP6 over a climate hotspot in South Asia. *Journal of Cleaner Production*, *345*, p.131106. https://doi.org/10.1016/j.jclepro.2022.131106

Huang, P., Xie, S.P., Hu, K., Huang, G. and Huang, R., 2013. Patterns of the seasonal response of tropical rainfall to global warming. *Nature Geoscience*, *6*(5), pp.357-361. https://doi.org/10.1038/ngeo1792

Ikram, F., Afzaal, M., Bukhari, S.A.A. and Ahmed, B., 2016. Past and future trends in frequency of heavy rainfall events over Pakistan. *Pakistan Journal of Meteorology Vol*, *12*(24).

IPCC (2013). *Summary for Policymakers Climate Change 2013: The Physical Science Basis. Contribution of Working Group I to the Fifth Assessment Report of the Intergovernmental Panel on Climate Change*. Cambridge: Cambridge University Press.

Izumo, T., Montégut, C.B., Luo, J.J., Behera, S.K., Masson, S. and Yamagata, T., 2008. The role of the western Arabian Sea upwelling in Indian monsoon rainfall variability. Journal of Climate, 21(21), 5603-5623. https://doi.org/10.1175/2008JCLI2158.1

Jamshadali, V.H., Reji, M.J.K., Varikoden, H. and Vishnu, R., 2021. Spatial variability of south Asian summer monsoon extreme rainfall events and their association with global climate indices. Journal of Atmospheric and Solar-Terrestrial Physics, 221, p.105708. https://doi.org/10.1016/j.jastp.2021.105708

Janicot, S., Mounier, F., Hall, N.M., Leroux, S., Sultan, B. and Kiladis, G.N., 2009. Dynamics of the West African monsoon. Part IV: Analysis of 25–90-day variability of convection and the role of the Indian monsoon. *Journal of Climate*, *22*(6), pp.1541-1565. https://doi.org/10.1175/2008JCLI2314.1

Jena, P., Azad, S. and Rajeevan, M.N., 2016. CMIP5 projected changes in the annual cycle of Indian monsoon rainfall. *Climate*, *4*(1), p.14. https://doi.org/10.3390/cli4010014

Joseph, P.V. and Sijikumar, S., 2004. Intraseasonal variability of the low-level jet stream of the Asian summer monsoon. Journal of Climate, 17(7), 1449-1458. https://doi.org/10.1175/1520-0442(2004)017<1449:IVOTLJ>2.0.CO;2

Joseph, S., Sahai, A.K. and Goswami, B.N., 2009. Eastward propagating MJO during boreal summer and Indian monsoon droughts. *Climate dynamics*, *32*, pp.1139-1153. https://doi.org/10.1007/s00382-008-0412-8

Joseph, S., Sahai, A.K., Chattopadhyay, R. and Goswami, B.N., 2011. Can El Niño–Southern Oscillation (ENSO) events modulate intraseasonal oscillations of Indian summer monsoon?. *Journal of Geophysical Research: Atmospheres*, *116*(D20). https://doi.org/10.1029/2010JD015510

Joseph, S., Sahai, A.K., Sharmila, S., Abhilash, S., Borah, N., Chattopadhyay, R., Pillai, P.A., Rajeevan, M. and Kumar, A., 2015. North Indian heavy rainfall event during June 2013:

diagnostics and extended range prediction. Climate Dynamics, 44(7), 2049-2065. https://doi.org/10.1007/s00382-014-2291-5

Joshi, M.K. and Pandey, A.C., 2011. Trend and spectral analysis of rainfall over India during 1901–2000. Journal of Geophysical Research: Atmospheres, 116(D6). https://doi.org/10.1029/2010JD014966.

Ju, J. and Slingo, J., 1995. The Asian summer monsoon and ENSO. *Quarterly Journal of the Royal Meteorological Society*, *121*(525), pp.1133-1168. https://doi.org/10.1002/qj.49712152509

Kale, V.S., Ely, L.L., Enzel, Y. and Baker, V.R., 1994. Geomorphic and hydrologic aspects of monsoon floods on the Narmada and Tapi Rivers in central India. In Geomorphology and natural hazards (pp. 157-168). Elsevier. https://doi.org/10.1016/B978-0-444-82012-9.50015-3

Kalnay, E., Kanamitsu, M., Kistler, R., Collins, W., Deaven, D., Gandin, L., Iredell, M., Saha, S., White, G., Woollen, J. and Zhu, Y., 1996. The NCEP/NCAR 40-year reanalysis project. Bulletin of the American meteorological Society, 77(3), 437-472. https://doi.org/10.1175/1520-0477(1996)077<0437:TNYRP>2.0.CO;2

Kapnick, S.B., Delworth, T.L., Ashfaq, M., Malyshev, S. and Milly, P.C., 2014. Snowfall less sensitive to warming in Karakoram than in Himalayas due to a unique seasonal cycle. NatureGeoscience, 7(11), 834-840. https://doi.org/10.1038/ngeo2269.

Karuna Sagar, S., Rajeevan, M. and Vijaya Bhaskara Rao, S., 2017. On increasing monsoon rainstorms over India. *Natural Hazards*, *85*, pp.1743-1757. https://doi.org/10.1007/s11069-016-2662-9

Katzenberger, A., Schewe, J., Pongratz, J. and Levermann, A., 2021. Robust increase of Indian monsoon rainfall and its variability under future warming in CMIP6 models. *Earth System Dynamics*, *12*(2), pp.367-386. https://doi.org/10.5194/esd-12-367-2021

Kayano, M.T., Capistrano, V.B., Andreoli, R.V. and de Souza, R.A., 2016. A further analysis of the tropical Atlantic SST modes and their relations to north-eastern Brazil rainfall during different phases of Atlantic Multidecadal Oscillation. *International Journal of Climatology*, *36*(12), pp.4006-4018. https://doi.org/10.1002/joc.4610

Kendall, M.G., 1975. Rank Correlation Methods. Griffin, London.

Khadka, D., Babel, M.S., Abatan, A.A. and Collins, M., 2022. An evaluation of CMIP5 and CMIP6 climate models in simulating summer rainfall in the Southeast Asian monsoon domain. *International Journal of Climatology*, *42*(2), pp.1181-1202. https://doi.org/10.1002/joc.7296

Kharol, S.K., Kaskaoutis, D.G., Sharma, A.R. and Singh, R.P., 2013. Long-term (1951–2007) rainfall trends around six Indian cities: current state, meteorological, and urban dynamics. *Advances in Meteorology*, *2013*. https://doi.org/10.1155/2013/572954

Kim, J.S., Yoon, S.K., Oh, S.M. and Chen, H., 2021. Seasonal precipitation variability and non-stationarity based on the evolution pattern of the Indian Ocean Dipole over the East Asia region. *Remote Sensing*, *13*(9), p.1806. https://doi.org/10.3390/rs13091806

Kiranmayi, L. and Maloney, E.D., 2011. Intraseasonal moist static energy budget in reanalysis data. Journal of Geophysical Research: Atmospheres, 116(D21). https://doi.org/10.1029/2011JD016031

Kistler, R., Kalnay, E., Collins, W., Saha, S., White, G., Woollen, J., Chelliah, M., Ebisuzaki, W., Kanamitsu, M., Kousky, V. and van den Dool, H., 2001. The NCEP–NCAR 50-year reanalysis: monthly means CD-ROM and documentation. *Bulletin of the American Meteorological society*, *82*(2), pp.247-268. https://www.jstor.org/stable/26215517

Klutse, N.A.B., Quagraine, K.A., Nkrumah, F., Quagraine, K.T., Berkoh-Oforiwaa, R., Dzrobi, J.F. and Sylla, M.B., 2021. The climatic analysis of summer monsoon extreme precipitation events over West Africa in CMIP6 simulations. *Earth Systems and Environment*, *5*, pp.25-41. https://doi.org/10.1007/s41748-021-00203-y

Knight, J.R., 2009. The Atlantic multidecadal oscillation inferred from the forced climate response in coupled general circulation models. *Journal of Climate*, *22*(7), pp.1610-1625. https://doi.org/10.1175/2008JCLI2628.1

Knight, J.R., Allan, R.J., Folland, C.K., Vellinga, M. and Mann, M.E., 2005. A signature of persistent natural thermohaline circulation cycles in observed climate. *Geophysical Research Letters*, *32*(20). https://doi.org/10.1016/j.neuroimage.2005.03.020

Knight, J.R., Folland, C.K. and Scaife, A.A., 2006. Climate impacts of the Atlantic multidecadal oscillation. *Geophysical Research Letters*, *33*(17). https://doi.org/10.1029/2006GL026242

Kohonen, T., 1990. The self-organizing map. *Proceedings of the IEEE*, *78*(9), pp.1464-1480. doi: 10.1109/5.58325

Kotal, S.D., Roy, S.S. and Bhowmik, S.R., 2014. Catastrophic heavy rainfall episode over Uttarakhand during 16–18 June 2013–observational aspects. *Current Science*, pp.234-245. https://www.jstor.org/stable/24103132

Kripalani, R.H., Kulkarni, A. and Singh, S.V., 1997. Association of the Indian summer monsoon with the Northern Hemisphere mid-latitude circulation. *International Journal of Climatology: A Journal of the Royal Meteorological Society*, *17*(10), pp.1055-1067. https://doi.org/10.1002/(SICI)1097-0088(199708)17:10<1055::AID-JOC180>3.0.CO;2-3

Kripalani, R.H., Kulkarni, A., Inamdar, S.R. and Prasad, K.D., 1999. Teleconnections: Northern hemisphere lower stratospheric geopotential heights and Indian monsoon rainfall. *Meteorology and Atmospheric Physics*, *69*, pp.195-203. https://doi.org/10.1007/BF01030421

Kripalani, R.H., Oh, J.H., Kulkarni, A., Sabade, S.S. and Chaudhari, H.S., 2007. South Asian summer monsoon precipitation variability: coupled climate model simulations and projections under IPCC AR4. *Theoretical and Applied Climatology*, *90*, pp.133-159. https://doi.org/10.1007/s00704-006-0282-0

Krishnamurthy, C.K.B., Lall, U. and Kwon, H.H., 2009. Changing frequency and intensity of rainfall extremes over India from 1951 to 2003. *Journal of Climate*, *22*(18), pp.4737-4746. https://doi.org/10.1175/2009JCLI2896.1

Krishnamurthy, L. and Krishnamurthy, V., 2016. Teleconnections of Indian monsoon rainfall with AMO and Atlantic tripole. Climate dynamics, 46(7-8), 2269-2285. https://doi.org/10.1007/s00382-015-2701-3.

Krishnamurthy, L. and Krishnamurthy, V.J.C.D., 2014. Influence of PDO on South Asian summer monsoon and monsoon–ENSO relation. *Climate Dynamics*, *42*, pp.2397-2410. https://doi.org/10.1007/s00382-013-1856-z

Krishnamurthy, V. and Goswami, B.N., 2000. Indian monsoon–ENSO relationship on interdecadal timescale. Journal of climate, 13(3), 579-595. https://doi.org/10.1175/1520-0442(2000)013<0579:IMEROI>2.0.CO;2.

Krishnamurthy, V. and Shukla, J., 2000. Intraseasonal and interannual variability of rainfall over India. Journal of climate, 13(24), 4366-4377. https://doi.org/10.1175/1520-0442(2000)013<0001:IAIVOR>2.0.CO;2

Krishnamurti, T.N., Ardanuy, P., Ramanathan, Y. and Pasch, R., 1981. On the onset vortex of the summer monsoon. *Monthly Weather Review*, *109*(2), pp.344-363. https://doi.org/10.1175/1520-0493(1981)109<0344:OTOVOT>2.0.CO;2

Krishnamurti, T.N., Jana, S., Krishnamurti, R., Kumar, V., Deepa, R., Papa, F., Bourassa, M.A. and Ali, M.M., 2017. Monsoonal intraseasonal oscillations in the ocean heat content over the surface layers of the Bay of Bengal. *Journal of Marine Systems*, *167*, pp.19-32. https://doi.org/10.1016/j.jmarsys.2016.11.002

Krishnan, R. and Sugi, M., 2003. Pacific decadal oscillation and variability of the Indian summer monsoon rainfall. *Climate Dynamics*, *21*, pp.233-242. https://doi.org/10.1007/s00382-003-0330-8

Krishnan, R., Sabin, T.P., Ayantika, D.C., Kitoh, A., Sugi, M., Murakami, H., Turner, A.G., Slingo, J.M. and Rajendran, K., 2013. Will the South Asian monsoon overturning circulation stabilize any further?. *Climate dynamics*, *40*, pp.187-211. https://doi.org/10.1007/s00382-012-1317-0

Krishnan, R., Sabin, T.P., Vellore, R., Mujumdar, M., Sanjay, J., Goswami, B.N., Hourdin, F., Dufresne, J.L. and Terray, P., 2016. Deciphering the desiccation trend of the South Asian monsoon hydroclimate in a warming world. *Climate dynamics*, *47*, pp.1007-1027. https://doi.org/10.1007/s00382-015-2886-5

Krishnan, R., Zhang, C. and Sugi, M., 2000. Dynamics of breaks in the Indian summer monsoon. Journal of the atmospheric sciences, 57(9), 1354-1372. https://doi.org/10.1175/1520-0469(2000)057<1354:DOBITI>2.0.CO;2

Krishnaswamy, J., Vaidyanathan, S., Rajagopalan, B., Bonell, M., Sankaran, M., Bhalla, R.S. and Badiger, S., 2015. Non-stationary and non-linear influence of ENSO and Indian Ocean Dipole on the variability of Indian monsoon rainfall and extreme rain events. *Climate Dynamics*, *45*, pp.175-184. https://doi.org/10.1007/s00382-014-2288-0

Kucharski, F., Bracco, A., Yoo, J.H. and Molteni, F., 2008. Atlantic forced component of the Indian monsoon interannual variability. Geophysical Research Letters, 35(4). https://doi.org/10.1029/2007GL033037.

Kug, J.S., Jin, F.F. and An, S.I., 2009. Two types of El Niño events: cold tongue El Niño and warm pool El Niño. Journal of Climate, 22(6), 1499-1515. https://doi.org/10.1175/2008JCLI2624.1.

Kumar, A., Dudhia, J., Rotunno, R., Niyogi, D. and Mohanty, U.C., 2008. Analysis of the 26 July 2005 heavy rain event over Mumbai, India using the Weather Research and Forecasting (WRF) model. *Quarterly Journal of the Royal Meteorological Society*, *134*(636), pp.1897-1910. https://doi.org/10.1002/qj.325

Kumar, K.K., Rajagopalan, B. and Cane, M.A., 1999. On the weakening relationship between the Indian monsoon and ENSO. Science, 284(5423), 2156-2159. https://doi.org/10.1126/science.284.5423.2156.

Kumar, K.N., Rajeevan, M., Pai, D.S., Srivastava, A.K. and Preethi, B., 2013. On the observed variability of monsoon droughts over India. *Weather and Climate Extremes*, *1*, pp.42-50. https://doi.org/10.1016/j.wace.2013.07.006

Kumar, P. and Sarthi, P.P., 2021. Intraseasonal variability of Indian Summer Monsoon Rainfall in CMIP6 models simulation. *Theoretical and Applied Climatology*, *145*(1-2), pp.687-702. https://doi.org/10.1007/s00704-021-03661-6

Kumar, S., Hazra, A. and Goswami, B.N., 2014. Role of interaction between dynamics, thermodynamics and cloud microphysics on summer monsoon precipitating clouds over

the Myanmar Coast and the Western Ghats. Climate dynamics, 43(3), 911-924. https://doi.org/10.1007/s00382-013-1909-3

Kumar, V., Jain, S.K. and Singh, Y., 2010. Analysis of long-term rainfall trends in India. *Hydrological Sciences Journal–Journal des Sciences Hydrologiques*, *55*(4), pp.484-496. https://doi.org/10.1080/02626667.2010.481373

Kuttippurath, J., Murasingh, S., Stott, P.A., Sarojini, B.B., Jha, M.K., Kumar, P., Nair, P.J., Varikoden, H., Raj, S., Francis, P.A. and Pandey, P.C., 2021. Observed rainfall changes in the past century (1901–2019) over the wettest place on the Earth. Environmental Research Letters. https://doi.org/10.1088/1748-9326/abcf78.

Kutzbach, J.E. and Liu, Z., 1997. Response of the African monsoon to orbital forcing and ocean.

Lakshmi, D.D., Satyanarayana, A.N.V. and Chakraborty, A., 2019. Assessment of heavy precipitation events associated with floods due to strong moisture transport during summer monsoon over India. Journal of Atmospheric and Solar-Terrestrial Physics, 189, 123-140. https://doi.org/10.1016/j.jastp.2019.04.013

Lau, W.K.M., Waliser, D.E., Lau, W.K., Waliser, D.E. and Goswami, B.N., 2012. *South asian monsoon* (pp. 21-72). Springer Berlin Heidelberg.

Lawrence, D.M. and Webster, P.J., 2001. Interannual variations of the intraseasonal oscillation in the South Asian summer monsoon region. Journal of Climate, 14(13), 2910-2922. https://doi.org/10.1175/1520-0442(2001)014<2910:IVOTIO>2.0.CO;2

Lawrence, D.M. and Webster, P.J., 2002. The boreal summer intraseasonal oscillation: Relationship between northward and eastward movement of convection. *Journal of the atmospheric sciences*, *59*(9), pp.1593-1606. https://doi.org/10.1175/1520-0469(2002)059<1593:TBSIOR>2.0.CO;2

Levine, R.C. and Turner, A.G., 2012. Dependence of Indian monsoon rainfall on moisture fluxes across the Arabian Sea and the impact of coupled model sea surface temperature biases. Climate Dynamics, 38(11), 2167-2190. https://doi.org/10.1007/s00382-011-1096-z

Levine, R.C., Turner, A.G., Marathayil, D. and Martin, G.M., 2013. The role of northern Arabian Sea surface temperature biases in CMIP5 model simulations and future projections of Indian summer monsoon rainfall. *Climate Dynamics*, *41*, pp.155-172. https://doi.org/10.1007/s00382-012-1656-x

Li, C., Zwiers, F., Zhang, X., Li, G., Sun, Y. and Wehner, M., 2021. Changes in annual extremes of daily temperature and precipitation in CMIP6 models. *Journal of Climate*, *34*(9), pp.3441-3460. https://doi.org/10.1175/JCLI-D-19-1013.1

Li, G., Xie, S.P., He, C. and Chen, Z., 2017. Western Pacific emergent constraint lowers projected increase in Indian summer monsoon rainfall. *Nature Climate Change*, *7*(10), pp.708-712. https://doi.org/10.1038/nclimate3387

Li, J., Huo, R., Chen, H., Zhao, Y. and Zhao, T., 2021. Comparative assessment and future prediction using CMIP6 and CMIP5 for annual precipitation and extreme precipitation simulation. *Frontiers in Earth Science*, *9*, p.687976. https://doi.org/10.3389/feart.2021.687976

Li, X., Zhou, Y., Eom, J., Yu, S. and Asrar, G.R., 2019. Projecting global urban area growth through 2100 based on historical time series data and future shared socioeconomic pathways. *Earth's Future*, *7*(4), pp.351-362. https://doi.org/10.1029/2019EF001152

Li, Z., Lin, X. and Cai, W., 2017. Realism of modelled Indian summer monsoon correlation with the tropical Indo-Pacific affects projected monsoon changes. *Scientific reports*, *7*(1), p.4929. https://doi.org/10.1038/s41598-017-05225-z

Liebmann, B., Kiladis, G.N., Vera, C.S., Saulo, A.C. and Carvalho, L.M., 2004. Subseasonal variations of rainfall in South America in the vicinity of the low-level jet east of the Andes and comparison to those in the South Atlantic convergence zone. *Journal of climate*, *17*(19), pp.3829-3842. https://doi.org/10.1175/1520-0442(2004)017<3829:SVORIS>2.0.CO;2

Liu, J., Hertel, T.W., Diffenbaugh, N.S., Delgado, M.S. and Ashfaq, M., 2015. Future property damage from flooding: sensitivities to economy and climate change. *Climatic change*, *132*, pp.741-749. https://doi.org/10.1007/s10584-015-1478-z

Liu, J., Wu, D., Liu, G., Mao, R., Chen, S., Ji, M., Fu, P., Sun, Y., Pan, X., Jin, H. and Zhou, Y., 2020. Impact of Arctic amplification on declining spring dust events in East Asia. *Climate Dynamics*, *54*, pp.1913-1935. https://doi.org/10.1007/s00382-019-05094-4

Liu, Y., Chen, J., Pan, T., Liu, Y., Zhang, Y., Ge, Q., Ciais, P. and Penuelas, J., 2020. Global socioeconomic risk of precipitation extremes under climate change. *Earth's future*, *8*(9), p.e2019EF001331. https://doi.org/10.1029/2019EF001331

Lu, E., Zeng, X., Jiang, Z., Wang, Y. and Zhang, Q., 2009. Precipitation and precipitable water: Their temporal-spatial behaviors and use in determining monsoon onset/retreat and monsoon regions. *Journal of Geophysical Research: Atmospheres*, *114*(D23). https://doi.org/10.1029/2009JD012146

Lu, R., Dong, B. and Ding, H., 2006. Impact of the Atlantic Multidecadal Oscillation on the Asian summer monsoon. *Geophysical Research Letters*, *33*(24). https://doi.org/10.1029/2006GL027655

Madden, R.A. and Julian, P.R., 1994. Observations of the 40–50-day tropical oscillation—A review. *Monthly weather review*, *122*(5), pp.814-837. https://doi.org/10.1175/1520-0493(1994)122<0814:OOTDTO>2.0.CO;2

Malik, A., Brönnimann, S., Stickler, A., Raible, C.C., Muthers, S., Anet, J., Rozanov, E. and Schmutz, W., 2017. Decadal to multi-decadal scale variability of Indian summer monsoon rainfall in the coupled ocean-atmosphere-chemistry climate model SOCOL-MPIOM. *Climate dynamics*, *49*, pp.3551-3572. https://doi.org/10.1007/s00382-017-3529-9

Malik, N., Bookhagen, B. and Mucha, P.J., 2016. Spatiotemporal patterns and trends of Indian monsoonal rainfall extremes. *Geophysical Research Letters*, *43*(4), pp.1710-1717. https://doi.org/10.1002/2016GL067841

Maloney, E.D., 2009. The moist static energy budget of a composite tropical intraseasonal oscillation in a climate model. Journal of Climate, 22(3), 711-729. https://doi.org/10.1175/2008JCLI2542.1

Mann, H.B., 1945. Nonparametric tests against trend. Econometrica: Journal of the econometric society, 245-259.https://doi.org/10.2307/1907187

Mantua, N.J. and Hare, S.R., 2002. The Pacific decadal oscillation. Journal of oceanography, 58(1), 35-44. https://doi.org/10.1023/A:1015820616384

Marengo, J.A., Liebmann, B., Grimm, A.M., Misra, V., Silva Dias, P.D., Cavalcanti, I.F.A., Carvalho, L.M.V., Berbery, E.H., Ambrizzi, T., Vera, C.S. and Saulo, A.C., 2012. Recent developments on the South American monsoon system. *International Journal of Climatology*, *32*(1), pp.1-21. https://doi.org/10.1002/joc.2254

Martin, G.M., Arpe, K., Chauvin, F., Ferranti, L., Maynard, K., Polcher, J., Stephenson, D.B. and Tschuck, P., 2000. Simulation of the Asian summer monsoon in five European general circulation models. *Atmospheric Science Letters*, *1*(1), pp.37-55. https://doi.org/10.1006/asle.2000.0004

Meehl, G. A., Arblaster, J. M., Tebaldi, C., 2005. Understanding future patterns of increased precipitation intensity in climate model simulations. Geophys. Res. Lett.32, L18719. https://doi.org/10.1029/2005GL023680.

Meehl, G.A., 1994. Coupled land-ocean-atmosphere processes and South Asian monsoon variability. *Science*, *266*(5183), 263-267. https://doi.org/10.1126/science.266.5183.263

Meehl, G.A., Boer, G.J., Covey, C., Latif, M. and Stouffer, R.J., 2000. The coupled model intercomparison project (CMIP). *Bulletin of the American Meteorological Society*, *81*(2), pp.313-318. https://www.jstor.org/stable/26215108

Meenu, S., Gayatri, K., Malap, N., Murugavel, P., Samanta, S. and Prabha, T.V., 2020. The physics of extreme rainfall event: An investigation with multisatellite observations and numerical simulations. *Journal of Atmospheric and Solar-Terrestrial Physics*, *204*, p.105275. https://doi.org/10.1016/j.jastp.2020.105275

Mishra AK, Dwivedi S, and Das S., 2020. Role of Arabian Sea warming on the Indian summer monsoon rainfall in a regional climate model. International Journal of Climatology, 40, 2226–2238. https://doi.org/10.1002/joc.6328

Mishra, S.K., Sahany, S. and Salunke, P., 2017. Linkages between MJO and summer monsoon rainfall over India and surrounding region. *Meteorology and Atmospheric Physics*, *129*, pp.283-296. https://doi.org/10.1007/s00703-016-0470-0

Mishra, V. and Shah, H.L., 2018. Hydroclimatological perspective of the Kerala flood of 2018. *Journal of the Geological Society of India*, *92*, pp.645-650. https://doi.org/10.1007/s12594-018-1079-3

Mishra, V., Bhatia, U. and Tiwari, A.D., 2020. Bias-corrected climate projections for South Asia from coupled model intercomparison project-6. *Scientific data*, *7*(1), p.338. https://doi.org/10.1038/s41597-020-00681-1

Misra, V. and DiNapoli, S., 2014. The variability of the Southeast Asian summer monsoon. *International Journal of Climatology*, *34*(3), pp.893-901. https://doi.org/10.1002/joc.3735

Misra, V., Mishra, A. and Bhardwaj, A., 2017. High-resolution regional-coupled ocean–atmosphere simulation of the Indian summer monsoon. *International Journal of Climatology*, *37*, pp.717-740. https://doi.org/10.1002/joc.5034

Misra, V., Mishra, A. and Bhardwaj, A., 2018. Simulation of the intraseasonal variations of the Indian summer monsoon in a regional coupled ocean–atmosphere model. *Journal of Climate*, *31*(8), pp.3167-3185. https://doi.org/10.1175/JCLI-D-17-0434.1

Mitra, A., 2021. A comparative study on the skill of CMIP6 models to preserve daily spatial patterns of monsoon rainfall over India. *Frontiers in Climate*, *3*, p.654763. https://doi.org/10.3389/fclim.2021.654763

MJ, Manton. and JL, McBride., 1992. Recent research on the Australian monsoon. *Journal of the Meteorological Society of Japan. Ser. II*, *70*(1B), pp.275-285. https://doi.org/10.2151/jmsj1965.70.1B_275

Mohanty, M.R., Baraik, S.K. and Mohanty, U.C., 2023. Comprehensive Trend Analysis of Past Century Indian Summer Monsoon Rainfall and its Variability. *Global Journal of Human-Social Science*, *23*, pp.25-38.

Mohanty, U.C., Pearce, R.P. and Tiedtke, M., 1984. Numerical experiments on the simulation of the 1979 Asian summer monsoon (No. 44). European Centre for Medium Range Weather Forecasts.

Mohtadi, M., Prange, M. and Steinke, S., 2016. Palaeoclimatic insights into forcing and response of monsoon rainfall. *Nature*, *533*(7602), pp.191-199. https://doi.org/10.1038/nature17450

Moss, R.H., Edmonds, J.A., Hibbard, K.A., Manning, M.R., Rose, S.K., Van Vuuren, D.P., Carter, T.R., Emori, S., Kainuma, M., Kram, T. and Meehl, G.A., 2010. The next generation of scenarios for climate change research and assessment. *Nature*, *463*(7282), pp.747-756. https://doi.org/10.1038/nature08823

Murray, V. and Ebi, K.L., 2012. IPCC special report on managing the risks of extreme events and disasters to advance climate change adaptation (SREX). *J Epidemiol Community Health*, *66*(9), pp.759-760. http://dx.doi.org/10.1136/jech-2012-201045

Nair, P.J., Chakraborty, A., Varikoden, H., Francis, P.A. and Kuttippurath, J., 2018. The local and global climate forcings induced inhomogeneity of Indian rainfall. Scientific reports, 8(1), 1-12. https://doi.org/10.1038/s41598-018-24021-x.

Naveendrakumar, G., Vithanage, M., Kwon, H.H., Chandrasekara, S.S.K., Iqbal, M.C.M., Pathmarajah, S., Fernando, W.C.D.K. and Obeysekera, J., 2019. South Asian perspective on temperature and rainfall extremes: A review. *Atmospheric Research*, *225*, pp.110-120. https://doi.org/10.1016/j.atmosres.2019.03.021

Newman, M., Alexander, M.A., Ault, T.R., Cobb, K.M., Deser, C., Di Lorenzo, E., Mantua, N.J., Miller, A.J., Minobe, S., Nakamura, H. and Schneider, N., 2016. The Pacific decadal oscillation, revisited. *Journal of Climate*, *29*(12), pp.4399-4427. https://doi.org/10.1175/JCLI-D-15-0508.1

Nikumbh, A.C., Chakraborty, A., Bhat, G.S. and Frierson, D.M., 2020. Large-Scale Extreme Rainfall-Producing Synoptic Systems of the Indian Summer Monsoon. Geophysical Research Letters, 47(11), p.e2020GL088403. https://doi.org/10.1029/2020GL088403

Nogués-Paegle, J., Mechoso, C.R., Fu, R., Berbery, E.H., Chao, W.C., Chen, T.C., Cook, K., Diaz, A.F., Enfield, D., Ferreira, R. and Grimm, A.M., 2002. Progress in Pan American CLIVAR research: understanding the South American monsoon. *Meteorologica*, *27*(12), pp.1-30.

Noska, R. and Misra, V., 2016. Characterizing the onset and demise of the Indian summer monsoon. *Geophysical Research Letters*, *43*(9), pp.4547-4554. https://doi.org/10.1002/2016GL068409

O'Neill, B.C., Kriegler, E., Ebi, K.L., Kemp-Benedict, E., Riahi, K., Rothman, D.S., Van Ruijven, B.J., Van Vuuren, D.P., Birkmann, J., Kok, K. and Levy, M., 2017. The roads ahead: Narratives for shared socioeconomic pathways describing world futures in the 21st century. *Global environmental change*, *42*, pp.169-180. https://doi.org/10.1016/j.gloenvcha.2015.01.004

O'Gorman, P.A. and Schneider, T., 2009. The physical basis for increases in precipitation extremes in simulations of 21st-century climate change. *Proceedings of the National Academy of Sciences*, *106*(35), pp.14773-14777. https://doi.org/10.1073/pnas.0907610106

Ogungbenro, S. B., & Morakinyo, T. E. (2014). Rainfall distribution and change detection across climatic zones in Nigeria. Weather and Climate Extremes, *5*, 1-6

Ohba, M., 2021. Precipitation under climate change. In *Precipitation* (pp. 21-51). Elsevier. https://doi.org/10.1016/B978-0-12-822699-5.00002-1

Olizver, J.E. ed., 2008. *Encyclopedia of world climatology*. Springer Science & Business Media.

O'Neill, B.C., Tebaldi, C., Van Vuuren, D.P., Eyring, V., Friedlingstein, P., Hurtt, G., Knutti, R., Kriegler, E., Lamarque, J.F., Lowe, J. and Meehl, G.A., 2016. The scenario model intercomparison project (Sce narioMIP) for CMIP6. *Geoscientific Model Development*, *9*(9), pp.3461-3482. https://doi.org/10.5194/gmd-9-3461-2016

Pai, D.S. and Rajeevan, M., 2007. *Indian summer monsoon onset: variability and prediction*. National Climate Centre, Indian Meteorological Department.

Pai, D.S., Rajeevan, M., Sreejith, O.P., Mukhopadhyay, B. and Satbha, N.S., 2014. Development of a new high spatial resolution (0.25× 0.25) long period (1901-2010) daily gridded rainfall data set over India and its comparison with existing data sets over the region. Mausam, 65(1), 1-18. https://doi.org/10.54302/mausam.v65i1.851

Pal, I. and Al-Tabbaa, A., 2010. Regional changes in extreme monsoon rainfall deficit and excess in India. *Dynamics of Atmospheres and Oceans*, *49*(2-3), pp.206-214. https://doi.org/10.1016/j.dynatmoce.2009.07.001

Pant, G.B. and Parthasarathy, S.B., 1981. Some aspects of an association between the southern oscillation and Indian summer monsoon. Archives for meteorology, geophysics, and bioclimatology, Series B, 29(3), 245-252. https://doi.org/10.1007/BF02263246.

Parkinson, C.L., 1989. Dangers of multiyear averaging in analyses of long-term climate trends. Climate dynamics, 4(1), 39-44. https://doi.org/10.1007/BF00207398.

Parthasarathy, B., Diaz, H.F. and Eischeid, J.K., 1988. Prediction of all-India summer monsoon rainfall with regional and large-scale parameters. *Journal of Geophysical Research: Atmospheres*, *93*(D5), pp.5341-5350. https://doi.org/10.1029/JD093iD05p05341

Pathan, J.M., 1994. Diurnal variation of southwest monsoon rainfall at Indian stations. *Advances in Atmospheric Sciences*, *11*, pp.111-120. https://doi.org/10.1007/BF02657000

Patil, C., Prabhakaran, T., Sinha Ray, K.C. and Karipot, A., 2019. Revisiting moisture transport during the Indian Summer Monsoon using the moisture river concept. Pure and Applied Geophysics, 176(11), 5107-5123. https://doi.org/10.1007/s00024-019-02224-1

Pattanaik, D.R. and Rajeevan, M., 2010. Variability of extreme rainfall events over India during southwest monsoon season. Meteorological Applications: A journal of forecasting, practical applications, training techniques and modelling, 17(1), 88-104. https://doi.org/10.1002/met.164.

Pattanaik, D.R., Sahai, A.K., Muralikrishna, R.P., Mandal, R. and Dey, A., 2020. Active-break transitions of monsoons over India as predicted by coupled model ensembles. *Pure and Applied Geophysics*, *177*, pp.4391-4422. https://doi.org/10.1007/s00024-020-02503-2

Pendergrass, A.G., Knutti, R., Lehner, F., Deser, C. and Sanderson, B.M., 2017. Precipitation variability increases in a warmer climate. *Scientific reports*, *7*(1), p.17966. https://doi.org/10.1038/s41598-017-17966-y

Pottapinjara, V., Girishkumar, M.S., Sivareddy, S., Ravichandran, M. and Murtugudde, R., 2016. Relation between the upper ocean heat content in the equatorial Atlantic during

boreal spring and the Indian monsoon rainfall during June–September. International Journal of Climatology, 36(6), 2469-2480. https://doi.org/10.1002/joc.4506.

Prakash, S., Mitra, A. K., Momin, I. M., Rajagopal, E. N., Basu, S., Collins, M., Turner, A. G. Rao, K. A., and Ashok, K. 2015. Seasonal intercomparison of observational rainfall datasets over India during the southwest monsoon season. International Journal of Climatology, 35, 2326-2338.

Preethi, B., Mujumdar, M., Kripalani, R.H., Prabhu, A. and Krishnan, R., 2017. Recent trends and tele-connections among South and East Asian summer monsoons in a warming environment. *Climate Dynamics*, *48*, pp.2489-2505. https://doi.org/10.1007/s00382-016-3218-0

Prodhomme, C., Batté, L., Massonnet, F., Davini, P., Bellprat, O., Guemas, V. and Doblas-Reyes, F.J., 2016. Benefits of increasing the model resolution for the seasonal forecast quality in EC-Earth. *Journal of Climate*, *29*(24), pp.9141-9162. https://doi.org/10.1175/JCLI-D-16-0117.1

Qiangen, Z., Jinhai, H. and Panxing, W., 1986. A study of circulation differences between East-Asian and Indian summer monsoons with their interaction. *Advances in Atmospheric Sciences*, *3*(4), pp.466-477. https://doi.org/10.1007/BF02657936

Qin, J., Zhou, L., Meng, Z., Li, B., Lian, T. and Murtugudde, R., 2022. Barotropic energy conversion during Indian summer monsoon: implication of Central Indian Ocean Mode Simulation in CMIP6. *Climate Dynamics*, pp.1-20. https://doi.org/10.1007/s00382-021-06087-y

Radhakrishnan, K., Sivaraman, I., Jena, S.K., Sarkar, S. and Adhikari, S., 2017. A climate trend analysis of temperature and rainfall in India. *Climate Change and Environmental Sustainability*, *5*(2), pp.146-153. 10.5958/2320-642X.2017.00014.X

Raghavan, K., 1973. Break-monsoon over India. *Monthly Weather Review*, *101*(1), pp.33-43.

Rajeevan, M., Bhate, J. and Jaswal, A.K., 2008. Analysis of variability and trends of extreme rainfall events over India using 104 years of gridded daily rainfall data. Geophysical research letters, 35(18). https://doi.org/10.1029/2008GL035143

Rajeevan, M., Bhate, J., Kale, J.D. and Lal, B., 2006. High resolution daily gridded rainfall data for the Indian region: Analysis of break and active monsoon spells. *Current science*, pp.296-306. https://www.jstor.org/stable/24094135

Rajeevan, M., Gadgil, S. and Bhate, J., 2010. Active and break spells of the Indian summer monsoon. *Journal of earth system science*, 119(3), 229-247. https://doi.org/10.1007/s12040-010-0019-4

Rajendran, K., Surendran, S., Varghese, S.J. and Sathyanath, A., 2022. Simulation of Indian summer monsoon rainfall, interannual variability and teleconnections: evaluation of CMIP6 models. *Climate Dynamics*, *58*(9-10), pp.2693-2723. https://doi.org/10.1007/s00382-021-06027-w

Ramage, C.S., 1971. Monsoon meteorology. https://lccn.loc.gov/73127697

Ramamurthy, K., 1969. Forecasting Manual. *Part IV, India Meteorological*.

Ramege, C.S., 1964. Diurnal Variation of Summer Rainfall of Malaya, J. *Tropical Geogr*, *19*, pp.62-68.

Rao, G.V., Reddy, K.V., Srinivasan, R., Sridhar, V., Umamahesh, N.V. and Pratap, D., 2020. Spatio-temporal analysis of rainfall extremes in the flood-prone Nagavali and Vamsadhara Basins in eastern India. *Weather and Climate Extremes*, *29*, p.100265. https://doi.org/10.1016/j.wace.2020.100265

Rao, J., Ren, R., Xia, X., Shi, C. and Guo, D., 2019. Combined impact of El Niño–Southern Oscillation and Pacific Decadal Oscillation on the northern winter stratosphere. *Atmosphere*, *10*(4), p.211. https://doi.org/10.3390/atmos10040211

Rao, Y.P., 1976. Southwest Monsoon (meteorological monograph). India Meteorological Department, New Delhi, 366.

Ratna, S.B., Cherchi, A., Joseph, P.V., Behera, S.K., Abish, B. and Masina, S., 2016. Moisture variability over the Indo-Pacific region and its influence on the Indian summer monsoon rainfall. Climate dynamics, 46(3), 949-965. https://doi.org/10.1007/s00382-015-2624-z

Ratnam JV, Behera SK, Masumoto Y, Takahashi K, Yamagata T. Anomalous climatic conditions associated with the El Niño Modoki during boreal winter of 2009. Climate dynamics. 2012 Jul;39(1-2):227-38. https://doi.org/10.1007/s00382-011-1108-z

Ray, K., Giri, R.K., Ray, S.S., Dimri, A.P. and Rajeevan, M., 2021. An assessment of long-term changes in mortalities due to extreme weather events in India: A study of 50 years' data, 1970–2019. *Weather and Climate Extremes*, *32*, p.100315. https://doi.org/10.1016/j.wace.2021.100315

Rayner, N.A.A., Parker, D.E., Horton, E.B., Folland, C.K., Alexander, L.V., Rowell, D.P., Kent, E.C. and Kaplan, A., 2003. Global analyses of sea surface temperature, sea ice, and night marine air temperature since the late nineteenth century. *Journal of Geophysical Research: Atmospheres*, *108*(D14). https://doi.org/10.1029/2002JD002670

Revadekar, J.V., Varikoden, H., Murumkar, P.K. and Ahmed, S.A., 2018. Latitudinal variation in summer monsoon rainfall over Western Ghat of India and its association with global sea surface temperatures. Science of The Total Environment, 613, 88-97. https://doi.org/10.1016/j.scitotenv.2017.08.285

Roe, G.H., 2005. Orographic precipitation. Annual Review of earth and planetary sciences, 33(1), 645-671. https://doi.org/10.1146/annurev.earth.33.092203.122541.

Roxy, M. and Tanimoto, Y., 2007. Role of SST over the Indian Ocean in influencing the intraseasonal variability of the Indian summer monsoon. Journal of the Meteorological Society of Japan. Ser. II, 85(3), 349-358. https://doi.org/10.2151/jmsj.85.349

Roxy, M.K., Ghosh, S., Pathak, A., Athulya, R., Mujumdar, M., Murtugudde, R., Terray, P. and Rajeevan, M., 2017. A threefold rise in widespread extreme rain events over central India. *Nature communications*, *8*(1), p.708. https://doi.org/10.1038/s41467-017-00744-9

Roxy, M.K., Ritika, K., Terray, P., Murtugudde, R., Ashok, K. and Goswami, B.N., 2015. Drying of Indian subcontinent by rapid Indian Ocean warming and a weakening land-sea thermal gradient. *Nature communications*, *6*(1), p.7423. https://doi.org/10.1038/ncomms8423

Sabeerali, C.T., Ajayamohan, R.S., Bangalath, H.K. and Chen, N., 2019. Atlantic zonal mode: an emerging source of Indian summer monsoon variability in a warming world.

Geophysical Research Letters, *46*(8), pp.4460-4467. https://doi.org/10.1029/2019GL082379

Sadhuram, Y. and Rao, D.P., 1998. Moisture source for summer monsoon rainfall over India, Journal of Applied Hydrology, 11, 630-70. http://drs.nio.org/drs/handle/2264/1959

Sagalgile, A.P., Chowdary, J.S., Srinivas, G., Gnanaseelan, C., Parekh, A., Attada, R. and Singh, P., 2018. Indian summer monsoon sub-seasonal low-level circulation predictability and its association with rainfall in a coupled model. Pure and Applied Geophysics, 175(1), 449-463. https://doi.org/10.1007/s00024-017-1702-z

Saha, A., Ghosh, S., Sahana, A.S. and Rao, E.P., 2014. Failure of CMIP5 climate models in simulating post-1950 decreasing trend of Indian monsoon. *Geophysical Research Letters*, *41*(20), pp.7323-7330. https://doi.org/10.1002/2014GL061573

Sahany, S., Venugopal, V. and Nanjundiah, R.S., 2010. Diurnal-scale signatures of monsoon rainfall over the Indian region from TRMM satellite observations. *Journal of Geophysical Research: Atmospheres*, *115*(D2). https://doi.org/10.1029/2009JD012644

Saji, N.H., Goswami, B.N., Vinayachandran, P.N. and Yamagata, T., 1999. A dipole mode in the tropical Indian Ocean. Nature, 401(6751), 360-363. https://doi.org/10.1038/43854.

Salma, S., Rehman, S. and Shah, M.A., 2012. Rainfall trends in different climate zones of Pakistan. *Pakistan Journal of Meteorology*, *9*(17). https://www.pmd.gov.pk/rnd/rnd_files/vol8_issue17/4.pdf

Sandeep, N., Swapna, P., Krishnan, R., Farneti, R., Kucharski, F., Modi, A., Prajeesh, A.G., Ayantika, D.C. and Manmeet, S., 2022. On the weakening association between South asian monsoon and atlantic multidecadal oscillation. *Climate Dynamics*, *59*(9-10), pp.2531-2547. https://doi.org/10.1007/s00382-022-06224-1

Sandeep, S. and Ajayamohan, R.S., 2015. Poleward shift in Indian summer monsoon low level jetstream under global warming. Climate Dynamics, 45(1-2), 337-351. https://doi.org/10.1007/s00382-014-2261-y.

Sankar, S., Svendsen, L., Gokulapalan, B., Joseph, P.V. and Johannessen, O.M., 2016. The relationship between Indian summer monsoon rainfall and Atlantic multidecadal

variability over the last 500 years. *Tellus A: Dynamic Meteorology and Oceanography*, *68*(1), p.31717. https://doi.org/10.3402/tellusa.v68.31717

Schär, C., Ban, N., Fischer, E.M., Rajczak, J., Schmidli, J., Frei, C., Giorgi, F., Karl, T.R., Kendon, E.J., Tank, A.M.K. and O'Gorman, P.A., 2016. Percentile indices for assessing changes in heavy precipitation events. Climatic Change, 137(1-2), 201-216. https://doi.org/10.1007/s10584-016-1669-2.

Schlesinger, M.E. and Ramankutty, N., 1994. An oscillation in the global climate system of period 65–70 years. *Nature*, *367*(6465), pp.723-726. https://doi.org/10.1038/367723a0

Seetha, C.J., Varikoden, H., Babu, C.A. and Kuttippurath, J., 2020. Significant changes in the ENSO-monsoon relationship and associated circulation features on multidecadal timescale. Climate Dynamics, 54(3), 1491-1506. https://doi.org/10.1007/s00382-019-05071-x

Seland, Ø., Bentsen, M., Olivié, D., Toniazzo, T., Gjermundsen, A., Graff, L.S., Debernard, J.B., Gupta, A.K., He, Y.C., Kirkevåg, A. and Schwinger, J., 2020. Overview of the Norwegian Earth System Model (NorESM2) and key climate response of CMIP6 DECK, historical, and scenario simulations. *Geoscientific Model Development*, *13*(12), pp.6165-6200. https://doi.org/10.5194/gmd-13-6165-2020

Sen, P.K., 1968. Estimates of the regression coefficient based on Kendall's tau. *Journal of the American statistical association*, *63*(324), pp.1379-1389. https://doi.org/10.1080/01621459.1968.10480934

Sharmila, S., Joseph, S., Sahai, A.K., Abhilash, S. and Chattopadhyay, R., 2015. Future projection of Indian summer monsoon variability under climate change scenario: An assessment from CMIP5 climate models. *Global and Planetary Change*, *124*, pp.62-78. https://doi.org/10.1016/j.gloplacha.2014.11.004

Shastri, H., Paul, S., Ghosh, S. and Karmakar, S., 2015. Impacts of urbanization on Indian summer monsoon rainfall extremes. Journal of Geophysical Research: Atmospheres, 120(2), 496-516. https://doi.org/10.1002/2014JD022061.

Shi, X., Chen, J., Gu, L., Xu, C.Y., Chen, H. and Zhang, L., 2021. Impacts and socioeconomic exposures of global extreme precipitation events in 1.5 and 2.0 C warmer climates.

Science of the Total Environment, *766*, p.142665. https://doi.org/10.1016/j.scitotenv.2020.142665

Shrestha, A.B., Bajracharya, S.R., Sharma, A.R., Duo, C. and Kulkarni, A., 2017. Observed trends and changes in daily temperature and precipitation extremes over the Koshi river basin 1975–2010. *International Journal of Climatology*, *37*(2), pp.1066-1083. https://doi.org/10.1002/joc.4761

Sikka, D.R. and Gadgil, S., 1980. On the maximum cloud zone and the ITCZ over Indian longitudes during the southwest monsoon. *Monthly Weather Review*, *108*(11), pp.1840-1853. https://doi.org/10.1175/1520-0493(1980)108<1840:OTMCZA>2.0.CO;2

Sikka, D.R., 1980. Some aspects of the large scale fluctuations of summer monsoon rainfall over India in relation to fluctuations in the planetary and regional scale circulation parameters. Proceedings of the Indian Academy of Sciences-Earth and Planetary Sciences, 89(2), 179-195. https://doi.org/10.1007/BF02913749.

Singh, D., Ghosh, S., Roxy, M.K. and McDermid, S., 2019. Indian summer monsoon: Extreme events, historical changes, and role of anthropogenic forcings. *Wiley Interdisciplinary Reviews: Climate Change*, *10*(2), p.e571. https://doi.org/10.1002/wcc.571.

Singh, D., Tsiang, M., Rajaratnam, B. and Diffenbaugh, N.S., 2014. Observed changes in extreme wet and dry spells during the South Asian summer monsoon season. *Nature Climate Change*, *4*(6), 456-461. https://doi.org/10.1038/nclimate2208.

Singh, P. and Nakamura, K., 2010. Diurnal variation in summer monsoon precipitation during active and break periods over central India and southern Himalayan foothills. *Journal of Geophysical Research: Atmospheres*, *115*(D12). https://doi.org/10.1029/2009JD012794

Singh, P., 2018. Indian summer monsoon rainfall (ISMR) forecasting using time series data: a fuzzy-entropy-neuro based expert system. *Geoscience Frontiers*, *9*(4), pp.1243-1257. https://doi.org/10.1016/j.gsf.2017.07.011

Singh, S., Ghosh, S., Sahana, A.S., Vittal, H. and Karmakar, S., 2017. Do dynamic regional models add value to the global model projections of Indian monsoon?. *Climate Dynamics*, *48*, pp.1375-1397. https://doi.org/10.1007/s00382-016-3147-y

Singh, S.V., Kripalani, R.H. and Sikka, D.R., 1992. Interannual variability of the Madden–Julian oscillations in Indian summer monsoon rainfall. Journal of Climate, 973-978. https://www.jstor.org/stable/26197144

Sooraj, K.P., Terray, P., Shilin, A. and Mujumdar, M., 2020. Dynamics of rainfall extremes over India: A new perspective. International Journal of Climatology, 40(12), 5223-5245. https://doi.org/10.1002/joc.6516

Sperber, K.R., Annamalai, H., Kang, I.S., Kitoh, A., Moise, A., Turner, A., Wang, B. and Zhou, T., 2013. The Asian summer monsoon: an intercomparison of CMIP5 vs. CMIP3 simulations of the late 20th century. *Climate dynamics*, *41*, pp.2711-2744. https://doi.org/10.1007/s00382-012-1607-6

Sudeepkumar, B.L., Babu, C.A. and Varikoden, H., 2018. Future projections of active-break spells of Indian summer monsoon in a climate change perspective. *Global and Planetary Change*, *161*, pp.222-230. https://doi.org/10.1016/j.gloplacha.2017.12.020

Suman, M. and Maity, R., 2020. Southward shift of precipitation extremes over south Asia: Evidences from CORDEX data. *Scientific reports*, *10*(1), p.6452. https://doi.org/10.1038/s41598-020-63571-x

Sumesh, K.G. and Ramesh Kumar, M.R., 2013. Tropical cyclones over north Indian Ocean during El-nino modoki years. *Natural hazards*, *68*, pp.1057-1074. https://doi.org/10.1007/s11069-013-0679-x

Suppiah, R., 1992. The Australian summer monsoon: A review. *Progress in Physical Geography*, *16*(3), pp.283-318. https://doi.org/10.1177/030913339201600302

Suthinkumar, P.S., Babu, C.A. and Varikoden, H., 2019. Spatial distribution of extreme rainfall events during 2017 southwest monsoon over Indian subcontinent. Pure and Applied Geophysics, 176(12), 5431-5443. https://doi.org/10.1007/s00024-019-02282-5

Suthinkumar, P.S., Varikoden, H. and Babu, C.A., 2023. Assessment of extreme rainfall events over the Indian subcontinent during the historical and future projection periods based on CMIP6 simulations. *International Journal of Climatology*. https://doi.org/10.1002/joc.8314

Sutton, R.T. and Hodson, D.L., 2005. Atlantic Ocean forcing of North American and European summer climate. *science*, *309*(5731), pp.115-118. DOI: 10.1126/science.1109496

Swain, M., Pattanayak, S. and Mohanty, U.C., 2018. Characteristics of occurrence of heavy rainfall events over Odisha during summer monsoon season. *Dynamics of Atmospheres and Oceans*, *82*, pp.107-118. https://doi.org/10.1016/j.dynatmoce.2018.05.004

Swapna, P. and RameshKumar, M.R., 2002. Role of low level flow on the summer monsoon rainfall over the Indian subcontinent during two contrasting monsoon years. http://drs.nio.org/drs/handle/2264/450

Tan, X., Wu, X. and Liu, B., 2021. Global changes in the spatial extents of precipitation extremes. *Environmental Research Letters*, *16*(5), p.054017. **DOI** 10.1088/1748-9326/abf462

Tang, M. and Reiter, E.R., 1984. Plateau monsoons of the Northern Hemisphere: A comparison between North America and Tibet. *Monthly Weather Review*, *112*(4), pp.617-637. https://doi.org/10.1175/1520-0493(1984)112<0617:PMOTNH>2.0.CO;2

Taylor, K.E., 2001. Summarizing multiple aspects of model performance in a single diagram. *Journal of geophysical research: atmospheres*, *106*(D7), pp.7183-7192. https://doi.org/10.1029/2000JD900719

Thapa, K., Endreny, T.A. and Ferguson, C.R., 2018. Atmospheric rivers carry nonmonsoon extreme precipitation into Nepal. Journal of Geophysical Research: Atmospheres, 123(11), 5901-5912. https://doi.org/10.1029/2017JD027626

Trenberth, K.E. and Shea, D.J., 2006. Atlantic hurricanes and natural variability in 2005. *Geophysical research letters*, *33*(12). https://doi.org/10.1029/2006GL026894

Trenberth, K.E., 2011. Changes in precipitation with climate change. *Climate research*, *47*(1-2), pp.123-138.

Trenberth, K.E., Branstator, G.W., Karoly, D., Kumar, A., Lau, N.C. and Ropelewski, C., 1998. Progress during TOGA in understanding and modeling global teleconnections associated with tropical sea surface temperatures. Journal of Geophysical Research: Oceans, 103(C7), 14291-14324.https://doi.org/10.1029/97JC01444.

Trenberth, K.E., Moore, B., Karl, T.R. and Nobre, C., 2006. Monitoring and prediction of the Earth's climate: A future perspective. *Journal of climate*, *19*(20), pp.5001-5008. https://doi.org/10.1175/JCLI3897.1

Turner, A.G. and Annamalai, H., 2012. Climate change and the South Asian summer monsoon. Nature Climate Change, 2(8), 587-595. https://doi.org/10.1038/nclimate1495

Ullah, W., Wang, G., Lou, D., Ullah, S., Bhatti, A.S., Ullah, S., Karim, A., Hagan, D.F.T. and Ali, G., 2021. Large-scale atmospheric circulation patterns associated with extreme monsoon precipitation in Pakistan during 1981–2018. *Atmospheric Research*, *253*, p.105489. https://doi.org/10.1016/j.atmosres.2021.105489

van Vuuren, D.P. and Carter, T.R., 2014. Climate and socio-economic scenarios for climate change research and assessment: reconciling the new with the old. *Climatic change*, *122*, pp.415-429. https://doi.org/10.1007/s10584-013-0974-2

Varikoden, H. and Babu, C.A., 2015. Indian summer monsoon rainfall and its relation with SST in the equatorial Atlantic and Pacific Oceans. International Journal of Climatology, 35(6), 1192-1200. https://doi.org/10.1002/joc.4056.

Varikoden, H. and Preethi, B., 2013. Wet and dry years of Indian summer monsoon and its relation with Indo-Pacific sea surface temperatures. International journal of climatology, 33(7), 1761-1771. https://doi.org/10.1002/joc.3547

Varikoden, H. and Reji, M.J.K., 2022. Features of regional Indian monsoon rainfall extremes. In *Climate Impacts on Extreme Weather* (pp. 83-100). Elsevier. https://doi.org/10.1016/B978-0-323-88456-3.00014-9Get rights and content

Varikoden, H. and Revadekar, J.V., 2020. On the extreme rainfall events during the southwest monsoon season in northeast regions of the Indian subcontinent. Meteorological Applications, 27(1), p.e1822. https://doi.org/10.1002/met.1822.

Varikoden, H., Hrudya, P.P.V.H., Vishnu, R.N. and Kuttippurath, J., 2022. Changes in the ENSO–ISMR relationship in the historical and future projection periods based on coupled models. *International Journal of Climatology*, *42*(4), pp.2225-2245. https://doi.org/10.1002/joc.7362

Varikoden, H., Mujumdar, M., Revadekar, J.V., Sooraj, K.P., Ramarao, M.V.S., Sanjay, J. and Krishnan, R., 2018. Assessment of regional downscaling simulations for long term mean, excess and deficit Indian Summer Monsoons. Global and Planetary Change, 162, 28-38. https://doi.org/10.1016/j.gloplacha.2017.12.002.

Varikoden, H., Preethi, B. and Revadekar, J.V., 2012. Diurnal and spatial variation of Indian summer monsoon rainfall using tropical rainfall measuring mission rain rate. Journal of Hydrology, 475, 248-258. https://doi.org/10.1016/j.jhydrol.2012.09.056.

Varikoden, H., Revadekar, J.V., Choudhary, Y. and Preethi, B., 2015. Droughts of Indian summer monsoon associated with El Niño and Non-El Niño years. *International Journal of Climatology*, *35*(8), 1916-1925. https://doi.org/10.1002/joc.4097

Varikoden, H., Revadekar, J.V., Kuttippurath, J. and Babu, C.A., 2019. Contrasting trends in southwest monsoon rainfall over the Western Ghats region of India. Climate Dynamics, 52(7-8), 4557-4566. https://doi.org/10.1007/s00382-018-4397-7.

Veiga, S.F. and Yuan, H., 2021. Performance-based projection of precipitation extremes over China based on CMIP5/6 models using integrated quadratic distance. *Weather and Climate Extremes*, *34*, p.100398. https://doi.org/10.1016/j.wace.2021.100398

Venkatesh, B. and Jose, M.K., 2007. Identification of homogeneous rainfall regimes in parts of Western Ghats region of Karnataka. Journal of Earth System Science, 116(4), 321-329. https://doi.org/10.1007/s12040-007-0029-z

Vera, C., Higgins, W., Amador, J., Ambrizzi, T., Garreaud, R., Gochis, D., Gutzler, D., Lettenmaier, D., Marengo, J., Mechoso, C.R. and Nogues-Paegle, J., 2006. Toward a unified view of the American monsoon systems. *Journal of climate*, *19*(20), pp.4977-5000. https://doi.org/10.1175/JCLI3896.1

Verdon, D.C. and Franks, S.W., 2006. Long-term behaviour of ENSO: Interactions with the PDO over the past 400 years inferred from paleoclimate records. *Geophysical Research Letters*, *33*(6). https://doi.org/10.1029/2005GL025052

Vialard, J., Jayakumar, A., Gnanaseelan, C., Lengaigne, M., Sengupta, D. and Goswami, B.N., 2012. Processes of 30–90 days sea surface temperature variability in the northern Indian

Ocean during boreal summer. Climate dynamics, 38(9-10), 1901-1916. https://doi.org/10.1007/s00382-011-1015-3.

Vibhute, A., Halder, S., Singh, P., Parekh, A., Chowdary, J.S. and Gnanaseelan, C., 2020. Decadal variability of tropical Indian Ocean sea surface temperature and its impact on the Indian summer monsoon. *Theoretical and Applied Climatology*, *141*, pp.551-566. https://doi.org/10.1007/s00704-020-03216-1

Waliser, D.E. and Gautier, C., 1993. A satellite-derived climatology of the ITCZ. *Journal of climate*, *6*(11), pp.2162-2174. https://doi.org/10.1175/1520-0442(1993)006<2162:ASDCOT>2.0.CO;2

Wang, B. and Ding, Q., 2006. Changes in global monsoon precipitation over the past 56 years. *Geophysical Research Letters*, *33*(6). https://doi.org/10.1029/2005GL025347

Wang, B. and Ding, Q., 2008. Global monsoon: Dominant mode of annual variation in the tropics. *Dynamics of Atmospheres and Oceans*, *44*(3-4), pp.165-183. https://doi.org/10.1016/j.dynatmoce.2007.05.002

Wang, B. and LinHo., 2002. Rainy Season of the Asian–Pacific Summer Monsoon. *Journal of Climate*, *15*(4), 386-398. https://doi.org/10.1175/1520-0442(2002)015<0386:RSOTAP>2.0.CO;2

Wang, B., 2006. *The asian monsoon*. Springer Science & Business Media.

Wang, B., Chang, C.P., Wang, Z. and Hendon, H., 2006. The Asian winter monsoon. *The Asian Monsoon*, pp.89-127.

Wang, B., Ding, Q., Fu, X., Kang, I.S., Jin, K., Shukla, J. and Doblas-Reyes, F., 2005. Fundamental challenge in simulation and prediction of summer monsoon rainfall. Geophysical Research Letters, 32(15). https://doi.org/10.1029/2005GL022734

Wang, B., Jin, C. and Liu, J., 2020. Understanding future change of global monsoons projected by CMIP6 models. *Journal of Climate*, *33*(15), pp.6471-6489. https://doi.org/10.1175/JCLI-D-19-0993.1

Wang, B., Kang, I.S. and Lee, J.Y., 2004. Ensemble simulations of Asian–Australian monsoon variability by 11 AGCMs. *Journal of Climate*, *17*(4), pp.803-818. https://doi.org/10.1175/1520-0442(2004)017<0803:ESOAMV>2.0.CO;2

Wang, B., Liu, J., Kim, H.J., Webster, P.J. and Yim, S.Y., 2012. Recent change of the global monsoon precipitation (1979–2008). *Climate Dynamics*, *39*, pp.1123-1135. https://doi.org/10.1007/s00382-011-1266-z

Wang, B., Wu, Z., Li, J., Liu, J., Chang, C.P., Ding, Y. and Wu, G., 2008. How to measure the strength of the East Asian summer monsoon. *Journal of Climate*, *21*(17), pp.4449-4463. https://doi.org/10.1175/2008JCLI2183.1

Wang, B., Xiang, B., Li, J., Webster, P.J., Rajeevan, M.N., Liu, J. and Ha, K.J., 2015. Rethinking Indian monsoon rainfall prediction in the context of recent global warming. *Nature communications*, *6*(1), p.7154. https://doi.org/10.1038/ncomms8154

Wang, C., Kim, D., Ekman, A.M., Barth, M.C. and Rasch, P.J., 2009. Impact of anthropogenic aerosols on Indian summer monsoon. *Geophysical Research Letters*, *36*(21). https://doi.org/10.1029/2009GL040114

Wang, J., Yang, B.A.O., Ljungqvist, F.C. and Zhao, Y.A.N., 2013. The relationship between the Atlantic Multidecadal Oscillation and temperature variability in China during the last millennium. *Journal of Quaternary Science*, *28*(7), pp.653-658. https://doi.org/10.1002/jqs.2658

Wang, L. and Lu, M.M., 2017. The east Asian winter monsoon. In *The global monsoon system: research and forecast* (pp. 51-61). https://doi.org/10.1142/9789813200913_0005

Wang, X. and Wang, C., 2014. Different impacts of various El Niño events on the Indian Ocean Dipole. Climate dynamics, 42(3-4), 991-1005. https://doi.org/10.1007/s00382-013-1711-2.

Wang, X., Tan, W. and Wang, C., 2018. A new index for identifying different types of El Niño Modoki events. *Climate Dynamics*, *50*, pp.2753-2765. https://doi.org/10.1007/s00382-017-3769-8

Wang, Y., Li, S. and Luo, D., 2009. Seasonal response of Asian monsoonal climate to the Atlantic Multidecadal Oscillation. Journal of Geophysical Research: Atmospheres, 114(D2). https://doi.org/10.1029/2008JD010929.

Wasko, C., Sharma, A. and Westra, S., 2016. Reduced spatial extent of extreme storms at higher temperatures. *Geophysical Research Letters*, *43*(8), pp.4026-4032. https://doi.org/10.1002/2016GL068509

WCRP, Monsoon factsheet, https://www.wcrp-climate.org/documents/monsoon_factsheet.pdf

Webster, P.J. and Yang, S., 1992. Monsoon and ENSO: Selectively interactive systems. Quarterly Journal of the Royal Meteorological Society, 118(507), 877-926. https://doi.org/10.1002/qj.49711850705.

Webster, P.J., 1987. The variable and interactive monsoon. *Monsoons*.

Webster, P.J., Magana, V.O., Palmer, T.N., Shukla, J., Tomas, R.A., Yanai, M.U. and Yasunari, T., 1998. Monsoons: Processes, predictability, and the prospects for prediction. Journal of Geophysical Research: Oceans, 103(C7), 14451-14510. https://doi.org/10.1029/97JC02719

Wei, W. and Lohmann, G., 2012. Simulated Atlantic multidecadal oscillation during the Holocene. Journal of Climate, 25(20), 6989-7002. https://doi.org/10.1175/JCLI-D-11-00667.1.

Wen, T., Chen, Q., Li, J., Ding, R., Tseng, Y.H., Hou, Z. and Li, X., 2020. Influence of the North Pacific Victoria mode on the madden–Julian oscillation. *Frontiers in Earth Science*, *8*, p.584001. https://doi.org/10.3389/feart.2020.584001

Weng, H., Ashok, K., Behera, S.K., Rao, S.A. and Yamagata, T., 2007. Impacts of recent El Niño Modoki on dry/wet conditions in the Pacific rim during boreal summer. Climate dynamics, 29(2-3), 113-129. https://doi.org/10.1007/s00382-007-0234-0.

WMO (2010). Report of the meeting of the management group of the commission for climatology. Geneva, 18- 21 May, 2010.

Xavier, A., Manoj, M.G. and Mohankumar, K., 2018. On the dynamics of an extreme rainfall event in northern India in 2013. *Journal of Earth System Science*, *127*, pp.1-13. https://doi.org/10.1007/s12040-018-0931-6

Xavier, A.K., Varikoden, H., Babu, C.A. and Reshma, T., 2023. Influence of PDO and ENSO with Indian summer monsoon rainfall and its changing relationship before and after 1976 climate shift. *Climate Dynamics*, pp.1-18. https://doi.org/10.1007/s00382-023-06865-w

Xavier, P.K. and Goswami, B.N., 2007. An analog method for real-time forecasting of summer monsoon subseasonal variability. *Monthly Weather Review*, *135*(12), 4149-4160. https://doi.org/10.1175/2007MWR1854.1.

Xie, X., Wang, H., Liu, X., Li, J., Wang, Z. and Liu, Y., 2016. Distinct effects of anthropogenic aerosols on the East Asian summer monsoon between multidecadal strong and weak monsoon stages. *Journal of Geophysical Research: Atmospheres*, *121*(12), pp.7026-7040. https://doi.org/10.1002/2015JD024228

Yaduvanshi, A., Nkemelang, T., Bendapudi, R. and New, M., 2021. Temperature and rainfall extremes change under current and future global warming levels across Indian climate zones. *Weather and Climate Extremes*, *31*, p.100291. https://doi.org/10.1016/j.wace.2020.100291

Yano, J.I. and Ambaum, M.H., 2017. Moist static energy: Definition, reference constants, a conservation law and effects on buoyancy. Quarterly Journal of the Royal Meteorological Society, 143(708), 2727-2734. https://doi.org/10.1002/qj.3121

Yao, C., Yang, S., Qian, W., Lin, Z. and Wen, M., 2008. Regional summer precipitation events in Asia and their changes in the past decades. *Journal of Geophysical Research: Atmospheres*, *113*(D17). https://doi.org/10.1029/2007JD009603

Yasunaga, K., Yokoi, S., Inoue, K. and Mapes, B.E., 2019. Space–time spectral analysis of the moist static energy budget equation. Journal of Climate, 32(2), 501-529. https://doi.org/10.1175/JCLI-D-18-0334.1

Yasunari, T., Saito, K. and Takata, K., 2006. Relative roles of large-scale orography and land surface processes in the global hydroclimate. Part I: Impacts on monsoon systems and

the tropics. *Journal of Hydrometeorology*, *7*(4), pp.626-641. https://doi.org/10.1175/JHM515.1

Yatagai, A., Kamiguchi, K., Arakawa, O., Hamada, A., Yasutomi, N. and Kitoh, A., 2012. APHRODITE: Constructing a long-term daily gridded precipitation dataset for Asia based on a dense network of rain gauges. Bulletin of the American Meteorological Society, 93(9), 1401-1415. https://doi.org/10.1175/BAMS-D-11-00122.1.

Yatagai, A., Maeda, M., Khadgarai, S., Masuda, M. and Xie, P., 2020. End of the day (EOD) judgment for daily rain-gauge data. *Atmosphere*, *11*(8), p.772. https://doi.org/10.3390/atmos11080772

Yihui, D. and Chan, J.C., 2005. The East Asian summer monsoon: an overview. *Meteorology and Atmospheric Physics*, *89*(1-4), pp.117-142. https://doi.org/10.1007/s00703-005-0125-z

Yim, S.Y., Wang, B., Liu, J. and Wu, Z., 2014. A comparison of regional monsoon variability using monsoon indices. *Climate dynamics*, *43*, pp.1423-1437. https://doi.org/10.1007/s00382-013-1956-9

You, Y. and Ting, M., 2021. Observed Trends in the South Asian Monsoon Low-Pressure Systems and Rainfall Extremes Since the Late 1970s. *Geophysical Research Letters*, *48*(9), p.e2021GL092378. https://doi.org/10.1029/2021GL092378

Yuan, D., Hu, X., Xu, P., Zhao, X., Masumoto, Y. and Han, W., 2018. The IOD-ENSO precursory teleconnection over the tropical Indo-Pacific Ocean: dynamics and long-term trends under global warming. *Journal of Oceanology and Limnology*, *36*(1), pp.4-19. https://doi.org/10.1007/s00343-018-6252-4

Zhai, J., Mondal, S.K., Fischer, T., Wang, Y., Su, B., Huang, J., Tao, H., Wang, G., Ullah, W. and Uddin, M.J., 2020. Future drought characteristics through a multi-model ensemble from CMIP6 over South Asia. *Atmospheric Research*, *246*, p.105111. https://doi.org/10.1016/j.atmosres.2020.105111

Zhang, C., 2005. Madden-julian oscillation. *Reviews of Geophysics*, *43*(2). https://doi.org/10.1029/2004RG000158

Zhang, J., Furtado, K., Turnock, S.T., Mulcahy, J.P., Wilcox, L.J., Booth, B.B., Sexton, D., Wu, T., Zhang, F. and Liu, Q., 2021. The role of anthropogenic aerosols in the anomalous cooling from 1960 to 1990 in the CMIP6 Earth system models. *Atmospheric Chemistry and Physics*, *21*(24), pp.18609-18627. https://doi.org/10.5194/acp-21-18609-2021

Zhang, M., Cao, Q., Zhu, F., Lall, U., Hu, P., Jiang, Y. and Kan, G., 2022. The asymmetric effect of different types of ENSO and ENSO Modoki on rainy season over the Yellow River basin, China. *Theoretical and Applied Climatology*, *149*(3-4), pp.1567-1581. https://doi.org/10.1007/s00704-022-04128-y

Zhang, R. and Delworth, T.L., 2007. Impact of the Atlantic multidecadal oscillation on North Pacific climate variability. *Geophysical Research Letters*, *34*(23). https://doi.org/10.1029/2007GL031601

Zhang, W. and Zhou, T., 2019. Significant increases in extreme precipitation and the associations with global warming over the global land monsoon regions. *Journal of Climate*, *32*(24), pp.8465-8488. https://doi.org/10.1175/JCLI-D-18-0662.1

Zhang, W. and Zhou, T., 2020. Increasing impacts from extreme precipitation on population over China with global warming. *Science Bulletin*, *65*(3), pp.243-252. https://doi.org/10.1016/j.scib.2019.12.002

Zhang, W., Zhou, T., Zou, L., Zhang, L. and Chen, X., 2018. Reduced exposure to extreme precipitation from 0.5 C less warming in global land monsoon regions. *Nature Communications*, *9*(1), p.3153. https://doi.org/10.1038/s41467-018-05633-3

Zhang, X., Alexander, L., Hegerl, G.C., Jones, P., Tank, A.K., Peterson, T.C., Trewin, B. and Zwiers, F.W., 2011. Indices for monitoring changes in extremes based on daily temperature and precipitation data. *Wiley Interdisciplinary Reviews: Climate Change*, *2*(6), pp.851-870. https://doi.org/10.1002/wcc.147

Zhang, X., Wu, M., Liu, Y., Hao, Z. and Zheng, J., 2018. The relationship between the East Asian Summer Monsoon and El Niño-Southern Oscillation revealed by reconstructions and a control simulation for millennium. *Quaternary International*, *493*, pp.106-113. https://doi.org/10.1016/j.quaint.2018.06.024

Zhang, Y. and Ayyub, B.M., 2021. Temperature extremes in a changing climate. *Climate Change and Extreme Events*, pp.9-23. https://doi.org/10.1016/B978-0-12-822700-8.00001-9

Zhang, Y., Wallace, J.M. and Battisti, D.S., 1997. ENSO-like interdecadal variability: 1900–93. *Journal of climate*, *10*(5), pp.1004-1020. https://doi.org/10.1175/1520-0442(1997)010<1004:ELIV>2.0.CO;2

Zhou, T., Turner, A.G., Kinter, J.L., Wang, B., Qian, Y., Chen, X., Wu, B., Liu, B., Zou, L. and He, B., 2016. GMMIP (v1. 0) contribution to CMIP6: global monsoons model inter-comparison project. *Geoscientific Model Development*, *9*(10), pp.3589-3604. https://doi.org/10.5194/gmd-9-3589-2016

Zhou, T., Wu, B. and Dong, L., 2014. Advances in research of ENSO changes and the associated impacts on Asian-Pacific climate. *Asia-Pacific Journal of Atmospheric Sciences*, *50*, pp.405-422. https://doi.org/10.1007/s13143-014-0043-4

Zhou, T., Zhang, L. and Li, H., 2008. Changes in global land monsoon area and total rainfall accumulation over the last half century. *Geophysical Research Letters*, *35*(16). https://doi.org/10.1029/2008GL034881

✼✼✼✼✼✼✼✼✼✼✼✼✼✼✼✼✼✼✼